Universität
Zürich^UZH

Physik-Institut

Annual Report
April 2015 - March 2016

Universität
Zürich^UZH

Physik-Institut

Annual Report
April 2015 - March 2016

Winterthurerstrasse 190, CH-8057 Zürich/Schweiz

Front picture: David Wolf of the electronics workshop assembling hardware for the CTA project (Sec. 6).

Picture on the back: 4-channel preamplifier for silicon photomultipliers of the GERDA project (Sec. 3) developped by our electronics workshop (Sec. 18).

Secretariat	044 635 5721	sekretariat@physik.uzh.ch
Prof. L. Baudis	044 635 5777	lbaudis@physik.uzh.ch
Prof. F. Canelli	044 635 5784	canelli@physik.uzh.ch
Prof. J. Chang	044 635 5748	johan.chang@physik.uzh.ch
Prof. H.-W. Fink	044 635 5801	hwfink@physik.uzh.ch
Prof. T. Gehrmann	044 635 5818	thomas.gehrmann@physik.uzh.ch
Prof. G. Isidori	044 635 5751	gino.isidori@physik.uzh.ch
Prof. B. Kilminster	044 635 5802	bjk@physik.uzh.ch
Prof. J. Osterwalder	044 635 5827	osterwal@physik.uzh.ch
Prof. S. Pozzorini	044 635 6014	pozzorin@physik.uzh.ch
Prof. A. Schilling	044 635 5791	schilling@physik.uzh.ch
Prof. N. Serra	044 635 5725	nicola.serra@physik.uzh.ch
Prof. A. Signer	056 310 3661	adrian.signer@psi.ch
Prof. U.D. Straumann	044 635 5768	strauman@physik.uzh.ch

The annual reports are available on the internet: http://www.physik.uzh.ch/reports.shtml.

Preface

Research at the Physik-Institut covers both experimental and theoretical physics. Experimental activities include the physics of biological systems, nanometer structures and surface physics, fundamental properties of materials and high-temperature superconductivity as well as accelerator and non-accelerator based elementary-particle and astroparticle physics. Theoretical research concentrates on precision calculations of processes in quantum chromodynamics and on fundamental aspects of high-energy physics.

In addition as many as seven research groups from other departments of our university are affiliated with the Physik-Institut, working in areas such as soft condensed matter at the nanoscale, computational science, medical physics, bio-imaging, astrophysics and cosmology and biophysics (see: `www.physik.uzh.ch/research.shtml`).

The physics department employs about 150 scientific, technical and administrative staff, originating from 28 countries. One quarter of them are female and 80% of the research group members are paid from third-party funds, mainly profiting from research programs of the Swiss National Science Foundation (SNF) and the European Union. The fifteen research groups are led by nine full professors, three independent group leaders and three SNF professors, where the latter receive in addition starting or consolidator grants from the European Research Council.

By covering many fields of modern research we remain an attractive place with lively intellectual interactions. To still reach a critical mass in the various activities we, however, try to have more than one group active in each field, balancing international visibility and diversity. As a result we receive many excellent international applications for PostDoc and PhD student positions.

The Schroedinger colloquium (`www.physik.uzh.ch/schroedinger`), introduced towards the end of 2014, is now well established. The monthly lectures, given by some of the world's leading scientists, are intended for a broad audience from our science faculty.

Over 1100 students are taught physics at any point in time. Students of the medical and vet-suisse faculty and of our science faculty in biology, chemistry, geography, biomedicine and mathematics learn the basic physics principles. In good European tradition we follow the concept of unification of research and education. All our physicists are involved in teaching, including all PostDocs and PhD students who are paid by third-party funds which results in significant subsidizing of the teaching duties of the University. In addition typically fifteen undergraduate physics students and some outside senior physicists support our teaching.

Our scientific success is based to a large extent on the highly qualified and strongly motivated technical experts from our mechanical- and electronics workshops, and information technology. They construct the state-of-the-art laboratory equipment required for new experimental methods, pushing back existing technical limitations. Our success also strongly benefits from our reliable, efficient and very friendly administrative staff.

Kurt Bösiger, former leader of the mechanical workshop, retired in autumn 2015 after more than forty years at our institute. We thank him for his many invaluable contributions, which include the mandatory mechanical machining course for physics bachelor students. Kurt always convincingly argued for the importance of keeping the tools up to date so he could hand over the workshop to his successor Reto Maier, excellently equipped and perfectly organized.

An enormous amount of work goes into the preparations for this years International Physics Olympiad taking place at our institute for a full week in July 2016. Coordinated by Andrea Schneider, preparations for hosting about thousand visitors from 82 countries have started. Many of us are involved in planning of exam questions, lab experiments, entertainment programs, ceremonies, and solving financial bottlenecks.

The professors of the department take part in many scientific organizations, including the national research council, research committees of the Paul Scherrer Institut and advisory boards and panels of numerous international research institutions. They also contribute to the academic self administration of the university and are members of many national and international search committees for new professors.

Members of the institute actively contributed to information events for future students, gave presentations at schools and guided highschool students through our labs. The department regularly participates in the European Masterclass for Particle Physics.

Zürich, May 2016

Prof. Dr. Ueli Straumann

Personnel

Scientific personnel

Thea Klæboe	Årrestad	Sec. 11
Mirco	Ackermann	Sec. 16
PD Dr. Christof	Aegerter	Sec. 16
Simone	Balmelli	Sec. 2
Peter	Barrow	Sec. 4
Prof. Laura	Baudis	Sec. 3, 4
Dr. Giovanni	Benato	Sec. 3
Carlo	Bernard	Sec. 14
Dr. Roland	Bernet	Sec. 10
Dr. Christopher	Betancourt	Sec 10, 9
Iaroslava	Bezshyiko	Sec 10, 9
Dr. Ruxandra	Bondarescu	Sec. 2
Marzia	Bordone	Sec. 1
Dr. Sophia	Borowka	Sec. 1
Yannik	Bötzel	Sec. 2
Espen	Bowen	Sec. 10
Federico	Buccioni	Sec 1
Dr. Albert	Bursche	Sec. 10
Dr. Dario	Buttazzo	Sec 1
Dr. Lea	Caminada	Sec. 11
Prof. Florencia	Canelli	Sec. 6, 11
Dr. Fabio	Cascioli	Sec. 1
Dr. Luca	Castiglioni	Sec. 14
Prof. Johan	Chang	Sec. 12
Dr. Xuan	Chen	Sec. 1
Dr. Nicola	Chiapolini	Sec. 10
Dr. Marcin	Chrząszcz	Sec. 10
Dr. Leandro	Cieri	Sec 1
Dr. Huanyao	Cun	Sec. 14
Paule	Dagenais	Sec 16
Dr. Annapaola	de Cosa	Sec. 11
Riccardo	del Burgo	Sec. 11
Daniel	Destraz	Sec. 12
Dr. Luis	de Lima	Sec. 14
Lorenzo	de Vittori	Sec. 2
David	Dreher	Sec. 16
Dr. Christian	Elsasser	Sec. 10
Dr. Andreas	Engel	Sec. 13
Dr. Conrad	Escher	Sec. 15
Prof. Hans-Werner	Fink	Sec. 15
Dr. Stefan	Förster	Sec. 14
Dr. Domenico	Franco	Sec. 4
Dr. Arno	Gadola	Sec. 6
Camilla	Galloni	Sec. 11
Dr. Michelle	Galloway	Sec. 4
Alsu	Gazizulina	Sec. 13
Dr. Aude	Gehrmann-De Ridder	Sec. 1
Prof. Thomas	Gehrmann	Sec. 1
Philip	Gloor	Sec. 10
Elena	Graverini	Sec. 9, 10
PD Dr. Massimiliano	Grazzini	Sec. 1
Prof. Thomas	Greber	Sec. 14
Roman	Gredig	Sec. 7
Dr. Michael	Greif	Sec. 14
Dr. Nicolas	Greiner	Sec. 1
Dr. Admir	Greljo	Sec. 1
Dr. Henrik	Grundmann	Sec. 13
Dr. Zurab Catalin	Hanga	Sec. 1
Dr. Matthias	Hengsberger	Sec. 14
Dr. Andreas	Hinzmann	Sec. 11
Shang-Xiong	Huang-fu	Sec. 13
Daniel	Hulme	Sec. 1
Dr. Tomas	Hreus	Sec. 11
Dr. Alexander	Huss	Sec. 1
Agnieszka	Ilnicka	Sec. 1
Prof. Gino	Isidori	Sec. 1
Dr. Dimitri	Ivanov	Sec. 1
Oleh	Ivashko	Sec. 12
Matthieu	Jaquier	Sec. 1
Prof. Philippe	Jetzer	Sec. 2
Dominik	Kara	Sec. 1
Dr. Hafiza Rizwana	Kausar	Sec. 2
Gaudenz	Kessler	Sec. 4
Prof. Benjamin	Kilminster	Sec. 11, 9, 5
Dr. Alexander	Kish	Sec. 3, 4
Pavlo	Kliuiev	Sec. 14
Aram	Kostanyan	Sec. 14
Rafael	Küng	Sec. 2
Valère	Lambert	Sec. 11
Flavio	Lanfranconi	Sec. 16
Dr. Clemens	Lange	Sec. 11
Dr. Dominik	Leuenberger	Sec. 14
Junhui	Liao	Sec. 5
Dr. Jonas	Lindert	Sec. 1
Federica	Lionetto	Sec. 10
Dr. Jean-Nicolas	Longchamp	Sec. 15
Dr. Adriano	Lopresti	Sec. 1
Marianna	Lorenzo	Sec. 15
Peter	Lowdon	Sec. 1
Archana	Mallavalli	Sec. 16
Dr. David	Marzocca	Sec. 1
Andrea	Mauri	Sec. 10
Daniel	Mayani Paras	Sec. 4
Dr. Gerson	Mette	Sec. 14

Michael	Miloradovic	Sec. 4
Dr. Elisa	Miniussi	Sec. 14
Rizalina	Mingazheva	Sec. 4
Irshad	Mohammed	Sec. 2
Dr. Claude	Monney	Sec. 14
Niccolo	Moretti	Sec. 1
Dr. Katharina	Müller	Sec. 10
Jan	Niehues	Sec. 1
Jennifer	Ngadiuba	Sec. 11
Deniz Gizem	Oeztürk	Sec. 1
Prof. Jürg	Osterwalder	Sec. 14
Payam	Pakarha	Sec. 4
Dr. Monalisa	Patra	Sec. 1
Andrea	Pattori	Sec. 1
Lionel	Philippoz	Sec. 2
Francesco	Piastra	Sec. 4
Deborah	Pinna	Sec. 11
Prof. Stefano	Pozzorini	Sec. 1
Sahil	Puri	Sec. 16
Dirk	Rathlev	Sec. 1
Giorgia	Rauco	Sec. 11
Dr. Peter	Robmann	Sec. 5, 7, 8, 11
PD Dr. Prasenjit	Saha	Sec. 2
Daniel	Salerno	Sec. 11
Mirna	Saliba	Sec. 14
Hayk	Sargsyan	Sec. 1
Andreas	Schärer	Sec. 2
Dr. Lukas	Schertel	Sec. 16
Prof. Andreas	Schilling	Sec. 13
Timo	Schmidt	Sec. 1
Dr. Jale	Schneider	Sec. 16
Dr. Marek	Schönherr	Sec. 1
Adrian	Schuler	Sec. 14
Dr. Lara	Selvaggi	Sec. 16
Prof. Nicola	Serra	Sec. 9, 10
Prof. Adrian	Signer	Sec. 1
Dr. Rafael	Silva Coutinho	Sec. 10
Roland	Stania	Sec. 14
Dr. Olaf	Steinkamp	Sec. 10
Dr. Barbara	Storaci	Sec. 9, 10
Prof. Ulrich	Straumann	Sec. 6, 7, 10
Denys	Sutter	Sec. 12
Dr. Alessandro	Torre	Sec. 1
Marco	Tresch	Sec. 10
Dr. Severine	Urdy	Sec. 16
Dr. Andries	van der Schaaf	Sec. 8
Dr. Denys	van Dyk	Sec. 1
Dr. Achim	Vollhardt	Sec. 6, 10, 18
Dr. Fabian	von Rohr	Sec. 13
Kay	Waltar	Sec. 14
Manuel	Walter	Sec. 3
Qiang	Wang	Sec. 13
Dr. Yuehuan	Wei	Sec. 4
Andreas	Weiden	Sec. 10
Dr. Rasmus	Westerström	Sec. 14
Flavio	Wicki	Sec. 15
Dr. Marius	Wiesemann	Sec. 1
Julien	Wulf	Sec. 4
Dr. Yong	Yang	Sec. 11
Wolf-Dietrich	Zabka	Sec. 14
Xiaofu	Zhang	Sec. 13
Max	Zoller	Sec. 1

Technical and adminstrative personnel

Dr. Carlos	Abellan Beteta	Sec. 10
Chris	Albrecht	Sec. 17
Kurt	Bösiger	Sec. 17
Tiziano	Crudeli	Technical support
Shiva	Farghar	Adminiatration
Daniel	Florin	Sec. 18, 6
Dario	Gabrielli	Sec. 17
Carmelina	Genovese	Secretariat
Ruth	Halter	Secretariat
Andreas	James	Sec. 3,4
Thomas	Kälin	Sec. 14
Gian	Knüsel	Sec. 17
Hanspeter	Koch	Lecture demonstrations
Bruno	Lussi	Sec. 17
Reto	Maier	Sec. 17
Brandon	Markwalder	Sec. 17
Esther	Meier	Secretariat
Lucien	Pauli	Lecture demonstrations
Maria del Pilar	Peco Regales	Sec. 10
Jan Ten	Pierick	Sec. 2
Monika	Röllin	Secretariat
Marcel	Schaffner	Sec. 17
Silvio	Scherr	Sec. 17
Regina	Schmid	Secretariat
Andrea	Schneider	IPhO
Karen	Schraader Frigg	Admistration
Stefan	Siegrist	Sec. 13
Stefan	Steiner	Sec. 6, 10
Marc	Türler	Administration
Jonas	Vergés	Sec. 15
Pascal	Weyeneth	Sec. 17
David	Wolf	Sec. 18

Contents

1 Theory of Elementary Particles

M. Bordone, S. Borowka, F. Buccioni, D. Buttazzo, X. Chen, L. Cieri, D. van Dyk, A. Gehrmann-De Ridder, T. Gehrmann, M. Grazzini, N. Greiner, A. Greljo, A. Ilnicka, C. Hanga, D. Hulme, A. Huss, D. Ivanov, M. Jaquier, D. Kara, G. Isidori, J. Lindert, P. Lowdon, N. A. Lo Presti, D. Marzocca, N. Moretti, J. Niehues, G. Oeztürk, M. Patra, A. Pattori, S. Pozzorini, D. Rathlev, H. Sargsyan, T, Schmidt, A. Signer, M. Schönherr, A. Visconti, M. Wiesemann, D. Wyler and M. Zoller

in collaboration with:
CERN, IMSc Chennai, Durham University, INFN Firenze, University of Buenos Aires, Freiburg University, Mainz University, INFN Genova, INFN Milano, University of Louvain, MPI Munich, INFN Padova, Peking University, Oxford University, INFN Roma, SLAC, ETH Zürich, DESY Hamburg, TU Dresden, TU Münich

The particle theory group at the Physik-Institut works on a broad spectrum of research projects related to the interpretation of data from high energy particle colliders. These cover precision calculations of benchmark observables, simulation of full collider events, identification of optimal observables for searches and measurements, physics beyond the Standard Model (SM), as well as developments of calculational techniques. We summarize some highlights of last year's research below.

1.1 Vector boson pair production at NNLO

The production of vector-boson pairs is a relevant process for physics studies within and beyond the SM. First of all, this process can be used to measure the vector boson trilinear couplings. Any deviation from the coupling structure predicted by $SU(2) \otimes U(1)$ gauge invariance would be a signal of new physics. The Tevatron collaborations have measured cross sections for vector-boson pair production at invariant masses larger than those probed at LEP2, setting limits on the corresponding anomalous couplings, and the LHC experiments are now continuing this research program. Vector boson pairs provide also an important background for new physics searches.

Up to a few years ago, the status of theoretical predictions for vector-boson pair production was essentially limited to next-to-leading order (NLO) in QCD perturbation theory. The bottleneck was essentially the knowledge of the relevant two-loop amplitudes. Recently, a major step forward has been carried out, with the evaluation of all the two-loop planar and non planar master integrals relevant for the production of off-shell vector boson pairs, and the calculation of the corresponding helicity amplitudes has been completed.

Even having all the relevant amplitudes, the computation of the next-to-next-to-leading order (NNLO) corrections is still a non-trivial task, due to the presence of infrared (IR) singularities at intermediate stages of the calculation, and numerical techniques cannot be straightforwardly applied. To handle and cancel these singularities at NNLO the q_T subtraction formalism [6] is particularly suitable, since it is fully developed to work in the hadronic production of heavy colourless final states.

In the following we present theoretical predictions [1] for the case of $Z\gamma$ and $W\gamma$ production at the LHC and compare them with the ATLAS data from Ref. [2]. The required tree-level and one-loop amplitudes were obtained with the OpenLoops [3] generator, which employs the Denner-Dittmaier algorithm for the numerical evaluation of one-loop integrals and implements a fast numerical recursion for the calculation of NLO scattering amplitudes within the SM. The two loop amplitudes are taken from [4].

For the electroweak couplings we use the so-called G_μ scheme, where the input parameters are G_F, m_W, m_Z. In particular we use the values $G_F = 1.16639 \times 10^{-5}$ GeV^{-2}, $m_W = 80.399$ GeV, $m_Z = 91.1876$ GeV, $\Gamma_Z = 2.4952$ GeV and $\Gamma_W = 2.1054$ GeV. We set the CKM matrix to unity. We use the MMHT 2014 [5] sets of parton distribution functions (PDFs), with densities and α_S evaluated at each corresponding order (i.e., we use $(n+1)$-loop α_S at N^{n}LO, with $n = 0,1,2$), and we consider $N_f = 5$ massless quarks/antiquarks and gluons in the initial state. The default renormalization (μ_R) and factorization (μ_F) scales are set to $\mu_R = \mu_F = \mu_0 \equiv \sqrt{m_V^2 + (p_T^\gamma)^2}$, where m_V is the mass of the vector boson and p_T^γ the transverse momentum of the photon. Scale uncertainties are estimated by varying μ_F and μ_R independently in the range $0.5\mu_0$ and $2\mu_0$.

The present formulation of the q_T subtraction formalism [6] is limited to the production of colourless sys-

Tab. 1.1 –
Results on fiducial cross sections to the ATLAS 7 TeV analyses on $pp \to \ell\nu\gamma$, $pp \to \ell\ell\gamma$, and $pp \to \nu\nu\gamma$. Event-selection criteria are detailed in Tables 1,4,6 of Ref. [1].

	$p_{\mathrm{T,cut}}^{\gamma}$ [GeV]	N_{jet}	σ_{LO} [pb]	σ_{NLO} [pb]	σ_{NNLO} [pb]	σ_{ATLAS} [pb]	$\frac{\sigma_{\mathrm{NLO}}}{\sigma_{\mathrm{LO}}}$	$\frac{\sigma_{\mathrm{NNLO}}}{\sigma_{\mathrm{NLO}}}$
$pp \to W\gamma \to \ell\nu\gamma + X$	15	≥ 0	$0.8726\,^{+6.8\%}_{-8.1\%}$	$2.058\,^{+6.8\%}_{-6.8\%}$	$2.453\,^{+4.1\%}_{-4.1\%}$	2.77 ± 0.03 (stat) ± 0.33 (syst) ± 0.14 (lumi)	2.36	1.19
@ $\sqrt{s} = 7\,\mathrm{TeV}$	15	$= 0$	$0.8726\,^{+6.8\%}_{-8.1\%}$	$1.395\,^{+5.2\%}_{-5.8\%}$	$1.493\,^{+1.7\%}_{-2.7\%}$	1.76 ± 0.03 (stat) ± 0.21 (syst) ± 0.08 (lumi)	1.60	1.07
	40	≥ 0	$0.1158\,^{+2.6\%}_{-3.7\%}$	$0.3959\,^{+9.0\%}_{-7.3\%}$	$0.4971\,^{+5.3\%}_{-4.7\%}$		3.42	1.26
$pp \to Z\gamma \to \ell^+\ell^-\gamma + X$	15	≥ 0	$0.8149\,^{+8.0\%}_{-9.3\%}$	$1.222\,^{+4.2\%}_{-5.3\%}$	$1.320\,^{+1.3\%}_{-2.3\%}$	1.31 ± 0.02 (stat) ± 0.11 (syst) ± 0.05 (lumi)	1.50	1.08
@ $\sqrt{s} = 7\,\mathrm{TeV}$	15	$= 0$	$0.8149\,^{+8.0\%}_{-9.3\%}$	$1.031\,^{+2.7\%}_{-4.3\%}$	$1.059\,^{+0.7\%}_{-1.4\%}$	1.05 ± 0.02 (stat) ± 0.10 (syst) ± 0.04 (lumi)	1.27	1.03
	40	≥ 0	$0.0736\,^{+3.4\%}_{-4.5\%}$	$0.1320\,^{+4.2\%}_{-4.0\%}$	$0.1543\,^{+3.1\%}_{-2.8\%}$		1.79	1.17
$pp \to Z\gamma \to \nu\bar{\nu}\gamma + X$	100	≥ 0	$0.0788\,^{+0.3\%}_{-0.9\%}$	$0.1237\,^{+4.1\%}_{-3.1\%}$	$0.1380\,^{+2.5\%}_{-2.3\%}$	0.133 ± 0.013 (stat) ± 0.020 (syst) ± 0.005 (lumi)	1.57	1.12
@ $\sqrt{s} = 7\,\mathrm{TeV}$	100	$= 0$	$0.0788\,^{+0.3\%}_{-0.9\%}$	$0.0881\,^{+1.2\%}_{-1.3\%}$	$0.0866\,^{+1.0\%}_{-0.9\%}$	0.116 ± 0.010 (stat) ± 0.013 (syst) ± 0.004 (lumi)	1.12	0.98

tems F and, hence, it does not allow us to deal with the parton fragmentation subprocesses. Therefore, we consider only direct photons, and we rely on the smooth cone isolation criterion. Considering a cone of radius $r = \sqrt{(\Delta\eta)^2 + (\Delta\phi)^2}$ around the photon, we require that the total amount of hadronic (partonic) transverse energy E_T inside the cone is smaller than $E_T^{\max}(r)$,

$$E_T^{\max}(r) \equiv \epsilon_\gamma \, p_T^\gamma \left(\frac{1-\cos r}{1-\cos R} \right)^n ;$$

the isolation criterion $E_T < E_T^{\max}(r)$ has to be fulfilled for all cones with $r \leq R$. All results presented here are obtained with $\epsilon_\gamma = 0.5$, $n = 1$ and $R = 0.4$.

Jets are reconstructed with the anti-k_T algorithm with radius parameter $D = 0.4$, and a jet must have a transverse momentum $p_T^{\mathrm{jet}} > 30$ GeV and pseudorapidity $|\eta^{\mathrm{jet}}| < 4.4$.

We compare our predictions to the ATLAS results for $W\gamma$ and $Z\gamma$ at a centre of mass energy of 7 TeV [2]. Experimental results and theoretical predictions on fiducial cross sections are collected in Table 1.1 for the different channels, with and without a veto against jets. The precise kinematic cuts to define these fiducial cross sections are detailed in Tables 1, 4, 6 of Ref. [1], and are not repeated here.

The predicted inclusive $W\gamma$ cross sections ($W^+\gamma$ and $W^-\gamma$ are always summed over) with the soft p_T^γ cut of 15 GeV are quite large: the NLO K factor is +136%, and the NNLO corrections increase the NLO results by +19%. The measurement of the inclusive cross section by ATLAS shows a 2σ excess with respect to the NLO prediction, which is reduced to well below 1σ when including the NNLO corrections. The impact of QCD corrections at NLO and NNLO is reduced to 60% and 7%, respectively, when a jet veto is applied ($N_{\mathrm{jet}} = 0$). Such an effect is expected and apparently leads to a more stable perturbative prediction, but also to the possible need of more conservative procedures to estimate perturbative uncertainties. In the exclusive case, the excess of the measured fiducial cross sections over the theoretical prediction is reduced from 1.6σ to 1.2σ when going from NLO to NNLO. We note that the scale variations at NLO significantly underestimate the impact of the NNLO corrections, in particular in the inclusive case.

The predicted $Z\gamma$ cross sections in the visible Z decay mode with the soft p_T^γ cut of 15 GeV get corrected by +50% (+27%) at NLO and by +8% (+3%) at NNLO in the inclusive (exclusive) case, respectively. Both the NLO and NNLO predictions are in agreement with the experimental results, and the NNLO corrections improve the agreement, especially in the inclusive case.

It is obvious that the $W\gamma$ process features much larger radiative effects with respect to the $Z\gamma$ process, which should be contrasted to what happens in the case of inclusive W and Z boson production, where QCD radiative corrections are essentially identical. It is thus the emission of the additional photon that breaks the similarity between the charged-current and the neutral-current processes. By studying the LO contributions to the $Z\gamma$ and $W\gamma$ cross sections it turns out that the additional Feynman diagram in which the photon is radiated off the W boson gives rise to a *radiation zero* [7], which does not exist in $Z\gamma$ production. This exact zero, present in the on-shell partonic $W\gamma$ tree-level amplitude at $\cos\theta^* = 1/3$, where θ^* is the scattering angle in the centre-of-mass frame, gets diluted by the convolution with the parton densities and by off-shell effects, but it is responsible for the suppression of the Born level $W\gamma$ cross section with respect to $Z\gamma$. Real radiation appearing beyond LO breaks the radiation zero, and thus the relative impact of higher-order corrections is significantly increased.

Besides the cross section in the fiducial region, ATLAS has also provided the measured cross sections differential in the photon transverse momentum. A comparison of the resulting distributions with our theoretical NLO and NNLO predictions is shown in Fig. 1.1 for the processes $pp(\to W\gamma) \to \ell\nu\gamma$ (upper plots) and $pp(\to Z\gamma) \to \ell^+\ell^-\gamma$ (lower plots), both for the inclusive (left plots) and the exclusive (right plots) case. In general, the inclusion of NNLO corrections significantly improves the agreement between data and theory. The improvement is particularly important in the inclusive $W\gamma$ case, and less pronounced for $Z\gamma$ and for the exclusive predictions, where the overall size of NNLO corrections is significantly smaller.

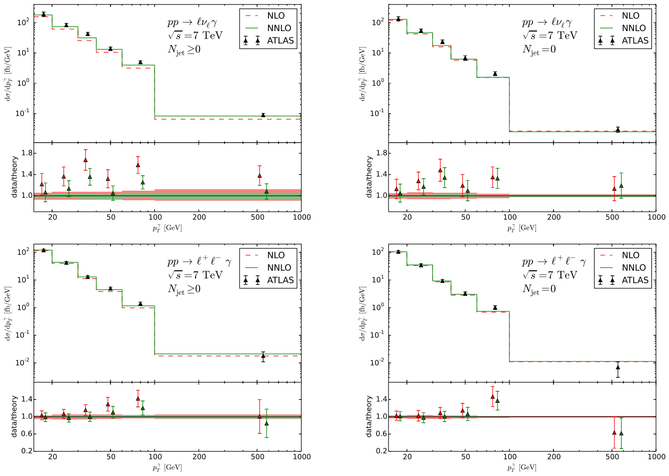

FIG. 1.1 – Photon transverse momentum distribution for the processes $pp(\to W\gamma) \to \ell\nu\gamma$ (upper plots) and $pp(\to Z\gamma) \to \ell^+\ell^-\gamma$ (lower plots) in the inclusive (left) and exclusive case (right) at NLO (red, dashed) and NNLO (green, solid) compared to ATLAS data. In the upper panel, only experimental uncertainties are shown. The lower panel shows the data/theory ratio for both theory predictions, and the bands indicate theoretical uncertainty estimates from scale variations.

When switching to a harder cut of 40 GeV on p_T^γ, Table 1.1 shows significantly increased corrections of +242% and +79% at NLO and of +26% and +19% at NNLO for the processes $pp(\to W\gamma) \to \ell\nu\gamma$ and $pp(\to Z\gamma) \to \ell^+\ell^-\gamma$, respectively.

The predicted fiducial cross sections for $pp \to \nu\bar{\nu}\gamma$ in the ATLAS setup at 7 TeV [2] are presented in Table 1.1, summed over three neutrino channels, and show relative corrections of +57% (+12%) at NLO and +12% (−2%) at NNLO in the inclusive (exclusive) case. The inclusive NNLO prediction is in good agreement with the cross section measured by ATLAS. In the exclusive case, $N_{\rm jet} = 0$, the NNLO corrections are very small, with most likely underestimated scale uncertainties at the 1% level, and we observe quite a significant discrepancy with respect to the ATLAS measurement. This can be understood by hadronization corrections, which are expected to be small for all the other discussed processes, but lead to sizeable effects in $\nu\bar{\nu}\gamma$, particularly for $N_{\rm jet} = 0$.

[1] M. Grazzini, S. Kallweit and D. Rathlev,
JHEP **1507** (2015) 085.

[2] G. Aad *et al.* [ATLAS Collaboration],
Phys. Rev. D **87** (2013) 11, 112003.
Erratum: [Phys. Rev. D **91** (2015) no.11, 119901].

[3] F. Cascioli, P. Maierhofer and S. Pozzorini,
Phys. Rev. Lett. **108** (2012) 111601.

[4] T. Gehrmann and L. Tancredi, JHEP **1202** (2012) 004.

[5] L. A. Harland-Lang, A. D. Martin, P. Motylinski and R. S. Thorne, Eur. Phys. J. C **75** (2015) no.5, 204.

[6] S. Catani and M. Grazzini,
Phys. Rev. Lett. **98** (2007) 222002.

[7] K. O. Mikaelian, M. A. Samuel and D. Sahdev,
Phys. Rev. Lett. **43** (1979) 746.

1.2 Two-loop five-point functions in QCD

The precise theoretical description of scattering reactions of elementary particles relies on the perturbation theory expansion of the scattering amplitudes describing the process under consideration. In this expansion, higher perturbative orders correspond to more and more virtual particle loops. At present, one-loop corrections can be computed to scattering amplitudes of arbitrary multiplicity, while two-loop corrections are known only for selected two-to-one annihilation or two-to-two scattering processes.

For many experimental observables at higher multiplicity, a substantial increase in statistical precision can

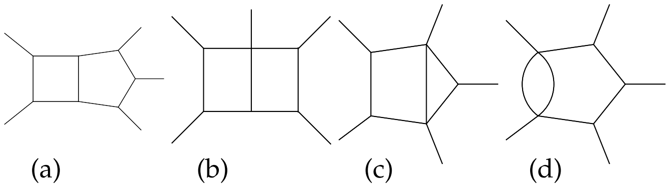

FIG. 1.2 – Genuine five-point planar two-loop integrals.

be expected from the CERN LHC in the near future. Perturbative predictions beyond one loop will be in demand for many precision applications of these data, for example in improved extractions of SM parameters or in search for indirect signatures of new high-scale physics in precision observables. Progress on multi-loop corrections to high-multiplicity amplitudes requires significant advances in two directions: the reduction of the large number of multi-loop Feynman integrals that appear in the amplitude to a small set of so-called master integrals, and the evaluation of the master integrals themselves.

During the last year, we analytically computed for the first time the full set of planar master integrals relevant to massless two-loop five-point scattering [8]. The calculation was made possible by technical advances in the calculation of multi-loop Feynman integrals.

The type of master integrals that appear in a given process depends only on the external kinematics, and on possible internal propagator masses. All two-loop five-parton amplitudes relate to a common set of master integrals: massless on-shell five-point functions at two loops. These can be further classified into genuine five-point functions, four-point functions with one off-shell leg, three-point functions with up to two off-shell legs and off-shell two-point functions. Up to the four-point level, these functions appeared in the context of the derivation of the two-loop amplitude for $\gamma^\star \to 3$ jets and were already computed long ago. For the genuine five-point functions, we find in total 25 new integrals (10 planar and 15 non-planar). The planar integrals can be given in terms of four integral topologies, displayed in Figure 1.2. There are 3, 3, 2, and 2 master integrals for topologies (a), (b), (c), and (d), respectively.

To compute the integrals, we derive differential equations for them in the Mandelstam invariants. The system of differential equations is then brought into a canonical form by means of a transformation of the basis of master integrals to integrals having unit leading singularities. The full set of master integrals can be obtained by direct integration of the differential equations, order-by-order in ϵ, in terms of Chen iterated integrals. Massless scattering is naturally parametrized using momentum twistor variables that solve both the on-shell as well as the momentum conservation constraints. When expressed in terms of these variables, the Chen iterated integrals degenerate to multiple poly-logarithms, for which efficient and precise numerical representations exist.

As a first application of our newly computed integrals, we consider the all-plus helicity five-gluon amplitude at leading color. Since this amplitude vanishes at tree level, it is finite at the one-loop level. Its reduction to master integrals has been derived earlier in the literature. By inserting our expressions for these integrals, we arrive at a relatively simple expression for its finite remainder

$$F_5^{(2)} = \frac{5\pi^2}{12} F_5^{(1)} + \sum_{i=0}^{4} \sigma^i \left\{ \frac{v_5 \mathrm{tr}\left[(1-\gamma_5)\not{p}_4\not{p}_5\not{p}_1\not{p}_2\right]}{(v_2+v_3-v_5)} I_{23,5} + \frac{1}{6}\frac{\mathrm{tr}\left[(1+\gamma_5)\not{p}_4\not{p}_5\not{p}_1\not{p}_2\right]^2}{v_1 v_4} + \frac{10}{3} v_1 v_2 + \frac{2}{3} v_1 v_3 \right\},$$

where the v_i are Mandelstam invariants of adjacent moments and σ^i cyclically shifts all indices by i, and where

$$I_{23,5} = \zeta_2 + \mathrm{Li}_2\left[\frac{(v_5-v_2)(v_5-v_3)}{v_2 v_3}\right] - \mathrm{Li}_2\left[\frac{v_5-v_3}{v_2}\right] - \mathrm{Li}_2\left[\frac{v_5-v_2}{v_3}\right].$$

The simplicity of our result for the all-plus amplitude in QCD is reminiscent of similar results for multi-leg amplitudes in supersymmetric theories. It opens up new possibilities for multi-loop calculations of high-multiplicity processes. Extensions to non-planar integrals and to the full set helicities for five-parton two-loop amplitudes are currently under way.

[8] T. Gehrmann, J. M. Henn and N. A. Lo Presti, Phys. Rev. Lett. **116** (2016) 062001.

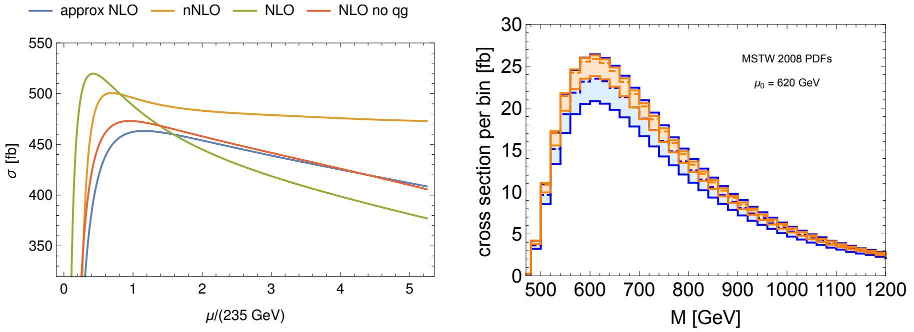

FIG. 1.3 – Scale dependence of various approximations to the total cross section for a Higgs and a top pair (left panel) and invariant mass distribution of the $t\bar{t}H$ system (right panel) for the 13 TeV LHC. The approximate NNLO prediction (orange band), denoted by nNLO, is compared to the NLO prediction (blue band).

1.3 Associated production of a Higgs and a top pair beyond NLO

According to the SM the coupling of a Higgs boson to a fermion is proportional to the mass of the fermion. Hence, the coupling between the Higgs and the top quark, the heaviest known elementary fermion, provides a stringent test of our understanding on how elementary particles obtain their mass. Information on this coupling can be obtained by studying the associated production of a top pair and a Higgs boson.

Typically, calculations at NLO in perturbation theory lead to uncertainties of about $20-30\%$ for this process. While a full NNLO calculation is currently technically not feasible, not even for the total cross section, in Ref. [9] results that go beyond a NLO calculation have been presented for the total cross section and for differential distributions. Approximate NNLO (nNLO) corrections have been computed by applying renormalization-group techniques. This allows to determine those NNLO terms that are enhanced by logarithms. Near threshold, these terms are expected to be dominant and give a reliable estimate of the full NNLO correction.

As an illustration in the left panel of Figure 1.3 the improvement on the scale dependence for the total cross section is shown when going from NLO (green curve) to nNLO (orange). To validate the method, a comparison between the NLO result (red) and approximate NLO result (blue) is also shown for those channels that are included in the approximation ($q\bar{q}$ and gg initial states). The neglect of the remaining subleading channels (qg and $\bar{q}g$ initial states) is compensated for by associating an additional uncertainty due to a conservative estimate of subleading terms.

The result of applying this method to the distribution of the invariant mass of the top pair and the Higgs is shown in the right panel of Figure 1.3. The uncertainty at NLO (blue band) is substantially reduced when going to nNLO (orange band). Results for other distributions also including cuts can be obtained similarly.

1.4 Physics beyond the Standard Model

1.4.1 Pseudo Observables in Higgs physics

Characterizing the properties of the Higgs boson with high precision and minimal theoretical bias is of great importance to investigate the nature of physics beyond the SM. This is the purpose of the so-called Higgs *Pseudo Observables* (PO) approach, developed by our research group in 2014. The Higgs PO are a set of quantities that are well defined from the quantum field theory point of view, that are experimentally accessible, and that allow to characterize possible deviations from the SM in great generality. In 2014 we have classified all the PO relevant to describe Higgs decays. In 2015 we have further developed the approach along three main directions: i) we have identified the PO necessary to describe also Higgs production processes [10]; ii) we have analyzed the effect of electroweak bounds on the PO under the hypothesis that the $h(125)$ particle is the massive excitation of a pure $SU(2)_L$ doublet [11, 12]; iii) we have investigated the effect of NLO radiative corrections in the description of Higgs decays in generic extensions of the SM [13].

In Fig. 1.4 we show the prediction of the $h \to 2e2\mu$ decay spectrum obtained using the PO decomposition (with PO set to their SM values), with and without the inclusion of radiative corrections [13]. The spectrum thus obtained is compared with the complete NLO SM result obtained using the numerical code Prophecy4f. The excellent agreement of the two results is a demonstration of the capability of the PO approach to recover the best up-to-date predictions in the SM case while, at the same, allowing a general description of physics beyond the SM.

One of the most difficult measurement of Higgs couplings at the LHC is the determination of the charm Yukawa couplings. In Ref. [14] we have proposed a new method to determine this coupling via the Higgs production in association with a charm-tagged jet: $\sigma(pp \to hc)$. As a first estimate, we have found that at the LHC with 3000 fb^{-1} it should be possible to derive a constraint of order one, relative to the SM value, for the charm Yukawa coupling.

[9] A. Broggio, A. Ferroglia, B. D. Pecjak, A. Signer and L. L. Yang, JHEP **1603** (2016) 124.

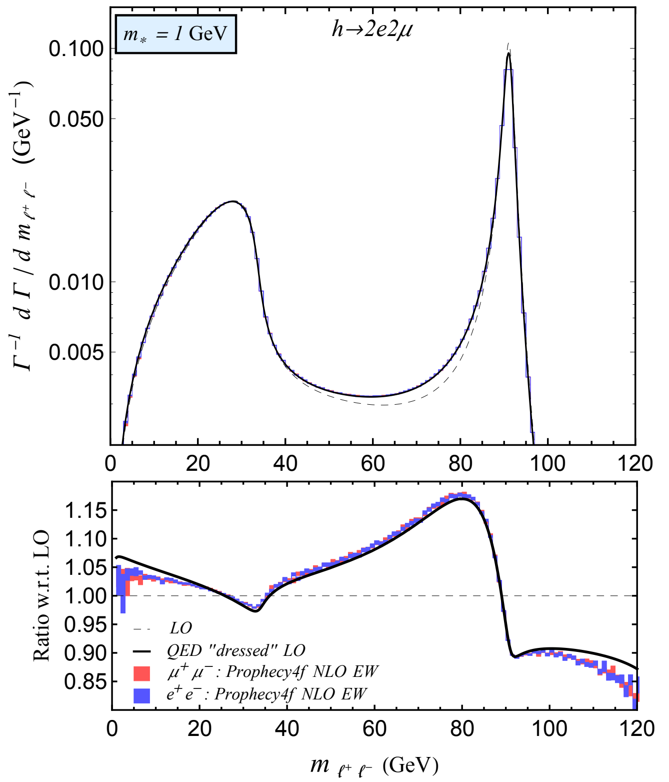

FIG. 1.4 – Dilepton invariant mass spectrum in the SM for the $h \to 2e2\mu$ decay (full line: PO decomposition "dressed" with QED corrections; red and blue bands: complete NLO result from Prophecy4f).

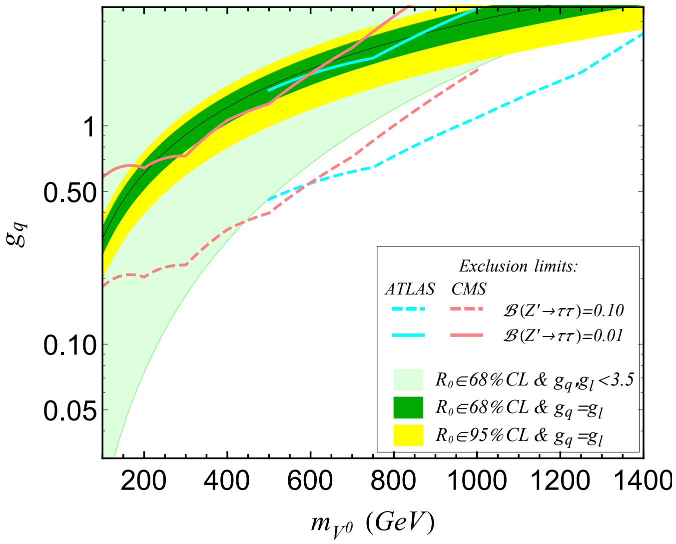

FIG. 1.5 – Mass and coupling of the vector mediator proposed in Ref. [15] to explain the anomalies observed in B decays. The preferred region from the low-energy fit is the green (yellow) band. The dotted lines denote the exclusion limits (below the curve) from direct searches of massive vectors decaying into $\tau^+\tau^-$ pairs at the LHC, assuming different branching ratios ($\mathcal{B}$). The minimal model predicts $\mathcal{B} = 0.1$, but smaller values can be obtained in extended models.

1.4.2 Anomalies in B decays

In view of recent experimental indications of violations of Lepton Flavor Universality (LFU) in B decays, we have analyzed the constraints and implications of LFU interactions, both using an effective theory approach, and employing explicit dynamical models [15, 16].

In Ref. [15] we have shown that a simple dynamical model based on a $SU(2)_L$ triplet of massive vector bosons, coupled predominantly to third generation fermions (both quarks and leptons), can significantly improve the description of present data. In particular, the model decreases the tension between data and SM predictions concerning: i) the breaking of τ–μ universality in $B \to D^{(*)}\ell\nu$ decays; ii) the breaking of μ–e universality in $B \to K\ell^+\ell^-$ decays. Indirectly, the model might also decrease the discrepancy between exclusive and inclusive determinations of $|V_{cb}|$ and $|V_{ub}|$. The minimal version of the model is in tension with ATLAS and CMS direct searches for the new massive vectors (decaying into $\tau^+\tau^-$ pairs), and shown in Fig. 1.5, but this tension can be decreased with additional non-standard degrees of freedom. Further predictions of the model both at low- and high-energies, in view of future high-statistics data, have also been discussed.

In Ref. [16] we have shown that an equally good explanation of present data can be obtained in the context of a weakly broken $U(2)^5$ flavor symmetry (similarly to the case discussed above), but with lepto-quark vector mediators rather than colorless vector fields.

1.4.3 The di-photon excess and other aspects of physics beyond the SM

At the end of 2015 the ATLAS and CMS experiments, after the analysis of the first 13 TeV data, have reported evidences of an excess in the $pp \to 2\gamma$ inclusive distribution for $m_{2\gamma} \approx 750$ GeV. While the evidence of this excess is not yet statistically very large, it is interesting to ask the question if this anomaly can be interpreted as the first direct hint of physics beyond the SM.

A first analysis along this line has been presented in Ref. [17], where it has been shown that interpretation of the signal as a new scalar resonance produced in gluon fusion and decaying to photons is consistent with all relevant exclusion bounds from the 8 TeV LHC run. A simple phenomenological framework to parametrize the properties of the new resonance has also been provided. Using this tool it has been shown in a model-independent way that, if the scalar is produced in gluon fusion, additional new colored and charged particles are required. Some more specific interpretations in various concrete setups, such as a singlet (pseudo-) scalar, composite Higgs, and the MSSM have also beed discussed.

In recent years there has been considerable interest in the problem of the stability of the SM ground state, in the limit where no new physics appear up to very high energy scales. In Ref. [18] we have reviewed the formalism by which the tunneling probability of an unstable ground state can be computed in quantum field theory, with special reference to the Standard Model of electroweak interactions. We have described in some detail the approximations implicitly adopted in such calculations, devoting particular attention to the role of scale invariance. By means of this analysis we have shown that new interactions characterized by a new energy scale, close to the Planck mass, do not invalidate the main conclusions about the stability of the Standard Model ground state derived in absence of such terms (contrary to recent claims of the opposite present in the recent literature). The scope of these analyses is answering the following well-defined physical question: *Does the extrapolation of the SM up to the Planck scale necessarily imply the existence of NP below such a scale?* According to the present experimental values of m_h and m_t, we can state that the answer to this question is *no*.

[10] A. Greljo, G. Isidori, J. M. Lindert and D. Marzocca, Eur. Phys. J. C **76** (2016) 158.

[11] M. Gonzalez-Alonso, A. Greljo, G. Isidori and D. Marzocca, Eur. Phys. J. C **75** (2015) 341.

[12] A. Falkowski, M. Gonzalez-Alonso, A. Greljo and D. Marzocca, Phys. Rev. Lett. **116** (2016) 011801.

[13] M. Bordone, A. Greljo, G. Isidori, D. Marzocca and A. Pattori, Eur. Phys. J. C **75** (2015) 385.

[14] I. Brivio, F. Goertz and G. Isidori, Phys. Rev. Lett. **115** (2015) 211801.

[15] A. Greljo, G. Isidori and D. Marzocca, JHEP **1507** (2015) 142.

[16] R. Barbieri, G. Isidori, A. Pattori and F. Senia, Eur. Phys. J. C **76** (2016) 67.

[17] D. Buttazzo, A. Greljo and D. Marzocca, Eur. Phys. J. C **76** (2016) 116.

[18] L. Di Luzio, G. Isidori and G. Ridolfi, Phys. Lett. B **753** (2016) 150.

2 Astrophysics and General Relativity

R. Angèlil, S. Balmelli, Y. Bötzel, R. Bondarescu, L. De Vittori, Ph. Jetzer, R. Kausar, R. Küng, I. Mohammed, L. Philippoz, P. Saha, A. Schärer

For describing most of astrophysical phenomena, Newtonian gravity is adequate, but for situations involving very strong gravitational fields, or cosmological distances, or the effect of gravity on light, or just extremely precise measurements, relativistic gravity is needed. After a hundred years, Einsteinian gravity continues to pass all tests thrown at it, and meanwhile reveals new manifestations as the first direct detection of gravitational waves. Exploring these is the area of our research.

2.1 Gravitational waves and LISA

This year saw very exciting developments in our field: on 3 December 2015 LISA Pathfinder was successfully launched in orbit from Kourou and reaching L1 Lagrange point around 22 January 2016. The satellite is since then performing as designed.

On 11 February 2016 the LIGO collaboration announced the first direct detection of a gravitational wave signal, originating from the coalescence of two black holes of about 30 solar masses each [1]. This discovery opens without any doubt a new window in the observation of the Universe. Although the existence of gravitational waves had been inferred indirectly, from the spin-down of binary pulsar systems, the first direct detection was an eagerly-awaited event, which took place 100 years after Einstein's final formulation of general relativity and his prediction of gravitational waves. Clearly, these developments will speed up the implementation of the LISA project, aimed to build a space-based observatory for gravitational waves at lower frequency than the Earth-based LIGO detectors. Within our group we addressed various topics on gravitational wave physics.

Simone Balmelli studied the problem of how to incorporate spin effects in the effective-one-body (EOB) approach used to compute in a semi-analytical way the complete waveform emitted during a coalescing process of two massive compact bodies, such as black holes or neutron-stars. He constructed the EOB Hamiltonian with next-to-leading order spin-spin coupling for two non-precessing black holes in the special case of aligned spin. Indeed, by adding a term of fractional 1 PN (post-Newtonian) order to the effective Kerr parameter squared of previously developed EOB models, it was possible to reproduce the next-to-leading order, spin-spin contribution of the PN expanded Hamiltonian for two black holes with spins aligned with the angular momentum vector. To achieve this a special canonical transformation quadratic in the spins had to be added to all the transformations used before in the literature. The additional spin-squared term vanishes whenever the mass-ratio tends to zero, so as to correctly reproduce the exact Kerr dynamics. As next the dynamics of circular orbits in the case of equal masses and spins has been evaluated. It was shown that the effective radial potential still preserves the usual structure, reproducing local minima and maxima, corresponding to stable and unstable orbits. These results were then generalized to the case with arbitrary spin orientations. This was possible by implementing the spin-spin terms after a suitable canonical phase-space transformation of the corresponding ADM Hamiltonian.

Fig. 2.1 –
LISA Pathfinder lift-off on VV06
©ESA - Stephane Corvaja, 2015

In a joint work of Simone Balmelli with Thibault Damour (from the Institut des Hautes Etudes Scientifiques located in Bures-sur-Yvette, France), they presented a new EOB Hamiltonian with next-to-leading order (NLO) spin-spin coupling for black hole binaries endowed with arbitrarily oriented spins. The Hamiltonian is based on the model for parallel spins and equatorial orbits previously developed, but differs from it in several ways. In particular, the NLO spin-spin coupling is not incorporated by a redefinition of the centrifugal radius r_C, but by separately modifying certain sectors of the Hamiltonian, which are identified according to their dependence on the momentum vector. We follow a gauge-fixing procedure, which allows to reduce the 25 different terms of the NLO spin-spin Hamiltonian in Arnowitt-Deser-Misner coordinates to only 9 EOB terms. This is an improvement with respect to a EOB model recently proposed, where 12 EOB terms were involved. Another important advantage is the remarkably simple momentum structure of the spin-spin terms in the effective Hamiltonian, which is simply quadratic up to an overall square root.

Lorenzo De Vittori developed a prescription to generate accurate gravitational wave signals from hyperbolic collisions of compact objects, like black holes or neutron stars. The methods developed by Lorenzo are valid for arbitrary eccentricities and masses of the colliding objects, and take into account radiation reaction effects and spin precession, as due to spin-orbit coupling correction terms. He studied in detail the gravitational wave forms from spinning compact binaries in hyperbolic orbits. In this work an efficient prescription to compute PN accurate gravitational wave polarization states for spinning compact binaries was developed. In hyperbolic encounters the dominant contribution comes from the spin-orbit interaction, which is taken into account up to 1.5 PN. It turns out that both polarization states exhibit the memory effect for gravitational waves from spinning compact binaries in hyperbolic orbits. In particular, an explicit expression for the memory effect was derived in the two polarization states up to first PN order and related to the general Liénard-Wiechert solution for the linearized field equations of unbound systems. Furthermore, some estimates for its possible observation with eLISA were discussed. Gravitational waveforms for precessing eccentric comparable-mass binaries were computed up to second PN. As an expansion parameter eccentricity was used. These gravitational waveforms are of relevance for the future eLISA mission.

The detection of gravitational waves and the corresponding determination of polarization modes is a powerful tool to discriminate between general relativity and alternative theories of gravity such as $f(R)$ theories. Working within the framework of the linearized approach, Rizwana Kausar and Lionel Philippoz investigated the polarization of gravitational waves in $f(R)$ theories, both in the metric and the Palatini formalisms. Besides the usual two transverse-traceless tensor modes present in general relativity, there are in general two additional scalar ones: a massive longitudinal mode and a massless transverse mode (the so-called breathing mode). This last mode has often been overlooked in the literature, due to the assumption that, in $f(R)$, the application of the Lorenz gauge also leads to transverse traceless wave solutions. We however show that this is in general not possible and, in particular, that the traceless condition cannot be imposed. Our findings are in agreement with the results found in the literature using the Newman-Penrose formalism, and thus clarify the inconsistencies found so far.

2.1.1 LISA Pathfinder

We are member of the LISA Pathfinder science team and of the eLISA consortium board. LISA Pathfinder is a dedicated technology demonstrator for the evolved Laser Interferometer Space Antenna (eLISA) ESA mission. The technologies required for eLISA are extremely challenging. LISA Pathfinder essentially mimics one arm of the eLISA constellation by shrinking the 1 million kilometer arm length down to a few tens of centimeters, giving up the sensitivity to gravitational waves, but keeping the measurement technology: the distance between the two test masses is measured using a laser interferometric technique similar to one aspect of the eLISA interferometry system. The scientific objective of the LISA Pathfinder mission consists then of the first in-flight test of low frequency gravitational wave detection metrology. LISA Pathfinder has been successfully launched by a Vega rocket on 3 December 2015 from the ESA spaceport in Kourou. On 22 January 2016 it arrived at L1 Sun-Earth Lagrange point in space. On 15 and 16 February both test masses have been successfully released and since beginning of March has started its science mission. The satellite now works as designed.

[1] B.P. Abbott *et al.*, LIGO and Virgo Collaborations, Phys. Rev. Lett. 116, 061102, 2016.

2.2 Gravitational Lensing

Gravitational lensing – specifically that light is affected by both space and time parts of the metric, unlike Newtonian bodies, which are affected by the time part only – needs no elaborations here. Nowadays, gravitational lensing is valued rather as a way of detecting matter that would be otherwise invisible.

On the scale of galaxies and clusters of galaxies, gravitational lensing is very important as a probe of dark matter. Extracting the information on mass distributions, however, requires solving a non-trivial inverse problem. R. Küng, I. Mohammed and P. Saha, together with external collaborators, have worked on the problem of mapping a mass distribution from lensing observables. One part of this work is the development of an improved method for modeling galaxy lenses and furthermore, a theoretical formulation and computational interface to enable modeling in a citizen-science context. The other aspect is mapping and interpreting dark-matter structure in strong-lensing galaxy-clusters

2.3 Space clocks and relativity

Together with S. Lecomte from CSEM in Neuchâtel, M. Rothacher from ETH Zürich, Q. Wang and P. Rochat from Spectratime in Neuchâtel and some of their collaborators we conducted a study on behalf of the Swiss Space Office (SSO) for a satellite mission called E-GRIP (Einstein Gravitational Red-shIft Probe) to test general relativity using an onboard hydrogen maser. The clock would be sensitive to 2×10^{-6} the level of the Earth's gravitational redshift, and would be sensitive to space-curvature around the Earth and frame-dragging by the Earth's spin. In addition, E-GRIP would provide a wealth of science for time and frequency metrology- and geodesy. We delivered by December 2015 a detailed report and on 11 December it has been presented at SSO in Bern. We have been requested to study this proposal further.

2.4 Atomic clocks applications in geophysics

According to general relativity, a clock experiencing a shift in the gravitational potential ΔU will measure a frequency change given by $\Delta f/f \approx \Delta U/c^2$. The best clocks are optical clocks. After about 7 hours of integration they reach stabilities of $\Delta f/f \sim 10^{-18}$ and can be used to detect changes in the gravitational potential that correspond to vertical displacements of the centimeter level. At this level of performance, ground-based atomic clock networks emerge as a tool that is complementary to existing technology for monitoring a wide range of geophysical processes by directly measuring changes in the gravitational potential. Vertical changes of the clock's position due to magmatic, post-seismic or tidal deformations can result in measurable variations in the clock tick rate. In this work Ruxandra Bondarescu and Andreas Schärer together with further authors computed the geopotential change arising due to an inflating magma chamber using the Mogi model and applied it to the Etna volcano. Its effect on an observer on the Earth's surface can be divided into two different terms: one purely due to uplift (free-air gradient) and one due to the redistribution of matter. Thus, with the centimeter-level precision of current clocks it is already possible to monitor volcanoes. The matter redistribution term is estimated to be 3 orders of magnitude smaller than the uplift term. Additionally, clocks can be compared over distances of thousands of kilometers over short periods of time, which improves our ability to monitor periodic effects with long wavelength like the solid Earth tide.

3 GERDA: Neutrinoless Double Beta Decay in ^{76}Ge

Laura Baudis, Giovanni Benato, Andreas James, Alexander Kish,
Michael Miloradovic, Rizalina Minghazeva, Manuel Walter

in collaboration with: INFN Laboratori Nazionali del Gran Sasso LNGS, Jagellonian University Cracow, Institut für Kern- und Teilchenphysik Technische Universität Dresden, Joint Institute for Nuclear Research Dubna, Institute for Reference Materials and Measurements Geel, Max Planck Institut für Kernphysik Heidelberg, Universitá di Milano Bicocca e INFN Milano, Institute for Nuclear Research of the Russian Academy of Sciences, Institute for Theoretical and Experimental Physics Moscow, Russian Research Center Kurchatov Institute, Max-Planck-Institut für Physik München, Dipartimento di Fisica dell Universitá di Padova e INFN, Physikalisches Institut Eberhard Karls Universität Tübingen.

(GERDA Collaboration)

Some of the most important questions in modern particle physics can be addressed by investigating the elusive neutrinos. What is the nature of these fundamental particles, their mass scale and hierarchy, and what is the explanation of the observed matter-antimatter asymmetry in our universe? One of the prime tools in neutrino research is the search for neutrinoless double beta decay ($0\nu\beta\beta$). The discovery of this decay channel would prove that total lepton number is not conserved in nature and that neutrinos have a Majorana mass component. The world's highest lower limit on the half-life of the $0\nu\beta\beta$ decay of ^{76}Ge comes from the Germanium Detector Array (GERDA) experiment [1], as we describe in the following. A recent review of the field can be found in [2].

[1] Gerda Collaboration, K.-H. Ackermann *et. al*, Eur. Phys. J. C **73** (2013) 2330.

[2] S. Dell'Oro, S. Marcocci, M. Viel, and F. Vissani, *Neutrinoless double beta decay: 2015 review*, arXiv[hep-ph]1601.07512.

3.1 The GERDA experiment

The GERDA experiment at the Laboratori Nazionali del Gran Sasso (LNGS) searches for the $0\nu\beta\beta$ decay using high-purity germanium diodes, isotopically enriched in ^{76}Ge [3]. These act simultaneously as the detector and source material. The germanium detectors are submerged in liquid argon (LAr). A water Cherenkov veto surrounds the LAr cryostat, and allows us to reject interactions from cosmic muons.

In the first stage of the experiment (Phase I), which lasted from 2011 to 2013, ten HPGe detectors with an active mass of 15 kg were used, resulting in a total exposure of 21.6 kg·y. A tenfold lower background than in previous experiments was obtained, with $1 \cdot 10^{-2}$ events/(keV · kg · y) at the Q-value of the decay ($Q_{\beta\beta}$). No $0\nu\beta\beta$-decay signal was observed in Phase I, and a lower limit of $T_{1/2}^{0\nu\beta\beta} > 2.1 \times 10^{25}$ y at 90% C.L. for the half-life of the decay was obtained [4].

[3] Gerda Collaboration, M. Agostini *et. al*, Eur. Phys. J. C **75** (2015) 39.

[4] Gerda Collaboration, M. Agostini *et. al*, Phys. Rev. Lett. **111** (2013) 122503.

3.2 GERDA Phase II

During the upgrade of the experiment (Phase II, see Fig. 3.1), new, enriched Broad Energy Germanium (BEGe) detectors were built and extensively tested [3], and an active LAr veto system was installed at LNGS. The aim of this stage is to reach a sensitivity of $T_{1/2} = O(10^{26})$y with a background index (BI) of 10^{-3} events/(keV·kg·y) after an exposure of 100 kg·y.

In the spring of 2015, the assembly of the upgraded detector array started, by mounting pairs of BEGe detectors in their new, low-background holders. It culminated with the mounting of all 40 detectors into the LAr cryostat, arranged in 7 strings (see Fig. 3.2). Each string is surrounded by a so-called *nylon mini-shroud* enclosing either 3 coaxial or 8 BEGe detectors. Only one string is composed of 6 BEGe's and 1 coaxial diode. The purpose of the mini-shrouds is to physically block ^{42}K ions, produced in ^{42}Ar decays in LAr, to reach the surface of the diodes and contribute to the background through β-decays. By December 2015, all the detectors were installed and characterised, and the Phase II data taking of GERDA started. We have contributed to the tests of the BEGe detectors, to the liquid argon veto [5] and to the calibration system hardware and software. We are now focussed on the physics data analysis.

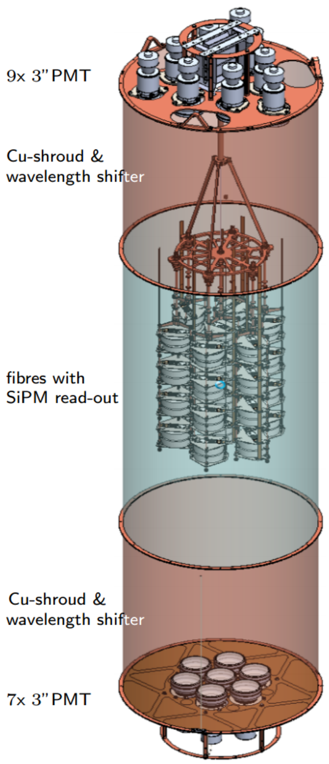

Fig. 3.1 – Schematic view of the Gerda Phase II germanium detector array and the surrounding liquid argon veto.

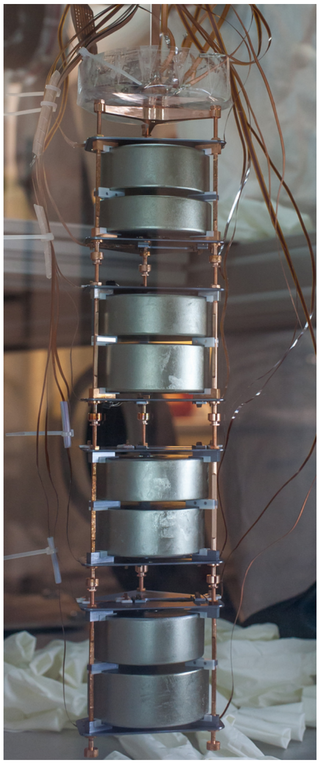

Fig. 3.2 – One of the Gerda Phase II strings containing eight broad-energy germanium detectors.

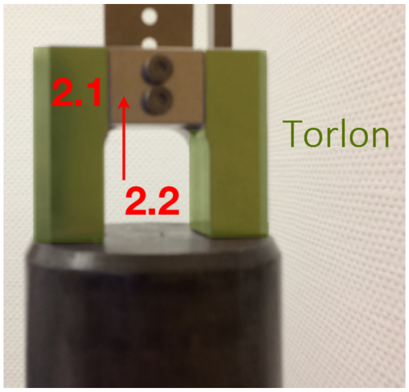

Fig. 3.3 – Source holder.
1. tantalum absorber
2. connection piece
3. position meter
4. steel band.
2.1 Torlon connection piece
2.2 aluminium mounting piece.

3.2.1 The Phase II calibration system

We have upgraded the three calibration systems that we had constructed and operated for GERDA Phase I [6]. We also produced new, low-neutron emission sources, in collaboration with PSI, and characterised these at the University of Zürich and at LNGS [7]. After the initial upgrade, we performed a modification of the ^{228}Th source holders, as shown in Fig. 3.3. The aluminium connection piece of the tantalum absorber was replaced with Torlon (polyamide-imide) to insulate it from the stainless steel band. We thereby prevented an observed high voltage instability in several germanium detectors.

We are currently acquiring 1-2 energy calibration runs per week, using the three ^{228}Th-sources. The purpose of the calibration procedure is to perform the energy and pulse shape calibration of all germanium detectors, and to monitor their energy resolution and energy scale stability in time.

3.2.2 Phase II calibration software

We have developed new calibration software tailored to the Phase II requirements. We have unified the code with all other packages used in the Gerda-ADA analysis framework (Gerda-Advanced-Analysis). We made major modifications to the program front-end. To handle and extract all relevant calibration information for each diode, the program now receives as input the detector and string settings, as well as the list of quality cuts which have to be applied to a given run. Since this part of the code also provides the interface between user and the executable program, it is flexible and intuitive for the user.

A new configuration file of quality cuts was developed which can be applied to all data types (background, calibration, physics run) in a similar fashion. The program can now use the class *TTreeFormula* of the ROOT analysis package. For this purpose, a new interface class to handle and apply the required cuts was developed. The calibration data is now loaded through key identifiers that allow the software to reconstruct the file system path in a performance optimised directory structure. Through dedicated key lists, all the resolved ROOT files are loaded in parallel. This procedure is now unified through all the layers of the Phase II data processing structure.

All these modifications have already been included into the latest, stable Gerda-ADA version.

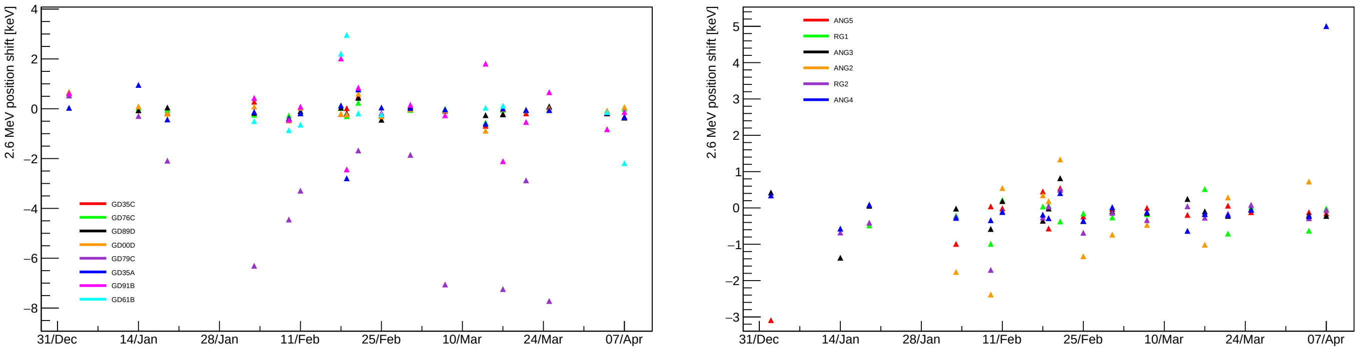

FIG. 3.4 – Coaxial (left) and BEGe (right) detector energy scale stability during the initial Phase II data taking. The relative shift in the position of the full energy peak at 2.6 MeV from the ^{208}Tl decay is quantified.

3.2.3 Phase II calibration data analysis

Using the calibration data, the energy scale and the resolution of the diodes can be monitored. Figure 3.4 shows the energy scale stability for coaxial and BEGe detectors, for calibration runs between December 2015 and April 2016. The energy scale is determined from the position of the full energy peak at 2.6 MeV from ^{208}Tl. Most coaxial detectors (6 out of 9) and most BEGe detectors show a stable behaviour. The BEGe detector GD79C revealed a high leakage current during data taking and was selected only for coincident events with multiple detectors.

The calibration data allowed an accurate study of possible shifts in the energy scale, needed in the final analysis. For this purpose, the energy gain stability both during the calibration runs, and during the actual physics runs (using a pulser) was investigated. Runs with instable detector operation are still under review.

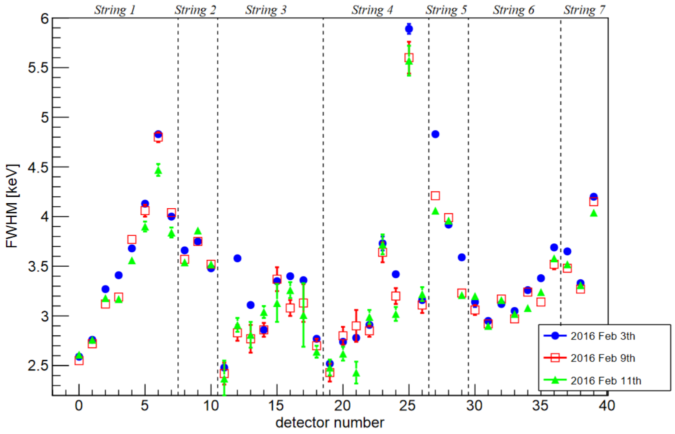

FIG. 3.5 – Energy resolution (at FWHM) of the 2.6 MeV γ-line of ^{208}Tl for 3 calibration runs and all 40 detectors. The vertical lines indicate the string boundaries.

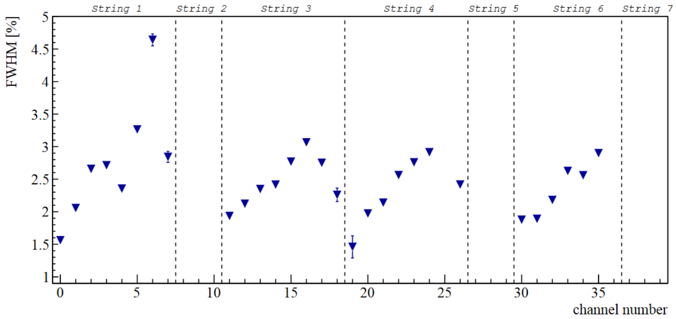

FIG. 3.6 – Resolution of the pulse shape analysis parameter A/E for BEGe detectors (strings 1, 3, 4 and 6). Several calibration runs are added in this analysis. The channel number is identical to the one shown in Fig. 3.5.

3.2.4 Phase II detector performance

An example of the spectroscopic performance of all 40 germanium detectors (30 BEGe and 10 coaxial diodes) is shown in Fig. 3.5 for the 2.6 MeV calibration line. Most detectors have an energy resolution (at FWHM) below 4 keV, superior to the Phase I performance of 4.3 keV [8]. For BEGe detectors, the top detectors in a string (lowest channel number in each group) exhibit the highest resolution. This might be caused by larger stray capacitances due to the increasing cable length for the lower detectors. The average BEGe resolution at 2.6 MeV is 3.2 keV compared to 2.8 keV during Phase I.

The A/E parameter, with A the area of the charge pulse and E the energy, allows to reject surface events and multiple interactions in a given diode [9]. The A/E resolution of events in the double escape peak of the 2.6 MeV gamma is shown in Fig. 3.6. Cuts on A/E remove about 15% of the total number of events in a calibration run.

3.2.5 The liquid argon veto and physics data

The LAr veto, new in Phase II (see Fig. 3.2), is a scintillating detector equipped with photomultiplier tubes

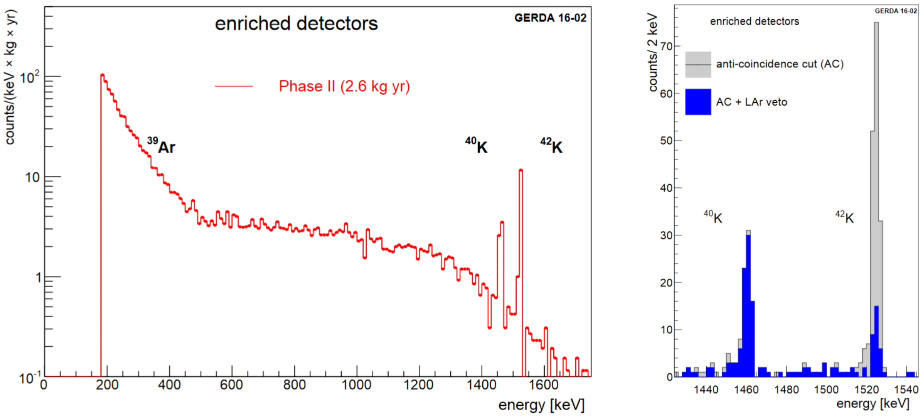

FIG. 3.7 – Left: background energy spectrum in the Ge detectors, for an exposure of 2.6 kg y. Right: γ-lines from ^{40}K decay in material close to the diodes, and from ^{42}Ar with and without argon veto.

(PMTs) and silicon photomultipliers (SiPMs). All channels are working and their performance is stable in time. Figure 3.7 shows the observed background energy spectrum below 1.8 MeV and the effect of the argon veto on the γ lines around 1.5 MeV. Clearly visible is the suppression of the ^{42}K peak at 1525 keV: if the β-decay occurs at some distance from the detectors (e.g. at the mini-shroud surface), the electron deposits energy in the argon too and the event can be vetoed.

The observed ^{40}K peak at 1461 keV is from electron capture and not accompanied by an energy deposition in the argon. Both peaks, however, contain to a large fraction multisite events (MSEs) which can be rejected by pulse shape discrimination (see Fig. 3.8). Single site events (SSEs) – similar to double beta decays of ^{76}Ge with neutrino emission – are located in a band around $A/E = 1$. These events dominate in an energy range around 1 MeV. MSEs and events on the n+ contact surface have $A/E < 1$, visible for the two γ lines mentioned above. Events at the p+ contact can be clearly identified by high A/E values. α decays originating from ^{210}Po with an endpoint of 5.3 MeV are also visible in the figure.

The accumulated statistics for the enriched detectors is about 4.8 kg·y, though not all might be used for physics analysis later on. The background level before using the active argon veto and event discrimination based on pulse shape analysis is similar to the one in Phase I [10].

[5] L. Baudis, G. Benato, R. Dressler, F. Piastra, I. Usoltsev and M. Walter, JINST 10 (2015) P09009.

[6] L. Baudis, A.D. Ferella, F. Froborg, and M. Tarka, Nucl. Instrum. Meth. A729 (2013) 557-564.

[7] L. Baudis, G. Benato, P. Carconi, C.M. Cattadori, P. de Felice, K. Eberhardt, R. Eichler, A. Petrucci, M. Tarka, and M. Walter, JINST **10** (2015) no.12, P12005.

[8] Gerda Collaboration, M. Agostini *et. al*, Eur. Phys. J. C **75** (2015) 255.

[9] Gerda Collaboration, M. Agostini *et. al*, Eur. Phys. J. C **73** (2013) 2583.

[10] Gerda Collaboration, M. Agostini *et. al*, Eur. Phys. J. C **74** (2014) 2764.

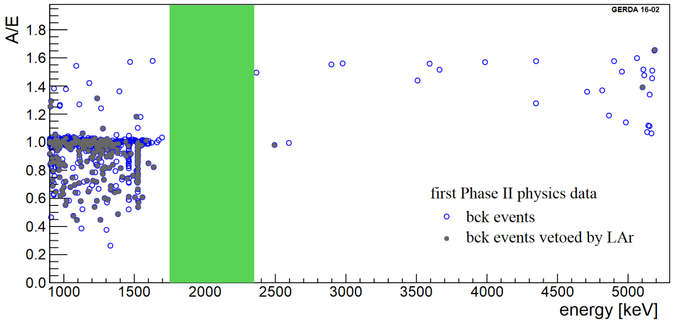

FIG. 3.8 – A/E versus E for the BEGe detectors. A 400 keV band around $Q_{\beta\beta}$=2039 keV is blinded.

3.3 Outlook

The entire array of 40 HPGe detectors was mounted successfully. They can be biased well above depletion voltage (except detector GD79C) and all readout channels are working. The active liquid argon veto is working well too, showing stable performance in time. Since the end of January 2016, the data is blinded, i.e. events in the window $Q_{\beta\beta} \pm 25$ keV are not reconstructed to ensure an unbiased analysis. We are now strongly involved in the analysis of the GERDA Phase II data. A first estimate of the remaining background at $Q_{\beta\beta}$ will be available in late spring, and unblinding is planned for summer 2016. Depending on the observed background level, some hardware modifications such as new readout cables from cleaner material (already available and screened) could be scheduled after a first physics result.

4 Dark Matter Detection with XENON and DARWIN

Peter Barrow, Laura Baudis, Sandro D'Amato, Domenico Franco, Michelle Galloway, Andrea Gmuer, Shingo Kazama, Gaudenz Kessler, Alexander Kish, Andreas James, Daniel Mayani, Francesco Piastra, Yuehuan Wei, Julien Wulf

in collaboration with:
Albert Einstein Center for Fundamental Physics Bern, Columbia University, UCLA, UCSD, INFN, University of Münster, Coimbra University, Subatech, The Weizmann Institute of Science, University of Mainz, SJTU, MPIK Heidelberg, Stockholm University, Rice University, University of Chicago, University of Bologna, Nikhef and Amsterdam University, Purdue University, NYU of Abu Dhabi

(XENON Collaboration)

Dark matter reveals its presence on various astronomical scales, including our own galaxy, through its gravitational attraction. Its intrinsic nature is largely unknown, and existing data are compatible with models where the dark matter consists of new particles, which are not part of the Standard Model [1]. A compelling class of candidates are weakly interacting massive particles (WIMPs), which are predicted by various extensions to the Standard Model, such as supersymmetry or large extra dimensions. WIMPs must be stable, or very long-lived and are expected to have very weak couplings to ordinary matter [2]. Direct detection experiments are designed to look for scattering signatures of galactic WIMPs off atomic nuclei. The expected nuclear recoil energies are below a few tens of keV, and the rates are lower than $\sim$1 event per year and kg of target material [3].

While no direct evidence for WIMPs exists, the sensitivity of direct searches has seen a dramatic increase over the last decade, a development which was largely lead by the dual-phase, xenon time projection chamber (TPC) technique [3–5]. Large liquid xenon TPCs such as XENON100 [6, 7], LUX [8, 9] and PandaX [10] constrain the cross section of WIMPs on nucleons down to $\sim$few $\times 10^{-46}$ cm^2 regime, while the upcoming XENON1T [11] and the planned DARWIN detector [12, 13] are expected to improve upon these results by two and three orders of magnitude, respectively [14].

We are still operating the XENON100 experiment at the Laboratori Nazionali del Gran Sasso (LNGS) and are in the process of commissioning the XENON1T detector in the underground laboratory. In the following we will present the latest XENON100 results, and discuss the status of the XENON1T experiment. We will conclude by presenting a sensitivity study to WIMP dark matter for the next-generation DARWIN detector.

[1] G. Bertone, D. Hooper and J. Silk, Phys. Rept. **405** (2005) 279.

[2] M.W. Goodman and E. Witten, Phys. Rev. D31 (1985) 3059.

[3] Laura Baudis, J.Phys. G43 (2016) no.4, 044001.

[4] L. Baudis, Phys. Dark Univ. 1 (2012) 94.

[5] Laura Baudis, Annalen der Physik 528 (2016) 74-83.

[6] E. Aprile *et al.*, XENON Collaboration, Phys. Rev. Lett. 107 (2011) 131302.

[7] E. Aprile *et al.*, XENON100, Astropart. Phys. 35 (2012) 573.

[8] D. S. Akerib *et al.* [LUX Collaboration], Nucl. Instrum. Meth. A **704** (2013) 111.

[9] D. S. Akerib *et al.* [LUX Collaboration], Phys.Rev. D93 (2016) no.7, 072009.

[10] A. Tan *et al.* [PandaX Collaboration], "Dark Matter Search Results from the Commissioning Run of PandaX-II," arXiv:1602.06563 [hep-ex].

[11] E. Aprile *et al.*, XENON Collaboration, JCAP 1604 (2016) no.04, 027.

[12] L. Baudis, DARWIN Consortium, J.Phys.Conf.Ser. 375 (2012) 012028.

[13] Laura Baudis, PoS IDM2010 (2011) 122.

[14] M. Schumann, L. Baudis, L. Bütikofer, A. Kish and M. Selvi, JCAP **1510** (2015) no.10, 016.

4.1 Annual Modulation Search with XENON100

XENON100 is a 161 kg double-phase xenon TPC, which employs two arrays of low-radioactivity, VUV-sensitive photomultipliers (PMTs) to detect the prompt (S1) and proportional (S2) scintillation light signals induced by particles interacting in the target volume, containing 62 kg of ultra-pure liquid xenon (LXe). The remaining 99 kg of LXe act as an active veto shield against background radiation.

In 2012, over an integrated period of 225 live days, the experiment has reached its design sensitivity of 2×10^{-45} cm^2 at 55 GeV/c^2 and 90% confidence level on the spin-independent

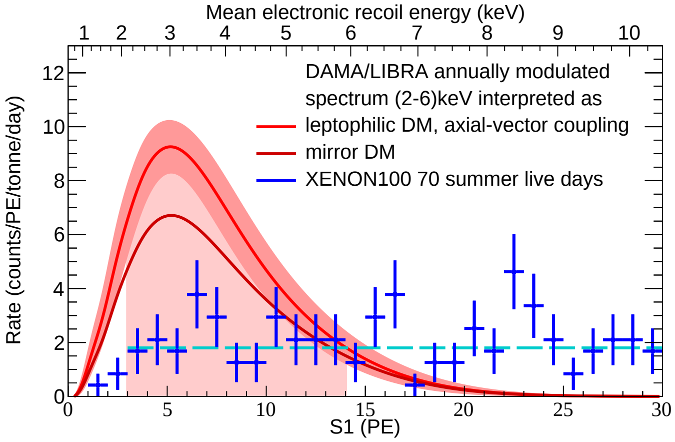

FIG. 4.1 – The DAMA/LIBRA modulated spectrum (red), interpreted as WIMPs scattering through axial-vector interactions, as it would be seen in the XENON100 detector. The 1σ band includes statistical and systematic uncertainties. The DAMA/LIBRA modulated spectrum interpreted as luminous dark matter is very similar, whereas the interpretation as mirror dark matter is indicated separately (dark red). The (blue) data points are XENON100 data from the 70 summer live days with their statistical uncertainty. The expected average XENON100 rate is also shown (dashed cyan). The shaded region from (3-14) PE was used to quantify the confidence level of exclusion. Figure from [18].

elastic WIMP-nucleon scattering cross section [15], and obtained the best limit at the time for spin-dependent interactions [16].

The same data have been used to search for axions and axion-like particles [17] and, most recently, to probe the DAMA/LIBRA modulation result, which is the only long-standing claim for a dark matter detection. Since DAMA/LIBRA has no discrimination power between nuclear recoils (NRs) and electronic recoils (ERs), a possibility to reconcile the observed signal with the null-results from other experiments consists in assuming a dark matter axial-vector coupling to electrons, in so-called *leptophilic models*. To test this hypothesis, we performed two analyses focused on the interaction between a potential dark matter candidate and electrons in the LXe. The first study used the overall electronic recoil rate and allowed to exclude leptophilic models as explanation for the DAMA/LIBRA signal [18]. Figure 4.1 shows the XENON100 ER rate, along with the expectations from DAMA/LIBRA in such models.

The second study exploited the periodic variations of the electronic recoil event rate in the 2 - 6 keV energy range [19]. The measured phase of 112±15 days (also observed for multiple-scatters, which are not WIMP candidates) disfavours the interpretation of a modulation due to a standard dark matter halo at $2.5\,\sigma$ confidence level, as shown in Fig. 4.2. In addition,

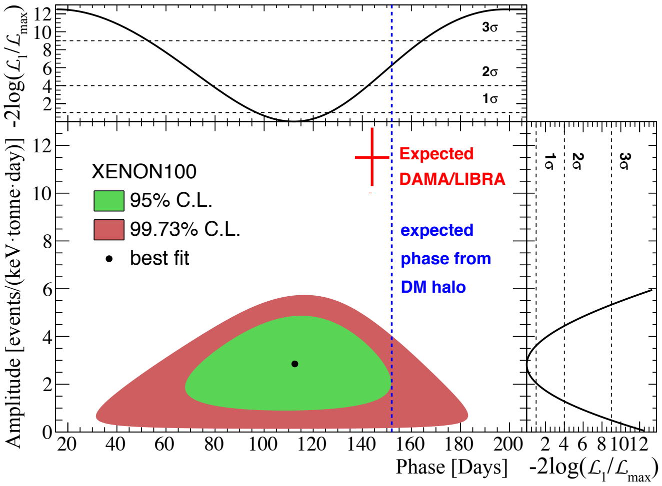

FIG. 4.2 – The XENON100 best-fit, 95% and 99.73% confidence level contours as a function of amplitude and phase relative to January 1, 2011 for period P = 1 year. The expected DAMA/LIBRA signal with statistical uncertainties only and the phase expected from a standard dark matter (DM) halo are overlaid for comparison. Top and side panels show -2log(Λ_1/Λ_{max}) as a function of phase and amplitude, respectively, along with two-sided significance levels. Figure from [19].

the annual modulation interpreted as a dark matter signature with axial-vector coupling of dark matter particles to electrons was excluded at $4.8\,\sigma$ confidence level [19].

[15] E. Aprile *et al.*, XENON Collaboration, Phys. Rev. Lett. 109 (2012) 181301.

[16] E. Aprile *et al.*, XENON Collaboration, Phys. Rev. Lett. 111 (2013) 021301.

[17] E. Aprile *et al.*, XENON Collaboration, Phys. Rev. D 90 (2014) 062009.

[18] E. Aprile *et al.* XENON Collaboration, Science **349** (2015) no.6250, 851.

[19] E. Aprile *et al.* XENON Collaboration, Phys. Rev. Lett. 115 (2015) 091302.

4.2 Improving the Sensitivity with XENON1T

The XENON1T experiment is under commissioning in Hall B at LNGS (see Fig. 4.3). It uses a total of 3.3 t of LXe operated in a cryostat surrounded by a 9.6 m diameter and 10 m high water Cherenkov shield [20]. The cryostat is a double-walled super-insulated pressure vessel, made of stainless steel. The inner vessel houses the liquid xenon, the TPC and two PMT arrays. The TPC is made of interlocking PTFE panels, and the drift field homogeneity is achieved with equidistant copper field shaping rings connected with high-ohmic HV resistors. The photo-sensors are arranged in two arrays, containing 127 PMTs above the target in the gas phase, and 121 PMTs at the bottom, immersed in the liquid.

FIG. 4.3 – The XENON1T experiment in Hall B of LNGS. The water Cherenkov shield with a picture of the cryostat, its support structure and the pipe housing the cryogenic lines and cabling are seen on the left side. The infrastructure building, containing the LXe storage and purification systems, the krypton distillation column, the electronics and DAQ, as well as the cryogenic systems on the top level is seen on the right.

At UZH, we contributed to the design, construction, tests and integration of the TPC, to the development and tests in liquid xenon of the photomultiplier tubes, to their readout electronics and light calibration system, to the signal and high-voltage cables and connectors, as well as to the radioassay of materials employed to construct the detector [21]. We are also involved in the background modeling and in simulating the electric drift field and the light collection efficiency of the TPC.

The performance of XENON1T and its sensitivity to WIMP interactions [11] were studied by Monte Carlo simulation. The radio-assays of all detector components were used for a realistic background model. The average rates of the various ER and NR backgrounds were calculated and their energy spectra are shown in Fig. 4.4, along with WIMP-induced signals. An inner fiducial region containing 1 t of LXe mass was considered here, as well as 99.75% ER rejection efficiency and a 40% acceptance for NRs.

The main contribution to the ER background originates in the decays of the ^{222}Rn daughters ($\sim$85%), assuming a 10 μBq radon level. Other sources of ER background are the radioactive isotope ^{85}Kr, present at the level of 2×10^{-11} in ^{nat}Kr ($\sim$4%), solar neutrinos scattering elastically off electrons in the medium ($\sim$5%), detector materials ($\sim$4%), and the double-beta decay of ^{136}Xe, which is present in natural Xe at 8.9% (1%) with a half-life of 2.17×10^{21} y.

The NR background is caused by radiogenic neutrons emitted by detector components (mostly in (α, n) reactions), by neutrons produced in interactions of cosmic muons with the rock, the concrete of the underground laboratory and the detector materials, and by coherent neutrino-nucleus scattering (CNNS) from ^{8}B neutrinos at low energies and atmospheric neutrinos at higher energies. The sensitivity to spin-independent WIMP-nucleon interactions after 2 t y exposure has a minimum cross section value of 1.6×10^{-47} cm^2, for a WIMP mass of 50 GeV/c^2 [11] which implies an improvement over XENON100 by two orders of magnitude.

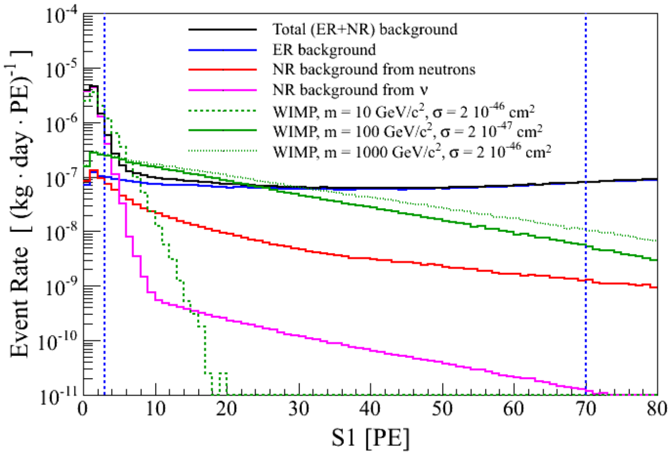

FIG. 4.4 –
Predicted energy spectra for the total background and its components. The three examples for WIMP signals correspond to different masses and interaction cross sections at the limit of the XENON1T sensitivity. The vertical blue lines delimit the energy region (in the prompt scintillation signal, S1) used for the sensitivity calculation. Events with S2 $>$ 150 PE are selected, and an 99.75% ER rejection with 40% acceptance to NRs is assumed. Figure from [11].

[20] E. Aprile *et al.*, XENON Collaboration,
JINST **9** (2014) 11006.

[21] E. Aprile *et al.*, XENON Collaboration,
Eur. Phys. J. C **75** (2015) no.11, 546.

4.3 The XENON1T Time Projection Chamber

In October 2015 the assembly of the XENON1T TPC began at LNGS in an above-ground cleanroom. After methodical cleaning to remove impurities and etch away radioactive surface contamination the 74 copper field-shaping rings of the field cage were mounted on the cylindrical PTFE support structure which has a height and a diameter of ≈1 m. Reflector panels and fibre optic cables were installed. The fibres are used to uniformly distribute light inside the TPC for PMT calibration. Two sets of high voltage chains were installed as well, each consisting of 73 resistors (5 GΩ each) bridging neighbouring rings, allowing for an optimal electric field of 1 kV/cm. In parallel the top PMT array was installed inside the TPC diving bell.

Next, cathode, anode and gate electrodes were mounted which provide a radially-uniform electric field across the TPC. They consist of wires or hexagonal meshes stretched across

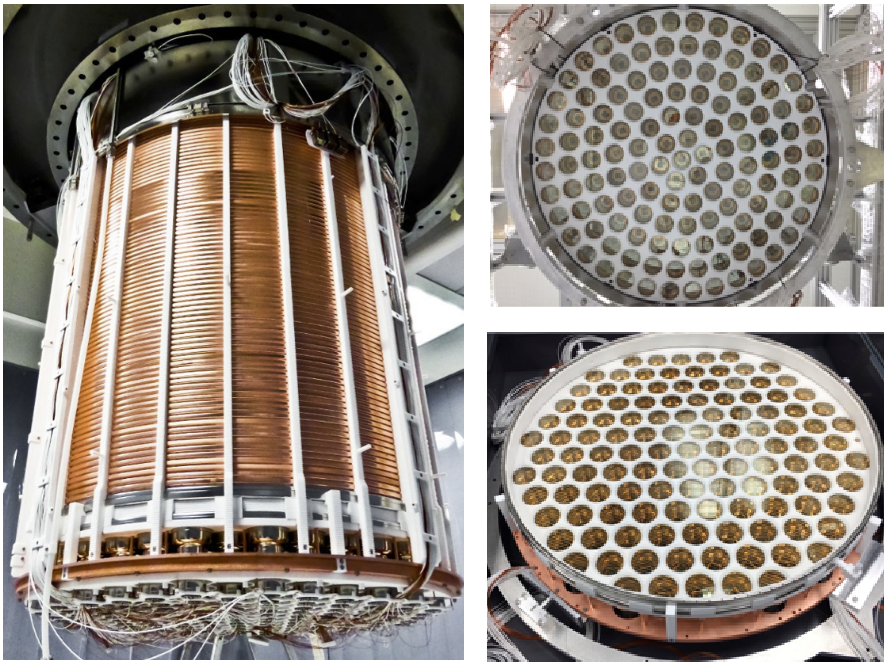

Fig. 4.5 –
Left: the XENON1T TPC during its installation in the underground cleanroom at LNGS. The PTFE pillars and the Cu field shaping rings are clearly visible, as well as the bottom PMT array and the dome of the inner cryostat.
Right: the top and bottom photodetector arrays. These detector 'eyes' contain 127 and 121 3-inch, Hamamatsu R11410-21 PMTs, respectively.

stainless steel rings (grids). The bottom screening mesh, cathode, and small PTFE reflectors were installed directly onto the bottom PMT array. The gate grid was gently lifted and affixed onto the top TPC ring, followed by the anode grid, with 5 mm insulating spacers in between the two grids. The xenon liquid/gas interface will reside between these two electrodes. Then the small PTFE reflector panels were assembled and the protective mesh for the PMTs was placed on top. Level meters that measure by capacitance the height of the liquid xenon were installed onto the top TPC ring. The bottom PMT array was mounted to the field cage, and monitoring devices such as temperature sensors and diagnostic PMTs were installed. Finally, the TPC was wrapped and secured to prepare for transport to the underground laboratory.

On November 4th the TPC was transported into Hall B and wheeled inside the water tank for installation. Using a set of 3 winches from the top dome of the water tank, the delicate instrument, now close to 500 kg, was slowly and carefully raised from the bottom of the tank, through a hole in the cleanroom floor, and up to the dome of the tank. Figure 4.5 shows the TPC mounted to the dome inside the underground water tank. At this point, the integration of the TPC with other XENON1T subsystems, such as the DAQ and cryogenics systems, began. The high voltage feed-through, piping for liquid xenon, and cabling for PMTs, fibre optics, sensors, and electrodes were connected. After many visual and mechanical checks, electrical tests, and a final cleaning, the stainless steel vessel that contains the liquid xenon was lifted and sealed to enclose the TPC. The installation of the XENON1T detector was a success, and the instrument is currently under commissioning.

[22] G. Angloher *et al.*, CRESST Collaboration,
Eur.Phys.J. C74 (2014) 3184.

[23] R. Agnese *et al.*, SuperCDMS Collaboration,
Search for Low-Mass WIMPs with SuperCDMS (2014)
arXiv:1402.7137.

[24] M. Xiao *et al.*, PandaX Collaboration,
Sci. China Phys. Mech. Astron. **57** (2014) 2024.

[25] M. Bossa, DarkSide Collaboration,
JINST 9 (2014) C01034.

[26] D.S. Akerib *et al.*, LUX Collaboration,
(2013) arXiv:1310.8214.

[27] M.G. Boulay, DEAP Collaboration,
J.Phys.Conf.Ser. 375 (2012) 012027.

[28] E. Aprile, XENON Collaboration,
Springer Proc. Phys. **148** (2013) 93.

[29] D.C. Malling *et al.*, *After LUX: The LZ Program*,
(2011) arXiv:1110.0103.

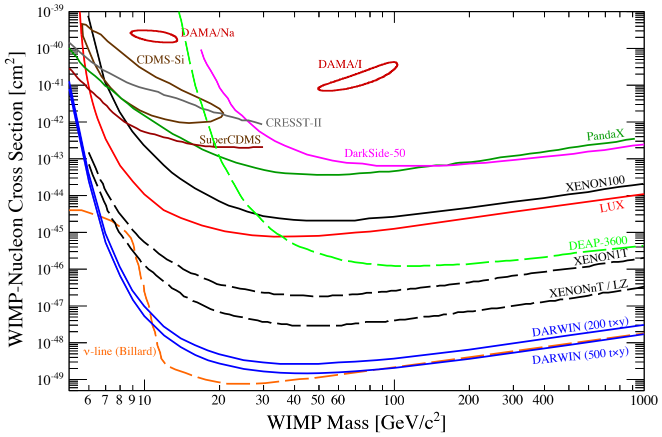

Fig. 4.6 – Spin-independent WIMP-nucleon scattering results: Existing upper limits from the CRESST-II [22], SuperCDMS [23], PandaX [24], DarkSide-50 [25], XENON100 [15], and LUX [26] experiments, along with projections for DEAP3600 [27], XENON1T [28], XENONnT [20], LZ [29], and DARWIN [12] are shown. DARWIN is designed to probe the entire parameter region for WIMP masses above ∼6 GeV/c^2, until the neutrino background (ν-line) will start to dominate the recoil spectrum. Figure adapted from [14].

4.4 The XENONnT and DARWIN projects

After the commissioning of the XENON1T detector, our efforts are focused on data analysis and on a new TPC design for the planned 7 t XENONnT upgrade for which we are testing new, improved photosensors. Many major components in XENON1T have been designed such that they can be reused in XENONnT, such as the water Cherenkov shield, the xenon storage vessel, the cryogenic and purification systems, the cryostat support, the outer cryostat vessel and the connection pipe to the building. The DAQ system for XENON1T can be upgraded for the ∼200 extra channels of XENONnT without new developments. The main challenge is to build a new, larger TPC and to further lower the intrinsic backgrounds from radon and krypton.

DARWIN is an ultimate, xenon-based WIMP detector with a sensitivity goal down to $\sim 10^{-49}$ cm^2. At these cross-sections, neutrino interactions, which cannot be reduced by target fiducialization, will limit the sensitivity to WIMP scatters [12]. With a total LXe mass of 50 t, this project would be the successor of XENONnT, and installed in the same Hall B at LNGS (possibly in a larger Cherenkov shield). Our R&D is focused on the design and prototyping of the time projection chamber, on Monte Carlo simulations of the radioactive background, on new light read-out schemes and tests of light sensors in noble liquids, material screening with high-purity germanium spectroscopy, as well as on the science impact of the facility. Recently we have performed a detail study of the sensitivity of the DARWIN instrument to spin-independent and spin-dependent WIMP-nucleon scattering interactions. Taking into account realistic backgrounds from the detector itself as well as from neutrinos, we examined the impact of exposure, energy threshold, background rejection efficiency and energy resolution on the dark matter sensitivity. With an exposure of 200 t y and assuming detector parameters which have been already demonstrated experimentally, spin-independent cross sections as low as 2.5×10^{-49} cm^2 can be indeed probed, as shown in Fig. 4.6. Additional improvements in terms of background rejection and exposure will further increase the sensitivity, while the ultimate WIMP science reach will be limited by neutrinos scattering coherently off the xenon nuclei [14].

We additionally perform charge and light yield measurements of nuclear and electronic recoils in LXe at low energies, which are necessary to define accurate energy scales in noble liquid dark matter detectors. To this end, we have built a new, small TPC (Xurich-II), that we are currently operating in the neutron beam at the D-D fusion generator at the Physik-Institut. Our goal is to measure the NR versus ER discrimination as a function of drift field, and to determine the charge and light yield of low-energy nuclear recoils.

5 DAMIC: search for dark matter using CCD detectors

J. Liao, B. Kilminster, and P. Robmann

in collaboration with: Fermi National Accelerator Laboratory, University of Chicago, University of Michigan, Universidad Nacional Autónoma de México, Universidad Nacional de Asunción de Paraguay

(DAMIC Collaboration)

DAMIC (Dark Matter in CCDs) is an experiment designed to provide high sensitivity to direct detection of weakly interacting dark matter particles (WIMPs) with mass below 5 GeV. There are a number of theoretical models favoring such low mass WIMPs, which offer an explanation for the coincidence of dark matter (DM) and baryon abundance, and the matter-antimatter densities [1–3].

The main challenge in searching for low mass DM is measuring the low energy deposit of the associated nuclear recoils in the detection material. DAMIC uses CCDs with an electronics noise of σ=7.2 eV corresponding to a 5σ=36 eV threshold, which is the lowest of any current DM detector. CCD detectors are silicon pixel detectors that shift charge from the capacitor of one pixel to the next by generating potential wells until reaching a charge amplifier which converts the charge to voltage (Fig. 5.1). The DAMIC CCD detectors were fabricated by Lawrence Berkeley National Laboratory [4] originally for the Dark Energy Camera (DECam) [5, 6]. DECam CCDs [7] are 30 times thicker (500 - 650 μm) than commercial CCDs, leading to correspondingly higher detection eficiencies. Each CCD has up to 16 million 15 μm x 15 μm pixels and is read out by two amplifiers in parallel. The electronic gain is $\sim$ 2.5 μV/e. The signal is digitized after correlated double sampling and the noise performance improves by reducing the readout speed. The lowest noise, $\sigma <$ 2e$^-$ (R.M.S.) per pixel, was achieved with readout times of 50 μs per pixel [8].

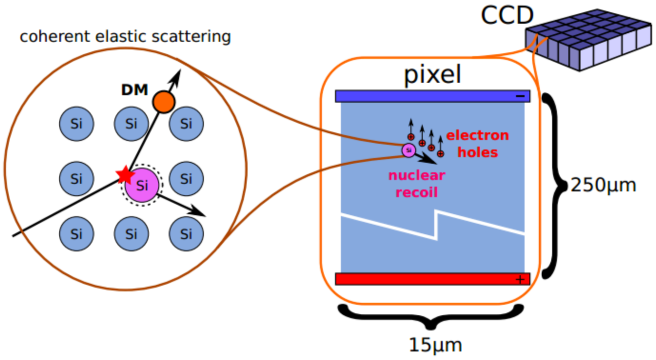

Fig. 5.1 –
DAMIC detection principle: hypothetical dark matter particles scatter coherently off silicon nuclei, producing a nuclear recoil that is recorded as charge on pixels in the CCD.

First results were obtained with a single 0.5 g CCD, installed ≈100 m underground in the NuMI [9] near-detector hall at Fermilab. Data were collected during 11 months in 2011. Standard techniques were used to interpret the results as a cross section limit for spin-independent DM interactions [10], and parameterizations were used allowing the direct comparison with other limits on low mass DM particles. At the time, the DAMIC results constituted the best limits for dark matter mass below 4 GeV.

[1] D.B. Kaplan, Phys. Rev. Lett. **68**, 741 (1992).

[2] D.E. Kaplan, M.A. Luty and K.M. Zurek,
Phys. Rev. D **79**, 115016 (2009).

[3] D. Hooper and W. Xue,
Phys. Rev. Lett., 110, 041302 (2013).

[4] S.E. Holland *et al.*,
IEEE Trans. Electron Dev., **50** 225 (2003).

[5] B. Flaugher,
Ground-based and Airborne Instrumentation for Astronomy, Ian S. McLean editor; Iye, Masanori, Proceedings of the SPIE, Volume 6269, (2006).

[6] Dark Energy Survey Collaboration, astro-ph/0510346.

[7] J. Estrada and R. Schmidt,
Scientific Detectors for Astronomy 2005, J.E. Beletic, J.W. Beletic and P. Amico editors, Springer (2006).

[8] Estrada *et al.*, Proceedings of SPIE 2010.

[9] http://www-numi.fnal.gov/PublicInfo/forscientists.html.

[10] J. Barreto *et al.* (DAMIC Collaboration),
Phys. Lett. B **711**, 264 (2012).

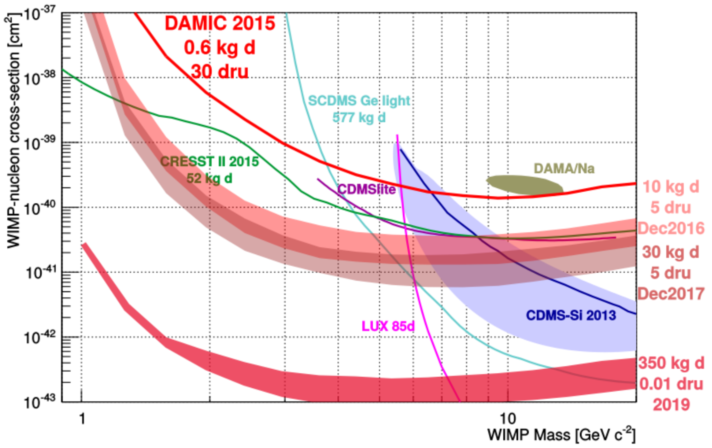

FIG. 5.2 – The limit of DAMIC 0.3 kg day and DAMIC-100(2016).

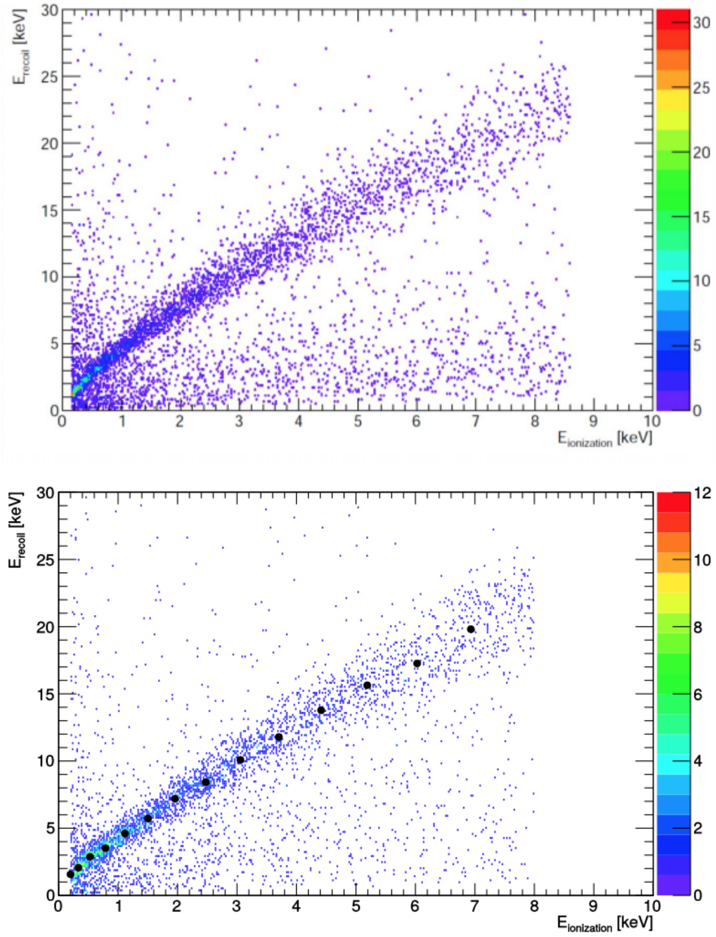

FIG. 5.3 – Distributions of nuclear recoil energy versus ionization energy, from which the quenching factor is determined, for simulation (top) and measurement (bottom). Note a disagreement towards low energy. See next figure too.

5.1 DAMIC-100

The next phase is DAMIC-100, which has begun collecting commissioning data in the summer of 2014. The experiment has been moved underground to SnoLab, which has a 6000 meter water equivalent shielding from cosmic rays, the shielding has been upgraded, and new, thicker detectors have been fabricated. The CCDs, with a total mass of 100 g, are installed inside a copper box cooled to -150°C to reduce dark current. The cold copper also shields the detectors against infrared radiation. A closed cycle helium gas refrigerator is used to maintain the low temperature. The detector is connected through a readout cable to the preamplifiers located outside the lead shield. The detector package is housed in a cylindrical vacuum vessel fabricated with oxygen-free copper, and maintained at 10^{-7} Torr with a turbo molecular pump. Lead and polyethylene shield against γ-rays and neutrons. The detector has been iteratively improved, with a low background lead shield machined at the University of Zurich, and newly designed readout cables provided by the University of Zurich. In 2015, we took 0.6 kg·days of commissioning data using four 5.5-gram CCDs designed for DAMIC-100. The results, in terms of upper limits on the cross-section for spin-independent WIMP - nucleon cross sections, are close to the best results obtained from CRESST II 2015 (Fig. 5.2). Since these DAMIC 2015 results, we have reduced the background from 30 to 5 dru, and we anticipate an order of magnitude improvement in sensitivity by 2016.

5.1.1 Calibration and testing

Energy calibration for DM in the detector is factorized into the ionization energy calibration as determined from direct X-rays and carbon and oxygen fluorescent X-rays from a Fe^{55} source and the signal quenching observed for ionizing nuclear recoils. The quenching factor has been measured in Si for recoil energies above 4 keV [11], showing good agreement with the Lindhard model [12, 13].

We have performed an experiment at the Tandem Van der Graaf of the University of Notre Dame in which monochromatic neutrons are scattered off a silicon target and the scattering angle and neutron time-of-flight are used to determine the nuclear recoil energy. The scattered neutrons are detected with a set of ∼20 scintillating bar counters placed at variant angles (from 20 to 70 degree) that correspond to the low recoil energies of interest (1 - 30 keV).

Besides designing and testing the detector for this calibration experiment, our group developed a Geant [14] simulation of the detector setup to confirm the neutron beam flux, to model resonances of neutrons on silicon, and to determine the energy using the timing. The experiment was performed in 2015. The results compared to our simulation are shown in Figure 5.3. The final calibration is compared to the Lindhard

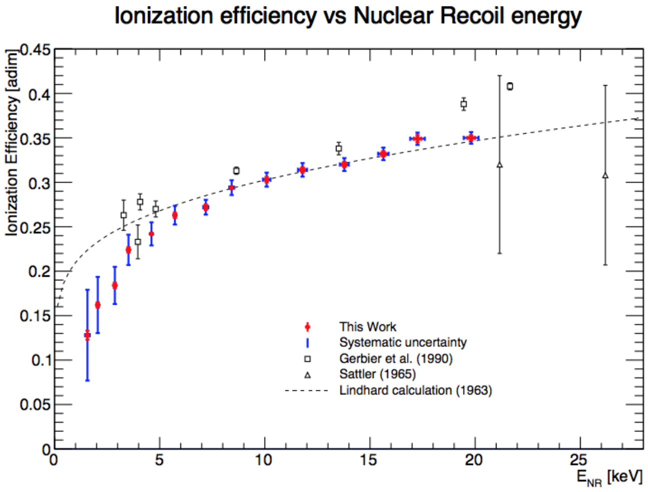

FIG. 5.4 – Results from Antonella data compared to the Lindhard model.

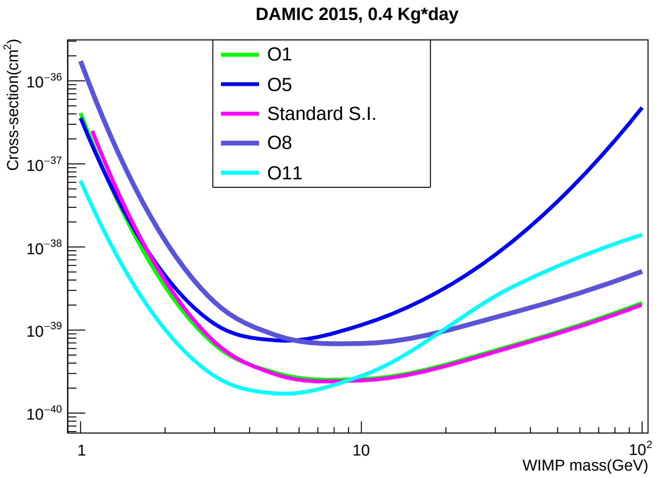

FIG. 5.5 – Limits using 0.38 kg·days of DAMIC 2015 data, comparing various EFT operators with the standard spin-independent interaction.

model and previous measurements in Fig. 5.4. These represent the first measurements of the quenching factor in the 1.5 - 4 keV range, and a deviation from the Lindhard model is observed.

[11] J.D. Lewin and P.F. Smith,
Astropart. Phys. 6, 87 (1996).

[12] J. Lindhard, V. Nielsen, M. Scharff, and P.V. Thomsen, Mat. Fys. Medd. Dan. Selsk **33**, 10 (1963).

[13] H. Chagani *et al.*, JINST 3 (2008) P06003.

[14] http://geant4.cern.ch.

[15] http://www.nndc.bnl.gov/sigma/index.jsp.

5.2 Analyzing DAMIC data using EFT

Most models of DM invoke new physics, such as supersymmetry or extra dimensions, associated with electroweak symmetry breaking, where new phenomena can appear at scales of $\geq$ 100 GeV. However, the momentum transfer in direct detection is much lower, typically a few hundred MeV or less. At this low energy scale, the DM-nucleus scattering in direct detection can be essentially described by a non-relativistic (NR) effective potential with parameters: DM velocity $\beta \equiv v/c \sim 10^{-3}$ and q/Λ, where q is the momentum transfer and Λ some large scale involved, such as the DM mass m_χ, the nucleus mass m_N, or a heavy mediator mass [16]. EFT (Effective Field Theory) provides a general and very efficient way to characterize experimental results with a small set of parameters, such as the mass of the WIMP and the effective coupling constants describing the strength of the contact coupling of the WIMP to the nucleon or nucleus [17–19].

For DM direct detection, there exist 14 "useful" EFT operators with varying powers of v, q and mass scales. We have modeled the expected signals in DAMIC with each of these operators, including detector response and the Lindhard model of energy deposition, and have evaluated the DAMIC 2015 data in terms of these interactions (Fig. 5.5). The $\mathcal{O}1$ operator produces approximately the same results as the standard spin-independent interaction as is expected, and the data is most sensitive to interactions of the $\mathcal{O}11$ operator. The results will be published in a follow-up to our DAMIC 2015 publication this year.

[16] J. Fan, M. Reece and L.-T. Wang,
Non-relativistic effective theory of dark matter
direct detection,
JCAP 11 (2010) 042, arXiv:1008.1591.

[17] B. A. Dobrescu and I. Mocioiu,
Spin-dependent macroscopic forces from
new particle exchange,
JHEP 0611, 005 (2006), arXiv: 0605342.

[18] Nikhil Anand *et al.*,
Physical Review C 89. 065501(2014).

[19] A. Liam Fitzpatrick *et al.*,
Journal of Cosmology and Astroparticle Physics (2013) 004, arXiv : 1203.3542.

6 Very High Energy Gamma Ray Astronomy with CTA

F. Canelli, D. Florin, A. Gadola, S. Steiner, U. Straumann, A. Vollhardt, D. Wolf

in collaboration with: MPI für Kernphysik Heidelberg, Universität Tübingen, Universität Erlangen, Universität Innsbruck and over two hundred other institutes from 31 countries

(CTA)

The Cherenkov Telescope Array (CTA) is currently the most promising candidate for the next generation of Imaging Atmospheric Cherenkov Telescopes (IACTs). IACTs, like the present H.E.S.S. [1], MAGIC [2], and VERITAS [3] are ground-based mirror telescopes used to detect gamma rays of energies from several 10 GeV up to hundreds of TeV. Sources of such very high energy (VHE) gamma rays are both galactic and extragalactic, including quasars, supernovae and their remnants, gamma-ray bursts, and possibly dark matter annihilations. The signal is a faint (100 photons/m^2 @ $E_\gamma =$ 1 TeV) and very fast (few ns) Cherenkov light flash, produced in the shower developing in the Earth's atmosphere after an initial $\gamma \rightarrow e^+e^-$ pair production, allowing the reconstruction of the primary gamma ray's energy and direction. First CTA telescopes may be installed on site in 2017.

[1] B. Opitz *et al.*, (HESS collaboration),
AIP Conf. Proc. 1223 (2010) 140.

[2] J. A. Coarasa *et al.*, (MAGIC collaboration),
J. Phys. Soc. Jap. Suppl. 77B (2008) 49.

[3] D. Hanna *et al.*, (VERITAS collaboration),
J. Phys. Conf. Ser. 203 (2010) 012118.

6.1 FlashCam camera body

Our group contributes two pre-series camera bodies (funding guaranteed) of the photomultiplier-based first fully digital IACT camera for the mid-sized telescope (MST) which has a 12 m dish diameter [4]. The production of additional fifteen camera bodies starts early 2017, if funding is secured by then. The FlashCam camera, as one of the two MST camera candidates, made an important step towards a fully functional prototype. The past years have been devoted to develop, test and build the enclosure. The main design goals were easy access to all parts for installation and maintenance, a good light and water tightness, low weight at low cost, and a design suitable for mass production. Combining proven techniques and materials used in industry with unconventional construction ideas lead to a 3x3x1.1 m^3 body of less than 1.7 tons, including the safety-, power- and filled cooling-systems and most of the cabling. The additional weight of the readout and detector electronics, to be installed in a next step, is estimated to be around 300 kg.

Fig. 6.1 – FlashCam body in Adlershof before installation. The lid has been opened to prevent accidental damage during transport and installation. The Plexiglas entrance window (here a non-UV transparent placeholder) was installed to study the system's mechanical stability under different elevation angles, as well as the cooling system under realistic conditions with a near-sealed body.

6.1.1 Test of the FlashCam body on a real telescope structure

End of June 2015 the body without the readout and detector electronics was transported to the MST prototype structure in Adlershof, Berlin for mechanical and electrical tests. Figure 6.1 shows the camera body with the transportation frame mounted on the sides and opened lid in Adlershof before being mounted into the camera frame of the MST prototype structure. The camera is installed with the help of a sledge system, which allows an easy and safe installation and removal of the camera (Fig. 6.2 left). The excellent teamwork of the two teams from the University of Zurich and from DESY Zeuthen permitted a quick and easy installation of the camera.

The communication with the in-house developed safety and slow control of FlashCam was tested with a dedicated Labview GUI as well as with a simple OPCUA framework. The piping, the flow and pressure of the cooling system was thoroughly tested under realistic coolant flow conditions. For this, the camera was connected to a simple

FIG. 6.2 – Rotating the telescope into the zenith position. The sledge, which can be moved with a winch, is visible below the camera body in the first picture. The camera lid is closed and the two installed detectors are read out for off-line study of possible light leaks and pick-up noise.

pump system (without heat exchanger) and was moved to different elevation angles (Fig. 6.2). Two photomultiplier modules with 12 PMTs each (see e.g. last year's report) and a readout crate was used to determine the light tightness of the camera at different elevation angles and also to investigate a possible noise pick-up from the drive system (Fig. 6.3).

The body was dismounted again in only two hours on July 30th and brought to the Max Planck Institut für Kernphysik (MPI-K) in Heidelberg for the subsequent integration of the readout and detector electronics for 800 pixels.

FIG. 6.3 – Camera rear doors open. The safety and power cabinet at the left lower rack position is being inspected. The slow control drawer is installed in the middle of the right rack. Fan drawers and heat exchangers can be noticed at top and bottom of the two racks.

6.2 Photon-detector module

The photon-detector (PDP) module, equipped with 12 PMTs, preamplifiers, high-voltage generators and some other functionality has been developed at our institute during the past years, see e.g. reports 2012-2014.

Seventy such modules have been ordered and tested in-house before they were sent last autumn to the MPI-K for their integration into the camera body. A single camera contains 147 PDP modules. A total of 1764 pixels cover a field of view of 7.7°. The partially-equipped camera revealed some problems, which were solved by minor changes of the schematics and the layout of the modules (Fig. 6.4). The second half of the detector modules were ordered by the University of Erlangen. All components, including the readout electronics, will be installed in the prototype camera body during the second half of 2016 to allow testing the functionality of a complete camera.

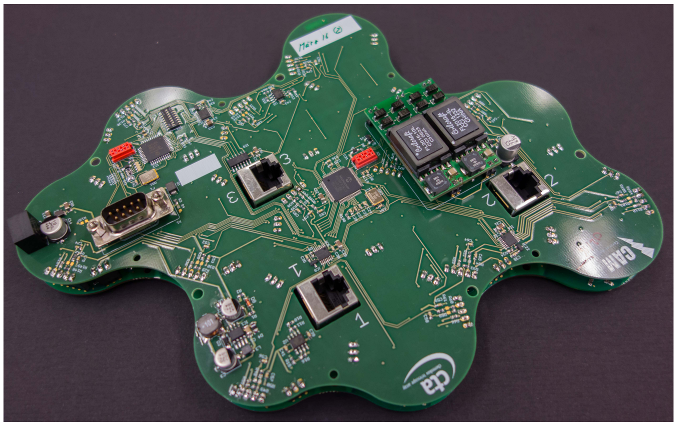

FIG. 6.4 – Improved electronics boards with reduced noise pick-up and reliable CAN-bus communication.

---

[4] G. Pühlhofer *et al.*, (FlashCam collaboration), arXiv 1211.3684 [astro-ph.IM] (2012).

7 Search for the rare decay $\mu^+ \to e^+e^-e^+$

R. Gredig, P. Robmann, and U. Straumann

in collaboration with: University of Geneva, Paul Scherrer Institute, ETH Zürich, University of Heidelberg, University of Mainz, Karlsruhe Institute of Technology

(Mu3e Collaboration)

Lepton flavor violation (LFV), as observed in neutrino oscillations, does not lead to measurable rates for LFV decays of charged leptons. Those would definitely be a clear signal for physics beyond the standard model. Mu3e plans to search for the decay $\mu \to e^+e^-e^+$ with a sensitivity at least three orders of magnitude beyond the present limit, set way back in the previous millennium by the SINDRUM I Collaboration [1] led by our institute. In the past years we have been working on the scintillating fibre tracker (see Fig. 7.1) and its readout and the results of these studies are presented below.

[1] W. Bertl, S. Egli, R. Eichler, R. Engfer, L. Felawka, C. Grab, E.A. Hermes, N. Kraus, N. Lordong, J. Martino, H.S. Pruys, A. v.d. Schaaf and H.K. Walter, Nucl. Phys. B260 (1985) 1.

7.1 Improved SiPM Electronics

Figure 7.2 shows a simplified schematic of the read-out electronics focusing on the sensor-board. Pictures of the board are shown in Fig. 7.3. Two different ways are allowed to bias each SiPM. Either a common voltage is used that powers all the SiPMs with the same voltage or an individual voltage for each sensor can be applied. The voltage distribution uses a low-pass filter before each SiPM to decouple them electronically.

If used with the amplifier the readout is single ended over the shunt resistor. The readout with the STiC chip is done differential. In this case all the pre-amplification electronics is provided by the chip and the sensor-board only needs to connect the SiPM to the STiC.

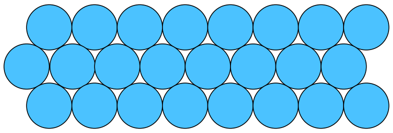

FIG. 7.1 – Cross-section through a scintillating-fibre ribbon.

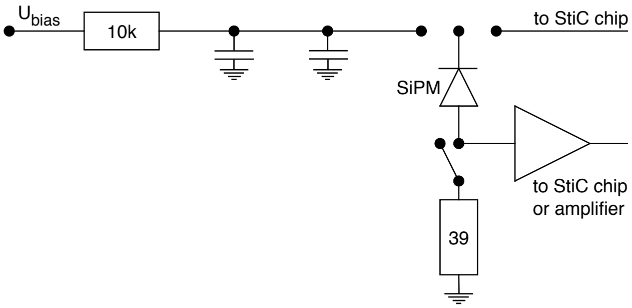

FIG. 7.2 – Electronic scheme of the sensor board. The wiring is repeated for each SiPM. The top switch is used to select a common bias voltage for single ended readout or an individual biasing for differential readout. In the differential readout case the signal goes to the amplifier before the shunt resistor and needs to be opened therefore.

7.2 Crosstalk Studies

Optical crosstalk between the fibres needs to be understood properly. The crosstalk not only worsens the time resolution but also increases the rate per channel.

Figure 7.4 shows a typical result of the crosstalk analysis. In this measurement the ribbon is irradiated in the middle with electrons from a ^{90}Sr source. Two layers are connected to the readout electronics. Events are selected in which in fibre a a signal is observed. The figure shows

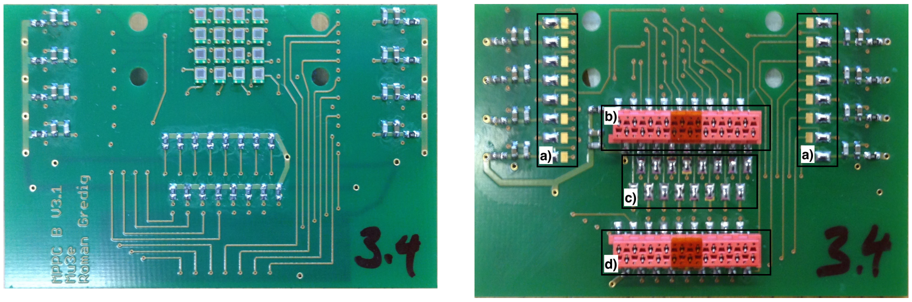

FIG. 7.3 – 3rd generation sensor board. The solder pads *a*) are used to change between common and individual high voltage from the STiC chip. The micro-match plug *b*) uses the same pin-out as the 2nd generation board. For use with the STiC chip the resistors to ground can be switched off with the solder-pads *c*) and the circuit connected to the STiC with *d*).

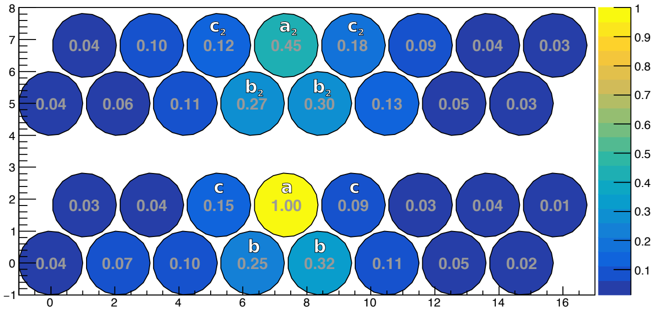

FIG. 7.4 – Result of our crosstalk studies with a ^{90}Sr source. The numbers in gray show the probability to observe a signal when there was a signal in fibre a. The upper and lower parts of the figure show the results from the two ends separately. See text for further details.

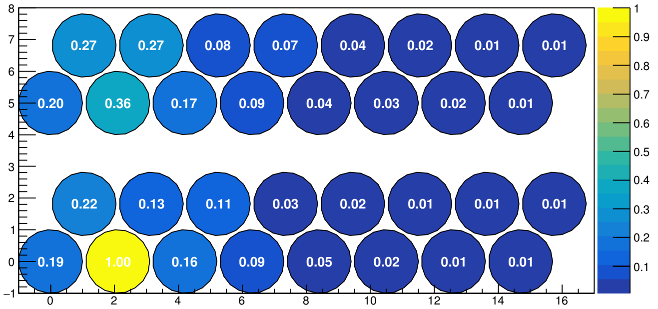

FIG. 7.5 – Crosstalk showing also some fake-crosstalk hits at the right side of the ribbon due to the high decay rate of the source used in the laboratory.

the probability of observing a signal in the other fibres too. The electrons crossing fibre a will also cross one of the fibres b (except when the particle crosses exactly in between them) which explains the observed high values for fibres b. The closest fibres for which crosstalk can be studied are fibres c. Those show crosstalk probabilities of up to 20 %.

Crosstalk depends on the position of the layer in the ribbon. Outside layers have neighbors on one side only. The inside layer has neighbors on both sides (cf. Fig. 7.1). The crosstalk probability for outside layers is on average $(11 \pm 3)\,\%$, for the inside layer we observe $(18 \pm 3)\,\%$. For the next neighbors the crosstalk is $(8.3 \pm 1.4)\,\%$ and $(5.0 \pm 1.6)\,\%$, respectively.

Our crosstalk probabilities must be corrected for accidental coincidences which depend on signal rate and time window. With a typical dark-count rate of $1 \cdot 10^5$ counts per second above a 0.5 photo-electron threshold, a source rate of similar magnitude, and a time window of 20 ns the probability for accidental background is about $4 \cdot 10^{-3}$. For large distances this is the dominant contribution to the observed probabilities.

7.3 Detector efficiencies

The detection efficiency was measured with 160 MeV electrons at the PSI cyclotron. As illustrated in Fig. 7.6 the ribbon was oriented horizontally so a single beam electron could cross many fibres. The beam energy is more than sufficient to guarantee that the electron crosses all fibres and does not stop within the ribbon. The measuring principle for the different fibres is shown in Fig. 7.6 as well. The fibre under investigation is compared with its two nearest neighbors. The efficiency is defined as the probability to detect one photon in the middle fibre when the two neighboring fibres observe at least one photon each. Results are shown in Table 7.1 for each of the 24 fibres under investigation.

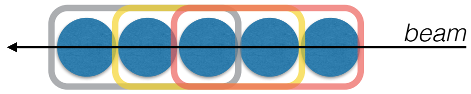

FIG. 7.6 – Principle of the efficiency measurement. For each fibre a cluster of three fibres is used (grey, yellow, red in this example) to specify the efficiency of the fibre in the middle of a cluster.

The results show that the fibre efficiency varies a lot between different channels for which we see two reasons. On the one hand there can be a large variety in the fibre quality caused by imperfections in the production process. Especially the extremely thin fibre cladding can be destroyed by improper handling. Also crazing, the production of micro cracks due to finger grease or sweat acids, can be a problem as the ribbons are manufactured manually. In this case the manufacturing procedures need to be improved. The second potential problem source is bad coupling of the fibres to the sensors. Especially in the case of single photon experiments a geometric misalignment, dirt or bad polishing can have strong influence

TAB. 7.1 –
Single fibre efficiency eff defined as the probability of detecting a photon in the middle fibre when each of the two surrounding fibres observed a signal.

fibre	eff	fibre	eff	fibre	eff	fibre	eff
1	0.73	7	0.47	13	0.65	19	0.72
2	0.64	8	0.72	14	0.64	20	0.55
3	0.68	9	0.50	15	0.69	21	0.74
4	0.70	10	0.51	16	0.65	22	0.70
5	0.68	11	0.37	17	0.71	23	0.71
6	0.70	12	0.74	18	0.66	24	0.67

Tab. 7.2 –
Efficiencies for two fibres. The values show the probability of detecting a photon in one of the middle fibres (OR condition) when there is a photon detected in the two surrounding fibres.

pair	eff	pair	eff	pair	eff	pair	eff
1	0.87	6	0.82	11	0.84	16	0.83
2	0.84	7	0.84	12	0.85	17	0.85
3	0.86	8	0.72	13	0.84	18	0.90
4	0.86	9	0.66	14	0.86	19	0.89
5	0.87	10	0.82	15	0.86	20	0.87

on the efficiency. The use of optical grease has not been envisaged as the transparency of the grease tends to degrade in time. A better coupling would certainly be reached by glueing the fibres to the sensors. In this early R&D stage with only one ribbon available and different sensors to be tested glueing was, however, no option.

As the final experiment will have more than one layer of fibres the efficiencies for two and three layers have been estimated as well. In case of two layers new clusters including four fibres have been used for measuring the efficiency. The probability to observe at least one photon in one of the two middle fibres (OR) when the two outer fibres show at least one photon each defines the new efficiency. The measured results are shown in Table 7.2.

Tab. 7.3 –
Predicted double fibre efficiencies.

fibre	eff	fibre	eff	fibre	eff	fibre	eff
1	0.93	7	0.72	13	0.88	19	0.92
2	0.87	8	0.92	14	0.87	20	0.80
3	0.90	9	0.75	15	0.90	21	0.93
4	0.91	10	0.76	16	0.88	22	0.91
5	0.90	11	0.60	17	0.92	23	0.92
6	0.91	12	0.93	18	0.88	24	0.89

The results can be cross-checked with the single fibre efficiencies. The probability to observe a signal in at least one of the two fibres ε_2 can be predicted from the measured single-fibre detection efficiency ε_1.

$$\varepsilon_2 = 1 - (1 - \varepsilon_1)^2$$

These predicted values vary typically 0.86 ± 0.08 (see Table 7.3) in agreement with the measured 0.84 ± 0.05.

With the same ansatz the efficiencies for three fibres have been calculated. These results are summarized in Fig. 7.7. The predicted values are overall 0.95 ± 0.05 and if we skip the fibres considered to be broken it even reaches 0.97 ± 0.01.

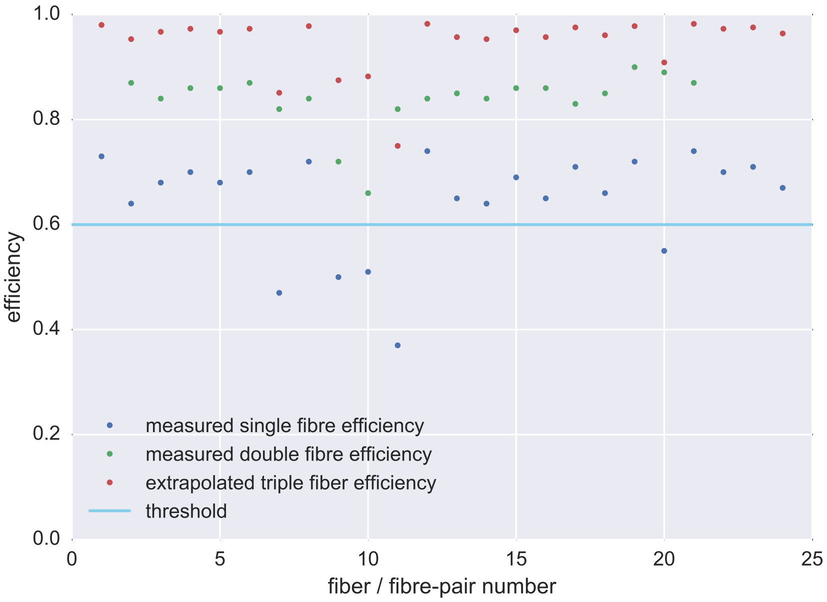

Fig. 7.7 – Cluster efficiency for electrons. The blue line highlights the threshold where the fibres are considered broken or where the coupling to the sensor was bad.

8 The $\pi^+ \to e^+\nu_e$ / $\pi^+ \to \mu^+\nu_\mu$ branching ratio

P. Robmann, A. van der Schaaf and P. Truöl

in collaboration with University of Virginia, Charlottesville, USA; Institute for Nuclear Studies, Swierk, Poland; JINR, Dubna, Russia; PSI, Villigen, Switzerland and Rudjer Bošković Intitute, Zagreb, Croatia

(PEN Collaboration)

Within the Standard Model, assuming $V-A$ structure of the electroweak interaction, pion decays are helicity-suppressed (l stands for e and μ):

$$\Gamma[\pi^+ \to l^+\nu_l(\gamma)] = \frac{G_\mu^2|V_{ud}|^2}{4\pi}F_\pi^2 m_\pi m_l^2[1-\frac{m_l^2}{m_\pi^2}] + h.c.\,,$$

where G_μ indicates that the Fermi coupling constant is taken from the muon lifetime. The largest uncertainty comes from the pion decay constant F_π which accounts for the non-perturbative strong interactions between the quarks inside the pion. In fact, the measured pion decay time τ_π=26.033(5) ns is used to measure F_π which is an important parameter in strong-interaction physics.

Most theoretical (and experimental!) uncertainties cancel when studying the branching ratio

$$B \equiv \Gamma[\pi^+ \to e^+\nu_e(\gamma)]/\Gamma[\pi^+ \to \mu^+\nu_\mu(\gamma)]\,.$$

The Standard Model value of the $\pi^+ \to e^+\nu_e$ / $\pi^+ \to \mu^+\nu_\mu$ branching ratio, calculated assuming $V-A$ and a universal $Wl_i\nu_i$ coupling strength, is $1.2353(1)\times10^{-4}$ [1]. A measurement of the branching ratio would allow sensitive tests of these two fundamental ingredients of the Standard Model. The present experimental result $1.2312(37)\times10^{-4}$ dates back over thirty years [2] and two new experiments [3] aim at a reduction of the error by almost an order of magnitude. A first result of our PIENU friends, $1.2344\pm0.0023(\text{stat})\pm0.0019(\text{syst})\times10^{-4}$ based on 10% of their data set, was published last year [4].

[1] V. Cirigliano and I. Rosell, JHEP **10** (2007) 5;
Phys. Rev. Lett. **99** (2007) 231801.

[2] G. Czapek *et al.*, Phys. Rev. Lett. **70** (1993) 17;
D. I. Britton *et al.*, Phys. Rev. Lett. **68** (1992) 3000.

[3] PEN Collaboration, PSI experiment R-05-01 (2005),
D. Počanić and A. van der Schaaf, spokespersons;
PIENU Collaboration, TRIUMF proposal 1072 (2006),
D. Bryman and T. Numao, spokespersons.

[4] A. Aguilar-Arevalo *et al.*, [PIENU Collaboration],
Phys. Rev. Lett. **115** (2015) 071801.

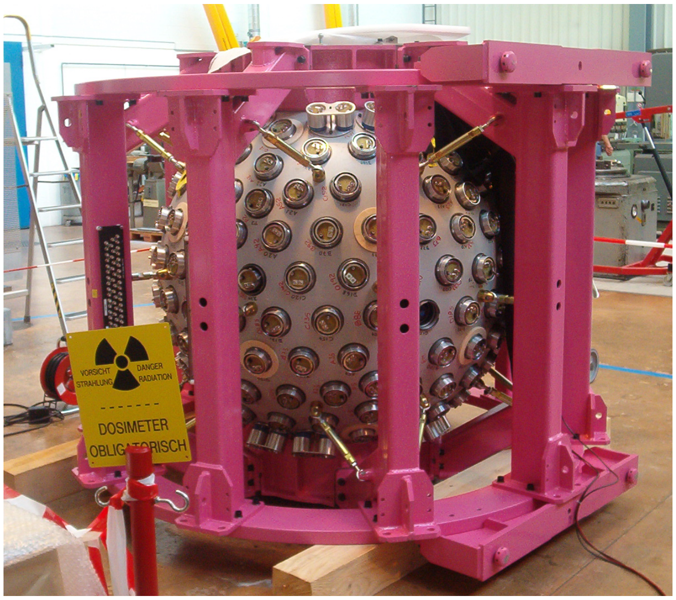

FIG. 8.1 – The PEN pure-CsI calorimeter in the PSI "Montagehalle" before it was mounted on the experimental platform and buried under cabling and thermo-shielding.

8.1 PEN data taking

The PEN experiment took data at PSI during the years 2008 - 2010, where the setup varied slightly over the years. The most expensive component by far is a 3π Sr spherical pure-CsI calorimeter (see Fig. 8.1) used to measure positron and photon energies. Pure CsI has its main scintillation decay-time component around 28 ns, much shorter than most other organic scintillators.

Pions from the πE1 beam line are brought to rest in a plastic scintillator after having crossed a thin scintillator in an intermediate focus 4 m upstream and a degrader scintillator, situated close to the target scintillator. During 2009/10 a small time-projection chamber (mini TPC) is used to record the trajectories of the incoming pions.

Decay positrons from $\pi \to e\nu$ and the sequence $\pi \to \mu\nu$, $\mu \to e\nu\bar{\nu}$, are tracked in two cylindrical MWPCs. The positron energy is determined primarily with the CsI calorimeter. A cylindrical plastic scintillator hodoscope in front of the calorimeter is used both for timing and for particle identification (in particular to separate decay positrons and protons from pion reactions) through $\Delta E - E$.

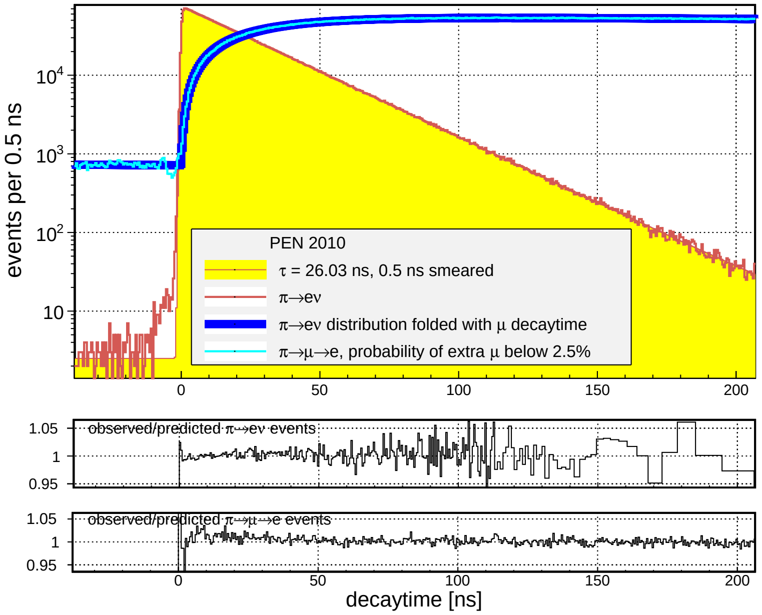

FIG. 8.2 – Observed year 2010 $\pi \to e\nu$ decaytime distribution. Note the very low background of accidental coincidences and the perfect fit with the expected exponential. Also shown are the prediction for the $\mu \to e\nu\overline{\nu}$ branch, obtained by folding with the muon lifetime.

8.2 Data analysis and outlook

PEN took data during 2008 - 2010 and has been studying them in great detail ever since. Calibrations are done and most features observed are reproduced by simulation (see previous annual reports for details).

Key observables are the e^+ energy and the $\pi^+ - e^+$ time delay $\Delta t_{\pi e}$ (see Figs. 8.2 and 8.3). The decay $\pi^+ \to e^+\nu(\gamma)$ peaks at $0.5{\times}m_\pi$ and falls with τ_π. The decay sequence $\pi^+ \to \mu^+\nu$ followed by $\mu^+ \to e^+\nu\overline{\nu}(\gamma)$ is characterized by an e^+ energy below $0.5{\times}m_\mu$ and $\Delta t_{\pi e}$ first rising with τ_π and then falling with τ_μ=2.197 μs.

Whereas the $\pi^+ \to e^+\nu(\gamma)$ decay was recorded with almost 100% efficiency for e^+ emitted in the calorimeter acceptance, the other branch was recorded only for $\Delta t_{\pi e} < 220$ ns. Events with e^+ energies below ≈ 48 MeV were pre-scaled by typically a factor 20.

Systematic uncertainties are associated with the fraction of $\pi^+ \to e^+\nu(\gamma)$ events with total energy below $0.5{\times}m_\mu$ and the fraction of $\pi^+ \to \mu^+\nu(\gamma)$ decays within the chosen $\Delta t_{\pi e}$ window. The tail fraction is typically 2% and its value ultimately relies on simulation. The error associated with the time window is minimized by choosing a window corresponding to the situation in which the event rate is equal at both ends. For a 100 ns wide window this happens for 81.4 - 181.4 ns (see Fig. 8.4).

Results for both B and the structure-dependence of $\pi \to e\nu\gamma$ are expected within a year from now.

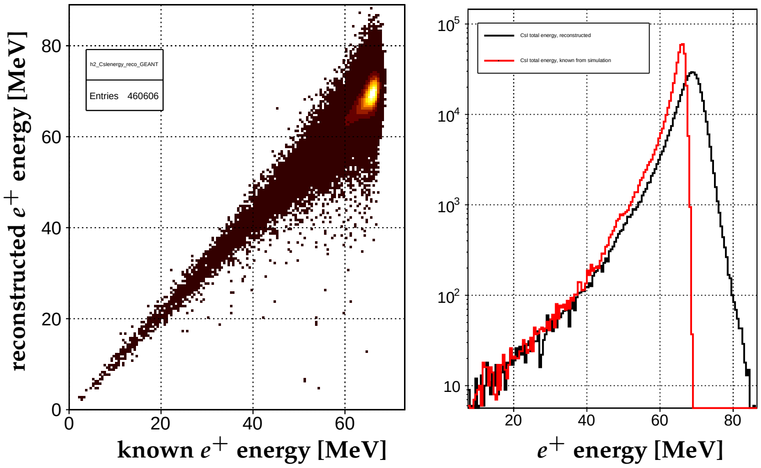

FIG. 8.3 –
Scatter plot of reconstructed and known energy deposits from a GEANT $\pi \to e\nu$ simulation (left). The right panel shows the two projections. Note the structure, around 50 MeV, for example, which is caused by hadronic interactions followed by neutron escape.

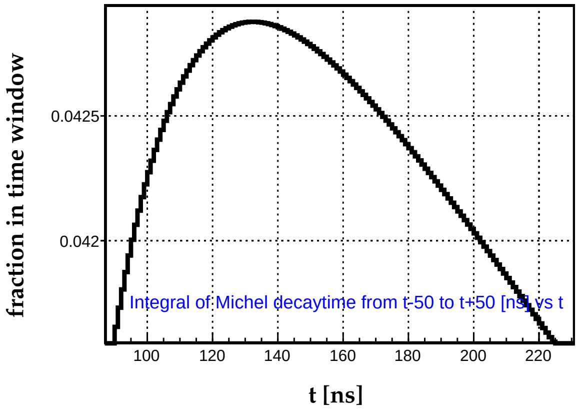

FIG. 8.4 –
Fraction of $\pi \to \mu \to e$ events with a $\pi - e^+$ time delay in a window t±50 ns, versus t. The distribution peaks at 131.4 ns but falls less than 10^{-5} when moving 1 ns away from that value.

9 Particle Physics with SHiP

C. Betancourt (since February 2016), I. Bezshyiko (since November 2015), N. Chételat (until December 2015), E. Graverini, N. Serra, B. Storaci

The full SHiP collaboration consists of 45 institutes from Bulgaria, Chile, Denmark, France, Germany, Italy, Japan, Russia, Sweden, Switzerland, Turkey, Ukraine, the United Kingdom and the United States of America.

(SHiP Collaboration)

SHiP is a newly proposed general purpose fixed target facility at the CERN SPS accelerator. A 400 GeV proton beam will be dumped on a heavy target in order to produce 2×10^{20} proton-target interactions in five years. A dedicated detector downstream of the target will allow one to probe a variety of models with light long-lived exotic particles with masses below $\mathcal{O}(10\ \text{GeV/c}^2)$. Active neutrino cross-sections and angular distributions will also be studied, thanks to a dedicated detector placed between the target and the downstream detector [1].

SHiP's flagship goal is to use decays of charm and beauty mesons to search for Heavy Neutral Leptons (HNLs), which are right-handed partners of the Standard Model (SM) neutrinos. The existence of such particles is strongly motivated by theory, as they can simultaneously solve multiple problems left open by the SM. In the Neutrino Minimal Standard Model (νMSM), HNLs can explain the baryon asymmetry of the Universe, account for the pattern of neutrino masses and oscillations and provide a dark matter candidate [2].

Our group was one of the founding groups since the Expression of Interest submitted in 2013 [1]. Since then, we played a leading role by taking responsibility of the physics programme (Nicola Serra is convener for the SHiP physics performance group) and of part of the detector design and R&D (Barbara Storaci is convener for the upstream veto and timing detectors).

The experiment has been recently positively reviewed by the relevant scientific committee at CERN (SPSC), who requested the preparation of a Comprehensive Design Report, which will be incorporated into the European Strategy Document of CERN that will be prepared by 2019.

[1] W. Bonivento *et al.*, arXiv:1310.1762, SPSC-EOI-010.

[2] A. Takehiko, S. Blanchet and M. Shaposhnikov, Phys. Lett. B631 151-156 (2005).

9.1 SHiP detector

A dedicated beam line extracted from the SPS will convey a 400 GeV/c proton beam at the SHiP facility [1,3]. Figure 9.1 shows an overview of the setup.. The beam will be stopped in a Molybdenum and Tungsten target, at a center-of-mass energy $E_{CM} = \sqrt{2E_b m_p} \simeq 27$ GeV. Approximately 2×10^{20} proton-target collisions are foreseen in 5 years of operation. The target will be followed by a hadron stopper and a system of shielding magnets to sweep muons away from the fiducial decay volume. A neutrino detector consisting of OPERA-like bricks of laminated lead and emulsions, followed by a tracker and a muon spectrometer, will allow measurement and identification of charged particles produced in charged current neutrino interactions. An upstream tagger will help to detect and veto charged particles produced in front of the main decay volume, which is contained in a 50 m long cylindrical vacuum vessel with elliptical section, of semi-axes 2.5 m and 5 m, at about 64 m from the target. A straw tagger is placed in vacuum 5 m downstream of the entrance lid of the vessel. An additional background tagger surrounds the fiducial decay volume, whose walls enclose 30 cm of liquid scintillator. The Hidden Sector (HS) detector will comprise: a tracking system placed in vacuum at the end of the vessel, made of 5 m long straw tubes organized in 4 stations in a magnetic field of 1 T; a high-accuracy timing detector; and a particle identification system featuring electromagnetic and hadronic calorimeters followed by a muon system made of four active layers interlaced with iron.

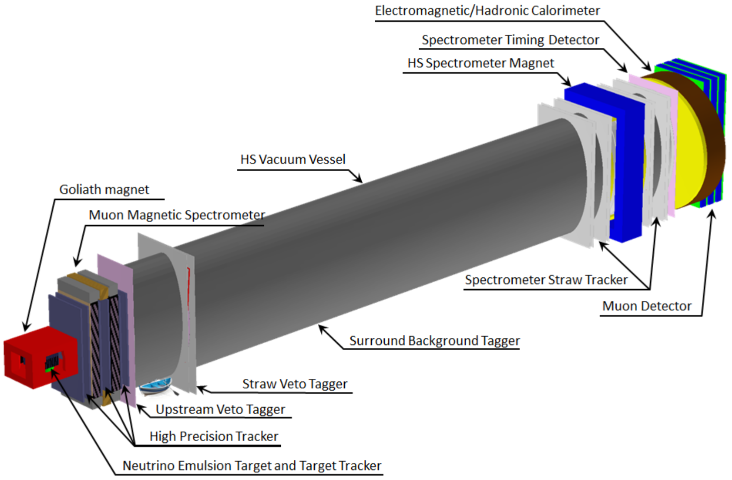

FIG. 9.1 – Overview of the SHiP detector.

Our group has also lead the optimization studies for the shape of the vacuum vessel containing the HS decay volume. The length of the decay volume is obtained by maximizing the acceptance to the hidden particle decay products given the transversal size, fixed by the muon sweeping power of the upstream magnet.

9.1.1 Timing detector

C. Betancourt, I. Bezshyiko, N. Serra and B. Storaci

Background muons crossing the decay volume represent a significant source of combinatorial background. It can be removed by requiring that the two tracks mimicking a genuine signal event are coincident in time. This requires a time resolution equal to, or even smaller than, 100 ps. For this reason, a dedicated timing detector, placed in front of the calorimeter system, is required.

Two technologies are considered for the timing detector: plastic scintillating bars and multi-gap resistive plate chambers (MRPC). Both technologies can be based on existing and well-studied designs and reach the desired time resolution of 100 ps [3]. Our group is involved in studies of scintillating bars read by Silicon Photomultiplier (SiPM) arrays. We are presently conducting tests in the laboratory to measure the time resolution for different geometry and configurations of SiPM arrays.

[3] M. Anelli *et al.*, [SHiP Collab.],
arXiv: .CERN-SPSC-2015-016.

9.2 SHiP physics performance

At the energy accessible at the SPS, the hidden particles are predominantly produced in decays of hadrons, in particular in decays of charmed and beauty hadrons above the kaon mass, and in proton bremsstrahlung. In comparison with the couplings between the particles of the SM, the hidden sector couplings with SM particles are very suppressed, leading to expected production rates of $\mathcal{O}(10^{-10})$ or less. The principal background to the hidden particle decay signal originates from the inelastic scattering of neutrinos and muons in the vicinity of the detector, producing long-lived V^0 particles. Another source of background comes from random combinations of tracks in the fiducial volume from the residual muon flux, or other charged particles from interactions in the proximity, which enter the decay volume and together mimic signal events. The contribution of cosmic muons to both types of background is expected to be small [3].

Since our group leads the studies about the SHiP physics performance, we have conducted a thorough study of the neutrino-induced background and coordinated the analyses of the other background sources. With our statistical power, no evidence of any irreducible background was found.

9.2.1 Background studies

I. Bezshyiko, N. Chételat, E. Graverini, N. Serra and B. Storaci

The neutrino flux is estimated to be 10^{11} neutrinos per spill, with an energy spectrum ranging from 2 GeV to about 100 GeV. A sample of neutrino interactions with the detector material was simulated, corresponding to five years of SHiP operation. Neutrino interactions were found to take place mainly in the muon magnetic spectrometer of the tau neutrino detector, in the entrance window of the vacuum vessel and in the surrounding walls of the vacuum vessel. The probability that neutrinos interact with the residual gas inside the decay volume is negligible if the vacuum pressure is set to 10^{-6} bar. A more sophisticated analysis showed that many of these background events can be rejected by making use of the surrounding veto tagger and topological cuts, which would relax the requirements on the vacuum pressure.

The topology of the products of the neutrino interactions is such that relatively loose selection requirements allow efficient rejection. In general the interaction products do not point to the target, do not have a reconstructed vertex inside the decay volume, and have very poor track quality. The requirement of having two tracks with a reduced χ^2 below 5, forming a vertex with a maximum width of 30 cm, and with an impact parameter with respect to the proton target below 5 m rejects 99.4% of the reconstructed background-induced candidates. At the level of online selection, the requirement of having at least one veto detector with a positive response, together with a loose requirement on the pointing of the interaction products to the target, rejects about 99.5% of tracks coming from neutrino interactions.

The combination of veto detectors and offline selections reduces the neutrino induced background to zero expected events in five years of running. The set of selections applied is highly redundant and can be trimmed down to study specific channels. Tab. 9.1 shows the effect of three sets of selections on two exotic decays (HNLs and dark photons) and on neutrino-induced background. Events with multiple reconstructed candidates are discarded, as well as those with vertices and tracks not fully contained in the fiducial decay volume. High quality tracks and vertices are then selected, and candidates not pointing back to the target or with activity registered in the background-tagging detectors are discarded.

Tab. 9.1 –
Efficiency of the selection requirements for the HNL and dark photon decays, and for neutrino-induced background.

Sample	Vertex Isolation	Fiducial Volume	Event Selection
$HNL \to \pi\mu$	97.5 %	76.1 %	82.0 %
$\gamma' \to \mu\mu$	99.6 %	85.2 %	88.4 %
ν bkg.	79.1 %	21.0 %	0.0 %

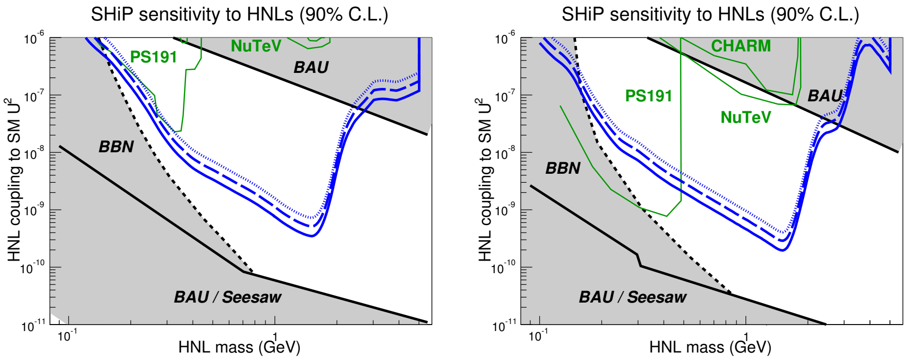

FIG. 9.2 – SHiP's sensitivity to HNLs assuming normal (left) or inverted (right) hierarchy of SM neutrino masses. The parameter space of the νMSM is superimposed. The solid blue curve represents the 90% C.L. upper limit assuming 0.1 background events in 2×10^{20} proton-target collisions. The dashed blue curve assumes 10 background events. The dotted blue curve assumes a 60% systematic uncertainty on the level of background, i.e. 10 ± 6 background events.

9.2.2 SHiP sensitivity

I. Bezshyiko, E. Graverini, N. Serra and B. Storaci

Our group has provided the official SHiP sensitivity estimates for the νMSM, the SHiP flagship theory, and for dark photons, the gauge bosons of a minimalistic theory based on the breaking of a $U(1)$ symmetry in the HS.

The SHiP physics sensitivities are evaluated on the basis of the official simulation and reconstruction package, called FAIRSHIP, to the development of which our group contributed substantially, and of a fast Monte Carlo simulation developed by Elena Graverini in order to determine both the rate of HNLs produced at the target and the acceptance of the HNL decay products. From these estimates, the expected number of events in 5 years of SHiP operation is calculated. The official software and the fast simulation were compared and validated against each other. The official software, that contains a full GEANT4 description of the material and detector geometry, was used to devise offline selections able to suppress the background while maintaining a large signal acceptance. To assess the impact of the reconstruction and selection on the signal, a correction to the fast simulation is applied using the full simulation outcomes as a function of the mass of the HNL, for two body and three body decays. SHiP's sensitivity to HNLs as a function of their mass and couplings, for normal and inverted hierarchy of SM neutrinos, is shown in Fig. 9.2.

A very similar method, analogous the one used by the authors of [4], was used to estimate SHiP's sensitivity to dark photons (see Fig. 9.3). To derive the limits, the results of the three channels identified earlier (meson decays, bremsstrahlung, and direct QCD production) were used. Bremsstrahlung production must be accompanied by a form factor suppression, if the mass of the dark photon is above the typical QCD scale.

Several other models with hidden particles can be studied at SHiP and are described in Ref. [5].

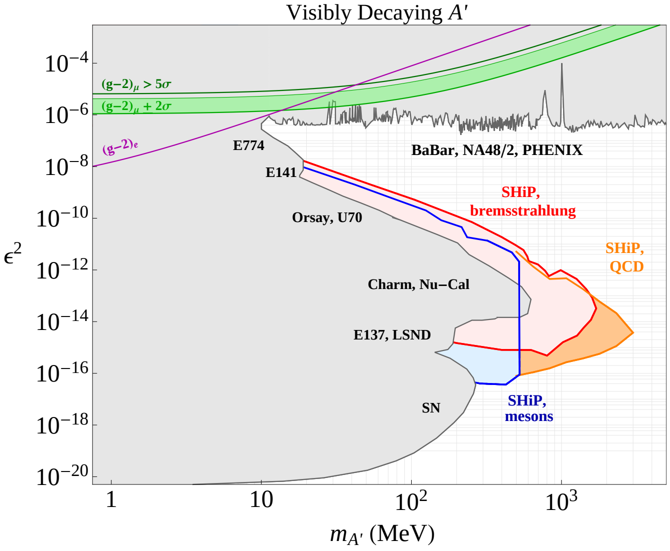

FIG. 9.3 – SHiP's sensitivity to dark photons. Previous searches, as well as limits from cosmological observations, are superimposed. The projected SHiP sensitivity contour is derived using three modes of production: mesons, bremsstrahlung, and QCD production.

[4] J. Blümlein and J. Brunner,
Phys. Lett. B731 (2014).

[5] S. Alekhin *et al.*,
arXiv:1504.04855, CERN-SPSC-2015-017.

10 Particle Physics with LHCb

C. Abellan, R. Bernet, Ch. Betancourt (since February 2016),
I. Bezshyiko (since December 2015), E. Bowen, A. Bursche (May-November 2015),
M. Chrząszcz[1], Ch. Elsasser (until July 2015), E. Graverini, F. Lionetto, A. Mauri,
K. Müller, N. Serra, R. Silva Coutinho (since May 2015), St. Steiner, O. Steinkamp,
B. Storaci, U. Straumann, M. Tresch, A. Vollhardt and A. Weiden

[1] also at Henryk Niewodniczanski Institute of Nuclear Physics, Polish Academy of Sciences, Kraków, Poland

The full LHCb collaboration consists of 69 institutes from Brazil, China, Colombia, France, Germany, Ireland, Italy, Poland, Romania, Russia, Spain, Switzerland, the Netherlands, Ukraine, the United Kingdom and the United States of America.

(LHCb Collaboration)

The LHCb forward spectrometer at the CERN Large Hadron Collider (LHC) [1], which is fully instrumented in the pseudorapidity range $2 < \eta < 5$, was optimised for precision tests of the Standard Model (SM) and for indirect searches for physics beyond the SM (BSM) through precision measurements of CP violating phases and rare heavy-quark decays. This forward acceptance and the ability to trigger on particles with relatively low transverse momentum allow to probe particle production in a unique kinematic range.

The Zurich group is responsible for the operation and maintenance of silicon detectors in the tracking system and for the luminosity measurements. We also contribute to the R&D for the upgraded LHCb detector. Furthermore, our group makes significant contributions to measurements of rare B-meson and τ lepton decays as well as measurements involving the electroweak gauge bosons. Members of our group play important coordination roles within the collaboration: N. Serra is member of the editorial board, B. Storaci operations coordinator and O. Steinkamp deputy project leader of the silicon tracker.

[1] A. A. Alves Jr. *et al.* [LHCb Collab.], JINST 3 S08005 (2008).

10.1 LHCb detector

The LHCb detector was successfully operated in Run I (2009-2013), where data corresponding to an integrated luminosity of 3 fb^{-1} was collected at centre of mass energies of 7 (1 fb^{-1}) and 8 (2 fb^{-1}) TeV. After the consolidation of LHC (2013-2015) the centre of mass energy increased to 13 TeV for Run II which started in May 2015. The detector coped well with the changed operating conditions at the higher collision energy and the reduction of the proton-proton (pp) bunch collision spacing from 50 to 25 ns. In the short 2015 data taking period, the experiment recorded pp collisions corresponding to an integrated luminosity of 321 pb^{-1}. In addition, the experiment was operated for the first time during $Pb-Pb$ collisions and a data sample corresponding to an integrated luminosity of about 5.6 μb^{-1} was collected.

A major improvement in the operation of the experiment has been the introduction of a novel approach in the software trigger which has been split into two stages. First, based on a partial event reconstruction, selection cuts are applied on generic event properties such as displaced tracks and vertices or pairs of muon candidates. All selected events are then temporarily buffered on disk, while a fully automated calibration and alignment of the detector is carried out on a dedicated computing farm consisting of 50'000 logical CPU cores. In the second stage, a full event reconstruction is performed, using the updated calibration and alignment constants. A mixture of inclusive and exclusive cuts selects the events to be stored for offline analyses. This new approach improves on the quality of the trigger selection algorithms and permits to apply more complex algorithms, thereby increasing the fraction of useful events that are saved for offline reconstruction.

10.1.1 TT Detector performance

E. Graverini, O. Steinkamp and B. Storaci

In 2015 the Tracker Turicensis (TT) detector performed as well as during the first LHC data taking period. At the end of 2015, more than 99.5% of its 143'360 readout channels were operational. The main reason for missing channels was again the failure of light-emitting diodes in the optical transmission lines. The single-hit detection efficiency remained almost 100% and the observed position resolution is 53 μm, compared to a simulated 48 μm. We

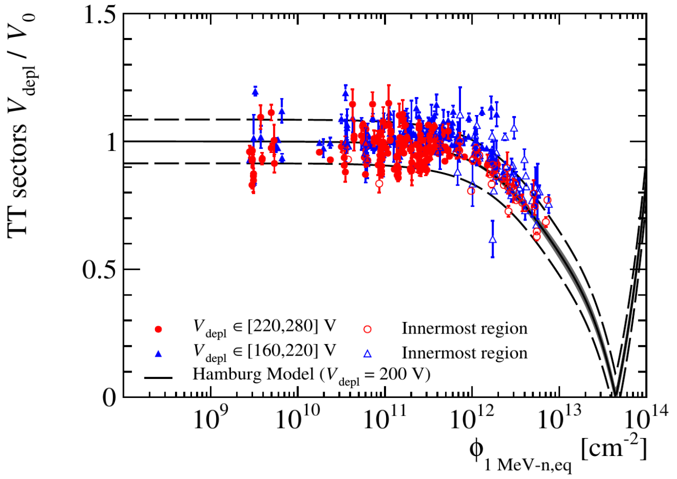

FIG. 10.1 – Measured full-depletion voltage as a function of the received particle fluence. Symbols show measurements done at different times and for various regions of the detector, while full and dashed lines indicate the expectation from model calculations with its uncertainty.

go on studying the spatial alignment of the detector elements and expect a further improvement in position resolution.

In view of the harsh radiation environment at the LHC, the monitoring of radiation damage in the silicon detectors remains an important task. Leakage currents in the detector are monitored continuously and regular charge-collection efficiency scans allow to determine the bias voltage at which the silicon sensors fully deplete. The evolution of this full-depletion voltage versus received radiation, which ultimately limits the lifetime of the detectors, is well described by a detailed model calculation (see Fig. 10.1) which gives confidence that radiation damage will not affect the performance of the detector until its foreseen replacement during the LHCb upgrade.

10.2 LHCb upgrade

C. Abellan, Ch. Betancourt, I. Bezshyiko, F. Lionetto and O. Steinkamp

The LHCb collaboration prepares for a comprehensive upgrade during the second long shutdown of the LHC in 2019/2020 [2] after which the instantaneous luminosity will have increased by a factor five. The detector will be fully read out at the LHC bunch-crossing frequency of 40 MHz, eliminating the need for a hardware-based trigger and thereby significantly increasing the trigger efficiencies for many final states of interest.

The current TT detector will have to be replaced, since its front-end readout electronics is not compatible with the new readout scheme. The replacement for the TT, dubbed Upstream Tracker (UT), is being developed in collaboration with CERN and six institutions from Italy, Poland and the US [3]. To best exploit our experience, we have taken the responsibility for the development of the hardware and control software for high- and low-voltage power, the monitoring of operational and environmental parameters, and the detector safety system. Moreover, we play a prominent role in the testing of the new front-end readout chip (SALT) and in test beam efforts to qualify radiation-hard silicon sensors for the UT.

[2] LHCb Collab.,
CERN-LHCC-2012-007, LHCB-TDR-007.

[3] LHCb Collab.,
CERN-LHCC-2014-001, LHCB-TDR-015.

10.3 Track reconstruction at software trigger level

E. Bowen, E. Graverini, B. Storaci and M. Tresch

Fast and efficient track reconstruction algorithms are crucial for the successful operation of the software trigger of the upgraded detector. We developed a new algorithm connecting track segments in the vertex detector to hits in the UT, significantly speeding up the track reconstruction at no loss in overall reconstruction efficiency [4]. We already back-ported this algorithm for use with the current TT in the software trigger during 2015. The faster track reconstruction allows for less stringent trigger requirements. This way selection biases due to trigger conditions could be removed in various analyses and trigger efficiencies could be increased correspondingly.

The successful operation of the algorithm in actual data taking provides an important proof-of-principle for the upgrade.

[4] E. Bowen and B. Storaci, CERN-LHCb-PUB-2013-023.

10.4 Luminosity measurements

K. Müller and A. Weiden

Absolute cross-section measurements require the precise knowledge of the luminosity. At LHCb the luminosity scale is calibrated periodically using Van der Meer scans [5] and a beam-gas imaging method [6].

A few weeks after the restart of LHC a luminosity calibration, based on the beam-gas imaging method, was available already with a precision of 3.8%. Our group is responsible for the analysis of the Van der Meer scans. We are presently studying the stability in time of the ratio between observed event rates and luminosity. The final luminosity calibration of the 2015 dataset should be available in summer 2016.

[5] S. van der Meer, CERN-ISR-PO68-31 (1968).

[6] M. Ferro-Luzzi, Nucl. Instrum. Meth. A553 (2005) 388.

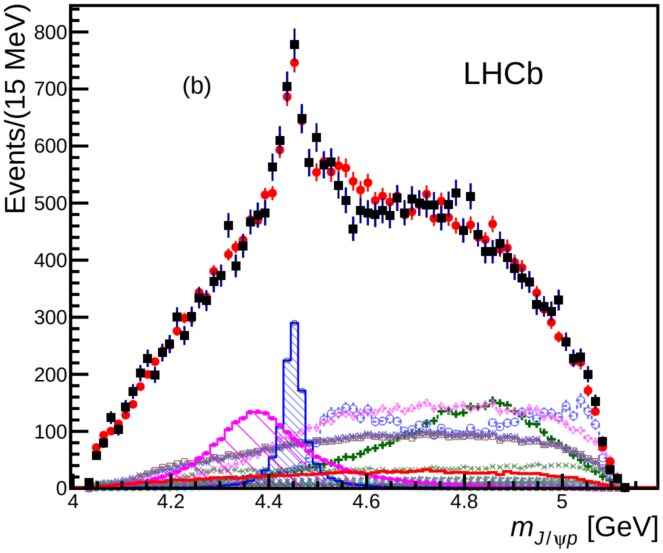

FIG. 10.2 – Fit to $m_{J/\Psi p}$ in $\Lambda_0 \to J/\Psi K p$. Data are shown as black squares and the fit result as red circles, blue open and purple solid squares show the two pentaquark states.

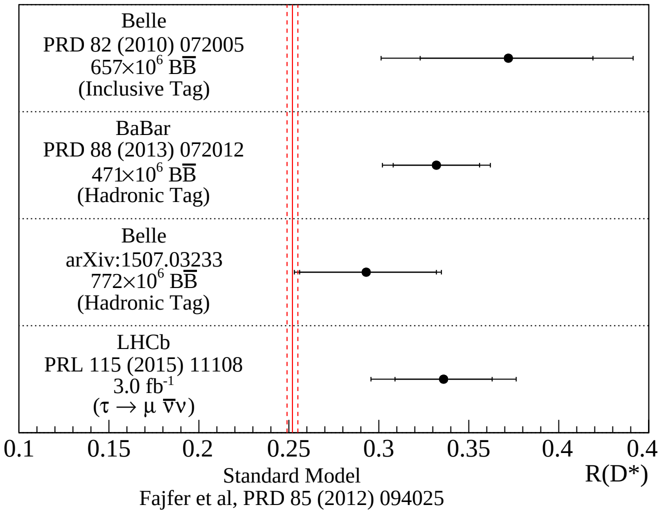

FIG. 10.3 – Experimental results for $\mathcal{B}(B \to D^{*-}\tau^{+}\nu_{\tau})/\mathcal{B}(B \to D^{*-}\mu^{+}\nu_{\mu})$.

10.5 Physics results

The LHCb collaboration published about 40 physics papers during the past year [7], covering a wide range of topics. Here we briefly highlight some of the main results, while in the next sections we will discuss in more detail analyses with direct contributions from our group.

In addition to b-hadron studies, LHCb has published several important results in the fields of spectroscopy and cross section measurements such as the first measurement of forward top production [8]. LHCb observed for the first time two resonances consistent with pentaquark states in decays $\Lambda_b^0 \to J/\psi K^- p$ [9]. Figure 10.2 shows the invariant $J/\psi p$ mass with the two exotic structures, $P_c^+(4450)$ and $P_c(4380)$. The preferred J^P assignments are of opposite parity, with one state having spin 3/2 and the other 5/2. Another exotic state is the resonance $X(3872)$. Its J^{PC} quantum numbers were measured by LHCb in the decay $B^+ \to X(3872)K^+$ with $X(3872)$ decaying into $\rho^0 J/\psi$ [10] to be 1^{++}. These results demonstrate that the LHCb experiment should be considered a general purpose detector in the forward region rather than a mere b-physics experiment.

Measurements of the parameters of the Unitarity Triangle and tests of the CKM paradigm are part of the core physics programme of the LHCb experiment. The element V_{ub} of the CKM matrix can be measured in semileptonic transitions of the type $b \to u$. There is a longstanding disagreement between inclusive and exclusive measurements of V_{ub}. LHCb measured the ratio $|V_{ub}|/|V_{cb}|$ using the exclusive decays $\Lambda_b^0 \to p\mu^-\overline{\nu}_\mu$ and $\Lambda_b^0 \to \Lambda_c^+\mu^-\overline{\nu}_\mu$ for the first time. The measured value is in good agreement with other exclusive measurements [11].

Another challenging measurement at hadron colliders is the determination of the ratio of the branching fractions $R(D^*) \equiv \mathcal{B}(B \to D^{*-}\tau^+\nu_\tau)/\mathcal{B}(B \to D^{*-}\mu^+\nu_\mu)$ [12]. In Fig. 10.3 our result and those from other measurements [13, 14] are compared with the SM prediction. A combination of these measurements by the HFAG collaboration gives a tension of about 4 standard deviations with the SM prediction [15].

CP violation parameters, measured in the decay $B_s^0 \to J/\psi K_s^0$, are in good agreement with the current world average and with SM predictions. In addition, the decay-time-dependent *CP* asymmetry in the decay $B_s^0 \to J/\psi K_s^0$ was measured for the first time. The $B^0 \leftrightarrow \overline{B}^0$ oscillation frequency was measured with the highest accuracy to date [16]. Determinations of parameters sensitive to the angle γ of the Unitarity Triangle, using several tree-level decays such as $B^\pm \to DK^\pm$, $B^\pm \to D\pi^\pm$, $B \to DK\pi\pi$ [17] and $B \to D\pi\pi\pi$ [18] yields the most precise determination of γ to date.

Several charmless B-meson decays have been studied. In particular, the angular analysis of the decay $B_s^0 \to K^{*0}\overline{K}^{*0}$ yielded the longitudinal polarisation fraction. An amplitude analysis was performed for the decay $B^0 \to \rho^0\rho^0$ [19]. In addition, LHCb observed for the first time the decay $B_s^0 \to \eta'\eta'$ [20].

Rare decays of b-hadrons are sensitive BSM probes, since the SM contribution is suppressed whereas BSM could enter at a similar level. The world's best measurements of the branching fractions and the forward-backward asymmetry of the decay $\Lambda_b^0 \to \Lambda^0\mu^+\mu^-$ [21] were done by LHCb. The differential branching fraction of the decay $B_s^0 \to \phi\mu^+\mu^-$ as a function of the di-muon invariant mass squared (q^2) was found in tension with current SM predictions at the level of 3 standard deviations [22]. Angular observables in this decay are in agreement with theory predictions. In addition, the angular analysis of the decay $B^0 \to K^* e^+ e^-$ in the low q^2 region found good agreement with SM predictions [23].

[7] http://lhcb.web.cern.ch/lhcb/

[8] R. Aaij *et al.* [LHCb Collab.],
Phys. Rev. Lett. 115 (2015) 112001.

[9] R. Aaij *et al.* [LHCb Collab.],
Phys. Rev. Lett. 115 (2015) 072001.

[10] R. Aaij *et al.* [LHCb Collab.],
Phys. Rev. D 92 (2015) 011102.

[11] R. Aaij *et al.* [LHCb Collab.],
Nature Phys. 11 (2015) 743-747.

[12] R. Aaij *et al.* [LHCb Collab.],
Phys. Rev. Lett. 115 (2015) 111803.

[13] J. P. Lees *et al.* [BaBar Collab.],
Phys.Rev.D 88, 072012 (2013).

[14] M. Huschle *et al.* [Belle Collab.],
Phys. Rev. D 92, 072014 (2015).

[15] HFAG Collaboration,
http://www.slac.stanford.edu/xorg/hfag/

[16] LHCb Collaboration, CERN-LHCb-CONF-2015-003.

[17] R. Aaij *et al.* [LHCb Collab.],
Phys. Rev. D 91 (2015) 112014.

[18] R. Aaij *et al.* [LHCb Collab.],
Phys. Rev. D 92 (2015) 112005.

[19] R. Aaij *et al.* [LHCb Collab.],
Phys. Lett. B 747 (2015) 468-478.

[20] R. Aaij *et al.* [LHCb Collab.],
Phys. Rev. Lett. 115 (2015) 051801.

[21] R. Aaij *et al.* [LHCb Collab.], JHEP 06 (2015) 115.

[22] R. Aaij *et al.* [LHCb Collab.], JHEP 09 (2015) 179.

[23] R. Aaij *et al.* [LHCb Collab.], JHEP 04 (2015) 064.

10.5.1 Angular analysis of the decay $B^0 \to K^* \mu^+ \mu^-$

E. Bowen, M. Chrząszcz, N. Serra and B. Storaci

The decay $B^0 \to K^* \mu^+ \mu^-$ is a flavour changing neutral current process with a branching ratio of about 10^{-6}. Angular observables in this decay are sensitive probes of BSM physics since heavy new particles can appear virtually in the loop processes with competitive amplitudes. The analysis, performed by our group with an integrated luminosity of 1 fb^{-1} [24], showed tension with respect to SM predictions at about 3.7 standard deviations. These results are widely discussed in the literature. Several authors interpret them as a possible sign of BSM physics [25, 26], while others point to possibly underestimated QCD uncertainties [27, 28].

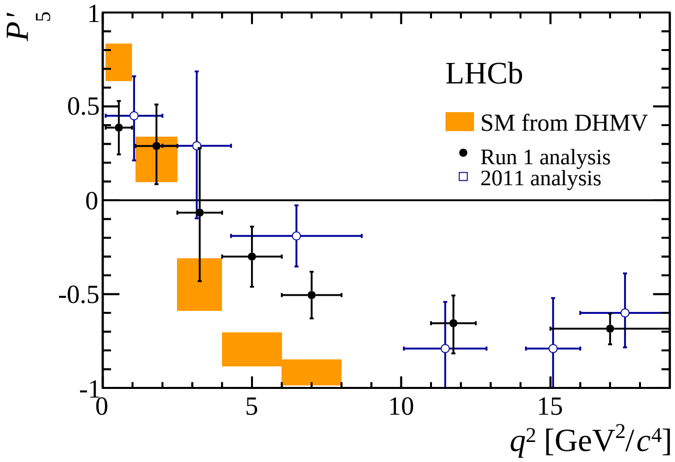

FIG. 10.4 –
The angular observable P'_5 in the decay $B^0 \to K^{*0} \mu^+ \mu^-$ as a function of q^2 compared to the SM predictions [30].

The analysis has been extended to the full Run I dataset, increasing the statistics by a factor 3. The results are in good agreement with the 2011 analysis. We contributed to various aspects including the signal selection, the correction of the detector acceptance and the determination of the angular observables. In particular, we introduced a novel method based on the moments of the angular distribution [29].

In Fig. 10.4 our measurements of the angular observable P'_5 are compared with SM predictions [30]. Discrepancies of about three standard deviations are found for each of the two bins in the region $4.0 < q^2 < 8.0\,\mathrm{GeV}^2$.

A natural extension of this analysis is the measurement of the angular terms in the higher $K\pi$ invariant mass region, outside the $K^{*0}(892)$ resonance. In this region several resonances with different spins ($S-$, $P-$ and $D-$wave) contribute, therefore there are 41 independent moments. Our group is performing this measurement, which is at the moment under the review by the collaboration.

[24] R. Aaij *et al.* [LHCb Collab.],
Phys.Rev.Lett. 111 (2013) 191801.

[25] S. Descotes-Genon, J. Matias and J. Virto,
Phys. Rev. D 88, 074002 (2013).

[26] W. Altmannshofer and D. M. Straub,
Eur. Phys. J. C73 (2013) 2646.

[27] J. Lyon, R. Zwicky, arXiv:1406.0566.

[28] M. Ciuchini et al., JHEP 1305 (2013) 043.

[29] F. Beaujean, M. Chrzaszcz, N. Serra and D. van Dyk,
Phys. Rev. D 91, 114012 (2015).

[30] S. Descotes-Genon *et al.*, JHEP 01 (2013) 048.

10.5.2 Study of $b \to se^+e^-$ transitions

F. Lionetto, N. Serra and R. Silva Coutinho

The measurement of the ratio of branching fractions $R_K = \mathcal{B}(B^+ \to K^+\mu^+\mu^-)/\mathcal{B}(B^+ \to K^+e^+e^-)$ by LHCb is found to be in tension with respect to SM predictions at the level of 2.6 standard deviations [31]. It has been argued that this deviation is consistent with the deviation observed in $B^0 \to K^*\mu^+\mu^-$ decays, which could be an indication of new physics breaking the lepton flavour universality of the SM [32, 33]. Our group is involved in several tests of lepton flavour universality comparing $b \to se^+e^-$ to $b \to s\mu^+\mu^-$ transitions. The first goal will be to measure asymmetries in combined angular observables, using $B^0 \to K^{*0}\mu^+\mu^-$ and $B^0 \to K^{*0}e^+e^-$ decays. In addition, measurements of the ratio of branching ratios in the electron and muon channels have the potential to test lepton flavour universality in rare decays.

[31] R. Aaij *et al.* [LHCb Collab.],
Phys. Rev. Lett. **113** (2014), 151601.

[32] S. Descotes-Genon, J. Matias and J. Virto,
Phys. Rev. D 88, 074002 (2013).

[33] W. Altmannshofer and D. M. Straub,
Eur. Phys. J. C73 (2013) 2646.

10.5.3 Search for new scalar particles in B decays

M. Chrząszcz, A. Mauri and N. Serra

The LHCb experiment offers the possibility to search for long lived particles produced in B decays with higher sensitivity than reached by previous experiments [34]. Many BSM models [35, 36] predict the existence of light particles, such as an inflaton or a dark matter mediator, that, via mixing with the Higgs boson, can couple to the visible SM sector.

We are analysing the full Run I dataset looking for the decay sequence $B^+ \to K^+\chi$, $\chi \to \mu^+\mu^-$ with χ a light scalar particle. The lifetime of such a particle can be long so that it could travel several centimetres before decaying. Simulations were made for different mass and lifetime values as a guidance to the optimal event selection based on machine-learning algorithms.

[34] J.-T. Wei *et al.* [Belle Collab.],
Phys.Rev.Lett.103:171801 (2009).

[35] J. D. Clarke, R. Foot and R. R. Volkas,
JHEP 02 (2014) 123.

[36] K. Schmidt-Hoberg, F. Staub and M. W. Winkler,
Phys. Lett. B727 (2013) 506-510.

10.5.4 Semileptonic decays

M. Chrząszcz, E. Graverini and N. Serra

The most significant deviation from SM predictions in B-meson decays comes from measurements of the branching fraction of semi-tauonic decays [37–39]. Our group is presently involved in a similar test of lepton universality, measuring the observable $R(\Lambda_c^*) \equiv \mathcal{B}(\Lambda_b \to \Lambda_c^*\tau\nu)/\mathcal{B}(\Lambda_b \to \Lambda_c^*\mu\nu)$. This measurement is important to test present tensions and also to provide complementary information, since it would be the first of such measurement using b-baryons.

[37] R. Aaij *et al.* [LHCb Collab.],
Phys. Rev. Lett. 115 (2015) 111803.

[38] J. P. Lees *et al.* [BaBar Collab.],
Phys.Rev.D 88, 072012 (2013).

[39] M. Huschle *et al.* [Belle Collab.],
Phys. Rev. D 92, 072014 (2015).

10.5.5 Charmless *b*-hadron decays

E. Graverini, N. Serra and R. Silva Coutinho

The Standard Model gives no explanation for the observed imbalance between baryonic and antibaryonic abundances in the universe. *CP* violation in weak interactions could allow matter to be produced more commonly than antimatter in conditions immediately after the Big Bang. Searches for new sources of *CP* violating asymmetries in addition to those predicted by the SM are thus among the main goals of current particle physics. In particular, studies of charmless three-body decays of either $B^0_{(\mathrm{s})}$ mesons or beauty baryons with a long-lived particle in the final state (*i.e.* K^0_S or Λ^0) are of great interest for improving the understanding of hadronic interactions and in the search for *CP* violation effects.

Amplitude analyses of the most prominent modes and a search for the as yet unobserved channel $B^0_\mathrm{s} \to K^0_\mathrm{S}K^+K^-$, lead by our group, may well provide new insights into the field.

Our group has also been involved in the searches for *b*-baryon decays to $\Lambda^0\pi^+\pi^-$, $\Lambda^0K^\pm\pi^\mp$ and $\Lambda^0K^+K^-$ [40]. The $\Lambda^0_b \to \Lambda^0K^\pm\pi^\mp$ and $\Lambda^0_b \to \Lambda^0K^+K^-$ decay modes were observed for the first time (see Fig. 10.5) and no evidence is seen for a *CP* asymmetry in their phase-space integrated decay rates. Finally, evidence is seen for the $\Lambda^0_b \to \Lambda^0\pi^+\pi^-$ decay and limits are set on the branching fractions of the decays $\Xi^0_b \to \Lambda^0\pi^+\pi^-$, $\Xi^0_b \to \Lambda^0K^\pm\pi^\mp$, and $\Xi^0_b \to \Lambda^0_bK^+K^-$.

Further studies of similar modes are rather compelling as no hints for *CP* violation have been found in *b*-hadron decays yet. An interesting channel to investigate is $\Lambda^0_b \to K^0_\mathrm{S}p\pi^-$, which has been previously studied by LHCb with

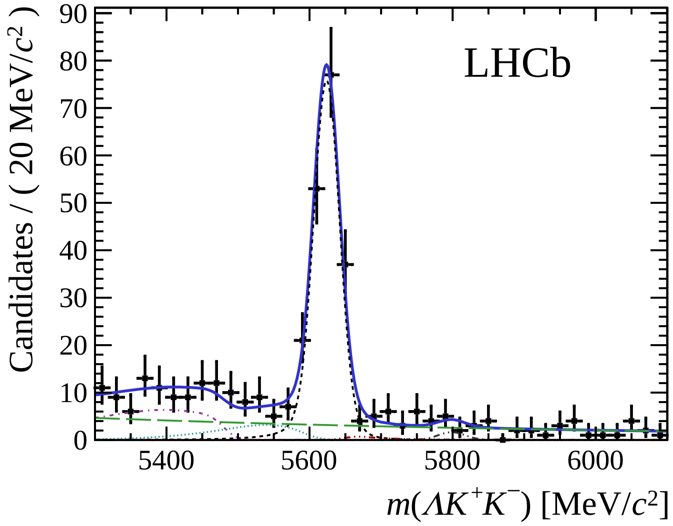

FIG. 10.5 – Invariant mass distribution for the $\Lambda^0K^+K^-$ final states. A signal for $\Lambda_b^0 \to \Lambda^0K^+K^-$ (shown as short-dashed black lines) is observed for the first time with a significance $15.8\,\sigma$ [40].

$1.0\,\mathrm{fb}^{-1}$ [41]. This measurement is statistically limited. An update of this analysis with the full Run I dataset is of great interest and is being performed by our group. Moreover, inspired by the methodology implemented in $B^{\pm} \to h^{\pm}h^{\mp}h^{\pm}$ (where h stands for pions or kaons) decays that recently revealed large anisotropies in the phase-space distribution [42], we are extending this treatment for $\Lambda_b^0 \to K_\mathrm{s}^0 p\pi^-$ decays, significantly enhancing the discovery potential of *CP* violation.

[40] R. Aaij *et al.* [LHCb Collab.], arXiv:1603.00413.

[41] R. Aaij *et al.* [LHCb Collab.], J. High Energy Phys. **04** (2014) 087.

[42] R. Aaij *et al.* [LHCb Collab.], Phys. Rev. D **90** (2014) 112004.

10.5.6 Electroweak boson and low mass Drell-Yan production

A. Bursche, M. Chrzązczcz, Ch. Elsasser, K. Müller and M. Tresch

Measurements of the production cross-section of electroweak bosons constitute an important test of the SM at LHC energies. Since predictions in pQCD are known at the percent level these measurements are sensitive to the momentum distribution of the partons in the proton (PDF). Our group contributed to various aspects of these analyses in the past years. Precision measurements of the differential cross sections and cross section ratios of W and Z bosons have been published using the datasets at centre of mass energies of 7 [43] and 8 TeV [44]. The systematic uncertainties are at the percent level and thus comparable to or even smaller than the theoretical uncertainties. A first measurement of Z production at 13 TeV has been released using a small dataset of the new Run II data [45]. All the cross sections are measured to be in good agreement with theoretical predictions.

In order to further exploit the unique phase space region of LHCb a measurement is performed by our group of Z bosons with the associated production of a long lived particle (K_s^0 or Λ^0). These measurements are important for the understanding of the hadronisation process and the tuning of Monte Carlo generators.

Another measurement performed in our group is the analysis of low mass Drell-Yan production down to invariant masses of 10 GeV. It was extended to include also the data at 8 TeV which allows to access lower momentum fractions of the struck quark. Backgrounds of jet-production are determined by a fit to the isolation distribution of the two muons with the templates determined from data. The analysis will enter the LHCb review process shortly.

[43] R. Aaij *et al.* [LHCb Collab.], JHEP **12** (2014) 079.

[44] R. Aaij *et al.* [LHCb Collab.], JHEP **01** (2016) 155.

[45] LHCb Collab., LHCb-CONF-2016-002.

10.6 Summary and Outlook

The LHCb experiment has performed very well throughout the 2015 LHC run with a very high data taking efficency and stable running even with heavy ion collisions. The LHCb collaboration continued to produce high quality results, which resulted in more than 40 publications and many conference contributions, many of these already based on the new data collected at a centre of mass energy of 13 TeV. The Zurich group made important contributions to the operation of the experiment, physics analyses and preparation for the upgrade.

11 Particle physics with the CMS experiment at CERN

T. Årrestad, L. Caminada, F. Canelli, A. de Cosa, R. del Burgo, C. Galloni,
A. Hinzmann, T. Hreus, B. Kilminster, C. Lange, J. Ngadiuba, D. Pinna,
G. Rauco, P. Robmann, D. Salerno, and Y. Yang

in collaboration with the:

CMS - Collaboration

In 2015, after the upgrade of the CERN Large Hadron Collider (LHC), the highest center of mass energy reached in proton-proton collisions went up from 8 to 13 TeV, resulting in a significant increase in sensitivity to elusive physics beyond the standard model (SM).

Here we present an overview of our CMS activities. We are involved in detector operation, maintenance and upgrade, trigger development and monitoring as well as physics data analysis. In particular, we are a major contributor to the CMS pixel detector. We maintain and operate the present detector which took its first data at 13 TeV in the middle of 2015. We help build the upgraded barrel pixel detector (Phase 1), to be installed towards the end of 2016. We also started work on the design and simulations of the Phase 2 upgrade, envisioned to be ready in 2023.

Our physics analysis program addresses fundamental questions in particle physics. After the discovery of a Higgs particle at the LHC [1], studying its properties is among the primary goals. Important open questions are: is this boson just one of several Higgs bosons, what are its couplings, and what mechanism localizes the Higgs boson at this particular mass scale? Many models predict new particle states at a few TeV that generate loop corrections with the necessary cancellations to stabilize the Higgs boson mass. The new energy regime would allow us to directly produce them and study their properties.

Members of our group play important coordination roles. In the period covered by this report F. Canelli and A. de Cosa act as subgroup conveners within the Beyond 2 Generations (B2G) physics group, B. Kilminster leads the Future Higgs group, a subgroup of the Higgs group, A. Hinzmann is the convener of the JetMET algorithms and reconstruction group, Y. Yang leads the Monte Carlo production for the Physics Performance and Dataset group (PPD), C. Lange and A. de Cosa act as conveners of the CMS pixel DAQ group and pixel monitoring group, respectively, T. Hreus coordinates the Tracker Detector Performance group and L. Caminada and C. Lange are members of the Swiss CMS Tier3 steering committee. Currently, F. Canelli holds the position of group leader.

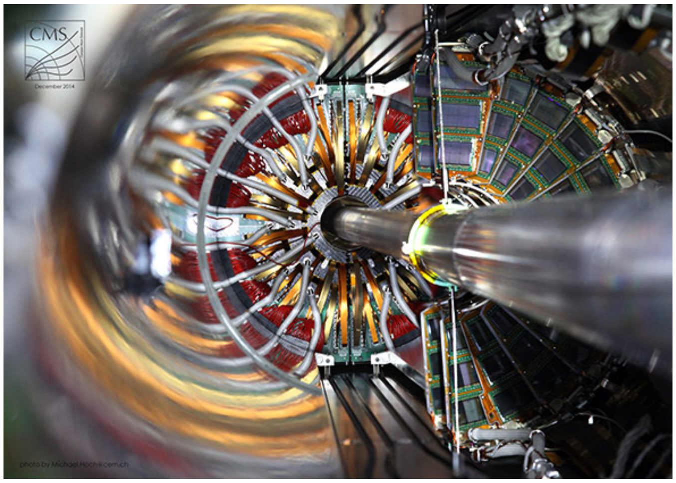

FIG. 11.1 – The CMS BPIX detector and a quadrant of the FPIX detector enclosing the beampipe. The picture has been taken during the re-installation in 2014.

11.1 The CMS experiment

CMS [2] is one of the multipurpose detectors at the LHC. It consists of different layers of detectors optimized for position and energy measurements of particles produced in collisions. An all-silicon tracker, an electromagnetic calorimeter, and a hadronic sampling calorimeter are all contained within a large-bore 3.8 T superconducting solenoid. Beyond the solenoid there are four layers of muon detectors. The CMS tracker is composed of the inner pixel detector and the outer silicon strip detector. The pixel detector, shown in Fig. 11.1 consists of three barrel layers (BPIX) at 4.4, 7.3, and 10.2 cm, and two forward/backward disks (FPIX) at longitudinal positions of ± 34.5 cm and ± 46.5 cm and extending in radius from about 6 to 15 cm. The high segmentation of the pixel detector allows for high-precision tracking in the region closest to the interaction point. The pixel detector information is crucial for primary vertex and pile-up vertex reconstruction, and identification of long-lived τ-leptons and B-hadrons. The performance of the current pixel detector has been excellent. It is noteworthy that the BPIX was built by the Swiss Consortium, PSI, ETH and the University of Zurich.

---

[1] ATLAS collaboration, Phys. Lett. B **716** (2012) 29; CMS collaboration, Phys. Lett. B **716** (2012) 30.

[2] CMS collaboration, JINST **3** (2008) S08004.

11.2 Detector maintenance and operation

The CMS pixel detector performed very reliably during the first period of LHC data taking. At the end of Run 1 the detector was installed on the surface for testing, maintenance and reparation work. We actively participated in this effort as well as the re-installation towards the end of 2014, which was completed within a week, allowing to quickly proceed with the closure of CMS. We were responsible for the BPIX calibration and commissioning. In order to limit the impact of radiation damage and minimize the leakage current during Run 2, we prepared the detector for operation at -10°C. This task was accomplished efficiently thanks to the expertise we acquired during the LHC shutdown when several calibration tools and routines have been developed.

Our efforts resulted in the successful and stable operation of the pixel detector during the data-taking at 13 TeV in 2015 when CMS recorded 3.8 fb^{-1} of proton-proton collision data with the pixel detector running at very high data-taking efficiency with more than 98% of its 66 million channels working.

Our group contributes to the monitoring of the detector operation parameters and performance which is crucial to allow for preventive actions and ensure high-quality physics data. In particular, we keep track of the evolution of the radiation damage of the silicon sensors with increasing luminosity, measure threshold and noise distributions as well as pixel hit resolutions and determine the impact of pixel dynamic inefficiencies. In case of signs of detector performance degradation we use the opportunity during LHC technical stops to re-calibrate the pixel detector and recover from these effects. The resolution of the BPIX detector during Run 2, about $10\,\mu$m in the transverse plane and $30\,\mu$m in the longitudinal direction, represents a slight improvement with respect to Run 1 and is a key ingredient for the excellent tracking performance at CMS.

Also we are responsible for maintaining and improving the pixel online software and contribute to the pixel detector operations by regularly taking shifts in the CMS control room, or acting as on-call experts.

Trigger rate studies are a continuous and fundamental activity for CMS as the trigger menu is constantly evolving due to changes in beam parameters, detector conditions and reconstruction software. We developed code for online monitoring of individual and global trigger rates using both measured and simulated samples, allowing to asses the impact of these changes to the trigger menu.

Last but not least, our group contributes to the preparation and production of simulation samples that are needed by all physics groups in CMS. Even when there is no need to produce new samples, most existing samples have to be reprocessed with more realistic simulation conditions after better understanding the data.

11.3 Higgs Properties

We have entered a new phase in Higgs-boson physics, in which the properties of this new particle are being determined by measuring its couplings to SM particles with ever increasing precision. A deviation from the SM couplings would hint at new physics. Furthermore, many models contain a light Higgs boson with properties similar to those of the SM Higgs boson.

Our analyses not only probe the Higgs couplings to heavy quarks, but we also look for final states with Higgs bosons (see also Sec. 11.4.1) and search for additional Higgs bosons predicted for instance in supersymmetric models (SUSY).

11.3.1 Higgs boson couplings to top-quarks

Since the top quark is the heaviest particle of the SM, the only way to directly probe its Yukawa coupling is by studying the associated production of a Higgs boson and a pair of top quarks ($t\bar{t}H$). This channel also provides a complementary probe of the Higgs boson coupling to b quarks in case the Higgs boson decays into b-quarks. The LHC has no evidence yet for this production process. The current best limits are two to four times larger than the SM predictions [3]. During the past years we introduced a new matrix element method (MEM) to this search in CMS (see last year's report) which gave a 20% improvement over the previous analysis. The result has been published in 2015 [4].

Our $t\bar{t}H(\rightarrow b\bar{b})$ result using the Run 2 data [5] is shown in Fig. 11.2. We have analyzed the single lepton and di-lepton decay channels with an integrated luminosity of 2.7 fb^{-1}. To increase the sensitivity different event categories were distinguished using a multivariate approach combining the MEM with methods from machine learning. A combined template fit to the data in all categories results in an observed (expected) upper limit of 2.6 (3.6) times the SM cross section at 95% CL.

During 2015 we have extended our search to include the all-hadronic channel which represents about 46% of the total $t\bar{t}H(\rightarrow b\bar{b})$ cross section. A fully reconstructed final state contains four b-tagged and four light-flavor jets, which poses significant challenges due to the large QCD multi-jet background and the combinatoric self-background. We developed and implemented dedicated trigger paths which are now included in the Run 2 trigger menus. The offline analysis is ongoing.

11.3.2 MSSM Higgs boson search

To find out whether the recently discovered Higgs boson belongs to a larger family of Higgs bosons, as predicted for instance in the minimal SUSY model (MSSM), our group has searched the 8 TeV data for a heavier Higgs boson, produced in association with a b quark and decaying into a pair of b-quarks. To suppress the dominant background, which comes

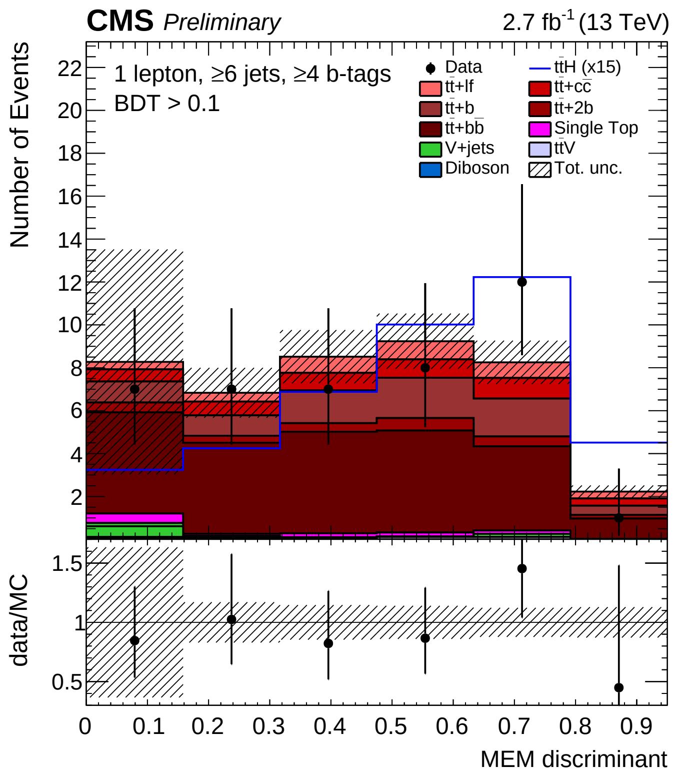

FIG. 11.2 – Matrix element method (MEM) discriminant for one category of events. The discriminant is calculated by the ratio of $t\bar{t}H$ and $t\bar{t}+b$ probabilities densities.

from multi-jet production, we developed new techniques for separating jets according to their flavor composition (b, c, and light quarks, as well as bb and cc jets from gluon-splitting). We also developed the signal modeling and contributed to the complex likelihood-fitting procedure needed to separate out the multiple flavors of jets in order to isolate the signal. The analysis was published in 2015 [6], and extends the tan β and MSSM Higgs boson mass reach (see Fig. 11.3).

[3] ATLAS collaboration, ATLAS-CONF-2014-011; CMS collaboration, arXiv:1303.0763v2.

[4] CMS collaboration, EPJ C **75** (2015) 251.

[5] CMS collaboration, CMS-PAS-16-004.

[6] CMS collaboration, JHEP **011** (2015) 071.

11.4 Searches for new phenomena

Our group exploits different search channels at the LHC to directly look for new phenomena and signs of new physics. This includes searches for massive resonances in different final states with bosons and jets as well as direct searches for dark matter particles. The increased center-of-mass energy of 13 TeV greatly improves the sensitivity of these searches and a signal might show up already early during Run 2.

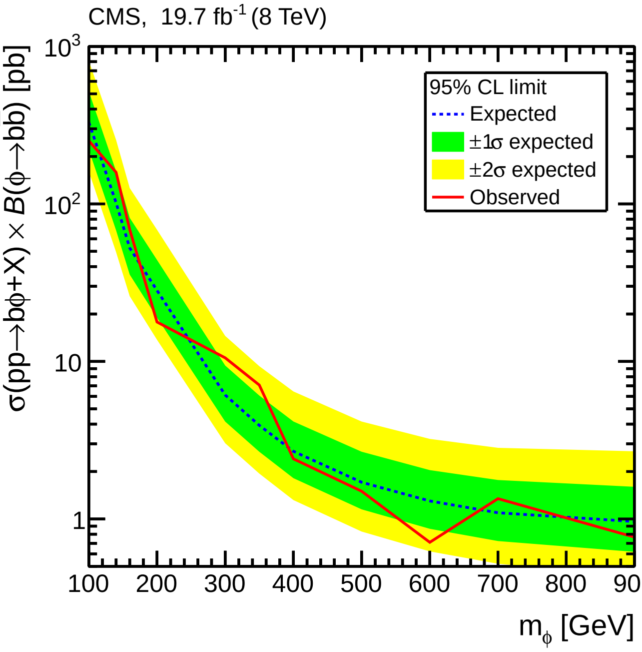

FIG. 11.3 – Expected and observed upper limits at 95% C.L. on $\sigma(pp \to b\phi + X)$ as a function of m_ϕ, where ϕ denotes a generic neutral Higgs-like state.

11.4.1 Search for heavy resonances in di-boson events

Over the past years our group has become the leading group at CMS in searches for heavy diboson resonances, motivated generically by many extensions to the SM, including extra dimensions, composite Higgs, heavy vector-triplets, and additional $U(1)$ gauge groups [7]. These models predict many new particles such as additional W' and Z' gauge bosons, which can have large branching ratios for decays into W, Z and H bosons, while decays into fermions are suppressed.

These final states require special identification techniques, as well as novel data-based approaches to model them. The di-boson pair from the decay of the heavy resonance in turn decays into highly boosted quarks and leptons that are merged into "fat" jets with substructure. In order to distinguish the substructure of these jets we have tested a variety of $W/Z/H$-tagging algorithms. The best scheme is based on the Lorentz invariant jet mass with the so-called pruning algorithm [8] and the jet shape variable N-subjettiness [9], which is an indicator for the number of hard quarks in the jet. Our approach, which efficiently separates the particles from quarks originating in boson decays from those originating in QCD radiation, has been employed in the most recent CMS searches.

Our efforts have focused on a wide variety of di-boson final states, mainly $X \to WW \to q\bar{q}q\bar{q}$, $X \to WW \to \ell\nu q\bar{q}$, $X \to WH \to \ell\nu b\bar{b}$, $X \to ZH \to q\bar{q}\tau^+\tau^-$, $X \to ZH \to q\bar{q}b\bar{b}$, and $X \to HH \to b\bar{b}\tau^+\tau^-$.

The interest in heavy di-boson resonances led to their consideration by CMS as high-priority analysis for the 13 TeV

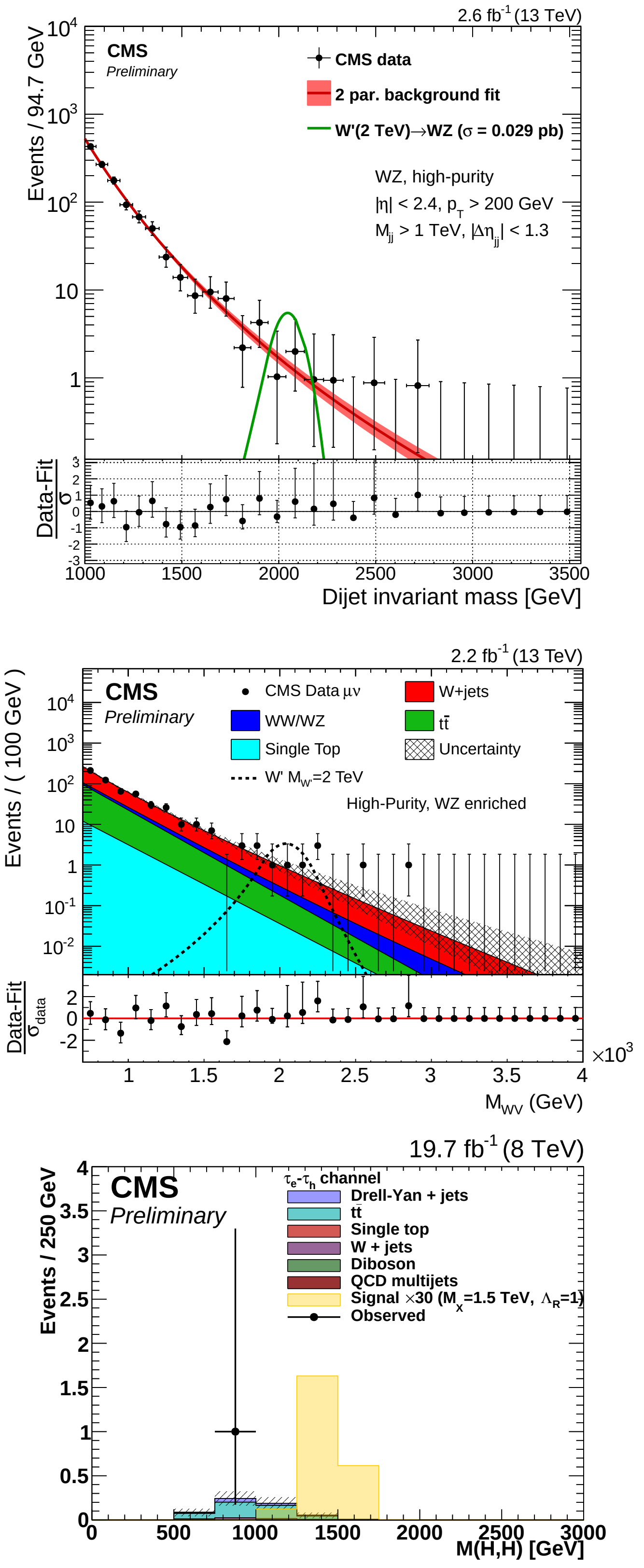

FIG. 11.4 –
Measured invariant mass spectra in the search for massive resonances decaying into pairs of boosted W/Z bosons in the all-hadronic (top) and semi-leptonic final states (center) or decaying into HH with $HH \to b\bar{b}\tau^+\tau^-$ (bottom).

2015 dataset. Although the 2015 dataset is only 2.6 fb^{-1} compared to 19.7 fb^{-1} in 2012, the energy increase from 8 to 13 TeV leads to a similar sensitivity to 2 TeV resonances.

Our preliminary results of the search for massive resonances decaying into pairs of boosted W and Z bosons using the all-hadronic and semi-leptonic decay channels [10] are presented in Fig. 11.4. The analysis reveals no significant excess in the mass spectrum, but allows us to set limits on the production of new heavy particles.

We also searched for heavy particles decaying to boosted Higgs bosons using the Run 1 dataset [11]. The search for a high-mass resonance decaying to a W boson and a Higgs boson, with $H \to b\bar{b}$, and a leptonic W-boson decay as well as the search in the final state with a hadronically decaying Z boson and a Higgs boson in the $\tau^+\tau^-$ final state has been presented in last year's report. The novel feature of the latter analysis is the reconstruction and selection of a pair of boosted τ leptons. While we did not discover a signal, we improved our knowledge on boosted τ reconstruction and separation from backgrounds that will be useful in our future 13 TeV analyses.

We next extended this search in the same dataset to consider a heavy resonance decaying as $X \to HH \to \tau\tau b\bar{b}$. Our analysis is the first search at colliders that probes the final state with boosted Higgs bosons that decay into tau-leptons and bottom-quarks pairs, challenging both for object reconstruction and background estimation. We observe one event in the HH mass spectrum as illustrated in Fig. 11.4, and are very curious to perform the analysis with the 13 TeV data.

11.4.2 Di-jet angular distributions

Di-jet events provide an ideal testing ground for perturbative QCD and for new phenomena such as quark compositeness or additional, compactified spatial dimensions. Such new physics models exhibit angular distributions that are more isotropic than those predicted by QCD. With the increased center-of-mass energy, the 2015 data are sensitive to a significantly higher scale for contact interactions and extra dimensions. Our group is a major contributor to the very first 13 TeV search that was made public already one month after the end of 2015 data taking [12]. The measured angular distribution is compared to theoretical predictions in Fig. 11.5. No signs of new physics are observed and the existing limits on scales of contact interaction and extra dimension scales improved by 20%.

11.4.3 Search for dark matter particles with top quarks

In several new physics models a weakly interacting massive particle arises naturally as a dark matter (DM) candidate. So far, however, there is no established knowledge about its properties and interactions with ordinary matter. Our group has made a significant impact in the search

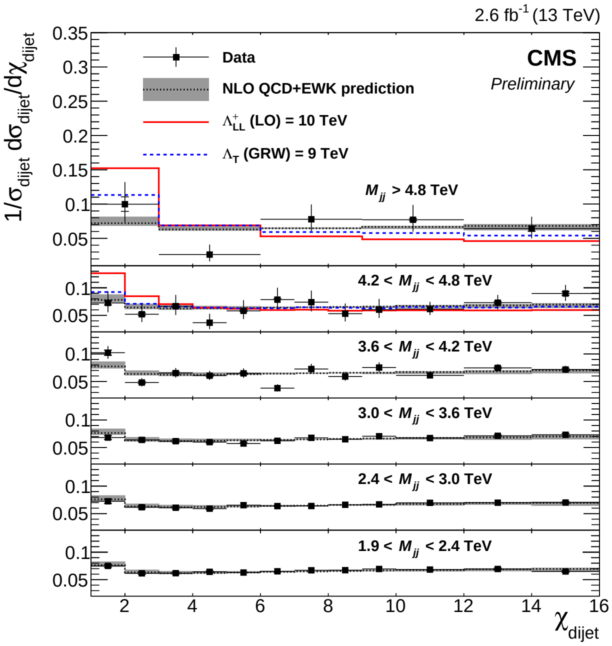

FIG. 11.5 – Normalized χ_{dijet} distributions in measured data compared to theoretical predictions, where $\chi_{\text{dijet}} = \exp(|y_1 - y_2|)$ with y_1 and y_2 the rapidities of the two highest p_T jets. The predictions quark compositeness (Λ^{+}_{LL}) and extra dimensions (Λ_T) are overlaid.

for DM in association with top quarks at CMS. This analysis is based on a model that assumes minimal flavor violation, for which couplings between fermionic DM and ordinary matter have the same structure as in the SM. In these models the discovery potential for scalar interactions is highly improved when investigating processes where DM couples to more massive third generation quarks, in particular top quarks [13].

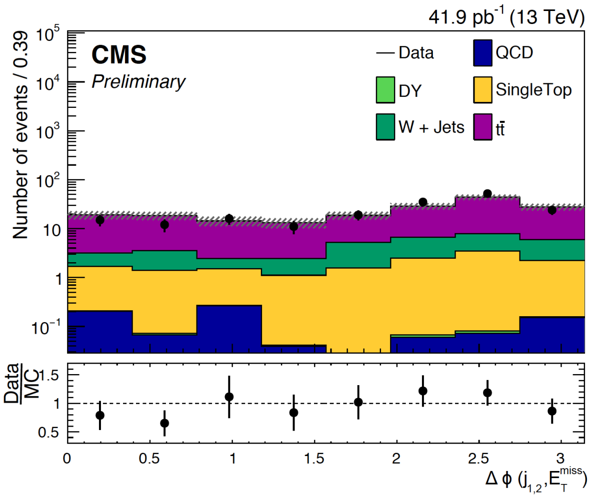

FIG. 11.6 – Distribution of minimum $\Delta\phi$ between the first two leading jets and the missing transverse energy in the events selected for the search for $t\bar{t}$+DM in the semi-leptonic channel at 13 TeV [16].

The DM particles escape detection and leave a signature of large missing energy recoiling against the top quarks. The result of the search performed at 8 TeV using the di-lepton and single-lepton top-pair decay channels [15] has been shown in last year's report.

The search for $t\bar{t}$+DM in the 13 TeV data is currently ongoing (see Fig. 11.6). Compared to our Run 1 results important improvements were achieved, such as an aceptance increase by including the hadronic final state, the use of simplified models with an explicit definition of the mediator for the interpretation of the results [14], and a shape-based fit for the signal extraction. The results are expected to be published soon.

[7] K. Agashe *et al.*, Phys. Rev. D **76** (2007) 036006; L. Randall, R. Sundrum, Phys. Rev. Lett. **83** (1999) 3370; D. Marzocca *et al.*, JHEP **08** (2012) 013; R. Rattazzi *et al.*, JHEP, 2011(10), 2011; D. Pappadopulo *et al.*, arXiv:1402.4431.

[8] S.D. Ellis *et al.*, Phys.Rev. D **81** (2010) 094023.

[9] J. Thaler and K. Van Tilburg, JHEP **1103** (2011) 015.

[10] CMS collaboration, CMS-PAS-EXO-15-002.

[11] CMS collaboration, arXiv:1601.06431; Phys. Lett. B 748 (2015) 255.

[12] CMS collaboration, CMS-PAS-EXO-15-009.

[13] J. M. Beltran *et al.*, HEP pp. 1 17, 2010;
T. Lin *et al.*, Phys. Rev. D, 88, (2013) 063510.

[14] D. Abercrombie *et al.*, arXiv:1507.00966.

[15] CMS collaboration, JHEP 06 (2015) 121.

[16] CMS collaboration, CMS-DP-2015-033.

11.5 Future upgrades

With a luminosity of 3.8 fb^{-1} recorded in 2015 the data-taking at 13 TeV has only started. During Run 2 we expect to collect about 100 fb^{-1} at a maximum instantaneous luminosity of 2×10^{34} cm^{-2}s^{-1}. In order to maintain the excellent tracking performance of the pixel detector in these conditions, we will install a new upgraded pixel system during the long LHC technical stop in 2016/17.

The CMS Phase 1 pixel upgrade combines a new pixel readout chip, which minimizes detection inefficiencies, with several other design improvements. The current 3-layer BPIX, 2-disk FPIX detector will be replaced with a 4-layer BPIX, 3-disk FPIX detector. The upgraded BPIX detector consists of four 57 cm long layers of silicon pixel modules serviced by 2.2 m of supply tubes which transport cooling tubes, electrical power, and optical signals to and from the pixel detector. The addition of an extra layer, closer to the beam pipe, demands a complete redesign of powering, cooling, and readout electronics.

We are in charge of three major areas in the Phase 1 BPIX upgrade: the supply tube mechanical structure, the cooling system, and the assembly, installation, testing and commissioning of the readout electronics, powering, and control of the pixel modules. All three moved from the prototyping to the production phase.

Together with the UZH workshop we have finished building half of the production supply tube mechanical structure. This multi-layer carbonized foam structure houses the electronics, cooling, power distribution, module control boards, and DC-DC converters (see Fig. 11.7). Work to finish the remaining half of the supply tube, and integrate the various components is ongoing. Furthermore, we have designed and are constructing a new light-weight cooling system, which differs from the current design in that the tubes are much narrower, operate at six times higher pressure, and use two-phase liquid-gas CO_2 cooling instead of single-phase C_6F_{14} liquid coolant. The system has a complicated looping structure in order to cool the individual detector components including pixel modules, DC-DC converters and opto-hybrids. We have tested our prototype in a cooling plant at CERN to demonstrate the expected two-phase cooling curves. To protect against corrosion, we moved to special-quality steel alloy for all parts, and are now implementing computerized, machine-automated laser welding. The system has undergone mechanical and temperature stress tests and was found to withstand 200 atmospheres of pressure and water tests without leaking or corrosion.

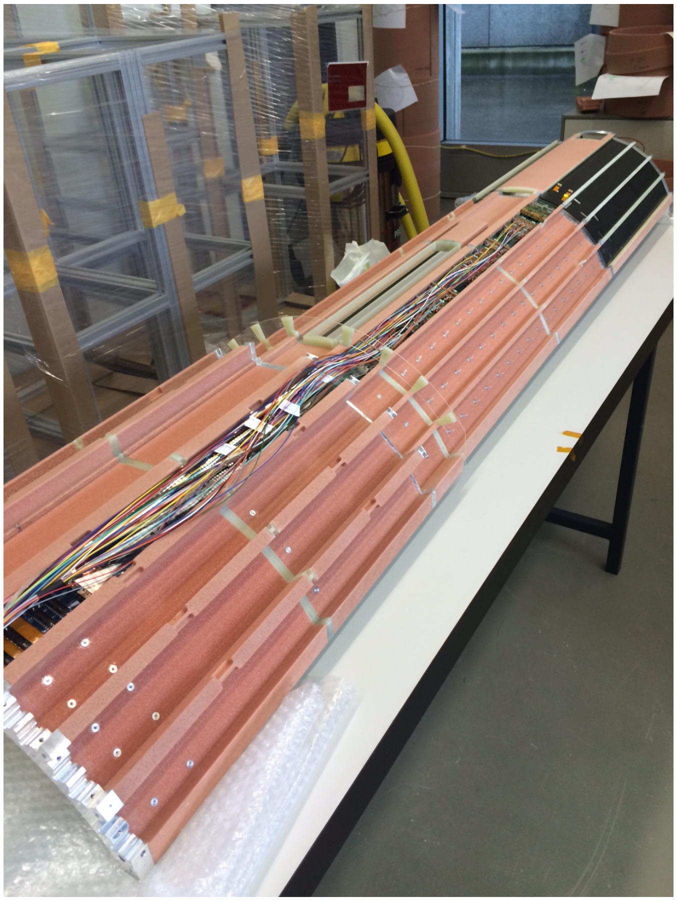

FIG. 11.7 – CMS Phase 1 pixel supply tube mechanics with readout electronics in one slot.

During the design and prototyping phase of the CMS BPIX Phase 1 upgrade detector, we were responsible for the testing of the complete system. In particular, we verified the proper interplay of the upgrade detector modules and supply tube electronics with the pixel DAQ and power system. For this purpose, we set up a slice of the full readout chain in our lab at UZH which consists of a group of pixel detector modules connected through optical links to the front-end boards for readout and control and powered using a set of DC-DC converters. We produced hardware tools and developed software algorithms to allow for a fast and efficient testing procedure. Thereby we became experienced in the operation of the new system and are able to evaluate its performance in detail, which is crucial for a reliable and fast testing of the production CMS Phase 1 pixel system. We have also set up a parallel DAQ system, using μTCA which makes it compatible with the future CERN standard.

[17] CMS collaboration, CERN-LHCC-2012-016 (2012).

12 Superconductivity and Magnetism

D. Sutter (since September 2015), O. Ivashko (since May 2015),
D. Destraz (since April 2015), J. Chang
Associated PhD student - SINERGIA Network: C. Fatuzzo (EPFL)

in collaboration with:
Paul Scherrer Institute (C. E. Matt, J. Mesot, V. Strocov, N. Plumb, M. Shi, M. Radovic, T. Schmitt & Ch. Rüegg), EPFL Lausanne (H. M. Rønnow & M. Grioni), University of Zurich (C. Monney), Bristol University (S. M. Hayden), Birmingham University (A. Holmes, E. Blackburn & Ted Forgan), University of British Columbia, Canada (R. Liang, W. Hardy D. Bonn), Deutsches Elektronen-Synchrotron DESY, Hamburg-Germany (U. Rütt & M. v. Zimmermann), Dipartimento di Fisica 'E.R. Caianiello', Salerno-Italy (R. Fittipaldi & A. Vecchione), Hokkaido University, Japan (T. Kurosawa, M. Oda, & N. Momono), Texas Materials Institute, USA (J.-S. Zhou & J. B. Goodenough)

We report on research projects in the field of high-temperature superconductors (HTS) and materials with novel electronic properties. Our studies involve various complementary techniques, such as x-ray diffraction (XRD), Resonant Inelastic x-ray Scattering (RIXS), and angle resolved photoemission spectroscopy (ARPES). Here we present some results from our recent investigations on cuprate high-temperature superconductors and ruthenate Mott insulators.

12.1 High-energy spin excitations in overdoped La_2CuO_4

Conventional superconductivity emerges as a result of electron-phonon interaction. Information about the phonon excitation spectrum (dispersions and lifetime effects) are therefore of great importance. Similarly, for magnetic superconductors [1], there is a strong interest in understanding and experimentally revealing the spin excitation spectrum. Mapping out the detailed evolution of the spin excitation spectrum across the high-temperature superconducting cuprate phase diagram, from the Mott insulator to the Fermi-liquid ground state, is hence important. Spin excitations have traditionally been studied by inelastic neutron scattering (INS). Studies of high-energy spin excitations have, however, been challenged by weak neutron cross sections. Over the last decade, resonant inelastic x-ray scattering (RIXS) has developed rapidly [2] and energy resolution now allows studies of spin excitations. RIXS is therefore an attractive complementary technique to neutron scattering. This has, in particular, lead to progress in understanding correlated low-dimensional $3d$ and $5d$ electron systems [3]. The spin excitation spectra of insulating one- and two-dimensional cuprates have, for example, been studied by soft x-ray RIXS using the copper L_3-edge. In recent years, spin excitations of doped cuprate and pnictide superconductors have also been investigated. These studies suggest that the high energy ($\omega > 100$ meV) spin excitation dispersion undergoes little change with doping [3]. This is in strong contrast to the low-energy part of the spectrum (studied by INS), that has a strong dependence on impurities, magnetic field and doping.

We have published [4] a systematic RIXS study of the spin and charge excitations found in overdoped $La_{2-x}Sr_xCuO_4$ (LSCO) $x = 0.23$. Examples of measured spectra are shown in Fig. 12.1. The line shape of the excitations in the spectra is analyzed using the response function of a damped harmonic oscillator. In this fashion, their dispersion and momentum dependence of the damping, γ, are extracted. Compared to previous RIXS reports [3], we obtain new information about these excitations along different high symmetry directions. We find that the spectral weight and damping γ are anisotropic in momentum space. The line shape is sharpest around the zone center. As reported for Bi-based cuprates [5], we also find a strong nodal / antinodal anisotropy of spectral weight. These observations are captured by susceptibility calculations based on the electronic band structure. The model calculation furthermore predicts a low-energy spin excitation branch, along the (π, π)-direction, which turns out to be particularly pronounced and dispersive in LSCO with $x = 0.23$ in comparison to other doped cuprates [5]. Future RIXS experiments with improved resolution should test this prediction.

[1] D. J. Scalapino, Rev. Mod. Phys. **84**, 1383 (2012).
[2] L. J. P. Ament *et al.*, Rev. Mod. Phys. **83**, 705 (2011).
[3] M. L. Tacon *et al.*, Nat. Phys. **7**, 725 (2011).
[4] C. Monney *et al.*, Phys. Rev. B **93**, 075103 (2016).
[5] M. Guarise *et al.*, Nat. Commun. **5**, 5760 (2014).

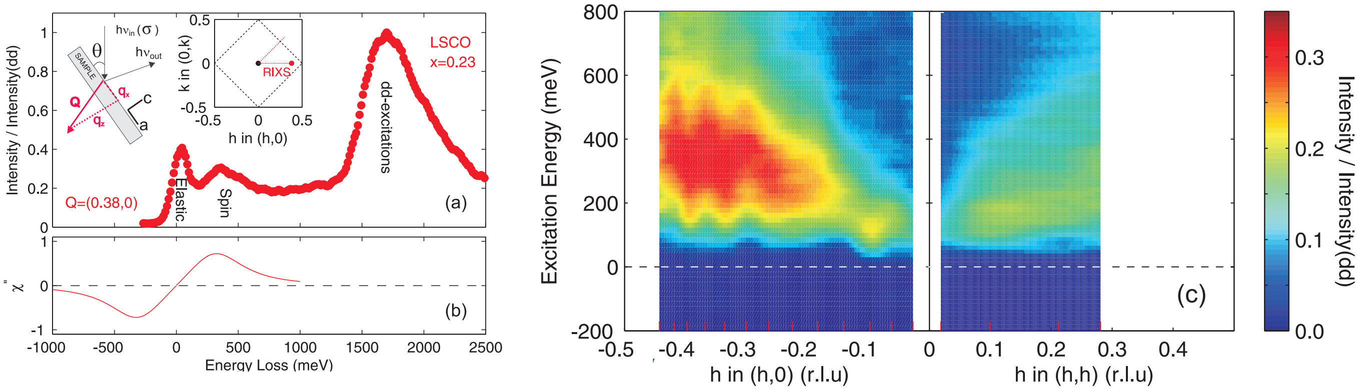

Fig. 12.1 – (a) RIXS spectrum, recorded on overdoped LSCO $x = 0.23$ using $\sigma-$polarized light, displaying elastic scattering, a low-energy excitation and a dd-excitation. The inset shows the scattering geometry and reciprocal space $(h,k,0)$ schematically. (b) Overdamped response function showing how $\chi'' \to 0$ for $\omega \to 0$. (c) Interpolated RIXS intensity, with elastic scattering subtracted, versus momentum $q = (h,0)$, (h,h) and photon energy loss ω. Red ticks indicate the grid of spectra used for the interpolation.

12.2 Magnetic field controlled charge density wave coupling in underdoped YBa$_2$Cu$_3$O$_{6+x}$

Charge density wave (CDW) correlations, that is, periodic modulations of the electronic charge density accompanied by a periodic distortion of the atomic lattice, have long been known to exist in underdoped La-based cuprate high-temperature superconductors [6]. More recently, it has been found that charge order is a universal property of underdoped high-temperature cuprate superconductors [7,8]. CDW correlations appear typically at temperatures well above the superconducting transition temperature T_c. Cooling through T_c suppresses the CDW and leads to a state in which the superconducting and CDW order parameters are intertwined and competing [11].

The application of magnetic fields suppresses superconductivity. In the case of underdoped YBCO, a number of changes in electronic properties have been reported in the field range $B \approx 10-20$ T. For example, new splittings occur in nuclear magnetic resonance (NMR) spectra [9], ultrasound shows anomalies in the elastic constants [10] and the thermal Hall effect suggests that there is an electronic reconstruction. At larger fields, $B \gtrsim 25$ T a normal state with quantum oscillations (QO) [12] and coherent transport along the c-axis is observed. The existence of QO, combined with a high-field negative Hall and Seebeck effect, is most easily understood in terms of electron pockets.

Magnetic fields with $B \approx 10-20$ T also cause changes in the CDW order which can be seen by x-ray measurements. Initial experiments [14] showed that a magnetic field causes an enhancement of the diffuse CDW scattering [13, 14]. A recent x-ray free-electron-laser experiment [15] has shown that a magnetic field of $B \gtrsim 15$ T induces a new CDW Bragg peak, with a propagation vector along the b-axis, corresponding to an extended range of ordering along the c-axis and an in-phase correlation of the CDW modulation between neighbouring bilayers.

It is important to determine the nature of the CDW correlations induced by the magnetic field in YBCO and their relationship to the electronic properties. Of particular interest are the high-field CDW phase diagram and whether a field also induces a new CDW order propagating along the a-axis.

We have therefore used hard x-ray scattering measurements to determine the the evolution of the CDW correlations with magnetic fields up to 16.9 T for several doping levels [16]. We investigated the CDW for propagation vectors along the crystallographic a- and b-directions, allowing us to extend the pulsed-field measurements [15] and identify new field-induced anisotropies in the CDW. By measuring the profile of the diffuse CDW scattering as a function of field we show that the CDW inter-bilayer coupling along the c-axis is strongly field dependent. We also show that field-induced changes in the CDW can be associated with many of the anomalies observed in electronic properties. In particular, the $B-T$ phase diagram has two boundary lines associated with the formation of high-field CDW order (see Fig. 12.2). Our data also provides insight into the likely high-field structure of the CDW (in the normal state) which is relevant to describe the Fermi surface reconstruction leading to QO.

[6] J. M. Tranquada *et al.*, Nature **375**, 561 (1995).
[7] R. Comin *et al.*, Science **343**, 390 - 392 (2014).
[8] E. H. da Silva Neto *et al.*, Science **343**, 393 - 396 (2014).
[9] T. Wu *et al.*, Nature **477**, 191 (2011).
[10] D. LeBoeuf *et al.*, Nat. Phys. **9**, 79 (2012).
[11] E. Fradkin *et al.*, Rev. Mod. Phys. **87**, 457 - 482 (2015).
[12] N. Doiron-Leyraud *et al.*, Nature **447**, 565 - 568 (2007).
[13] G. Ghiringhelli *et al.*, Science **337**, 821 (2012).

[14] J. Chang *et al.*, Nat. Phys. **8**, 871 (2012).

[15] S. Gerber *et al.*, Science **350**, 949 - 952 (2015).

[16] J. Chang *et al.*, to appear in Nat. Comms. (2016).

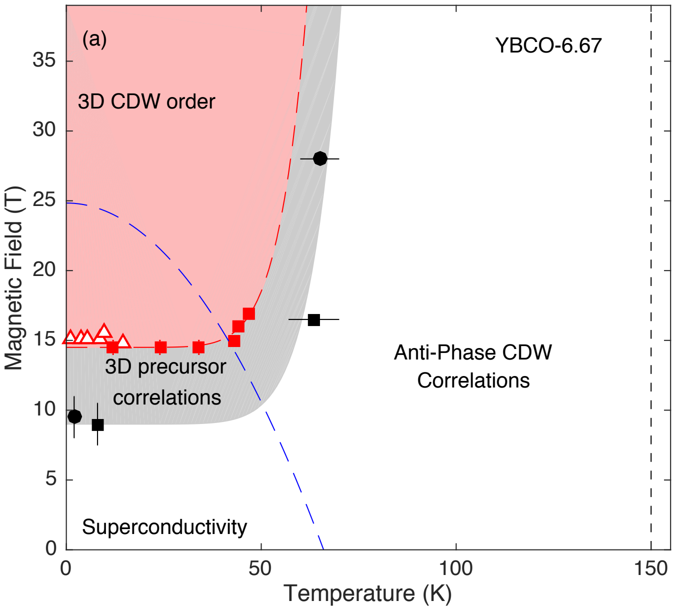

FIG. 12.2 – Temperature-magnetic field phase diagram. The pink shaded areas represent the regions where short range 3D CDW order exists. Grey bands indicate the regions where growing 3D CDW precursor correlations are observed. Solid red square points indicate the onset of a 3D CDW order with $\mathbf{q}_\mathrm{b}$ =(0,δ_b,0) determined from the variation of the $\xi_{\mathrm{c},\ell=1}$ correlation length and the intensity of the 3D peak.

12.3 Electron scattering, charge order, and pseudogap physics in $\mathrm{La}_{1.6-x}\mathrm{Nd}_{0.4}\mathrm{Sr}_x\mathrm{CuO}_4$

For the past 30 years, high-temperature superconductivity (SC) presented itself as one of the most important problems for physicists in the field of condensed matter physics. Layered copper-oxide compounds, which still hold the ambient pressure record of the maximum achievable T_c, exhibit a rich phase diagram including Mott and pseudogap physics along with CDW and spin-density wave (SDW) orders. An outstanding question is to understand how these phenomena are related. There exists compelling evidence for SC and charge-wave-order co-existing through an intertwined competing relation [17–19]. How this composite order (SC + CDW) relates to the pseudogap phase is, however, much less clear. For this reason, we have investigated [20] the charge stripe ordered system $\mathrm{La}_{1.6-x}\mathrm{Nd}_{0.4}\mathrm{Sr}_x\mathrm{CuO}_4$ (Nd-LSCO) by angle-resolved photoemission spectroscopy – one of the best probes for pseudogap physics.

In the system $\mathrm{La}_{1.6-x}\mathrm{Nd}_{0.4}\mathrm{Sr}_x\mathrm{CuO}_4$ (Nd-LSCO), CDW order around the special 1/8 doping suppresses strongly T_c. This allows a low-temperature spectroscopy study of the relation between pseudogap and CDW order [21]. These two effects are difficult to disentangle, as they both manifest themselves by a spectral gap [22]. By varying doping concentration $p = x$, photoemission-spectra were recorded in the overdoped metallic phase ($p > 0.25$), just inside the pseudogap phase ($p = 0.15, 0.2$) and at the so-called $p = 1/8$ doping where stripe order is the strongest. In the metallic phase, gap-less excitations have been observed all around the Fermi surface manifesting themselves as a single peak in the symmetrized energy distribution curve (EDC). By slightly reducing the doping just into the pseudogap phase a partial gap opens in the so-called anti-nodal region around the zone boundary. In this process spectral weight is conserved but shifted by the presence of the pseudogap. At $p = 1/8$ doping, a particularly strong enhancement of non-conservative, anti-nodal spectral-weight suppression is found inside the CDW (stripe ordered) phase. The suppression of spectral weight also extends up to much larger energies ($\approx$ 100 meV). It is thus a possibility that CDW order manifests itself in the antinodal spectra at the 1/8 doping. If so, the implication is that in Nd-LSCO, charge-stripe order and the pseudogap phase contributes differently to the suppression of anti-nodal spectral-weight. These results suggest that CDW order, which recently has been identified as a universal property of copper oxide compounds, is not directly linked to the pseudogap phase.

[17] J. M. Tranquada *et al.*, Nature **375**, 561 (1995).

[18] G. Ghiringhelli *et al.*, Science **337**, 821 (2012).

[19] J. Chang *et al.*, Nat. Phys. **8**, 871 (2012).

[20] C. E. Matt *et al.*, Phys. Rev. B **92**, 134524 (2015).

[21] R. Daou *et al.*, Nat. Phys. **5**, 31 (2009).

[22] G. Gruner, Rev. Mod. Phys. **60**, 1129 (1988).

12.4 Spin-Orbit-Induced Orbital Excitations in Sr_2RuO_4 and Ca_2RuO_4

The relativistic coupling between electronic spin and orbital momentum was long thought to have marginal influence on electrons in solids. Following the prediction and observation of topological surface states on Bi-based compounds [23], this paradigm has changed. Discovery of novel quantum phases realized through strong spin-orbit interaction is now a vivid field of research [24]. The demonstration of spin-orbit coupling driving a new type of Mott insulating state in layered iridates [25] is a good example of this. It has been proposed that doping of this effective $J_{1/2}$-Mott insulating state could lead to an exotic type of superconductivity [26], where Cooper pairs are composed of strongly spin-orbit coupled electrons.

In this context, it is interesting to study other systems that display Mott physics and superconductivity in conjunction with strong spin-orbit interaction. The $4d$-transition metal oxide system $Ca_{2-x}Sr_xRuO_4$ represents such a case. For $x = 0$, the system is a Mott insulator, whose exact nature is not clarified. At the opposite stoichiometric end ($x = 2$), the system has a superconducting ground state ($T_c = 1.5$ K) originating from a correlated Fermi liquid [27]. Although triplet p-wave superconductivity was proposed early on, the mechanism and symmetry class of the superconducting order parameter is still debated.

A fundamental question is how strongly spin-orbit interaction influences the electrons in these materials and whether it has an impact on the Mott insulating and superconducting ground states. Current experimental evidence for a strong spin-orbit interaction stems from absorption spectroscopy, that has revealed a considerable admixture of the Ruthenium t_{2g} orbitals. More recently, spin-resolved photoemission spectroscopy has reported spin-polarized bands in Sr_2RuO_4. However, the most direct consequence of strong spin-orbit interaction – the splitting of t_{2g} states – has not yet been probed directly by experiments. Orbital excitations transferred across this splitting are in fact not accessible to optical spectroscopies. Furthermore, the Ru L-edge ($\approx$ 3 keV) is currently inaccessible to high-resolution RIXS instrumentation (as it lies right between soft and hard x-ray optics).

To overcome these experimental challenges, we accessed the Ru $4d$-orbital excitations through their hybridization with oxygen $p-$orbitals [28]. Exploiting a combination of x-ray absorption (XAS) and oxygen K-edge resonant inelastic x-ray spectroscopy (RIXS), we provide direct evidence for a splitting of the ruthenium t_{2g} states. This evidence is directly visible in the RIXS spectra shown in Fig. 12.3 where the 300 meV excitation stems from intra t_{2g} transitions. Our RIXS study of Ca_2RuO_4 and Sr_2RuO_4 reveals excitations that allow an estimation of the spin-orbit coupling, in the same fashion as for the iridates. These results suggest a spin-orbit coupling λ_{so} of $\approx$ 200 meV – only about two times weaker than in the iridates. The presence of strong spin-orbit interaction implications for the symmetry class of the p-wave superconducting ground state.

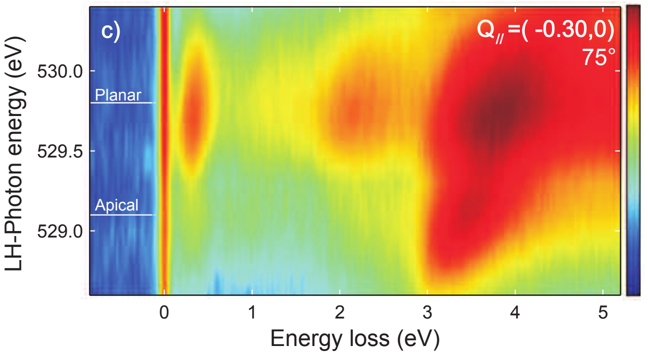

FIG. 12.3 – Resonant inelastic x-ray spectra collected with momentum transfer and polarization as indicated and displayed using a logarithmic color scale as a function of incident photon energy.

[23] M. Z. Hasan *et al.*,Rev. Mod. Phys. **82**, 3045 (2010).

[24] W. Witczak-Krempa *et al.*, Ann. Rev. Condens. Matter Phys. **5**, 57 (2014).

[25] B. J. Kim *et al.*, Phys. Rev. Lett. **101**, 076402 (2008).

[26] F. Wang *et al.*, Phys. Rev. Lett. **106**, 136402 (2011).

[27] A. P. Mackenzie *et al.*, Rev. Mod. Phys. **75**, 657 (2003).

[28] C. G. Fatuzzo *et al.*, Phys. Rev. B **91**, 155104 (2015).

13 Phase transitions and superconducting photon detectors

D. Destraz (Master student until June 2015), A. Engel (until January 2016), A. Gazizulina, F. von Rohr (until December 2015) , H. Grundmann, S. Huangfu (since October 2015), A. Schilling, S. Siegrist, Q. Wang (since November 2015) and Z. Xiaofu

in collaboration with:
University of Bern (K. Krämer), Forschungszentrum Karlsruhe (Th. Wolf, H. Küpfer), Karlsruhe Institut für Technologie (K. Ilín), Deutsches Zentrum für Luft- und Raumfahrt (H.-W. Hübers, A. Semenov), University of Wellington (B. Ruck), FIRST Lab ETH Zürich, PSI Villigen (K. Conder, V. Pomjakushin, M. Medarde), ETH Zürich (R. Nesper), LMU München (W. Schnick), Princeton University (R. J. Cava), HZ Berlin (D. Quintero-Castro, B. Lake, I. Glavatskyi)

13.1 X-ray sensitive superconducting photon detectors

As one of the most interesting early results in our project on X-ray sensitive superconducting nanowire single-photon detectors (SNSPD) we had observed an X-ray energy dependence of the detector pulse height histograms [1] (see also annual report 2011/12). A quantitative analysis of the X-SNSPD energy resolution was impossible since our X-ray tube produces a continuous energy spectrum. In a bachelor project [2] we have developed an X-ray fluorescence setup that produces quasi-monochromatic X-rays at the cost of a significant intensity loss. The new setup allows to vary the photon energy by a simple exchange the target material.

In another bachelor project [3] we have amended a numerical model simulating the detection process in optical SNSPD to include the effects of an applied magnetic field. One of the most important predictions of our model is a dependence of the threshold current (the applied current that results in nearly 100% detection probability) on the absorption site of the photon [4]. A photon absorbed in the center of the superconducting strip requires a higher threshold current than a photon of the same energy absorbed close to the edge. Furthermore, we expect a linear relation between the photon energy and the threshold current that holds for each absorption site.

The magnitude of the slope increases from the center to the edge of the strip. Extrapolated to zero photon energy, the linear relations intersect at roughly the vortex-entry current, which defines the current at which vortices can enter the superconducting strip without photon absorption and without thermal excitation. This model has been successfully used to interpret experimental results that confirmed the position-dependent threshold current [5]. The application of an external magnetic field induces Meissner screening currents. The resulting magnetic field inside the superconductor can be calculated with the help of the London equation $\Delta H = H\lambda^2$, where λ is the magnetic penetration depth. The magnetic field is applied perpendicular to the strip in the z-direction $\vec{H} = (0, 0, H)$. For strip width and thickness below λ the field in the undisturbed equilibrium situation is found to be proportional to $\cosh\left(\frac{x}{\lambda}\right)$ and the current density varies linearly across the strip. The non-equilibrium situation after the absorption of a photon results in a diffusive cloud of excess quasi-particles and as a consequence in a time- and position-dependent magnetic penetration depth λ. Using the density of excess quasi-particles and relating that to a change in λ, we were able to compute $H(r,t)$ for a series of times after the absorption of a photon at different positions across the strip.

The most interesting result from these simulations is an increased photon detection at the edges compared to the center of the strip. The linear relations between photon energy and threshold current change in response to the magnetic field in a way that the magnitude of the slope decreases in the center, but becomes even larger in a narrow area about 15 nm wide near the edge. This is visualized in Fig. 13.1 that shows the slope of the linear relation for selected photon positions as a function of the applied magnetic field. This particular simulation was done for a 150 nm wide strip, i.e. a position $x = 0$ indicates a photon absorbed in the center, and x=70 stands for a photon absorbed 5 nm from the edge.

[1] K. Inderbitzin *et al.*,
Appl. Phys. Lett. **101**, 162601 (2015).

[2] M. Hotz, Bachelor thesis, University of Zurich (2015).

[3] G. Meili, Bachelor thesis, University of Zurich (2015).

[4] A. Engel *et al.*,
IEEE Trans. Appl. Supercond., **25(3)**, 2200407 (2015).

[5] J. J. Renema *et al.*,
Nano Letters, **15(7)**, 4541-4545 (2015).

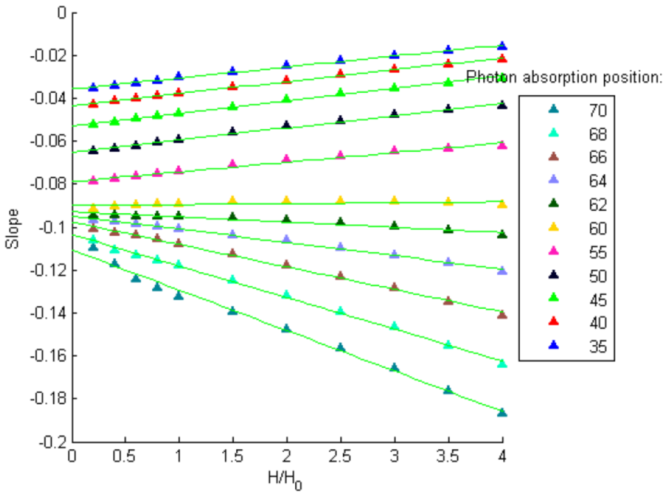

FIG. 13.1 – Slope of the linear relation between the threshold current and photon energy as a function of the applied magnetic field and photon absorption position.

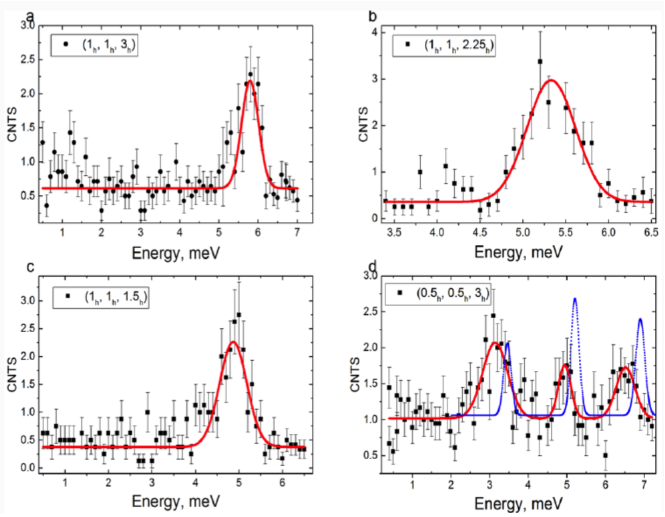

FIG. 13.2 – Energy scan of several neutron scattering Bragg peaks of $Ba_{0.1}Sr_{2.9}Cr_2O_8$ in comparison to $Sr_3Cr_2O_8$ (blue curve). The peaks are shifted towards lower energies as compared to pure $Sr_3Cr_2O_8$.

13.2 Experiments with $Ba_{3-x}Sr_xCr_2O_8$

The purpose of our experiments with $Ba_{3-x}Sr_xCr_2O_8$ has been twofold, both aimed at examining changes of the Jahn-Teller effect in the system and at inducing changes to the high-field phase transition of the spin system.

13.2.1 Manipulating the spin system

As described in previous annual reports, we have mainly examined polycrystalline samples of $Ba_{3-x}Sr_xCr_2O_8$. Such samples are well suited for macroscopic techniques such as magnetization experiments. However, coherence based techniques such as inelastic neutron scattering that allow a more direct examination of the magnetic interactions in the system require large and high quality single crystals. A next step was thus the preparation of single crystals based on a mirror furnace floating zone technique. This work has been carried out by our PhD student Alsu Gazizulina at the *Helmholtz-Institut für Materialien und Energie* in Berlin (HZB) in collaboration with the group of Prof. Bella Lake. We have successfully synthesized single-crystalline samples of $Ba_{3-x}Sr_xCr_2O_8$ with $x \in \{2.9,\ 2.8\}$.

To assess the anticipated changes of the magnetic spin interactions, we have carried out inelastic neutron scattering experiments on $Ba_{0.1}Sr_{2.9}Cr_2O_8$. From the preliminary results, we can conclude that the intra-dimer interaction constant J_0 indeed decreases with decreasing Sr content x (see Fig. 13.2). This is in accordance with our corresponding magnetization experiments [6].

These experiments will be extended to examine additional Bragg reflections for $Ba_{0.1}Sr_{2.9}Cr_2O_8$, allowing us to correctly estimate the changes of all relevant interaction constants and greatly decreasing the corresponding experimental uncertainty.

13.2.2 Examining the Jahn-Teller effect

As we have already established that the strength of the Jahn-Teller distortion in $Ba_{3-x}Sr_xCr_2O_8$ depends on the Sr content x, our current experiments aim at estimating the transition temperature T_{JT} as a function of x and examining the implications for the electronic interactions aside from the magnetic interaction constants.

The crystal structure has been investigated using neutron powder diffraction experiments on $Ba_{0.2}Sr_{2.8}Cr_2O_8$ and $Ba_{0.8}Sr_{2.2}Cr_2O_8$ for temperatures between 2 K and 300 K. We have observed the scattering intensity of Bragg peaks that are suppressed in the highly symmetric room temperature phase, but gradually gain in intensity due to the structural distortion upon cooling the crystal system.

From these experiments, we found that T_{JT} is decreasing strongly for decreasing x. However, as we used powder samples, the uncertainty of about 20 K is rather large, and the number of different stoichiometries is too small to make more general statements. To address this issue, we have performed additional heat capacity experiments, where the Jahn-Teller distortion can be identified by a fea-

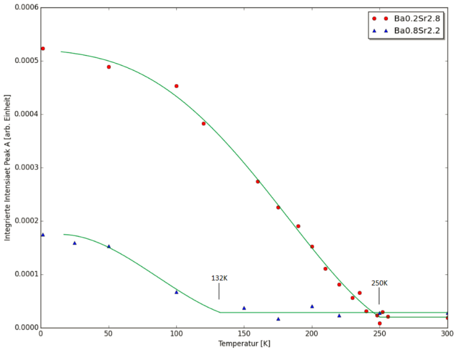

FIG. 13.3 – Integrated neutron powder diffraction intensity of Bragg peaks that are suppressed in the symmetric high temperature phase of $Ba_{3-x}Sr_xCr_2O_8$.

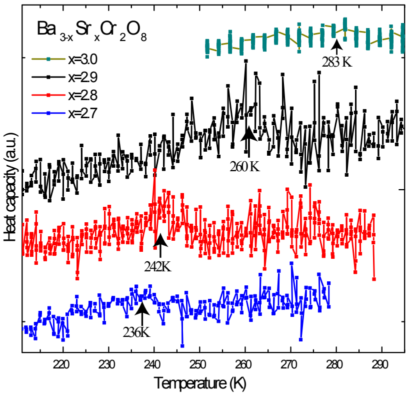

FIG. 13.4 – Heat capacity traces for $Ba_{3-x}Sr_xCr_2O_8$. The arrows mark the Jahn-Teller transitions.

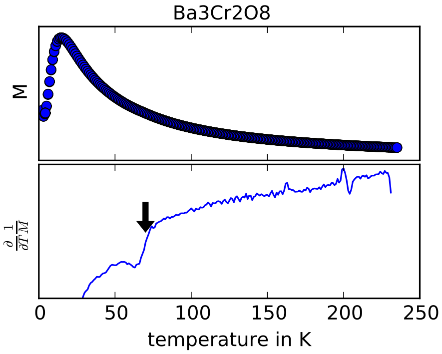

FIG. 13.5 – Magnetization M and temperature derivative $\frac{\partial}{\partial T}\frac{1}{M}$ of the inverse magnetization of $Ba_3Cr_2O_8$ as a function of the temperature. The arrow marks the Jahn-Teller transition.

ture in the heat capacity versus temperature. These experiments, performed for $x \in \{3.0,\ 2.9,\ 2.8, 2.7\}$, confirm the decrease of T_{JT} with decreasing x (see Fig. 13.4).

We have very recently established that the Jahn-Teller transition temperature can also be obtained by carefully analyzing the magnetization of $Ba_3Cr_2O_8$ as a function of the temperature (see Fig. 13.5). Here, the transition temperature can be obtained as a feature of the first temperature derivative $\frac{\partial}{\partial T}\frac{1}{M(T)}$ of the inverse magnetic moment $M(T)$. These experiments are currently being expanded to the full solid solution series $Ba_{3-x}Sr_xCr_2O_8$.

[6] H. Grundmann *et al.*,
New Journal of Physics, **18**, 033001 (2016).

13.3 Metamagnetism in $CsCo_2Se_2$

Antiferromagnetically ordered (AFM) compounds that can undergo a phase transition to a ferromagnetically ordered (FM) state upon the application of an external magnetic field are referred to as metamagnets [7]. If an external magnetic field is large enough, the magnetic moments of all unbound electrons will eventually line up with the applied magnetic field, causing a large overall magnetic moment [8]. Commonly, very large magnetic fields are necessary in order to observe so-called spin-flip or spin-flop metamagnetic transitions of compounds with an AFM ground-state.

Among the compounds ACo_2X_2 (with A = K, Rb, Cs, Tl and X = S, Se), which are related to the iron-based superconductors, $CsCo_2Se_2$ and $TlCo_2Se_2$ are the only two antiferromagnets [9, 10]. The other compounds have been found to order ferromagnetically at temperatures between $T_C \approx 50$ K and 110 K [9, 10]. In $TlCo_2Se_2$ the magnetic moments were found to order in a non-collinear incommensurate magnetic structure leading to an overall zero net magnetic moment [11, 12]. This phase has received considerable experimental and theoretical attention, because it is one of the few cobalt-based compounds with non-collinear magnetic ordering (see, e.g., reference [13, 14]). We investigated the magnetic properties of the highly air-sensitive compound $CsCo_2Se_2$ [15], which we find to be an A-type antiferromagnet displaying a metamagnetic field-induced transitions initiated in external magnetic fields even below $\mu_0 H < 1$ T [16].

The magnetic structure of the ground state of $CsCo_2Se_2$ was investigated by a series of neutron powder diffraction (NPD) experiments. In Fig. 13.6a, we show the NPD data of pulverized $CsCo_2Se_2$ crystals at 100 K, which was collected with a wavelength of $\lambda = 1.886$ Å. Most reflections of the diffraction pattern can be well explained with a $ThCr_2Si_2$ structure type model with space group $I4/mmm$. The cell parameters are $a \approx 3.842$ Å and $c \approx 15.041$ Å at 100 K. Several additionally observed Bragg reflections cannot be explained solely with this structure model, or with known phases of the Cs-Co-Se phase diagram. They can most likely be attributed to a decomposition product of the extremely air-sensitive $CsCo_2Se_2$ compound. A similar sensitivity to moisture and air has earlier been observed for the chemically closely related $A_{1-x}Fe_{2-y}Se_2$ phases [17, 18].

At the bottom of Fig. 13.6, we show the NPD data of the same polycrystalline $CsCo_2Se_2$ sample at 1.5 K collected with a wavelength of $\lambda = 1.886$ Å. We observe a single magnetic diffraction peak at $2\Theta = 7.2°$ that corresponds to the (001) reflection of the tetragonal crystal structure on hand. It can be indexed with the propagation vector $\vec{k} = [1, 0, 0]$. This implies an AFM order for the body centered Bravais lattice. We can explain our data if the magnetic moments form FM sheets with the spin direction in the *ab* plane with a magnetic coupling of $0.20(1)\mu_{\mathrm{Bohr}}$/Co. The corresponding real-space magnetic structure is depicted in Fig. 13.7. This magnetic structure it commonly referred to as A-type antiferromagnetism.

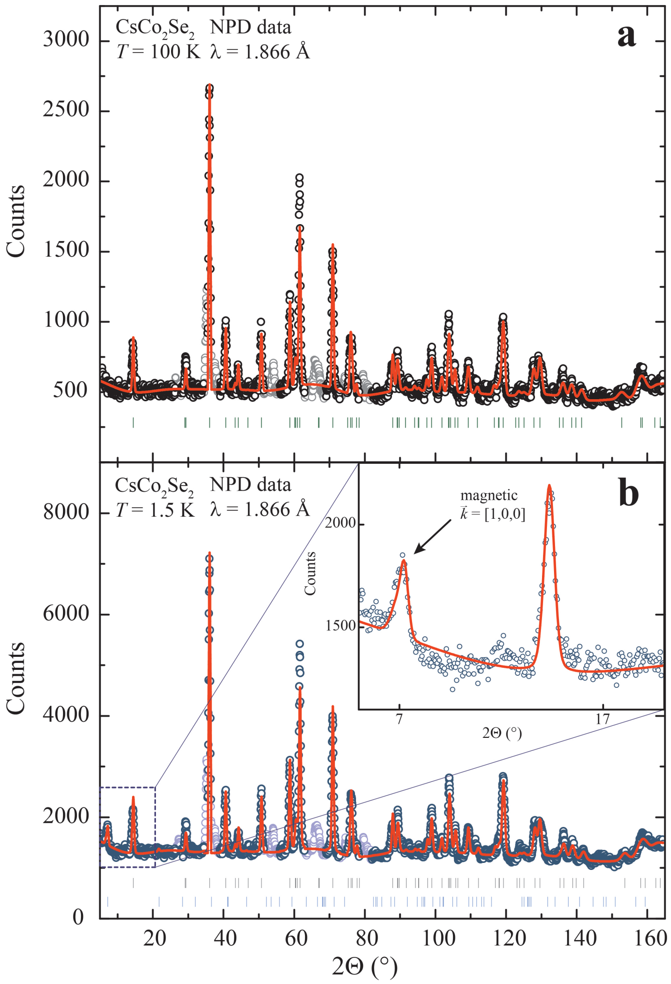

FIG. 13.6 – Neutron powder diffraction pattern of polycrystalline $CsCo_2Se_2$ at 100 K (a) and 1.5 K (b) collected with a wavelength of $\lambda = 1.886$ Å. Black and blue circles: observed patterns; red curves: calculated patterns; black tic marks: calculated peak positions for the crystal structure of $CsCo_2Se_2$; blue tic marks: calculated peak positions for the magnetic reflections of $CsCo_2Se_2$.

FIG. 13.7 – Crystal and magnetic structure of $CsCo_2Se_2$, the magnetic moments on the cobalt position of the A-type AFM structure are displayed as red arrows.

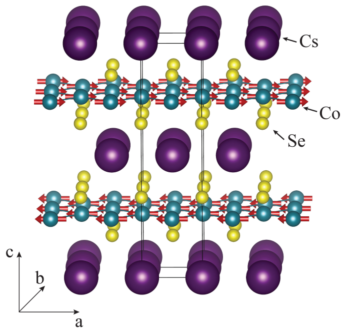

In Fig. 13.8, we show the magnetic susceptibility as $\chi = M/H$ (a) and the magnetization (b) in a temperature range between $T = 5$ K to 100 K with the external field $\mu_0 H$ perpendicular to the c axis of $CsCo_2Se_2$. The clearly pronounced metamagnetic transition from a AFM orientation to a FM orientation of the magnetic moments can be observed in these measurements. The transition temperature is shifted only slightly to lower temperatures with higher magnetic fields. A clear saturation of the magnetic moments in a FM or canted AFM alignment is found in fields greater than $\mu_0 H \approx 6$ T, while the transition is observed to be continuous. As expected, the field dependence of the magnetization $M(H)$ of $CsCo_2Se_2$ deviates from a common AFM behaviour and further supports the scenario of a spin reorientation and therefore of a metamagnetic transition (not shown here).

Four different magnetic phases can be identified in $CsCo_2Se_2$: a paramagnetic high-temperature phase (PM), an antiferromagnetically ordered phase (AFM), one or more metamagnetic phase transitions (MM), and a ferromagnetically ordered phase (FM) (see Fig. 13.9). This nomenclature is chosen on the basis of earlier reports of similar magnetic properties. It should be noted that all of the observed transitions are continuous and that all here determined critical fields are not strict quantities.

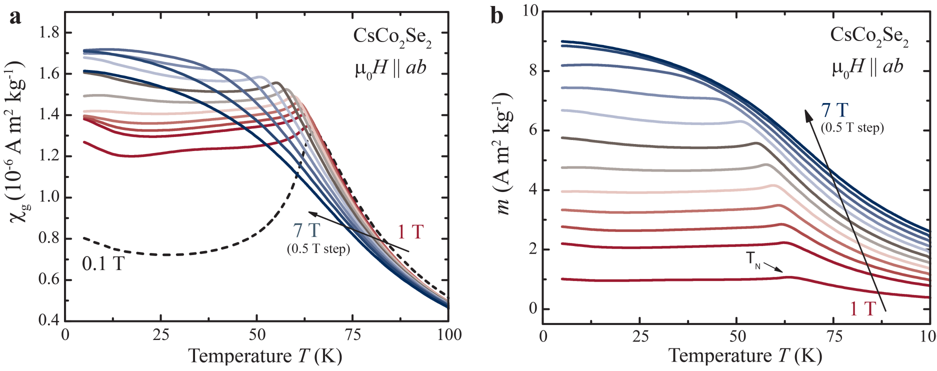

FIG. 13.8 – Magnetic susceptibility χ (a) and the magnetization m (b) in a temperature range of $T = 5$ K to 100 K in magnetic fields $\mu_0 H$ from 1 T to 7 T in 0.5 T steps.

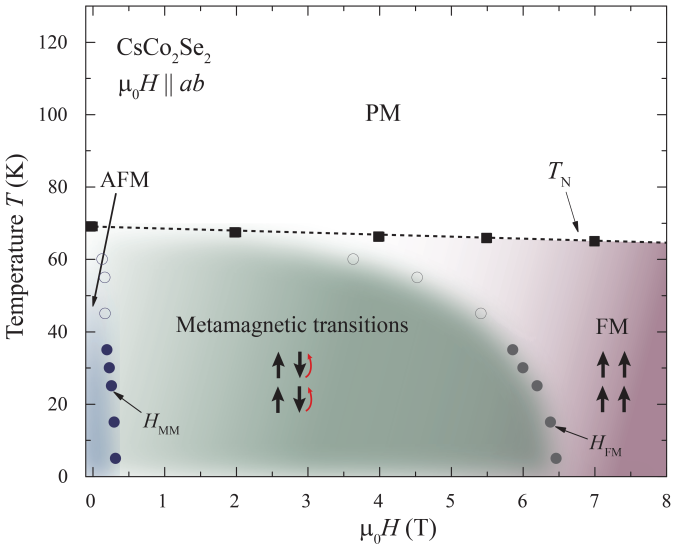

FIG. 13.9 – Phase diagram of $CsCo_2Se_2$ for magnetic fields up to 7 T, determined from field dependent magnetization measurements.

Furthermore, at higher temperatures the transitions broaden and are less pronounced in the field-dependent magnetization $M(H)$ (represented in Fig. 13.9 by open circles). The observed phase diagram is in qualitative agreement with other metamagnetic materials. Layered A-type antiferromagnetic materials often undergo metamagnetic transitions in external magnetic fields parallel to the antiferromagnetically ordered spin lattices, because the interlayer AFM coupling is in such an alignment comparably weak.

Our study [15] characterizes $CsCo_2Se_2$, which is chemically and electronically posed closely to the $A_xFe_{2-y}Se_2$ superconductors, as a host of versatile magnetic interactions that likely can be tuned by chemical variation of the interlayer distance. In further studies, the strong correlation between the structure and magnetism in these materials may give new insights into the nature of the magnetic and superconducting interactions in the $ThCr_2Si_2$-related superconductors and magnets.

[7] E. Stryjewski and N. Giordano,
1977 *Advances in Physics* **26** 487.

[8] E.P. Wohlfarth and P. Rhodes P,
1962 *Philosophical Magazine* **7** 1817.

[9] G. Huan G and M. Greenblatt,
1989 *J. Less-Common Met.* **156** 247.

[10] J. Yang, B. Chen, H. Wang, Q. Mao, M. Imai, K. Yoshimura, and M. Fang,
2013 *Phys. Rev. B* **88** 064406.

[11] R. Berger, M. Fritzsche, A. Broddefalk, P. Nordblad, and B. Malaman, 2002 *J. Alloys Compd.* **343** 186.

[12] R. Lizarraga, S. Ronneteg, R. Berger, A. Bergman, O. Eriksson, and L. Nordström,
2004 *Phys. Rev. B* **70** 024407.

[13] H. K. Jeong, T. Valla, R. Berger, P. D. Johnson, and K. E. Smith, 2007 *EPL* **77** 27001.

[14] S. Ronneteg, S. Felton, R. Berger, and P. Nordblad,
2003 *J. Magn. Magn. Mater.* **299**, 53.

[15] F. von Rohr *et al.*,
accepted in *J. Phys: Condensed Matter.*

[16] F. von Rohr, A. Krzton-Maziopa, V. Pomjakushin, H. Grundmann, Z. Guguchia, W. Schnick, A. Schilling, http://arxiv.org/abs/1605.01113.

[17] S. Weyeneth, M. Bendele, F. von Rohr, P. Dluzewski, R. Puzniak, A. Krzton-Maziopa, S. Bosma, Z. Guguchia, R. Khasanov, Z. Shermadini, A. Amato, E. Pomjakushina, K. Conder, A. Schilling, and H. Keller,
2012 *Phys. Rev. B* **86** 134530.

[18] V. Y. Pomjakushin, E. V. Pomjakushina, A. Krzton-Maziopa, K. Conder and Z. Shermadini,
2011 *J. Phys.: Condens. Matter* **23** 156003.

14 Surface Physics

M. Hengsberger, R. Westerström, L. Castiglioni, H. Cun, G. Mette, E. Miniussi, S. Förster, C. Monney, D. Leuenberger, L. H. de Lima, R. Stania, C. Bernard, A. Kostanyan, A. Schuler, W.-D. Zabka, P. Kliuiev, K. Waltar, Y. Kubota, M. Baumgartner, M. Graf, T. Stöckli, T. Kälin, T. Greber, and J. Osterwalder

For the investigation of surface and interface phenomena at the atomic level, our laboratory is well equipped for the preparation and characterization of clean single-crystalline surfaces, metal and molecular monolayer films, as well as sp^2-bonded single layers on surfaces, using a wide variety of experimental techniques. In addition, we are part of a user consortium of the soft x-ray beam-line *PEARL (PhotoEmission and Atomic Resolution Laboratory)* at the Swiss Light Source. Our group has further built and commissioned a compact and mobile angle-resolved photoemission (ARPES) instrument, to be used at advanced laser sources within the NCCR *Molecular Ultrafast Science and Technology (MUST)*, while a second ARPES spectrometer is currently being set up together with a high-harmonic gas jet source for producing high-energy UV light.

The research carried out during the report period can be grouped into four topics:

- 2D Materials
  Monolayer hexagonal boron nitride (h-BN) and graphene are grown by chemical vapor deposition (CVD) on metal surfaces. Using well controlled ultrahigh vacuum (UHV) conditions and single-crystal metal films as substrates, we are in a position to grow these 2D materials in a single crystalline domain. A strong effort has been made to optimize methods for de-laminating these films from their metal substrate, in order to explore further their transport properties in the case of graphene, or their applicability for nanofiltration purposes in the case of h-BN. Sec. 14.1 presents some first promising results for monolayer graphene transferred from the Ir(111) substrate onto an amorphous and insulating SiO_2 film.

- Ultrafast processes at surfaces
  Charge transfer processes upon optical excitation of adsorbed molecules are studied by time-resolved two-photon photoemission (2PPE). Specifically, a visible pump pulse populates the lowest unoccupied molecular orbital (LUMO), which can be detected in photoemission by a second, delayed photon. The goal is to extract lifetimes and charge transfer rates from the observed transients. In a second project the motion of adsorbed molecules is addressed by time-resolved photoelectron diffraction. A first successful proof-of-principle study of this type, showing coherent phonon excitation in Bi(111), is discussed in Sec. 14.3.

- Adsorbed molecular catalysts and photosensitizers
  Within the University Research Priority Program *Light to Chemical Energy Conversion* (LightChEC) our role is to develop and study model catalyst surfaces for solar water splitting. Currently these are based on pyrphyrin ligands (see Sec. 14.2) that we have learned to immobilize on Au(111) and $TiO_2(110)$ surfaces, where the Co-metalated molecules readily form upon Co evaporation. Rhenium-based photosensitizers are grafted onto ultrathin alumina films of various thicknesses via covalent bonds. This is achieved by self-assembly from solution. For this purpose, a chamber with a liquid reservoir has been built from which the sample can be transferred directly into our UHV system for further preparation and characterization. The goal is to measure charge transfer times via tunneling through the alumina film.

- Spin shuttles
  Endohedral single molecule magnets (*spin shuttles*) of the type $RE_3N@C_{80}$ where RE are one, two or three different rare earth ions (e.g. $Dy_2ScN@C_{80}$) offer a broad variety of magnetic behavior at low temperatures. In a collaboration with IFW Dresden (A. Popov) and PSI Villigen (C Piamonteze) the magnetic and structural properties of these largely unexplored systems are studied by means of SQUID magnetometry and x-ray magnetic circular dichroism (XMCD).

In the following, three highlights of last year's research are presented in more detail.

14.1 Large-scale transfer of single-crystal graphene from Ir thin films

In collaboration with: Benjamin Probst, Chemistry Department, Universität Zürich; Miroslav Haluska, Micro- and Nanosystems, D-MAVT, ETH Zürich.

In the framework of the European Flagship for Future and Emerging Technologies (FET) 'GRAPHENE', we investigate the growth of single crystalline boron nitride and graphene (g). In–situ chemical vapour deposition (CVD) is an established method for the synthesis of high–quality epitaxial graphene on the close–packed surfaces of many transition metals. An alternative to expensive and size–limited bulk single crystals is offered by twin-free, single crystal films of metals of the Pt group grown on YSZ-buffered Si(111) substrates [1]. We are able to synthesize single-domain graphene films on 150 nm–thick Ir(111)/YSZ/Si(111) four–inch wafers [2]. In comparison with graphene synthesis on metal foils (e.g. copper), which implies growth of multiple domains, this method leads to large–area graphene flakes with a crystalline orientation matching that of the substrate.

For most applications in electronics and nanotechnology, however, graphene needs to be transferred onto an insulating substrate, typically SiO_2. An alternative to the traditional chemical etching of the metal substrate is offered by the electrochemical delamination of the graphene sheet (*bubbling*) [3]. This method performs very well for graphene on platinum and copper [4, 5], but until recently only limited transfer rates could be achieved for graphene transferred from Ir thin films. We made progress in this respect by introducing an additional step in the transfer protocol, as reported by L. Koefoed *et al.* [6]. While Raman spectra indicate a high defect concentration in the graphene layer, we are able to directly measure the average charge carrier density by photoemission.

Figure 14.1 shows the Raman spectrum of single crystalline graphene on an amorphous SiO_2 film and a Fermi surface map from this sample. Clearly, the six Dirac cones of graphene appear at the corners of the Brillouin zone, though rather smeared out, likely due to the presence of local charges and roughness effects on the insulating substrate. Nevertheless the carrier density can be inferred from such data. The photoemission result directly indicates large scale single crystallinity, since the photon beam in our instrument has a diameter of about 2 mm. This opens the doors to many more experiments on two-dimensional materials other than graphene, where the electrons may be directly observed in reciprocal space.

[1] S. Gsell *et al.*, J. Cryst. Growth **311**, 3731 (2009).

[2] A. Hemmi *et al.*, Rev. Sci. Instrum. **85**, 035101 (2014).

[3] G. Lupina *et al.*, ACS Nano **9**, 4776 (2015).

[4] Y. Wang *et al.*, ACS Nano **5**, 9927 (2011).

[5] L. Gao *et al.*, Nature Commun. **3**, 699 (2012).

[6] L. Koefoed *et al.*,
J. Phys. D: Appl. Phys. **48**, 115306 (2015).

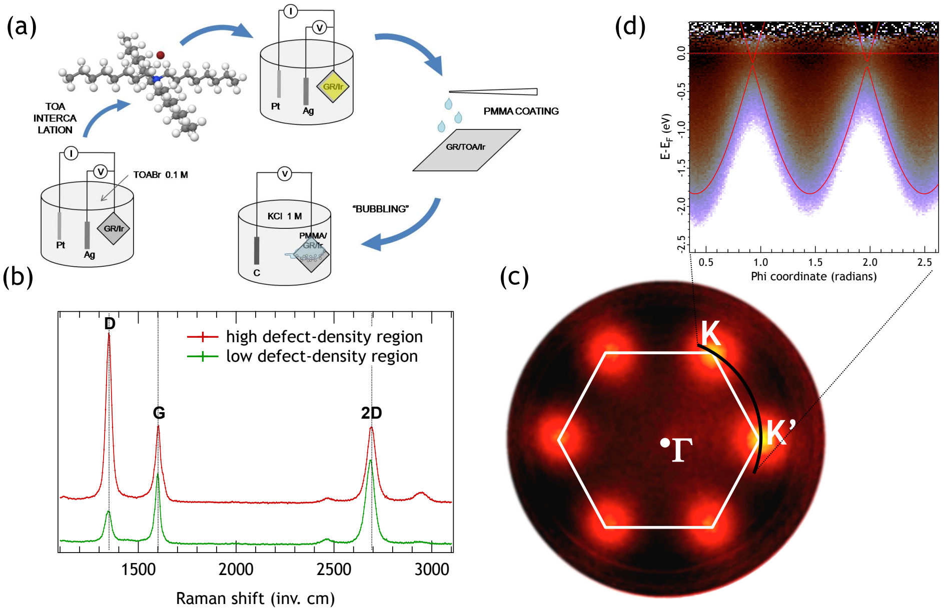

Fig. 14.1 –
(a) Schematics of the TOA-assisted electrochemical delamination procedure.
(b) Raman spectra of the transferred samples (excitation wavelength: 532 nm) acquired in a high– and low–defect density region, respectively.
(c) Fermi surface map of g/SiO_2 acquired with He IIα radiation.
(d) Background-subtracted azimuthal scan acquired with He IIα radiation along the K-K' direction normalized by the Fermi function. The Fermi level obtained from the fit, as well as the valence and conduction bands, simulated via a basic tight-binding model, are superimposed.

14.2 Adsorption and metalation of pyrphyrin on Au(111)

In collaboration with:
Yeliz Gurdal, Stephan Schnidrig, Benjamin Probst,
Marcella Iannuzzi, Jürg Hutter and Roger Alberto,
Chemistry Department, Universität Zürich.

Metal complexes based on pyrphyrin ligands have recently shown promise as water reduction catalysts in homogeneous photo-chemical water splitting reactions [7]. We have studied the adsorption of pyrphyrin on a single crystalline surface and examined its controlled metalation in ultra-high vacuum (UHV) [8]. Coverages up to one monolayer were obtained by sublimation of the molecules on a Au(111) surface kept at room temperature. Deposition of Co metal at the level of 5% of a monolayer and subsequent annealing then led to the formation of 90% of Co-pyrphyrin (CoPyr) molecules.

Fig. 14.2 - left shows an STM image of the hexagonally-ordered Pyr molecules which appear donut-shaped with a weak indication of two-fold symmetry. After Co deposition at a sample temperature of 323 K (Fig. 14.2 - center), most of the molecules have maintained their donut shape, but some of them appear brighter and exhibit two distinct lobes. Successive annealing up to 423 K increases the number of brighter molecules, but their contrast changes from the two lobes to a single central protrusion (Fig. 14.2 - right). The metalation thus appears to be temperature driven. After the Co evaporation, one part of the Co atoms assembles in clusters that are observed in STM scans over a larger area, whereas another part is already ligated to the cores of Pyr molecules. Due to the annealing, on the one hand Co atoms dissociate from the initially formed clusters and diffuse along the surface, before they are captured by Pyr molecules. On the other hand, the changing sub-molecular contrast of the Co-ligated Pyr species indicates the existence of an intermediate state (CoPyr-2H) prior to the annealing.

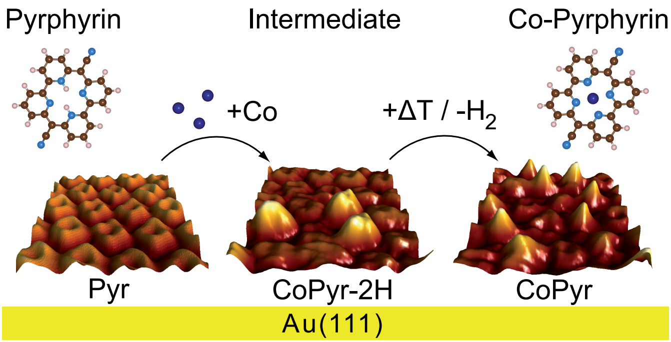

Fig. 14.2 – STM images of free-base pyrphyrin molecules (left), after deposition of cobalt at 323 K (center), and after annealing the surface to 423 K (right).

Our assignments are corroborated by of XPS measurements and density functional theory (DFT) calculations. The N 1s spectra in Fig. 14.3 directly probe the local chemistry within the pyrphyrin molecules. Due to the three types of chemical environment of N atoms within the free-base molecule, pyridinic (-NH-), iminic (-C=N-) and cyano (-C≡N) nitrogen, the spectrum of Pyr/Au(111) (top panel) can be well fitted with three components. After Co evaporation and subsequent annealing of the sample (bottom spectrum), the spectrum seemingly collapses into a single peak. It can be fitted with four components, a major one at 399.2 eV, a smaller one at the cyano nitrogen position forming the shoulder, as well as two small remnant pyridinic and iminic components, reflecting few unmetalated molecules. Co deposition without annealing yields a distinct shift of the N 1s spectra to higher binding energies (middle spectrum). The 4-component does not lead to a satisfactory fit and, to account for the probable CoPyr-2H intermediate, two additional nitrogen components (the light-blue and light-green curves) were introduced in the N 1s model. The reaction steps for the Co metalation of a monolayer of pyrphyrin molecules on Au(111) could thus be established.

[7] E. Joliat, *et al.*, *Dalton Trans.* **45**, 1737 (2016).

[8] G. Mette *et al.*, *Nanoscale* **8**, 7958 (2016).

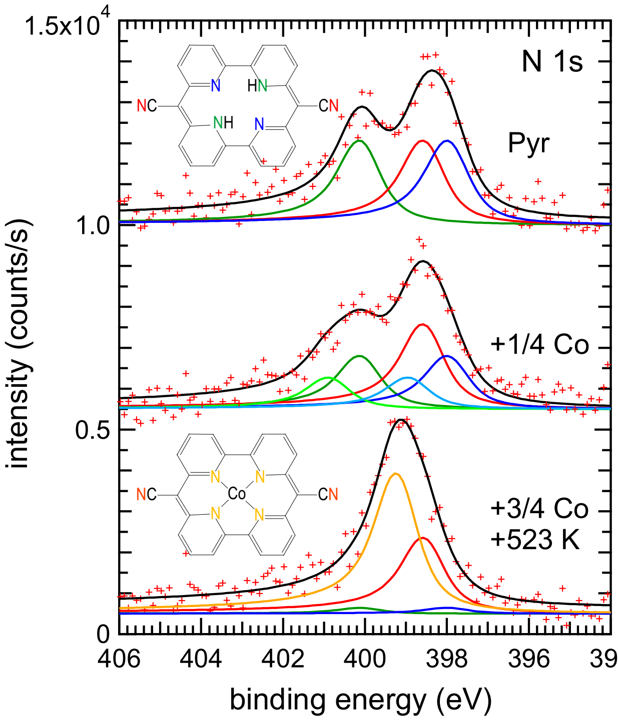

Fig. 14.3 – XPS data and corresponding fits of N 1s spectra before the Co evaporation (top), after partial Co evaporation without annealing (middle) and after the complemented Co evaporation with subsequent annealing to 523 K (bottom).

14.3 Structural dynamics studied by time-resolved photoelectron diffraction

In collaboration with:
Lamia Kasmi, Matteo Lucchini, Lukas Gallmann and Ursula Keller, Physics Department, ETH Zürich; NCCR MUST.

Coherent phonons are an excellent tool to investigate the interplay between electronic and structural dynamics. The displacive excitation of coherent phonons in elemental bismuth is one of the most widely studied processes for this purpose. In a simple model, phonons are kick-started coherently by a short pulse promoting electrons into unoccupied states and shifting the atomic equilibrium positions. As a consequence of the electronic response to the lattice modulation, the phonon mode drives an oscillation of the electronic charge density. The phase lag between the forced oscillation and the driving force is determined by the ratio of friction represented by the electron population decay rate and the phonon frequency. We employed time-resolved photoelectron diffraction to access the structural dynamics by recording the energy-integrated valence photoemission intensity as function of emission angle.

Photoelectrons excited by absorption of x-ray or extreme ultraviolet (XUV) light will undergo scattering processes at nearest-neighbors of the emitter atoms. The resulting interference pattern carries information about the local environment of the emitter [9]. The time-resolved structural response of a solid after excitation with an intense infrared pump pulse can thus be monitored by photoelectron diffraction produced by XUV probe pulses. The temporal resolution in such a pump-probe experiment is determined by the cross correlation of the pump and probe light pulses.

In Fig. 14.4(a) the photoemission yield from emission from the valence band close to the Fermi energy E_F is shown as function of time delay for three different high-symmetry points in the surface Brillouin zone. At time delay zero a steep increase in intensity can be seen as a consequence of the excitation of electrons to unoccupied states above E_F. The increase is followed by an exponential decay. On top of the decay an intensity modulation is observed with a period of about 360 fs or a frequency of 2.76 THz.

The generation of the hot-electron gas at delay zero can be modeled by decoupling electronic and lattice temperature; assuming thermal equilibrium within the electron gas only, the excess energy of the electron gas can be converted into a formal electronic temperature of about 2000 K [11, 12]. The modulations were already investigated previously with tr-ARPES and attributed to transient changes in the bulk electronic structure caused by the coherent excitation of A_{1g} phonons [11]. We performed tight-binding calculations [13] once for the equilibrium lattice and once for the distorted lattice corresponding to the maximum A_{1g} amplitude of 0.04 Å expected for the fluence used here [14, 15] (Fig. 14.4(b)). The so-called photoemission density of states (DOS) is then obtained by integrating the density of states over a small volume in reciprocal space which matches the solid angle covered by the detector and is centered at the initial state momenta where the photo-excitation takes place. The calculations indeed predict a *decrease* of the DOS near the L-point upon increasing distortion away from the rhombohedral and towards the simple cubic lattice. Thus, the photoemission intensity modulation shows a minimum for maximum distortion at half a phonon period. This explains why the modulation phase is such that the increasing edge is followed by a minimum and then by a maximum at about 360 fs (bottom two curves in Fig. 14.4(a)).

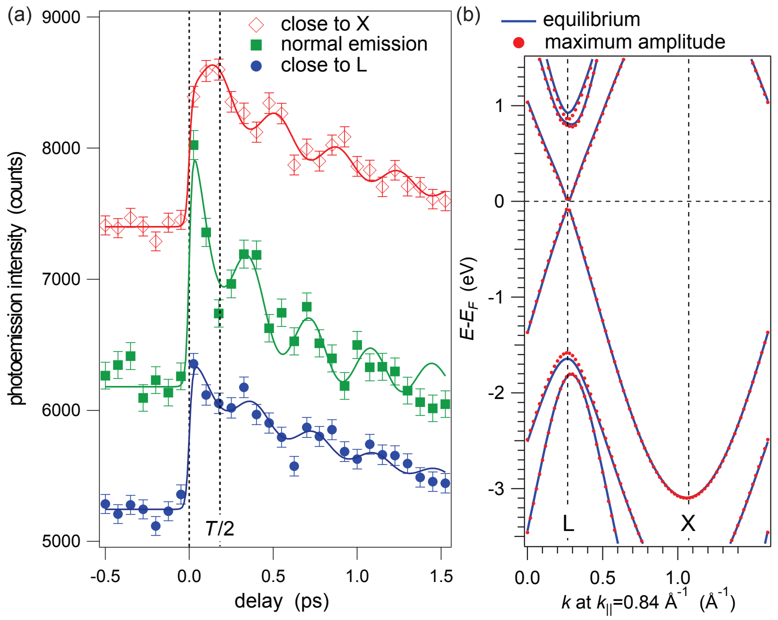

Fig. 14.4 – Time- and angle-resolved photoemission from Bi(111) after absorption of an intense IR pump pulse.
(a) Integrated valence band intensity as function of time delay for normal emission $\overline{\Gamma}$ (ΓT-line) and the $\overline{\mathrm{M}}$ (L) and $\overline{\mathrm{M}}'$ (X) points at the border of the first surface (bulk) Brillouin zone.
(b) Tight-binding calculation of the band structure for the bulk L- and X-points.

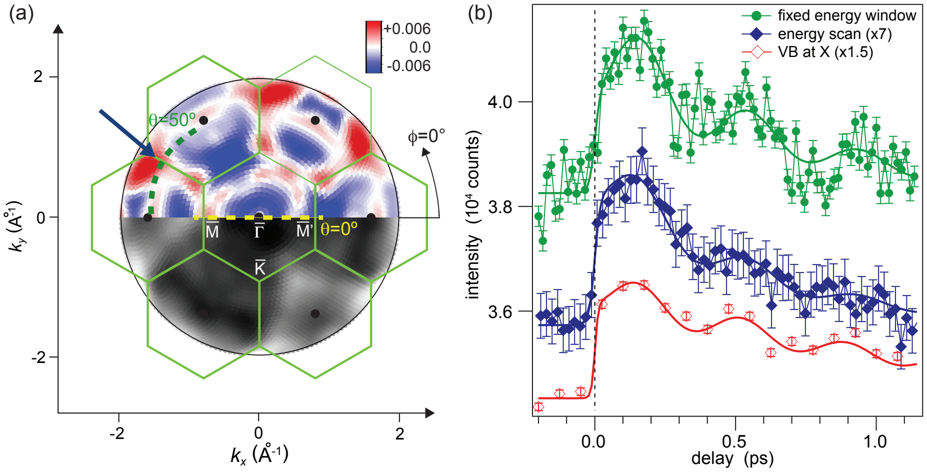

Fig. 14.5 –
(a) SSC calculation of the photoelectron diffraction pattern for the Bi(111) surface: upper part difference excited-equilibrium, lower part equilibrium structure. The blue arrow indicates the measurement position for the data in the right panel. (b) Comparison of two diffraction transients (green and blue symbols) and the intensity recorded at the bulk X-point (red symbols).
The curves are fits to the data.

In contrast to L, the X-point exhibits a large energy gap around E_F. The time-dependent photoemission intensity at X is dominated by photoelectron diffraction effects. The structural distortion by the $\text{A}_{1\text{g}}$ mode leads to a change in distance between emitter and scatterer along the [111]-axis and, thereby, to a displacement of the interference fringes. Depending on the solid angle sampled in the experiment, this shift of the fringes results in an increase or decrease in photoemission intensity. Single-scattering cluster (SSC) calculations show that an increase of photoemission intensity at angles corresponding to emission from the X-point is expected for increasing lattice distortion, as can be seen in stereographic representation in Fig. 14.5(a). This explains the shift of about 2.8 rad between the intensity modulations at the X-point ($\overline{\text{M}}$) and at the $\overline{\Gamma}$- or L-point ($\overline{\text{M}}'$).

Further strong diffraction effects can be found at the emission angle $\theta = 50^\circ$ in the direction indicated by the blue arrow in Fig. 14.5(a). The valence band yield measured at this angle is shown as function of time delay in Fig. 14.5(b) and compared to the spectral intensity recorded at the X-point. At time delay zero, a slow increase is observed reaching maximum intensity after half a phonon period. The phase offset of the cosine function is close to that of the modulation at $\overline{\text{M}}$. The average phase lag of $\varphi \approx 2.80$ rad appears to be significantly smaller than π with respect to the electronic excitation. In order to elucidate this large difference, we estimate the decay time constant necessary to obtain the observed phase shift based on a semi-classical model of Zeiger *et al.* [10]. The experimental values lead to a value close to the thermalization time $\tau_e(\overline{\Gamma}) = 0.44$ ps of the initial hot-electron distribution. This suggests that the early dynamics of the hot electrons determine the phase lag between electrons and phonons. Indeed, the nuclear acceleration due to the large initial displacement of electronic charge density is expected to be stronger than for the subsequent phonon cycles. At the same time, the initial hot electron distribution decays fast leading to an initial overshooting and over-damping of the $\text{A}_{1\text{g}}$ mode, which yet is fluence dependent as evidenced by our experimental data.

[9] M. Greif *et al.*, Phys. Rev. B **87**, 085429 (2013).
[10] H. J. Zeiger *et al.*, Phys. Rev. B **45**, 768 (1992).
[11] E. Papalazarou *et al.*, Phys. Rev. Lett. **108**, 256808 (2012).
[12] D. Leuenberger *et al.*, Phys. Rev. Lett. **110**, 136806 (2013).
[13] Y. Liu and R.E. Allen, Phys. Rev. B **52**, 1566 (1995).
[14] D.M. Fritz *et al.*, Science **315**, 633 (2007).
[15] G. Sciaini *et al.*, Nature **457**, 56 (2009).

15 Physics of Biological Systems

Conrad Escher, Hans-Werner Fink, Tatiana Latychevskaia, Jean-Nicolas Longchamp, Marianna Lorenzo, Jonas Verges and Flavio Wicki

in collaboration with: Dr. Roger Morin, CNRS Marseille (France), Prof. Peter Hommelhoff, University of Erlangen (Germany), Prof. Klaus Kern and Dr. Stephan Rauschenbach, Max Planck Institut, Stuttgart (Germany), Prof. Jannik C. Meyer, University of Vienna (Austria), Prof. Ute Kaiser, University of Ulm (Germany), Dr. Yuriy Chushkin and Dr. Federico Zontone, The European Synchrotron Radiation Facility, Grenoble (France), Dr. Annette Niehl and Dr. Manfred Heinlein, CNRS Strasbourg (France), Prof. Christian Schönenberger, University of Basel (Switzerland).

Our central activity, the structural investigation of individual biological objects with coherent low-energy electrons, involves in-line holography as well as coherent diffraction imaging and is assisted by micro-structuring techniques using a focussed gallium ion beam for miniaturized electron optics and sample preparation. In the past year, it became possible for the first time in the history of structural biology to image individual proteins as will be discussed in this report.

Our current activities are divided in the following interconnected individual projects:

- Electron Holography and Coherent Diffraction
  Major experimental challenges are ongoing to improve the interference resolution, establish methods for creating free standing thin films of graphene transparent for low-energy electrons as well as appropriate techniques to present a single protein to the coherent electron wave front. Next to these experimental issues, a second, equally important aspect for achieving high resolution structural information is the numerical reconstruction of the electron holograms respectively iterative phase retrieval in coherent diffraction. This is achieved by employing newly developed numerical algorithms to solve the integrals governing these coherent optics problems.

- Coherent Diffraction Imaging of Graphene-Supported Single Biomolecules at Atomic Resolution
  While this is an independent effort by Jean-Nicolas Longchamp, well worth a seperate and detailed report by itself, we include it here in view of the frame and scope of this report. Methods to deposit biomolecules onto freestanding graphene, in particular in-situ electrospray deposition have been explored and successfully implemented. The results, which led to the imaging of individual proteins in a collaboration with a group from the Max Planck Institute in Stuttgart are described further below.

- Detection of individual elementary charges and charge transfer processes
  A comparison of experimental observations with simulations reveals that it is not only possible to observe individual charges on free-standing graphene but that charge transfer processes involving a single charge and the mobility of moving charge carriers can be detected too. From the mean square displacement the diffusion coefficient has been derived.

- Direct mapping of the unoccupied states in freestanding graphene
  Electrons with kinetic energies below 30 eV originating from a coherent electron point source are transmitted through freestanding graphene. Under those angles where the *k*-vector component of the incoming electron parallel to graphene matches unoccupied states in graphene, high absorption is observed. This directly translates into a mapping of the unoccupied bands of graphene revealed by a hexagonal structure in the transmission image observed on a distant detector. These hexagons grow as expected when decreasing the beam energy from 30 down to 18 eV. The measurement principle is illustrated in Fig. 15.1.

- Instrumentation
  A new Low Energy Electron Point Source (LEEPS) microscope (Fig. 15.2) has been designed and build by our machine shop. It is currently operated to investigate the adsorption of individual alkali atoms onto free-standing graphene.

- Direct writing of sub-micron sized structures
  A so-called super ink jet printer was purchased by the R'Equip fund SPOT (Single Protein on Target), to be used to the benefit of research groups in physics and physical chemistry. So far, it has been possible to pattern surfaces with silver lines by direct printing in an application aiming at carrying out four point measurements to explore transport through graphene layers.

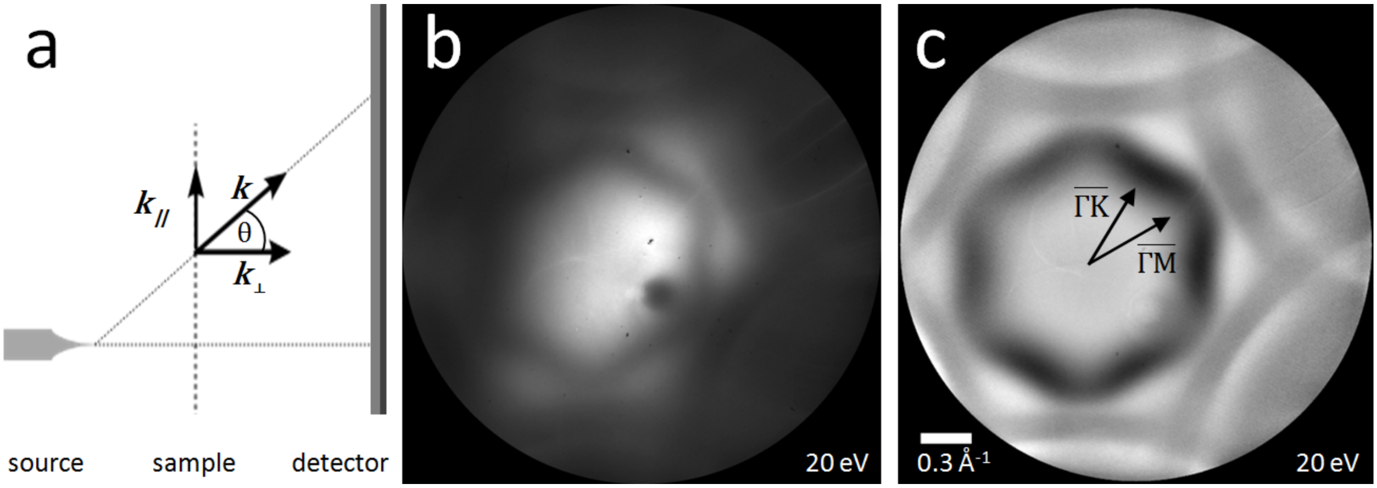

FIG. 15.1 – The in-plane k vector of the electrons impinging onto graphene under a certain angle is illustrated in (a). The in-plane momentum dependency of the transmission through free-standing graphene thus allows probing the unoccupied bands by observing the electron transmission pattern at a distant detector. In (b) raw data of such transmission pattern for 20 eV electrons are shown while at (c) the same data are displayed after background subtraction and transformed into coordinates of the k vector parallel to graphene. The arrows indicate the direction of the high symmetry points K and M in the Brillouin zone, determined from the first order diffraction disks observed at higher electron energies.

15.1 Overall Motivation and Research Goals

Most of the protein structural information available today has been obtained from crystallography experiments by means of averaging over many molecules assembled into a crystal. Since biological molecules exhibit different conformations, averaging smears out structural details. That is why a strong desire to gain structural data from just a single molecule is emerging. We are working towards the objective of deriving atomic structure information from experiments carried out on just one individual molecule subject to the interaction with a coherent low-energy electron wave. Meanwhile, it has been thoroughly established that electrons with kinetic energies below 200 eV are the only radiation known today where elastic scattering dominates. Radiation damage-free imaging of a single biological molecule is thus possible by recording holograms and coherent low-energy electron diffraction patterns. Recently, by adopting a method to deposit individual proteins onto free-standing graphene in a collaboration with colleagues from the Max Planck Institute in Stuttgart, it has become possible to actually derive structural information on a single molecule level.

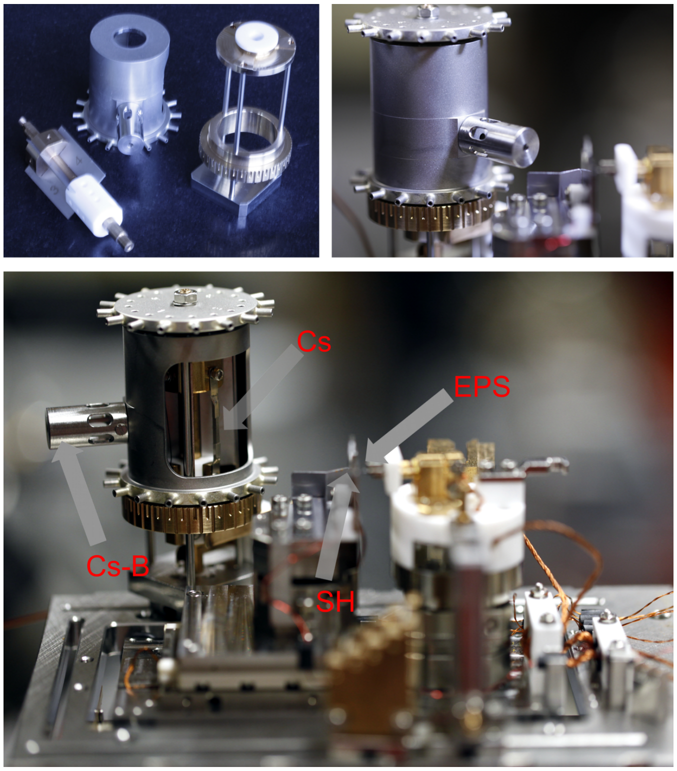

FIG. 15.2 – View into a new LEEPS microscope for exploring in situ adsorption of alkali atoms onto freestanding graphene. Top: dedicated rotatable alkali metal evaporator. Bottom: Cesium atom beam (Cs-B) tube to be directed towards free-standing graphene. Up to four cesium (Cs) sources are incorporated into the evaporator. The sample holder (SH) carries the free-standing graphene sample which can be transferred onto the system without breaking the ultra-high vacuum. The coherent electron point source (EPS) allows observing the adsorption processes by recording low energy electron holograms while Cs atoms settle onto the transparent graphene.

15.2 Imaging proteins at the truly single molecule level

Jean-Nicolas Longchamp, Stephan Rauschenbach, Sabine Abb, Conrad Escher, Tatiana Latychevskaia, Klaus Kern, Hans-Werner Fink

Imaging a single protein has been a long-standing aspiration for advancing structural biology along with various fields in natural science. In particular, revealing the distinct conformations of an individual protein is of utmost importance. Below, we show the imaging of individual proteins and protein complexes by low-energy electron holography. Samples of individual proteins and protein complexes on ultraclean freestanding graphene were prepared by soft-landing electrospray ion beam deposition, which allows chemical- and conformational-specific selection and gentle deposition. Low-energy electrons do not induce radiation damage, which enables acquiring sub-nanometer resolution images of individual proteins (cytochrome C and bovine serum albumin) as well as of protein complexes (hemoglobin), which are not the result of an averaging process.

15.2.1 Introduction

Most of the currently available information on protein structures has been obtained from either X-ray crystallography experiments or cryo-electron microscopy investigations by means of averaging over many molecules assembled into a crystal or over a large ensemble selected from low signal-to-noise ratio electron micrographs, respectively. Despite the impressive coverage of the proteome by the available data, a strong desire for acquiring structural information from just one individual molecule is emerging. The biological relevance of a protein lies in its structural dynamics, which is accompanied by distinct conformations. The associated structural details however, remain undiscovered when averaging is involved. Moreover, a large subset of the entirety of proteins, in particular from the important category of membrane proteins, are extremely difficult, if not impossible, to obtain in a crystalline form. If just one individual protein or protein complex can be analyzed in sufficient detail, those objects will finally become accessible.

For a meaningful contribution to structural biology, a tool for single molecule imaging must allow for observing an individual protein long enough to acquire a sufficient amount of data to reveal its structure without altering it. The strong inelastic scattering cross-section of high-energy electrons as employed in the state-of-the-art aberration-corrected Transmission Electron Microscopes (TEMs) inhibits accumulation of sufficient elastic scattering events to allow high-resolution reconstruction of just one molecule before it is irremediably destroyed. Staining proteins with heavy metal atoms is unfortunately not a viable alternative; it is well known that the chemical processes involved alter the protein structure. Moreover, heavy metal atoms are highly mobile under high-energy electron beams leading to ambiguous images. A new approach to the problem of structural biology is associated with the X-ray Free Electron Laser (XFEL) projects. With this impressive technological development and novel experimental tool, it is now possible to elucidate the structure of proteins brought in the form of crystals of just nanometer size. This method even originally appeared as a way of gaining information at the atomic scale from just a single biomolecule. Meanwhile it has become clear that averaging over a large number of molecules will unfortunately not be avoidable. In contrast to the radiation problem experienced when using high-energy electrons or X-rays, biomolecules, for instance DNA, can withstand prolonged irradiation by electrons with a kinetic energy in the range of 50 – 250 eV. Even after exposure to a total dose of at least five orders of magnitude larger than the permissible dose in X-ray or high-energy electron imaging, biomolecules remain unperturbed. This, combined with the fact that the de Broglie wavelengths associated with this energy range are between 0.7 and 1.7 Å, makes microscopy techniques taking advantage of this energy range, especially low-energy electron holography, auspicious candidates for structural biology at the single molecule level. In this lens-less microscopy scheme inspired by Gabor's original idea of holography, the samples are presented to a highly coherent beam of low-energy electrons generated by an atomically sharp field emitter tip placed as close as 100 nm in front of the sample. The interference pattern formed by the scattered and un-scattered electron waves, the so-called hologram, is recorded at an electron detector several centimeters away. While highly coherent sources for low-energy electrons have been available for more than two decades, holography has long suffered from the lack of a substrate transparent to low-energy electrons but still robust enough that nanometer-sized objects can be deposited onto it. Recently, we have shown that ultraclean freestanding graphene fulfils these two requirements. While the damage-free radiation of low-energy electrons and the conceptual simplicity of the experimental scheme for holography are appealing, this tool for single protein imaging critically relies on the sample preparation method. The protein must be brought into an ultra-high vacuum (UHV) environment and fixed in space for an appropriate period of time for to accumulate sufficient structural information on the one hand, while avoiding the emergence of contaminants on the other hand. In the following, we show how sub-nanometer resolution images of individual proteins are obtained by means of low-energy electron holography. Native proteins are transferred from aqueous solution to the gas phase and deposited onto ultraclean freestanding graphene in an UHV

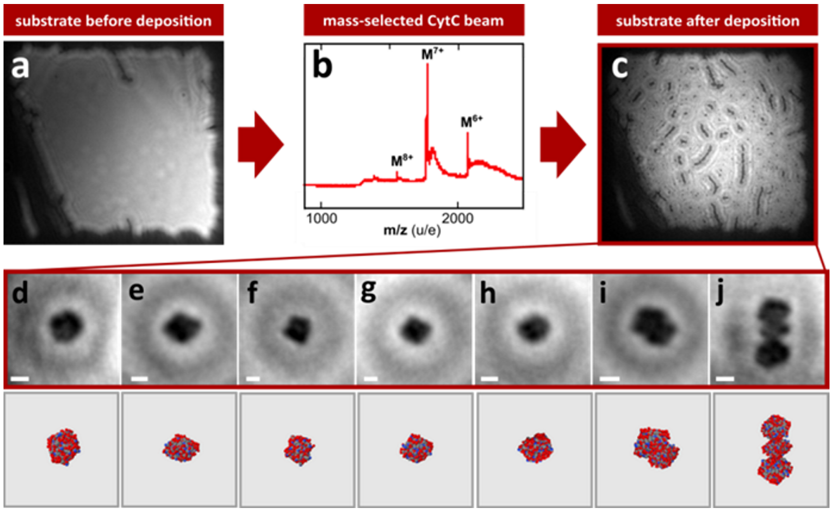

FIG. 15.3 – Complete data set for the imaging of CytC. (a) Low-energy electron image of ultraclean graphene before protein deposition. (b) Mass-spectrum of the mass-selected CytC beam. (c) A survey image of the very same freestanding graphene region after the deposition of CytC. (d) – (j) Low-energy electron micrographs with suggestions for possible protein orientations based on the averaged protein structure derived from X-ray crystallography data and documented in the protein data bank (pdb id: 1HRC). The scale bars correspond to 2 nm.

environment by means of soft-landing electrospray ion beam deposition (ES-IBD).

The workflow for imaging a single protein involves several steps. An ultraclean freestanding graphene sample covering 500×500 nm^2 apertures milled in a 100 nm thick SiN membrane is prepared following the recently developed platinum metal catalysis method and is characterized in the low-energy electron holographic microscope. The sample is subsequently transferred to an ES-IBD system under permanent UHV conditions by means of a UHV suitcase operating in the 10 − 11 mbar regime. Native cytochrome C (CytC), bovine serum albumin (BSA), and hemoglobin (HG) ion beams are generated by electrospray ionization and mass filtering. The charge states $z = 5 - 7$ are selected for CytC and the charge states $z = 15 - 18$ are selected for BSA13. In the case of HG, the charge states $z = 16$ or $z = 17$ of the intact complex are known to be of native conformation and hence the corresponding m/z region is selected. In all three cases, the ions are decelerated to a very low kinetic energy of 2 - 5 eV per charge, which ensures the intact deposition and retention of the native state upon deposition onto the ultraclean freestanding graphene substrate

15.2.2 How to image a single protein

After the deposition of a fraction of a monolayer of proteins, well-separated globular objects of similar size as well as agglomerations thereof, probably due to surface diffusion, are found on the graphene substrate. Control experiments involving the complete transfer process between the two vacuum chambers but without deposition have been performed, demonstrating that this process does not introduce any contamination onto freestanding graphene. At high magnification, the shape of the individual CytC proteins is revealed in several distinct orientations on graphene (Fig. 15.3(d) – 3(j)). It is not surprising to find the protein in different orientations since the deposition process is random in this respect.

The high-magnification low-energy electron micrographs of CytC presented in Fig.15.3 are of sufficiently high resolution to allow comparison with the structural data information obtained from X-ray crystallography investigations and available from the protein data bank. The overall size of the imaged CytC corresponds to the expected dimensions, and the low-energy electron images can clearly be associated with proteins in several distinct orientations. Imaging single objects over an extended period of time never led to any changes in the images. In particular, no sign of decomposition of the protein during electron exposure was observed, which is similar to what was demonstrated previously with DNA.

The same experimental workflow was used in the case of imaging BSA, a much larger protein than CytC (66 kDa versus 12 kD). A collection of low-energy electron micrographs of BSA is presented in Fig.15.4 (top). Similar to CytC, high-contrast images reveal features that suggest a globular structure with the correct dimensions of the protein. In contrast to CytC, which is nearly spherical in shape, the three-dimensional shape of BSA is traditionally described as heart-shaped. The micrographs of individual BSA molecules reflect this structure as well as the protein in other but very characteristic orientations. The agreement between the micrographs and the atomic model for a protein like BSA, not purely globular but exhibiting very pronounced structural features, clearly demonstrates that proteins are found in UHV in structures closely related to their native structure.

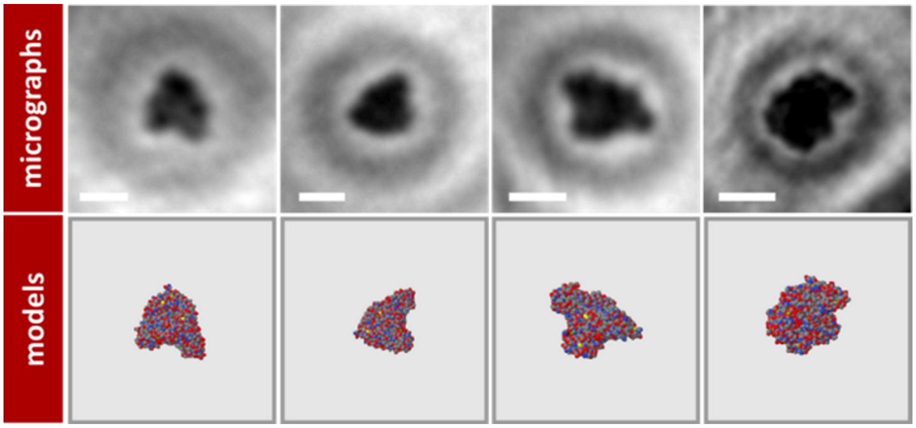

Fig. 15.4 – Low-energy electron micrographs of BSA in different orientations on graphene. Top: low-energy electron micrographs of BSA. Bottom: the atomic model of BSA (pdb id: 3V03) in the corresponding orientations. The scale bars correspond to 5 nm.

In biology, a non-covalently bonded complex of several proteins rather than a single protein is often performing a function. Next to the atomic structure of a protein, the composition and structure of protein complexes are of utmost importance. The data of Fig.15.4 shows that protein agglomerations formed of two and three CytC can be resolved. It has been extensively shown that by means of electrospray ionization, it is possible to ionize entire protein complexes while keeping their native conformations. In Fig.15.5, two micrographs of individual hemoglobin (HG), a complex of four protein subunits, are presented, demonstrating that with our method, entire protein complexes in their native configuration can be deposited and individually imaged. While for the cases of CytC and BSA the agreements between the low-energy electron images and the atomic models are almost perfect, differences can be observed for the case of HG. As mentioned above, HG is a protein complex composed of four sub-units. Therefore, HG has a large conformational flexibility related to its function in a living organism. When an averaging process over millions of molecules is involved in the imaging of a highly flexible protein, distinct conformations cannot be revealed and an average structure is obtained. In contrast, the micrographs of HG presented here are obtained from individual entities and the structural differences between our images and the model confidently demonstrate the benefit of a method for single protein imaging. In Fig.15.5 (top right) structural features of 7 – 8 Å can clearly be identified and may serve as a resolution estimate for this low-energy electron image. A similar resolution is found for all other micrographs. In a hologram, the spacing between consecutive interference fringes gradually decreases towards higher orders. Hence, high-order interference fringes and consequently high-resolution structural details are most susceptible to mechanical vibrations. The latter currently limit the resolution, and intense efforts are ongoing to increase the mechanical stability of the low-energy electron holographic microscope in order to overcome this limitation and approach atomic resolution. While the current resolution already reveals the outer shape of single proteins and protein sub-units, an enhanced resolution of 2 Å will permit the inner structural details to be imaged as well, as hinted by the inner contrast variations apparent in the images above. As three-dimensional information is encoded in a single inline hologram, improved spatial resolution will permit these structural data to also be uncovered. Furthermore, tomographic capability could be added to the experimental setup to reveal the complete three-dimensional structure of a single protein.

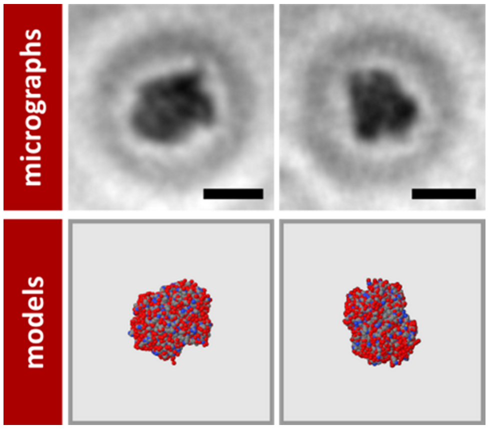

Fig. 15.5 – Low-energy electron micrographs of two individual hemoglobin molecules and the atomic model in the corresponding orientations. Top: two micrographs of hemoglobin soft-landed onto freestanding graphene. Bottom: suggestions for possible orientations based on the averaged protein structure derived from X-ray crystallography data and documented in the protein data bank. The scale bars correspond to 5 nm.

The ultimate goal of directly uncovering the structure of unknown proteins or protein complexes and describing their conformations at the atomic level still requires efforts towards improving the experimental setup and the imaging resolution. It is, however, not limited by fundamental physical constraints. At this stage, the comparison of the low-energy electron micrographs with atomic models available at the protein data bank has the character of a control experiment, proving the feasibility of this novel methodology. Nevertheless, fundamental questions remain. Most crucial is the influence of the environment on the protein's structure as graphene in vacuum represents for proteins a different environment than the aqueous medium of the cell. There is an important body of evidence, especially from ion-mobility/mass-spectrometry investigations, demonstrating that proteins and protein complexes can be transferred from a liquid phase to a vacuum environment while maintaining unperturbed their tertiary and quaternary structures, respectively. The low-energy electron micrographs presented here are further strong evidence that proteins in a folded sate are stable in UHV. Nevertheless, the possibility of adding a protein hydration shell under UHV conditions, as recently demonstrated for a small peptide and the possible induced conformational changes imaged by low-energy electron holography will be pursued in the future. Furthermore, questions related to transport, such as diffusion of proteins and subsequent association into protein complexes, will be addressed. First observations of the diffusion of folded proteins on freestanding graphene by means of low-energy electron holography illustrate that the method described here is also capable of accessing dynamic processes.

To conclude, we have shown here how to image a single protein by combining ES-IBD technology with low-energy electron holography. This has led to the first ever tool for revealing structural details of native single proteins and protein complexes without destroying them. With the recent advances in electrospray ionization and mass spectrometry of large protein complexes, and in particular membrane proteins, even the structure of these biologically important but reluctant to readily crystalize entities may become accessible in the near future.

For a complete list of references concerning our recent achievements in imaging single proteins using low energy electron holography, see:
`http://arxiv.org/abs/1512.08958`.

16 Disordered and Biological Soft Matter

M. Ackermann, C.M. Aegerter, F. Atzeni, P. Dagenais (since September 2015),
D. Dreher, D. Eder, A. Keller, F. Lanfranconi, A. Mallavalli, A. Pataki (Master student),
S. Puri, R. Rüttimann (Master student), L. Schertel (since April 2015), J. Schneider,
L. Selvaggi and S. Urdy

in collaboration with:
Institute of Molecular Life Sciences (K. Basler, T. Aegerter-Wilmsen, L. Pelkmans, D. Brunner), ETH Zürich (P. Koumoutsakos), MPI für Planzenforschung Köln (R.S. Smith), University of Fribourg (A. Jazwinska), University of Bern (C. Kulemeier, S. Robinson, P. Barbier de Reuille), Biozentrum Basel (M. Affolter), University of Konstanz (G. Aubry, G. Maret, T. Sperling), MPI für Selbstorganisation Göttingen (C.C. Maass), Deutsches Luft- und Raumfahrtzentrum (M. Sperl), University of Twente (A. Mosk), Université Joseph Fourier Grenoble (S. Skipetrov), Université Paris Denis Diderot (F. Graner), Technion Haifa (E. Akkermans).

The group of disordered and biological soft-matter, is interested in problems of disordered materials outside of thermal equilibrium, such that instabilities can arise that lead to the emergence of structures. Our specific investigations fall into three overarching themes: The first is concerned with light transport in disordered media, where the wave-nature of light leads to the emergence of a transition in transport, known as Anderson localization, which we have studied in detail. Furthermore we investigate the transport in turbid media with the development of novel imaging techniques. These are also useful in the second class of problems, the regulation of biological development via mechanical forces. The growth of the Drosophila wing and its folds or the regeneraton of fins of the zebrafish are used for this study. Finally, the control of developmental processes by mechanical forces is also studied in the morphogenetic process of dorsal closure in Drosophila embryos. To complement these biological systems, we are also studying purely physical non-equilibrium systems such as granular gases and foams in diamagnetic levitation to obtain overall properties of instabilities in disordered non-equilibrium systems.

In the last year, we have made progress in several of these areas, which are discussed in detail below. These subjects concern Anderson localization, imaging in turbid media, the growth of Drosophila wing imaginal discs as well as the application of minute forces to tissues in the Drosophila embryo via magnetic tweezers.

16.1 Anderson localization of light

When considering wave-transport in extremely disordered samples, where the scattering is strong enough to lead to a mean free path that is of the order of the wave length of light, Anderson predicted more than 50 years ago that a transition to localization of the waves can occur [1]. In spite of the age of this prediction, the experimental realization of an Anderson localization transition in three dimensions [2] still remains elusive and has lead to intense discussions in the research community [3–6]. We have studied this question in recent years in time resolved transmission data that show non-classical behavior, in that the width of the transmission profile shows a saturation [7] and the integrated time-of flight spectra show a sub-exponential tail [8–10], see Fig. 16.1.

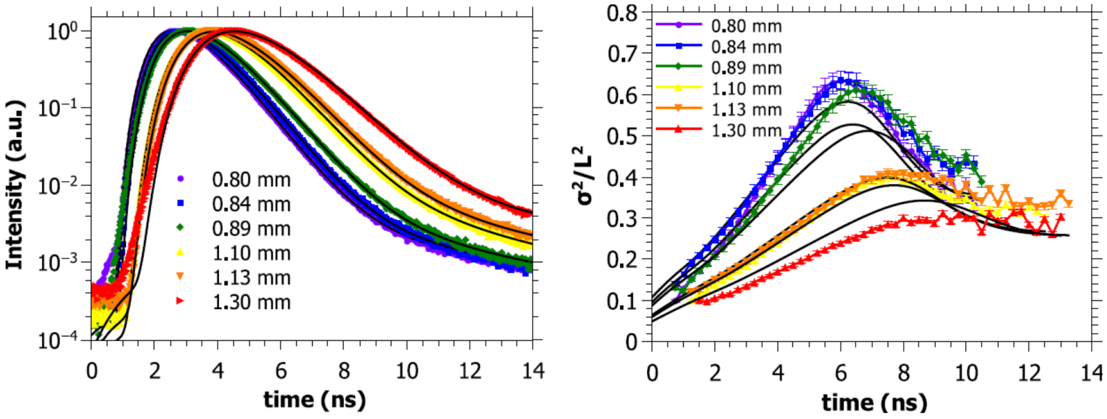

FIG. 16.1 – Time of flight (a) and time dependence of the transmission profile (b) of TiO_2 samples with different thickness showing non-classical diffusion.

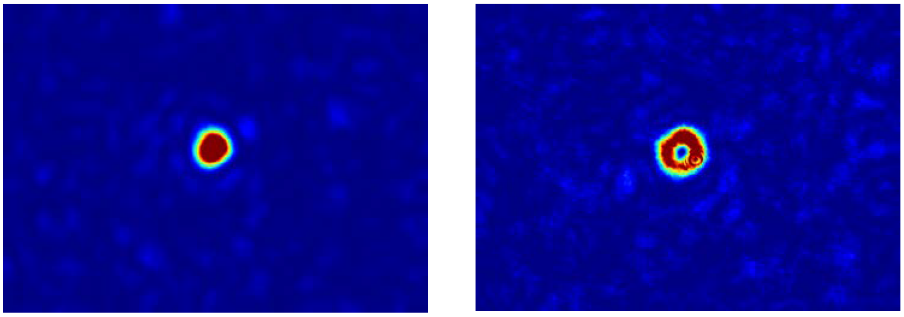

FIG. 16.2 – Wave-front shaping after optimization is used to produce a structured illumination with a wider angular imaging range in Fourier-space reaching up to 36 regularly spaced spots. The procedure allows to increase the spatial resolution of such an image by using several such illuminations akin to structured illumination microscopy.

However, studying samples of decreasing thickness as well as the wave-length dependence of these results has shown that additional processes can be at work, such as fluorescence [11]. With a time resolved spectral measurement and a theoretical model including time delayed fluorescence, we can completely describe the non-classical diffusion in these samples (black curves in Fig. 16.1) without invoking effects of Anderson localization [11].

[1] P.W. Anderson, Phys. Rev. **109**, 5 (1958).

[2] E. Abrahams *et al.*, Phys. Rev. Lett. **42**, 673 (1979).

[3] D.S. Wiersma, P. Bartolini, A. Lagendijk, *et al.*, Nature **390**, 671 (1997).

[4] F. Scheffold, R. Lenke, R. Tweer, *et al.*, Nature **398**, 206 (1999).

[5] F. Scheffold and D. Wiersma, Nature Photonics **7**, 933 (2013).

[6] G. Maret, T. Sperling, W. Bührer, M. Ackermann, A. Lubatsch, R. Frank, and C.M. Aegerter, Nature Photonics **7**, 934 (2013).

[7] T. Sperling, W. Bührer, C.M. Aegerter, and G. Maret, Nature Photonics **7**, 48 (2013).

[8] M. Störzer, P. Gross, C.M. Aegerter and G. Maret, Phys. Rev. Lett. **96**, 063904 (2006).

[9] C.M. Aegerter M. Störzer, and G. Maret, Europhys. Lett. **75**, 562 (2006).

[10] T. Sperling, W. Bührer, M. Ackermann, C.M. Aegerter, and G. Maret, New J. of Phys. **16**, 112001 (2014).

[11] T. Sperling, L. Schertel, M. Ackermann, G. Aubroy, C.M. Aegerter, and G. Maret, New J. of Phys. **18**, 013039 (2016).

16.2 Structured illumination using spatial light modulation

We used the principle of wave-front shaping to image structures behind turbid layers [12–14] to control the sample illumination [15]. The structured illumination is used as a reference sample to resolve structures beyond the wavelength of the light. For this purpose, we for instance change the focus after wave-front shaping to a doughnut shape, see Fig. 16.2.

With such an illumination in addition to the scanning of the focus, an edge enhancement of the structures can be achieved, which leads to a sharper image of the structure of interest [15], as illustrated in Fig. 16.3 for a single fluorescent particle of 500 nm diameter, which has been scanned

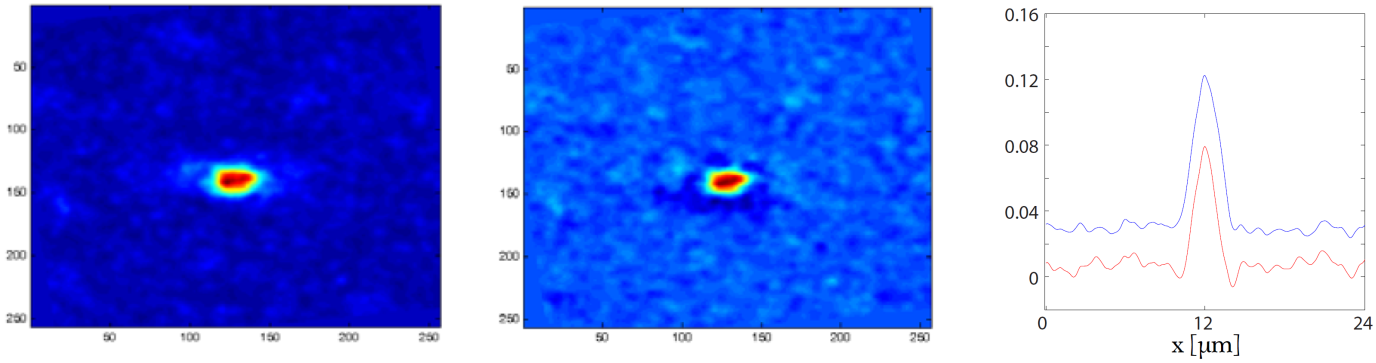

FIG. 16.3 – Using a doughnut-shaped beam to illuminate a fluorescent bead in addition to a focused beam can lead to an increase in sharpness of an image. Left: imaging with a scanning focus, middle: a combination of two images, obtained with a scanning focus as well as a scanning doughnut, right: cross-sections of the two images, red with, blue without scanning doughnut.

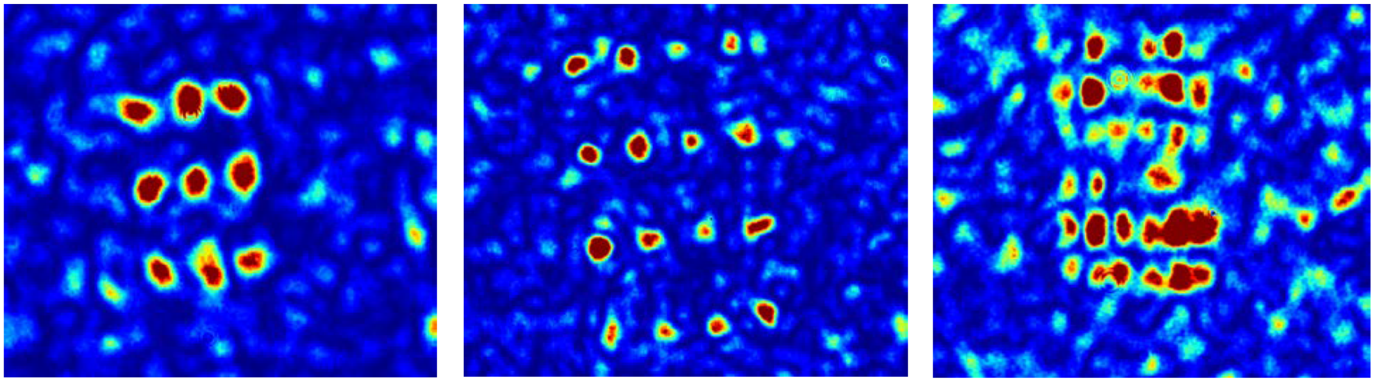

FIG. 16.4 – Wave-front shaping after optimization is used to produce a structured illumination with a wider angular imaging range in Fourier-space reaching up to nine (left), sixteen (middle) and up to 36 (right) regularly spaced spots. This points a way to increase the spatial resolution of such an image akin to structured illumination microscopy.

both with a focused as well as a doughnut-shaped beam. The difference of these two illuminations gives the center image showing a sharper outline of the bead, as indicated by the cross-section shown on the right [15]. We are in the process of extending these techniques of structured illumination for a possible application as a super-resolution microscope without tailored fluorophores or light sources. As has been discussed in [16, 17], such a superposition of incoming light with effectively two different wave vectors can lead to an increase in resolution beyond the Abbe limit in real space by a factor given by the number of wave vectors superposed.

The fact that there is an additional periodicity in the illumination, gives an additional intensity of the light emitted by the fluorophore, i.e. the sample in a shifted region of reciprocal space. The total wave-vector is then enlarged, leading to an increase in resolution in direct space. Another way to see this is that the comparison of a modulated periodic illumination (from the sample) with the unchanged periodic illumination gives a Moiré-pattern from which the modulating structure can be derived directly [16]. For this purpose, we are changing the focus formed by the wave-front shaping through the turbid layer into a range of multiple spots, which can then be used in conjunction with a reference image to increase the range of the image in Fourier space [18]. Examples are shown in Fig. 16.4, where a single spot has been distributed into nine, sixteen or 36 spots. This way it is possible to create a version of structured light illumination microcopy that does not rely on the alignment of several beams, but uses wave-front shaping instead.

[12] I. M. Vellekoop and C.M. Aegerter,
Opt. Lett. **35**, 1245 (2010).

[13] G. Ghielmetti and C.M. Aegerter,
Opt. Express **20**, 3744 (2012).

[14] G. Ghielmetti and C.M. Aegerter,
Opt. Express **22**, 1981 (2014).

[15] G. Ghielmetti, PhD thesis, University of Zurich (2014).

[16] M.G.L. Gustafsson,
Proc Natl Acad Sci U S A. **102**, 13081 (2005).

[17] J.T. Frohn, H.F. Knapp, and A. Stemmer,
Proc Natl Acad Sci U S A. **97**, 7232 (2000).

[18] A. Malavalli, M. Ackermann, C.M. Aegerter,
to be published (2016).

16.3 In-vivo imaging of Drosophila wing disc development

We have used a modification of a confocal microscope in conjunction with index matching of the cuticle to image the development of organs in the Drosophila larvae in order to study the additional information that can be gained using live imaging in turbid situations [19]. Two examples are presented here in more detail. The first example concerns a direct study of the time evolution of cell shapes in the wing disc in order to investigate the connection between cell proliferation and mechanical forces [20]. This has been put forward as a mechanism for the regulation of size in the wing disc [21–24], akin to the regulation of bone structure due to mechanical stresses [25]. Sample images of cell shapes at different time points in development are shown in Fig. 16.5. It can be seen that cells are well resolved and one can not only determine cell area, but also cell deformations and therefore one has a measure of forces acting on the cells at different times [20].

We have found that tension and cell proliferation are correlated during the growth of the wing disc. This has then also been corroborated by direct application of forces to the tissue, while simultaneously determining the proliferation rate.

In the second example, we have studied the positional information within the growing wing disc, see Fig. 16.6, by investigating the position and size of fluorescently labeled clones in the wing disc all through development [19, 26].

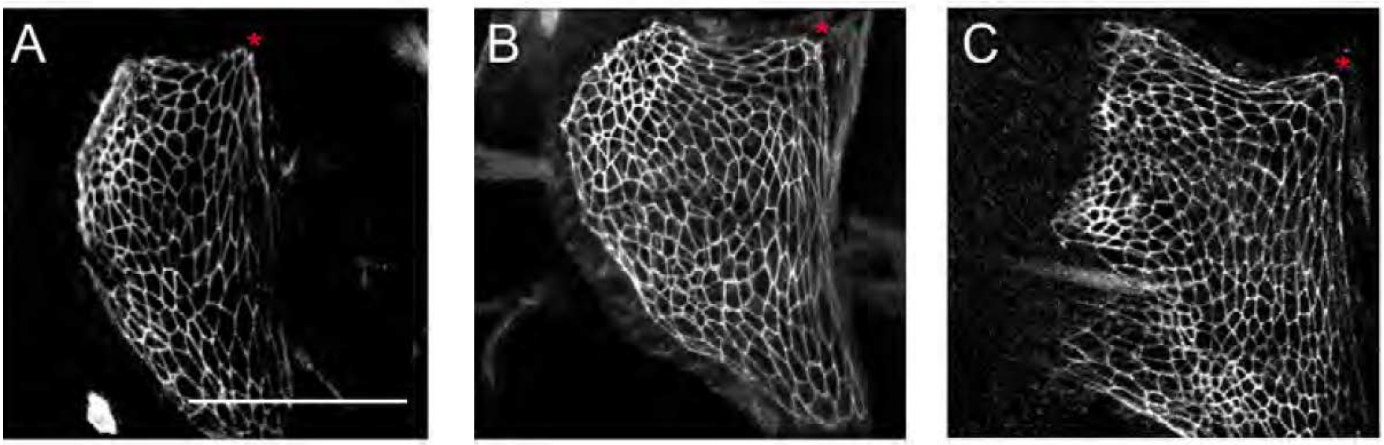

FIG. 16.5 – Fluorescent cell images in a developing wing imaginal disc after the second instar phase, allowing to determine the external forces exerted by a muscle fiber attached at the red asterisk and to study their effect on proliferation of the tissue. The scale bar corresponds to 50 μm.

This yields information on developmental boundaries as well as how differential growth rate lead to the overall shape of the tissue. Fig. 16.6 shows positional paths of several clones in two wing imaginal discs, where the initial position of the clones during the first instar is above (left) and below (right) the wing-notum boundary respectively [26]. To align the images of the different time steps during which the wing disc increases in size more than tenfold the attachment point of the muscle fibre, shown in Fig. 16.5, has been used as a reference point (see Fig. 16.6), since it presents an external point of reference [26].

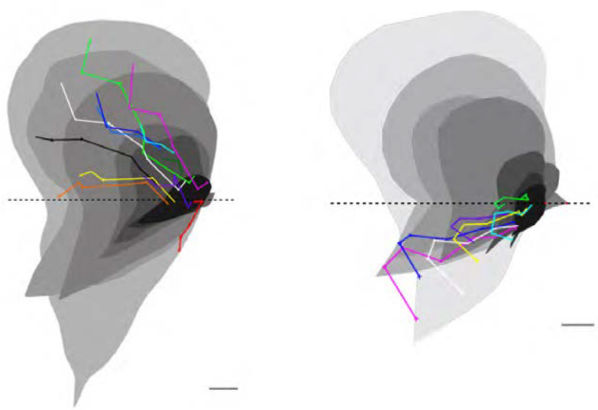

FIG. 16.6 – Time-dependent analysis of growth in two wing imaginal discs from the analysis of initially single cell clones. Using in-vivo imaging inside the Drosophila larva, it was possible to study the growth path of cells in the wing imaginal disc and therefore the shaping of the tissue due to proliferation. Aligning all time points on the attachment of the muscle fibre connecting the wing disc to the haltere, one can see that positions above and below the wing-notum boundary (dashed line) stay separated all through development. The scale bars correspond to 50 μm.

[19] U. Nienhaus, T. Aegerter-Wilmsen, and C.M. Aegerter, PLoS One **7**, e47594 (2012).

[20] T. Schluck, U. Nienhaus, T. Aegerter-Wilmsen, and C.M. Aegerter, PLoS One **8**, e76171 (2013).

[21] T. Aegerter-Wilmsen, C.M. Aegerter, E. Hafen, and K. Basler, Mechanisms of Development **124**, 318 (2007).

[22] L. Hufnagel *et al.*, Proc. Nat. Acad. Sci USA **104**, 3835 (2007).

[23] T. Aegerter-Wilmsen *et al.*, Development **139** 3221 (2012).

[24] U. Nienhaus, T. Aegerter-Wilmsen, and C.M. Aegerter, Mechanisms of Development **126**, 942 (2009).

[25] F.M. Lambers *et al.*, Bone **52**, 587 (2013).

[26] U. Nienhaus, PhD thesis, University of Zurich 2013.

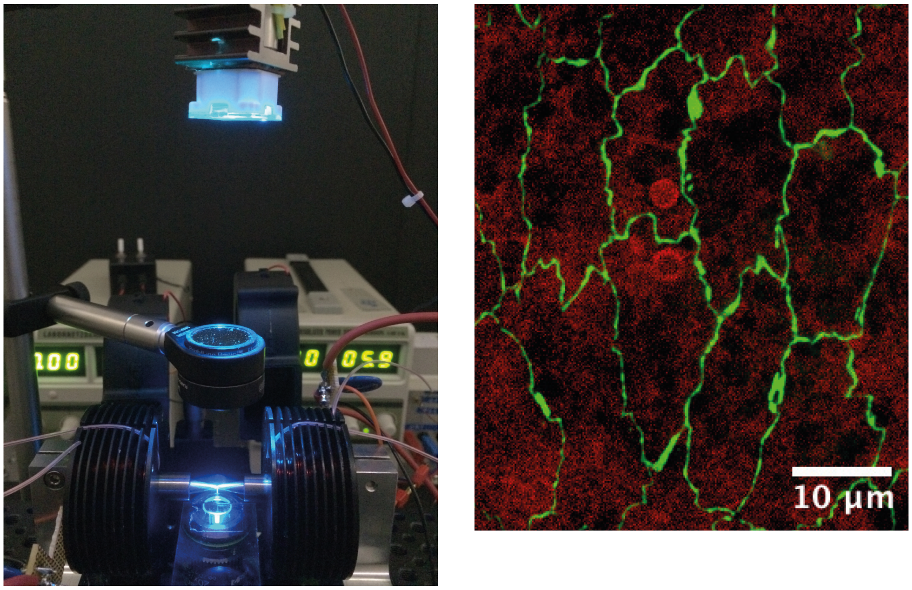

FIG. 16.7 – The magnetic tweezer setup and custom built fluorescence microscope is shown on the left. This magnetic tweezer is used to exert forces in AS tissues during dorsal closure in the embryonal development of Drosophila. As shown on the right, super-paramagnetic beads can be enclosed in AS cells, shown by green fluorescent protein-tagged Armadillo (GFP-Arm), a marker of the apical cell circumference. This will allow the application of forces of 100 pN to individual AS cells during development.

16.4 Magnetic tweezers for influencing tissue development in Drosophila embryos

We also investigate the process of dorsal closure in the Drosophila embryo [27], where mechanical forces lead to a generation of shape in the epidermal tissue of the Drosophila embryo. This happens by closing an opening in the tissue filled with large cells, called Amnioserosa (AS) cells, which during dorsal closure contract strongly, thus closing the opening in the epidermis.

In order to study the forces acting during that process, and to influence at the same time the mechanics of the process, we have built a magnetic tweezer setup [28]that allows to apply forces on individual super-paramagnetic beads of up to 200 pN. It was calibrated by determining the displacement speeds in a fluid of known viscosity. Using direct feedback in the application of the current to the magnetic tweezer, compressional as well as tension forces can be applied [29].

To allow to apply forces to AS cells during dorsal closure, the super-paramagnetic beads have to be inserted into these cells, which is possible to achieve using microinjection during early embryonic development as shown in Fig. 16.7. Here, the beads are seen inside the AS cells which are marked fluorescently.

[27] J. Solon, A. Kaya-Copur, J. Colombelli, and D. Brunner, Cell **137**, 1331-42 (2009).

[28] M. Tanasa, N. Biais, and M. Sheetz, Methods Cell Biol. **83**, 473-93 (2007).

[29] P.Kollmannsberger, B. Fabry, Rev. Sci. Inst. **78**, 114301 (2007).

17 Mechanical Workshop

C. Albrecht, K. Bösiger, B. Lussi, R. Maier, M. Schaffner and S. Scherr
Apprentices: D. Gabrielli, G. Knüsel, B. Markwalder and P. Weyeneth

Last year we again encountered a variety of challenges, which were all mastered with flying colours! While three major projects were in the pipeline, our building infrastructure was enlarged by several new installations. A new laser-cutting machine (Kern Laser Systems) in the welding shop required a new exhaust fan too. In the dust-free zone of our workshop both heat control and ventilation have been upgraded. Last but not least the frequently used entrance door to our material storage area was replaced after having served for quite some years.

To foster the exchange with many of our internal and external customers from UZH, ETHZ, Universities of Applied Sciences and local High Schools we organized our annual aperitif in autumn.

A fine table lathe by the Swiss tradition company Schaublin expands our broad repertoire of machines and technologies. Its high working precision in combination with an increased revolution frequency allows us to achieve still better results when working with small parts. The new laser machine was finally delivered in August 2015. This thoroughly planned acquisition allows us to produce a great variety of different laser cutting designs, including specialized engravings, utilizing a broad range of metals.

- The new fine table lathe

In June we welcomed Chris Albrecht as our new co-worker. Meanwhile Chris is well incorporated and an important support. On the first of August 2015, Gian Knüsel joined us as new apprentice.

Our annual workshop courses for bachelor students, which took place in August/September 2015 and January/February 2016 were received with great enthusiasm. During the autumn months ETHZ apprentices trained their welding skills in our workshop.

In the following we high-light some internal and external projects to which we made major contributions:

- Astroparticle Physics (Sec. 4)
  In 2015 we focused our efforts on constructing and producing parts for the XENON experiment. 85 copper ring electrodes, used in the field forming structure of the time projection chamber, were welded together. These rings are made of high-purity copper for highest precision for the voltage divider. Besides many single parts, a transport unit was produced for the Teflon pieces.

- Copper rings for the XENON experiment

- CTA Cherenkov Telescope Array (Sec. 6)
  The prototype camera was put together and shipped to DESY Zeuthen in Berlin. The work for two additional cameras has already started. Custom-designed racks with integrated cooling unit and parts of the insulation shield are currently being produced. Other parts such as spindles and nuts for the active mirror control were already produced successfully.

- Physics on the nanometer scale (Sec. 15)
  In this project the main goal was the production of the scanning tunnelling microscope as well as its very core, the sample preparation stage. Within the linear transfer section the probes can be purified and prepared in an Argon atmosphere.

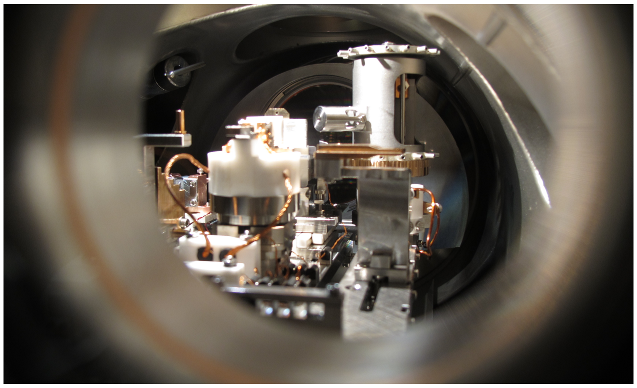

- Sample preparation stage

- Phase transitions, materials and applications (Sec. 13)
  A complete probe stick (Dipstick Desy) and a complete series of pucks were produced in the past few months for this project. Pucks represent a connection part between the cryostat and the probe stick.

- Surface Physics (Sec. 14)
  After having extended several on-going projects a major new project was the installation of the so-called wolf chamber and the reflector-vaporizer. In the latter alkali metals are vaporized onto a graphene surface. In addition to these tasks we completed another production series made from the not easily editable material molybdenum.

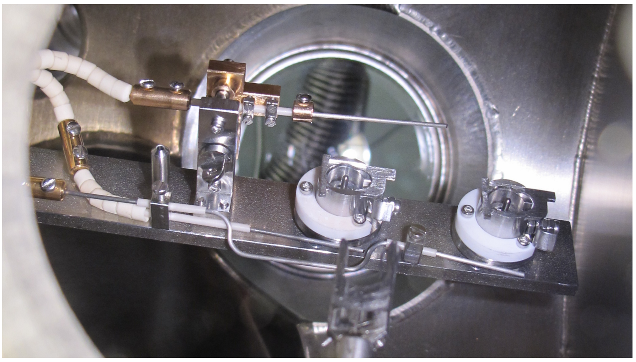

- Reflector vaporizer

- CMS Barrel Pixel detector upgrade (Sec. 11)
  Several milling- and rotating pieces were made for the production of the supply tube we. In addition we had to establish several soldering and gluing gauges. Airex had to be tempered and preformed in an oven prior to the production of the supply tube.

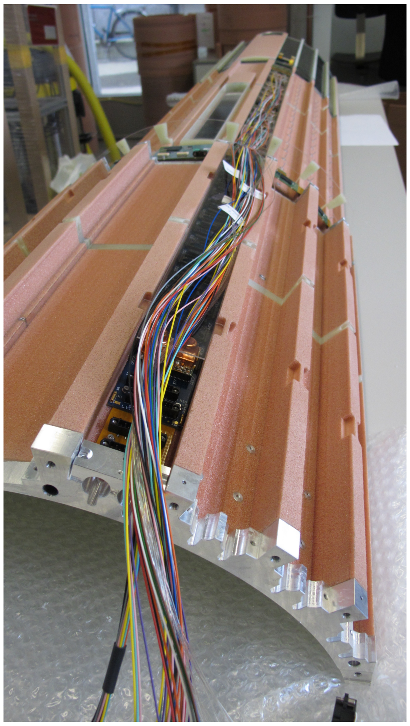

- CMS supply tube

- Disordered and Biological Soft Matter (Sec. 16)
  A complete fish-stage was prepared. A microscope was rebuilt and different work-pieces for laboratory use were manufactured.

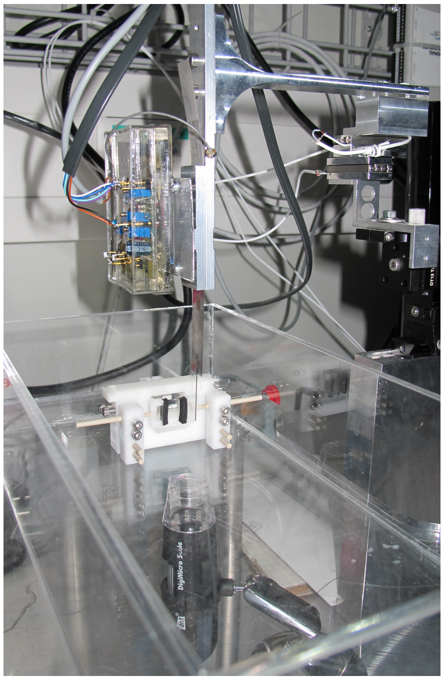

- Fish stage

- Demonstration experiments for the lectures

  In order to guarantee excellent demonstration experiments for the student lectures we designed and produced some new devices and revised and maintained several older parts.

- External orders and activity duties

  Thanks to our highly motivated and competent workshop team our workshop is well known outside the Physics Institute and we again received orders from external institutions and private companies.

  We created CAD constructions and prototypes and performed complete assemblies for about 25 institutes of the University of Zurich. The tasks were manifold, ranging from the construction of simple plastic parts to engraved metal parts further to complex 5-axis milling workpieces. Very popular were also welding works, technical consulting in the choice of materials and in the design as well as bonding services.

  Private companies that appreciate our technical expertise, are active in engineering and in lighting technology. For the latter we constructed complete lamps whereas milling, turning, welding and laser work was performed for the engineering companies.

18 Electronics Workshop

D. Florin, A. Vollhardt and D. Wolf

Besides maintenance work for the existing laboratory infrastructure and small-scale prototype designs, the electronics workshop contributed to the following projects.

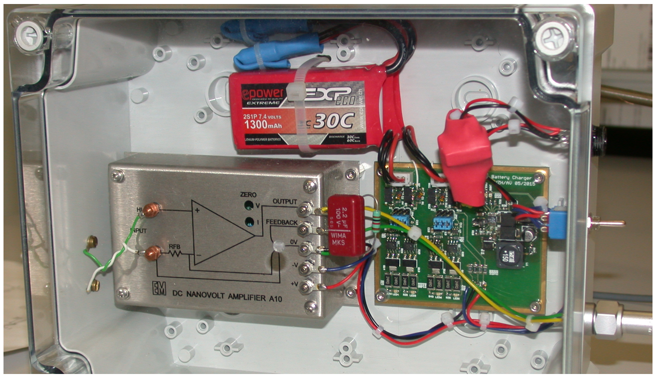

- Battery power supply for nanovolt amplifier

For the group of Prof. Chang, a low-noise floating power supply was designed and built. Featuring state-of-the-art Lithium-polymer accumulators, the design has a significantly reduced mass and size compared to conventional solutions based on lead-acid batteries.

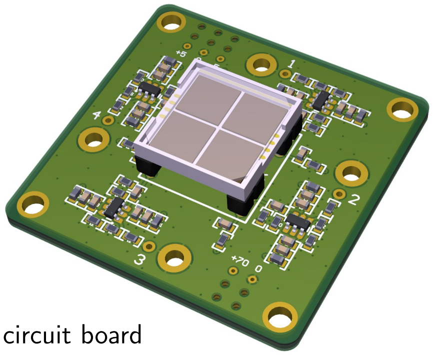

- MPPC preamplifier circuit board

The readout of a multi-pixel photon counter (MPPC) required a dedicated four-channel preamplifier (group of Prof. Baudis) which was designed and assembled in the workshop. Key features of this amplifier are its compactness and low power consumption while preserving the fast rise time of the original detector signal.

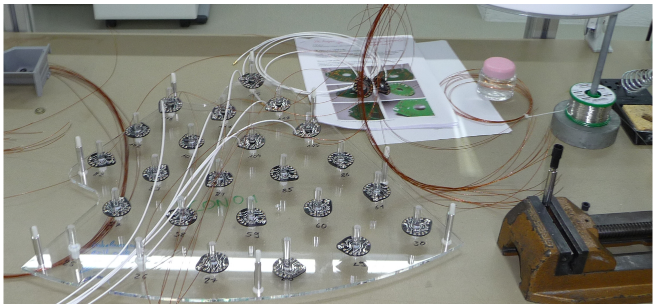

- Production of PMT bases

Another project for this group involved the organization of the mass production of photomultiplier base circuit boards and their cabling.

- RF generator for UHV plasma

The UHV chamber of the group of Prof. Greber required a new RF generator for creating a plasma for cleaning purposes. The electronics workshop took care of design and construction of the 13.56 MHz signal exciter and purchasing/commissioning of the required RF power amplifiers and impedance matching units. Special attention was paid to the long duration of the required plasma generation (8-10 hours) where the power amplifier is required to run unattended with internal safeguards to prevent damage to either the UHV chamber or the amplifier itself.

For a new advanced labcourse experiment (μSR: muon spin resonance), an interface was designed which allows measuring the magnetic flux density and temperature inside the main coil with standard digital multimeters.

- Monitoring interface for μSR magnets

Several high-intensity light sources based on modern LED modules have been built for the group of Prof. Aegerter. These include pulsed light sources for the green and blue part of the color spectrum and an infrared device for sample illumination.

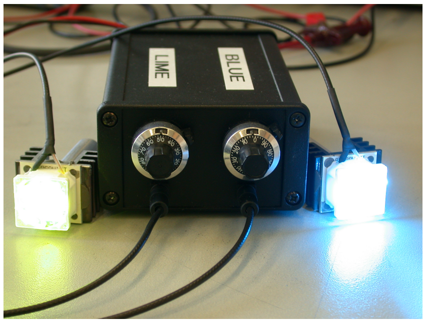

- High power LEDs including electronic pulse generator

- High power IR LED

For the CTA FlashCam project, testing and optimizing of the safety system has been ongoing, both for the prototype camera and for a second setup which is located at the institute. In parallel to the documentation work parts for safety/power cabinets for two more FlashCam cameras have been purchased and their assembly has started. Measuring the precise phase noise of an oscillator allows to evaluate their contribution to the overall noise of any data acquisition system which is of particular importance for FlashCam. For evaluation of the quality of the clock and timing distribution network a phase noise measurement system was developed and commissioned.

- David Wolf assembling power cabinets including safety devices for CTA

- Phase noise measurement unit

In preparation for the International Physics Olympiad 2016, various prototypes have been assembled and tested. The workshop is also participating in the series production of the experimental setups for the candidates.

The electronics workshop was granted an electronics apprenticeship position starting in August 2016. In parallel to the selection of a candidate for this position, the workshop is in the process of preparing the lab space and the educational program for the apprentice.

19 Publications

19.1 Elementary particles and their interactions

19.1.1 Theory of Elementary particles

Articles

- Analytic form of the two-loop planar five-gluon all-plus-helicity amplitude in QCD
  T. Gehrmann, J. M. Henn, and N. A. Lo Presti, Phys. Rev. Lett. **116** (2016) no.6, 062001
  Erratum: [Phys. Rev. Lett. **116** (2016) no.18, 189903].

- Pseudo-scalar Form Factors at Three Loops in QCD
  T. Ahmed, T. Gehrmann, P. Mathews, N. Rana, and V. Ravindran, JHEP **1511** (2015) 169.

- The rare decay $H \to Z\gamma$ in perturbative QCD
  T. Gehrmann, S. Guns, and D. Kara, JHEP **1509** (2015) 038.

- Generalized threshold resummation in inclusive DIS and semi-inclusive electron-positron annihilation
  A. A. Almasy, N. A. Lo Presti and A. Vogt, JHEP **1601** (2016) 028.

- Spectral density constraints in quantum field theory
  P. Lowdon, Phys. Rev. D **92** (2015) no.4, 045023.

- Renormalization scheme dependence of the two-loop QCD corrections to the neutral Higgs-boson masses in the MSSM
  S. Borowka, T. Hahn, S. Heinemeyer, G. Heinrich and W. Hollik, Eur. Phys. J. C **75** (2015) no.9, 424.

- Calculation of multi-scale, multi-loop integrals using SecDec 3
  S. Borowka, Acta Phys. Polon. B **46** (2015) no.11, 2137.

- Interference contributions to gluon initiated heavy Higgs production in the Two-Higgs-Doublet Model
  N. Greiner, S. Liebler and G. Weiglein, Eur. Phys. J. C **76** (2016) no.3, 118.

- The q_T subtraction method for top quark production at hadron colliders
  R. Bonciani, S. Catani, M. Grazzini, H. Sargsyan and A. Torre, Eur. Phys. J. C **75** (2015) no.12, 581.

- Vector boson production at hadron colliders: transverse-momentum resummation and leptonic decay
  S. Catani, D. de Florian, G. Ferrera and M. Grazzini, JHEP **1512** (2015) 047.

- ZZ production at the LHC: fiducial cross sections and distributions in NNLO QCD
  M. Grazzini, S. Kallweit and D. Rathlev, Phys. Lett. B **750** (2015) 407.

- Transverse-momentum resummation for vector-boson pair production at NNLL+NNLO
  M. Grazzini, S. Kallweit, D. Rathlev and M. Wiesemann,JHEP **1508** (2015) 154.

- Wγ and Zγ production at the LHC in NNLO QCD,
  M. Grazzini, S. Kallweit and D. Rathlev, JHEP **1507** (2015) 085.

- Resummation ambiguities in the Higgs transverse-momentum spectrum in the Standard Model and beyond
  E. Bagnaschi, R. V. Harlander, H. Mantler, A. Vicini and M. Wiesemann, JHEP **1601** (2016) 090.

- Heavy charged Higgs boson production at the LHC
  C. Degrande, M. Ubiali, M. Wiesemann and M. Zaro, JHEP **1510** (2015) 145.

- Hadronic Higgs production through NLO + PS in the SM, the 2HDM and the MSSM
  H. Mantler and M. Wiesemann, Eur. Phys. J. C **75** (2015) no.6, 257.

- Pseudo-observables in electroweak Higgs production
  A. Greljo, G. Isidori, J. M. Lindert and D. Marzocca, Eur. Phys. J. C **76** (2016) no.3, 158.

- Anomalies in B-decays and $U(2)$ flavour symmetry
  R. Barbieri, G. Isidori, A. Pattori and F. Senia, Eur. Phys. J. C **76** (2016) no.2, 67.

- Stability of the electroweak ground state in the Standard Model and its extensions
  L. Di Luzio, G. Isidori and G. Ridolfi, Phys. Lett. B **753** (2016) 150.

- Supersymmetric Dark Matter after LHC Run 1
  E. A. Bagnaschi *et al.*, Eur. Phys. J. C **75** (2015) 500.

- Probing the Charm Quark Yukawa Coupling in Higgs+Charm Production
  I. Brivio, F. Goertz and G. Isidori, Phys. Rev. Lett. **115** (2015) no.21, 211801.

- Higgs Pseudo Observables and Radiative Corrections
  M. Bordone, A. Greljo, G. Isidori, D. Marzocca and A. Pattori, Eur. Phys. J. C **75** (2015) no.8, 385.

- On the breaking of Lepton Flavor Universality in B decays
  A. Greljo, G. Isidori and D. Marzocca, JHEP **1507** (2015) 142.

- Electroweak bounds on Higgs pseudo-observables and $h \to 4\ell$ decays
  M. Gonzalez-Alonso, A. Greljo, G. Isidori and D. Marzocca, Eur. Phys. J. C **75** (2015) 341.

- Knocking on new physics' door with a scalar resonance
  D. Buttazzo, A. Greljo and D. Marzocca, Eur. Phys. J. C **76** (2016) no.3, 116.

- Global constraints on anomalous triple gauge couplings in effective field theory approach
  A. Falkowski, M. Gonzalez-Alonso, A. Greljo and D. Marzocca, Phys. Rev. Lett. **116** (2016) no.1, 011801.

- Dark Matter and Gauged Flavor Symmetries
  F. Bishara, A. Greljo, J. F. Kamenik, E. Stamou and J. Zupan, JHEP **1512** (2015) 130.

- Associated production of a top pair and a Higgs boson beyond NLO
  A. Broggio, A. Ferroglia, B. D. Pecjak, A. Signer and L. L. Yang JHEP **1603** (2016) 124.

- NLO QCD+EW predictions for V + jets including off-shell vector-boson decays and multijet merging
  S. Kallweit, J. M. Lindert, P. Maierhofer, S. Pozzorini and M. Schönherr, JHEP **1604** (2016) 021.

- Measuring the signal strength in $t\bar{t}H$ with $Hb\bar{b}$
  N. Moretti, P. Petrov, S. Pozzorini and M. Spannowsky, Phys. Rev. D **93** (2016) no.1, 014019.

- Phenomenological analysis of Higgs boson production through gluon fusion in association with jets
  N. Greiner, S. Höche, G. Luisoni, M. Schönherr, J. C. Winter and V. Yundin, JHEP **1601** (2016) 169.

- Electroweak corrections to squark-antisquark production at the LHC
  W. Hollik, J. M. Lindert, E. Mirabella and D. Pagani, JHEP **1508** (2015) 099.

Oral Presentations

- S. Borowka: Renormalization scheme dependences in Higgs mass calculations
  KUTS working group meeting, LPTHE Paris (FR), May 2015.

- S. Borowka: Renormalization scheme dependence and O(eps) terms in MSSM Higgs-boson mass predictions
  Radcor-Loopfest 2015 Conference, UCLA (US), June 2015.

- S. Borowka: Numerical evaluation of multi-scale integrals with SecDec 3
  Amplitudes 2015 International Conference, Zurich (CH), July 2015.

- S. Borowka: Calculation of multi-scale, multi-loop integrals with SecDec 3
  Matter To The Deepest International Conference, Ustron (PL), September 2015.

- T. Gehrmann: Two loop corrections to vector boson pair production
  Higgstools meeting, Freiburg, 15. 04. 2015.

- T. Gehrmann: Forming higher orders QCD
  JosFest Meeting, NIKHEF, Amsterdam, 03. 07. 2015.

- T. Gehrmann: Conference Summary
  QCD@LHC 2015, London, 05. 09. 2015.

- T. Gehrmann: Lectures on QCD calculations
  Atrani doctoral school "Methods for precision calculations", Atrani, Italy, 5-9. 10. 2015.

- T. Gehrmann: Precision Physics with jet observables
  Kolloquium Wuerzburg, 12. 11. 2015.

- M. Grazzini: Recent developments in inclusive and differential Higgs cross sections
  Higgstools Meeting, Freiburg, 14. 04. 2015.

- M. Grazzini: Precise SM predictions for the LHC
  CHIPP plenary meeting, Chateau de Bossey, 29. 06. 2015.

- M. Grazzini: Higgs theory
  Les Houches Workshop "Physics at TeV colliders", Les Houches, 02. 06. 2015.

- M. Grazzini: Standard Model Theory for Collider Physics
  EPS Vienna, Austria, 27. 07. 2015.

- M. Grazzini: Vector boson pair production at NNLO
  QCD@LHC, London, 03. 09. 2015.

- M. Grazzini: Lectures on QCD resummation
  Atrani doctoral school, "Methods for precision calculations", Atrani, Italy, 5-9. 10. 2015.

- M. Grazzini: Transverse-momentum resummation for heavy-quark production at hadron colliders
  REF2015 Workshop, DESY, 03. 11. 2015.

- N. Greiner: Higgs production in gluon fusion in association with jets
  QCD@LHC Queen Mary University, London 1-5. 09. 2015.

- N. Greiner: LHC physics with GoSam 2.0
  Desy theory workshop, Hamburg, 29. 9.-2. 10. 2015.

- N. Greiner: BSM physics with GoSam
  Non-conventional searches at the LHC, , Daejeon, Korea, 14.-18. 12. 2015

- A. Greljo: Pseudo-observables in Higgs decays
  Portoroz 2015: Particle Phenomenology From Early Universe to High Energy Colliders, Slovenia, 08. 04. 2015.

- A. Greljo: Precision Higgs beyond the SM
  Flavour 2015: New Physics at High Energy and High Precision, MIAPP, Munich, 01. 06. 2015.

- A. Greljo: Going beyond the "kappa-framework": Higgs Pseudo-observables
  The 27th International Symposium on Lepton Photon Interactions at High Energies, Ljubljana, 21. 08. 2015.

- A. Greljo: Going beyond the "kappa-framework": Higgs Pseudo-observables
  Seminaire de Physique des Particules du LPT, LPT Orsay, 29. 10. 2015.

- A. Ilnicka: Effects of higher dimension operators on Higgs cross sections
  First HiggsTools Annual Meeting, Freiburg, 17. 05. 2015.

- A. Ilnicka: Effects of higher dimensional operators on the Higgs p_T spectrum
  Higgs Hunting, Orsay, 31. 07. 2015.

- A. Ilnicka: Effects of Beyond Standard Model physics on Higgs p_T spectra in Effective Field Theory approach
  European Physical Society Conference on High Energy Physics, Wien, 2. 07. 2015.

- G. Isidori: Higgs Pseudo-observables
  Higgs Days workshop, Santander, Spain, 14-18. 09. 2015.

- G. Isidori: Rare Higgs decays
  HL-LHC workshop, CERN 11-13. 05. 2015.

- G. Isidori: On the breaking of LFU in B decays
  LHCb implication workshop CERN, 3-5. 11. 2015.

- G. Isidori: Theoretical considerations on low-energy physics
  CHIPP plenary meeting, Chateau de Bossey, 30. 06. 2015.

- C. L. Javier: The resummed Higgs p_t spectrum
  Higgs couplings 2015, Lumley Castle, 12-15. 10. 2015.

- D. Kara: The rare decay $H \to Z\gamma$ in perturbative QCD
  Radcor-Loopfest 2015, UCLA, USA, 15. 06. 2015.

- J. Lindert: Automated NLO QCD+EW simulations with OpenLoops and predictions for V+multijet production
  Invited Seminar, University of Mainz, Mainz, Germany, 28. 04. 2015.

- J. Lindert: Automated NLO QCD+EW simulations with OpenLoops and predictions for V+multijet production
  Invited Seminar, University of Freiburg, Freiburg, Germany, 19. 5. 2015.

- J. Lindert: Automated NLO QCD+EW corrections with OpenLoops for W + Multijet production at the LHC
  Radcor-Loopfest 2015, UCLA, LA, USA, 16. 06. 2015.

- J. Lindert: Automated NLO QCD+EW simulations with OpenLoops and predictions for V+multijet production
  Invited Seminar, University of Dresden, Dresden, Germany, 02. 07. 2015.

- J. Lindert: Automated NLO QCD+EW corrections for V+multijet production
  QCD@LHC 2015, Queen Mary University of London, London, UK, 04. 09. 2015.

- J. Lindert: Automated NLO QCD+EW corrections for the LHC
  DESY Theory Workshop, DESY, Hamburg, Germany, 30. 09. 2015.

- J. Lindert: NLO QCD+EW predictions for W+jets at 100 TeV
  QCD, EW and tools at 100 TeV, CERN, Switzerland, 08. 10. 2015.

- J. Lindert: Electroweak corrections to squark and gluino production at the LHC
  Annual Meeting of the Helmholtz Alliance "Physics at the Terascale", DESY, Hamburg, Germany, 18. 12. 2015.

- J. Lindert: Automated NLO QCD+EW corrections for the LHC and precise predictions for V+multijet production
  Invited Seminar, University of Bonn, Bonn, Germany, 07. 12. 2015.

- J. Lindert: Precise predictions for V+multijet production including electroweak corrections
  Invited Seminar, Université catholique de Louvain, Louvain-la-Neuve, Belgium, 16. 12. 2015.

- J. Lindert: Applications of NLO EW corrections
  Sherpa user annual meeting, Dresden, Germany, 07. 01. 2016.

- N. A. Lo Presti: Five-point two-loop Master Integrals in QCD
  QCD@LHC 2015, Queen Mary, University of London, United Kingdom, 01. 09. 2015.

- N. A. Lo Presti: Threshold resummation from the D-dimensional structure of partonic cross sections
  Workshop "Threshold logarithms beyond leading power", Higgs Centre for Theoretical Physics, University of Edinburgh, United Kindgom, 29. 02. 2016.

- P. Lowdon: Boundary terms in the decomposition of nucleon spin
  XXIII international workshop on Deep Inelastic Scattering, Dallas, 28. 04. 2015.

- D. Marzocca: Higgs to 4-fermion decays
  9th Workshop of the LHC Higgs Cross Section Working group, CERN, Switzerland, 23. 01. 2015.

- D. Marzocca: Higgs pseudo-observables
  Invited Seminar, DAMPT, Cambridge, 15. 05. 2015.

- D. Marzocca: Pseudo-observables in Higgs decays
  DIS 2015, Dallas, Texas, USA, 28. 05. 2015.

- D. Marzocca: Violation of lepton-flavor universality in B decays
  Invited Seminar, Montpellier, 11. 06. 2015.

- D. Marzocca: Pseudo-observables in Higgs decays
  27th Rencontres de Blois 2015, Blois, France, 30. 06. 2015.

- D. Marzocca: PO from continuous deformations
  10th Workshop of the LHC Higgs Cross Section Working group, CERN, Switzerland, 15. 07. 2015.

- D. Marzocca: Higgs physics with heavy new physics
  LHCP 2015, St. Petersburg, Russia, 31 August 2015.

- D. Marzocca: Higgs PO, production and decay beyond the kappa framework
  Particle Theory Seminar, UZH, 13. 10. 2015.

- N. Moretti: ttH searches in the $H \to bb$ channel: precision theory simulation
  Sinergia meeting, Lausanne, 17. 12. 2015.

- S. Pozzorini: Precise electroweak predictions for V+multijet production
  Standard Model at LHC, Florence, 23. 4. 2015.

- S. Pozzorini: Scattering Amplitudes and (N)NLO Simulations with OpenLoops
  Theory Seminar, LPTHE, Paris VI University, 4. 5. 2015.

- S. Pozzorini: Scattering Amplitudes and (N)NLO Simulations with OpenLoops
  Theory Seminar, Universita degli Studi, Milano, 21. 5. 2015.

- S. Pozzorini: Electroweak Theory at the LHC
  Large Hadron Collider Physics Conference, St.Petersburgh, 2. 9. 2015.

- S. Pozzorini: Monte Carlo for ttH and Standard Model Background
  Higgs Couplings 2015, Lumley Castle, 13. 10. 2015.

- S. Pozzorini: Scattering Amplitudes and Precision Simulations for the LHC
  Theory Colloquium, DESY Hamburg, 2. 12. 2015.

- S. Pozzorini: Scattering Amplitudes and Precision Simulations for the LHC
  Particle Physics Seminar, Vienna University, Austria, 26. 1. 2016.

- S. Pozzorini: ttH/tH working group: status of YR4 preparation and future activities
  Workshop of LHC Higgs Cross Section Working Group, CERN, Geneva, Switzerland, 14. 1. 2016.

- S. Pozzorini: Precision Theory Simulations for the LHC
  Meeting of the German Physical Society, DESY, Hamburg, Germany, 4. 3. 2016.

- S. Pozzorini: Recent Theoretical Progress in QCD and EW Corrections
  Rencontres de Physique de la Vallée d'Aoste, La Thuile, Italy, 9. 3. 2016.

- D. Rathlev: Theory review on diboson production
  SM@LHC, Florence; 22. 04. 2015.

- D. Rathlev: NNLO QCD predictions for WW and ZZ production
  Radcor-Loopfest 2015, Los Angeles, 18. 06. 2015.

- D. Rathlev: QCD corrections to $pp \to VV$ at NNLO
  MBI, DESY, Hamburg; 03. 09. 2015.

- D. Rathlev: Vector pair cross sections at 100 TeV
  FCC workshop, CERN, Geneva; 07. 10. 2015.

- H. Sargsyan: Higgs p_T in the Standard Model
  HXSWG meeting, CERN, 07. 05. 2015.

- A. Signer: What is m_t?
  Workshop on the Top mass, Frascati, 6-8. 05. 2015.

- A. Signer: Low-energy LFV and Precision Physics
  Flavour 2015, Munich 1-3. 06. 2015.

- A. Signer: Ein Blick in die innersten Eigenschaften der Materie
  Naturwissenschaftliche Gesellschaft, Sankt Gallen 07. 10. 2015.

- A. Visconti : Regularization scheme dependence of two-loop amplitudes
  Seminar, Max-Planck-Instituts, Munich, 27. 05. 2015.

- M. Wiesemann: aMCSusHi: combining MG5 aMC@NLO with SusHi
  ERC miniworkshop, CERN, 01. 06. 2015.

- M. Wiesemann: Transverse momentum resummation of colorless final states at the NNLO+NNLL
  Radcor-Loopfest 2015, Los Angeles, 15. 06. 2015.

- M. Wiesemann: bbH : Theory report
  10th Workshop of the LHC Higgs Cross Section Working Group, CERN, 10. 07. 2015.

- M. Wiesemann: Automation of transverse momentum resummation at NNLO+NNLL and its application to ZZ and WW pairs
  Theorie-Palaver Seminar (Mainz), 21. 07. 2015.

- M. Wiesemann: Higgs (and top) physics from the theory perspective
  Matter to the Deepest: XXXIX International Conference of Theoretical Physics, Ustron, 14. 09. 2015.

- M. Wiesemann: BSM effects on the resummed transverse momentum spectrum of the Higgs in the EFT approach
  Sinergia Meeting, Lausanne, 17. 12. 2015.

- M. Wiesemann: bbH: Status report for YR4
  11th Workshop of the LHC Higgs Cross Section Working Group, CERN, 13. 01. 2016.

- M. Zoller: Stability of the Standard Model ground state: a precision analysis
  International School of Subnuclear Physics (ISSP), Erice, 28. 06. 2015.

19.1.2 Astrophysics and General Relativity

Articles

- The remains of a spinning, hyperbolic encounter
  L. De Vittori, A. Gopakumar, A. Gupta and Ph. Jetzer,
  Proceedings of the LISA Symposium X (Gainesville, May 18-23, 2014), J. Phys. Conf. Ser. 610 (2015) 1, 012048.

- A Time Domain Waveform for Testing General Relativity
  C. Huwyler, Ed. Porter and Ph. Jetzer,
  Proceedings of the LISA Symposium X (Gainesville, May 18-23, 2014), J. Phys. Conf. Ser. 610 (2015) 1, 012046.

- Testing General Relativity and Alternative Theories of Gravity with Space-based Atomic Clocks and Atom Interferometers
  R. Bondarescu, A. Schärer, Ph. Jetzer, R. Angélil, P. Saha and A. Lundgren,
  in the Proceeding for ICNFP 2014, EPJ Web Conf. **95** (2015), 02002.

- Free-flight experiments in LISA Pathfinder
  (The LISA Pathfinder Collaboration) M. Armano, H. Audley, G. Auger, J. Baird, P. Binetruy, M. Born, D. Bortoluzzi, N. Brandt, A. Bursi, M. Caleno, A. Cavalleri, A. Cesarini, M. Cruise, C. Cutler, K. Danzmann, I. Diepholz, R. Dolesi, N. Dunbar, L. Ferraioli, V. Ferroni, E. Fitzsimons, M. Freschi, J. Gallegos, C. Garcia Marirrodriga, R. Gerndt, LI. Gesa, F. Gibert, D. Giardini, R. Giusteri, C. Grimani, I. Harrison, G. Heinzel, M. Hewitson, D. Hollington, M. Hueller, J. Huesler, H. Inchauspé, O. Jennrich, P. Jetzer, B. Johlander, N. Karnesis, B. Kaune, N. Korsakova, C. Killow, I. Lloro, R. Maarschalkerweerd, S. Madden, P. Maghami, D. Mance, V. Martin, F. Martin-Porqueras, I. Mateos, P. McNamara, J. Mendes, L. Mendes, A. Moroni, M. Nofrarias, S. Paczkowski, M. Perreur-Lloyd, A. Petiteau, P. Pivato, E. Plagnol, P. Prat, U. Ragnit, J. Ramos-Castro, J. Reiche, J.A. Romera Perez, D. Robertson, H. Rozemeijer, G. Russano, P. Sarra, A. Schleicher, J. Slutsky, C.F. Sopuerta, T. Sumner, D. Texier, J. Thorpe, C. Trenkel, H.B. Tu, D. Vetrugno, S. Vitale, G. Wanner, H. Ward, S. Waschke, P. Wass, D. Wealthy, S. Wen, W. Weber, A. Wittchen, C. Zanoni, T. Ziegler, P Zweifel,
  Proceedings of the LISA Symposium X (Gainesville, May 18-23, 2014)
  J. Phys. Conf. Ser. 610 (2015) 1, 012006.

- Ground-based optical atomic clocks as tools to monitor vertical surface motion
  R. Bondarescu, A. Schärer, A. Lundgren, G. Hetény, N. Houlié, Ph. Jetzer and M. Bondarescu,
  Geophysical Journal International **202** (2015) 1770-1774.

- The potential of continuous, local atomic clock measurements for earthquake prediction and volcanology
  M. Bondarescu, R. Bondarescu, Ph. Jetzer and A. Lundgren,
  in the Proceeding for ICNFP 2014, EPJ Web Conf. **95** (2015), 04009.

- In-flight thermal experiments for LISA Pathfinder: Simulating temperature noise at the Inertial Sensors
  The LISA Pathfinder Collaboration,
  Proceedings of the LISA Symposium X (Gainesville, May 18-23, 2014) J. Phys. Conf. Ser. 610 (2015) 1, 012023.

- Disentangling the magnetic force noise contribution in LISA Pathfinder
  The LISA Pathfinder Collaboration,
  Proceedings of the LISA Symposium X (Gainesville, May 18-23, 2014) J. Phys. Conf. Ser. 610 (2015) 1, 012024.

- A Strategy to Characterize the LISA-Pathfinder Cold Gas Thruster System
  The LISA Pathfinder Collaboration,
  Proceedings of the LISA Symposium X (Gainesville, May 18-23, 2014) J. Phys. Conf. Ser. 610 (2015) 1, 012026.

- Bayesian statistics for the calibration of the LISA Pathfinder experiment
  The LISA Pathfinder Collaboration,
  Proceedings of the LISA Symposium X (Gainesville, May 18-23, 2014) J. Phys. Conf. Ser. 610 (2015) 1, 012027.

- A noise simulator for eLISA: Migrating LISA Pathfinder knowledge to the eLISA mission
  The LISA Pathfinder Collaboration,
  Proceedings of the LISA Symposium X (Gainesville, May 18-23, 2014) J. Phys. Conf.Ser. 610 (2015) 1, 012036.

- Planck revealed bulk motion of Centaurus A lobes
  F. De Paolis, V.G. Gurzadyan, A.A. Nucita, G. Ingrosso, A.L. Kashin, H.G. Khachatryan, S. Mirzoyan, G. Yegorian, Ph. Jetzer, A. Qadir and D. Vetrugno, Astron. and Astrophys. **580**, (2015) L8.

- Planck view of the M 82 galaxy
  V.G. Gurzadyan, F. De Paolis, A.A. Nucita, G. Ingrosso, A.L. Kashin, H.G. Khachatryan, S. Sargsyan, G. Yegorian, Ph. Jetzer, A. Qadir and D. Vetrugno, Astron. and Astrophys. **582**, (2015) A77.

- New effective-one-body Hamiltonian with next-to-leading order spin-spin coupling
  S. Balmelli and T. Damour, Phys. Rev. D92 (2015), 124022.

- Tidal polarizability effects in neutron star mergers
  S. Bernuzzi, A. Nagar, S. Balmelli, T. Dietrich and M. Ujevic, J. Phys. Conf. Ser. 610 (2015) 1, 012047.

- Lensing time delays as a substructure constraint: a case study with the cluster SDSS J1004+4112
  Mohammed, Irshad; Saha, Prasenjit; Liesenborgs, Jori,
  Publications of the Astronomical Society of Japan, Volume 67, id.219 pp.

- The behaviour of dark matter associated with four bright cluster galaxies in the 10 kpc core of Abell 3827
  R. Massey, L. Williams, R. Smit, M. Swinbank, T.D. Kitching, D. Harvey, M. Jauzac, H. Israel, D. Clowe, A. Edge, M. Hilton, E. Jullo, A. Leonard, J. Liesenborgs, J. Merten, I. Mohammed, D. Nagai, J. Richard, A. Robertson, P. Saha, R. Santana, J. Stott, E. Tittley,
  Monthly Notices of the Royal Astronomical Society, Volume 449, Issue 4, p.3393-3406

- Geometrical versus wave optics under gravitational waves
  Angélil, Raymond; Saha, Prasenjit, Physical Review D, Volume 91, Issue 12, id.124007

- SPACE WARPS - I. Crowdsourcing the discovery of gravitational lenses
  P.J. Marshall, A. Verma, A. More, C.P. Davis, S. More, A. Kapadia, M. Parrish, C. Snyder, J. Wilcox, E. Baeten, C. Macmillan, C. Cornen, M. Baumer, E. Simpson, C.J. Lintott, D. Miller, E. Paget, R. Simpson, A.M. Smith, R. Küng, P. Saha, T.E. Collett,
  Monthly Notices of the Royal Astronomical Society, Volume 455, Issue 2, p.1171-1190

- SPACE WARPS- II. New gravitational lens candidates from the CFHTLS discovered through citizen science
  A. More, A. Verma, P.J. Marshall, S. More, E. Baeten, J. Wilcox, C. Macmillan, C. Cornen, A. Kapadia, M. Parrish, C. Snyder, C.P. Davis, R. Gavazzi, C.J. Lintott, R. Simpson, D. Miller, A.M. Smith, E. Paget, P. Saha, R. Küng, T.E. Collett,
  Monthly Notices of the Royal Astronomical Society, Volume 455, Issue 2, p.1191-1210

- Light versus dark in strong-lens galaxies: dark matter haloes that are rounder than their stars
  C. Bruderer, J.I. Read, J.P. Coles, D. Leier, E.E. Falco, I. Ferreras, P. Saha,
  Monthly Notices of the Royal Astronomical Society, Volume 456, Issue 1, p.870-884

Oral Presentations

- Simone Balmelli: The description of next-to-leading order spin-spin effects in an Effective-One-Body Hamiltonian
  14th Marcel Grossmann Meeting, Rome, July 12-18 2015.

- Philippe Jetzer: Gravitational wave detection from space with eLISA
  PSI, Kolloquium, 21 May 2015.

- Philippe Jetzer: Gravitational wave detection from space with eLISA
  Kolloquium University of Oldenburg, 8 June 2015.

- Philippe Jetzer: From LISA Pathfinder to LISA
  Special seminar ETH Zürich, 11 December 2015.

- Rizwana Kausar: Gravitational wave polarization modes in f(R) theories
  14th Marcel Grossmann Meeting, Rome, July 12-18 2015.

- Rafael Küng: Lensing galaxies in the CFHT legacy survey
  14th Marcel Grossmann Meeting, Rome, July 12-18 2015.

- Andreas Schärer: Prospects for testing general relativity and alternative theories with clocks on satellites in Earth orbit
  14th Marcel Grossmann Meeting, Rome, July 12-18 2015.

19.1.3 GERDA

Articles

- Production and Characterization of 228-Th Calibration Sources with Low Neutron Emission for GERDA
  L. Baudis, G. Benato, P. Carconi, C.M. Cattadori *et al.*, JINST 10 12, P12005 (2015).

- Double beta decay of 76-Ge into Excited States with GERDA Phase I
  M. Agostini, M. Allardt, A.M. Bakalyarov, M. Balata, I. Barabanov, N. Barros, L. Baudis, C. Bauer et al. (GERDA Collaboration), Journal of Physics G 42 11, 115201 (2015).

Oral Presentations

- L. Baudis: Double Beta Decay: non-Ge Experimental Programmes
  Meeting on the Next Generation ^{76}Ge Experiment, Arnold Sommerfeld House, Munich, April 26, 2016.
- M. Miloradovic: The GERDA experiment: Search for the Neutrinoless Double Beta Decay
  Magellan Workshop 2016, DESY Hamburg, Germany, March 2016.
- G. Benato: Status and perspectives of the GERDA experiment
  Seminar at LNGS, 30 September 2015.
- M. Miloradovic: Gas Emanation System for the GERDA experiment
  SPS/OEPG meeting, TU Wien, Vienna, Austria, September 2015.
- L. Baudis: Neutrinoless Double Beta Decay and GERDA
  CHIPP plenary meeting, Chateau de Bossey, July 1, 2015.
- G. Benato: Improvement of the Energy Resolution via an Optimized Digital Signal Processing in GERDA Phase I
  ISSP 2015, Erice, 24 June - 3 July 2015.
- L. Baudis: Double Beta Decay an Experimental Overview
  Invisibles Workshop, Madrid, June 24, 2015.
- G. Benato: Digital Signal Shaping for Germanium Detectors: Theory and Practice
  PhD workshop on experimental aspects of rare event searches, Tübingen, 18-19 June 2015.
- M. Walter: The GERDA Experiment for the Search of Neutrinoless Double Beta Decay
  Rencontres de Blois, Chateau Royal de Blois, May 31, 2015.
- G. Benato: Search for Neutrinoless Double Beta Decay with the GERDA Experiment
  Seminar at Yale University, 29 May 2015.
- G. Benato: Search for Neutrinoless Double Beta Decay with the GERDA Experiment
  CIPANP 2015, Vail Colorado, 19-24 May 2015.

Outreach

- L. Baudis: Dark matter
  zurich.minds Deep Dive Zurich Uniturm, April 6, 2016.
- M. Galloway: Dark Matter
  St. Elhelburga's Centre for Reconciliation and Peace, London March 11, 2016.
- L. Baudis: Die unerträgliche Leichtigkeit der Neutrinos
  Senioren-Universität Zurich, Zurich, March 8, 2016.

19.1.4 XENON/DARWIN

Articles

- Dark Matter Detection
  Laura Baudis, J. Phys. G43 4, 044001 (2016).
- Physics Reach of the XENON1T Dark Matter Experiment
  E. Aprile *et al.* (XENON Collaboration) JCAP 1604 04, 027 (2016).
- Dark Matter Searches
  Laura Baudis, Ann. Phys. (Berlin), 1-10 (2015).

- Search for Event Rate Modulation in XENON100 Electronic Recoil Data
  E. Aprile *et al.* (XENON Collaboration), Phys. Rev. Lett. 115, 091302 (2015).

- Exclusion of Leptophilic Dark Matter Models using XENON100 Electronic Recoil Data
  E. Aprile *et al.* (XENON Collaboration), Science 349, 851 (2015).

- Cosmogenic Activation of Xenon and Copper
  Laura Baudis, Alexander Kish, Francesco Piastra, Marc Schumann, Eur. Phys. J. C75 10, 485 (2015).

- Dark Matter Sensitivity of Multi-ton Liquid Xenon Detectors
  Marc Schumann, Laura Baudis, Lukas Buetikofer, Alexander Kish, Marco Selvi, JCAP 1510 10, 016 (2015).

- Lowering the Radioactivity of the Photomultiplier Tubes for the XENON1T Dark Matter Experiment
  E. Aprile *et al.* (XENON Collaboration), Eur. Phys. Journal C 75/11, 546 (2015).

Oral Presentations

- L. Baudis: Dark Matter Detection with XENON and DARWIN
  Seminar, Department of Physics, University of Oslo, Oslo, May 4, 2016.

- L. Baudis: Searching for Dark Matter with XENON and DARWIN
  UCSC seminar, Santa Cruz, February 22, 2016.

- L. Baudis: Dark Matter and Other Rare Event Searches with DARWIN
  UCLA Dark Matter, Los Angeles, February 19, 2016.

- L. Baudis: XENONnT
  the Next Step XENON1T Inauguration, Gran Sasso Laboratory, November 11, 2015.

- L. Baudis: Searching for Dark Matter with XENON and DARWIN
  Graduiertenkolleg Seminar, RWTH Aachen, July 14, 2015.

- L. Baudis: Dark Matter Detection with XENON and DARWIN
  KCETA Colloquium, Karlsruhe Institute of Technology, May 21, 2015.

- L. Baudis: The State-of-the-Art in the Search for Dark Matter
  Physics at FOM, Veldhoven, January 20, 2016.

- L. Baudis: Dark Matter Detection - an Experimental Overview
  28th Texas Symposium on Relativistic Astrophysics, Geneva, December 14, 2015.

- A. Kish: Xenon Detectors for Dark Matter Searches
  Seminar at EPFL, Lausanne, November 30, 2015.

- L. Baudis: Dark Matter Detection in the Milky Way
  Physics Colloquium, University of Barcelona, November 26, 2015.

- A. Kish: Searches for Particle Dark Matter with the XENON100 and XENOn1T Experiments
  Seminar at Imperial College London, November 5, 2015.

- L. Baudis: Dark Matter Detection in the Milky Way
  Physics Colloquium, Princeton University, NJ, October 15, 2015.

- L. Baudis: Dark Matter Detection in the Milky Way
  Physics Colloquium, Columbia University, NY, October 12, 2015.

- F. Piastra: Cosmogenic Activation of Xenon
  6th Young Researchers Meeting, L'Aquila, October 12, 2015.

- L. Baudis: Direct Dark Matter Detection
  Brookhaven Forum 2015, Brookhaven, October 9, 2015.

- P. Pakarha: The XENON1T Light Calibration System
  SPS meeting, TU Wien, Vienna, Austria, September 2015.

- L. Baudis: The State-of-the-Art in the Search for Dark Matter
  Inaugural Zwicky Symposium, Braunwald, September 4, 2015.

- P. Pakarha: The XENON1T Light Calibration System
  Joint UZH-ETH PhD seminar, PSI Villigen, August 27, 2015.

- P. Barrow: Searching for Bosonic SuperWIMPs in XENON100
  Joint UZH-ETH PhD seminar, PSI Villigen, August 27, 2015.

- D. Mayani: Studies of the XENON100 electromagnetic background
  Joint UZH-ETH PhD seminar, PSI Villigen, August 27, 2015.

- F. Piastra: Cosmogenic Activation of Xenon
  Joint UZH-ETH PhD seminar, PSI Villigen, August 27, 2015.

- G. Kessler: XENON Dark Matter Project
  17th Lomonosov Conference on Elementary Particle Physics 2015, Moscow, Russia, 24. August 2015.

- L. Baudis: Direct Detection of Dark Matter
  Lepton Photon 2015, Ljubljana, August 20, 2015.

- A. Kish: Wavelength-shifters for Argon, VUV-sensitive SiPMs, and Measurements of Xenon Response to Low Energy Neutrons
  LIDINE-2015, Light Detection in Noble Liquids, State University of New York, Albany, USA, August 29, 2015.

- A. Kish: Dark Matter Searches with Liquid Xenon and Latest Results from the XENON100 Experiment
  Seminar at Royal Holloway, University of London, August 12, 2015.

- A. Kish: The XENON Project for Direct Dark Matter Detection
  EPS HEP-2015, European Physical Society Conference on High Energy Physics, Vienna, Austria, July 24, 2015.

- P. Barrow: Searching for Bosonic SuperWIMPs in XENON100
  Invisibles Workshop, Madrid, June 25, 2015.

- D. Mayani: Studies of the XENON100 Electromagnetic Background
  Invisibles Workshop, Madrid, June 25, 2015.

- L. Baudis: Direct Dark Matter Detection Experiments
  an Overview CRC 634 Achievements and Outlook, Darmstadt, June 10, 2015.

- L. Baudis: Highlights from the XENON Dark Matter Search
  The Spacetime Odyssey Continues, Stockholm, June 3, 2015.

- L. Baudis: Direct dark matter detection experiments: an overview
  Solvay-Francqui workshop on neutrinos, Brussels, May 28, 2015.

- L. Baudis: R&D for Dark Matter Experiments Based on Liquefied Noble Gases and on Crystals Operated at mK Temperatures
  APPEC SAC meeting, Rome, May 19, 2015.

19.1.5 DAMIC

Articles

- Measurement of Radioactive Contamination in the High-Resistivity Silicon CCDs of the DAMIC Experiment
  DAMIC Collaboration, A. Aguilar-Arevalo *et al.*, JINST **10** (2015) no.08, P08014

- The DAMIC Dark Matter Experiment
  DAMIC Collaboration, J. R. T. de Mello Neto *et al.*, Proceedings, 34th International Cosmic Ray Conference (ICRC 2015): The Hague, The Netherlands, July 30-August 6, 2015, C15-07-30

- Status of the DAMIC Direct Dark Matter Search Experiment
  DAMIC Collaboration, A. Aguilar-Arevalo *et al.*, Proceedings, 12th Conference on the Intersections of Particle and Nuclear Physics (CIPANP 2015), C15-05-19

Oral Presentations

- J. Liao: DAMIC : Low mass WIMP detection with scientific CCDs
  DPF 2015, Ann arbor, U Michigan, U.S., Aug 5th, 2015.

- J. Liao: Low mass WIMP detection with scientific CCDs
  New perspective 2015, Fermilab, Chicago, U.S., June 9, 2015.

- B. Kilminster: DAMIC: Dark matter in CCDs for low energy recoil searches
  Munich Low mass dark matter conference Max Planck, Munich, Germany, December 1st, 2015.

- B. Kilminster: DAMIC: Dark matter in CCDs, recent developments to low threshold
  Cairo Dark Matter Conference, Cairo, Egypt, December 16, 2015.

19.1.6 SHiP

Articles

- Facility to Serach for Hidden Particles (SHiP) at the CERN SPS
  SHiP-Collaboration, M. Anelli *et al.*, arXiv:1504.04956v1, CERN-SPSC-2015-016.

- New facility with a dedicated detector to search for new long-lived neutral particles
  Elena Graverini, PoS (EPS-HEP2015) 103, Proceeding of EPS-HEP 2015.

Conference contributions

- Elena Graverini: A new facility with a dedicated detector to search for long-lived neutral particles
  PS-HEP 2015, Vienna (Austria), 22-29th July 2015.

- Elena Graverini: SHiP: A new facility with a dedicated detector to search for long-lived neutral particles and the tau neutrino properties
  Université Libre de Bruxelles, 26th February 2016.

- Nicola Serra: Heavy Neutrinos
  nuFact 2015, CBPF, Rio de Janeiro, 10th-15th August 2015.

- Nicola Serra: Searching for New Particles at high and low energies
  Universidad de Santiago de Compostela (USC), Spain, 24th February 2016.

- Nicola Serra: Searching for New Particles at high and low energies
  Universidad de Santiago de Compostela (USC), Spain, 24th February 2016.

19.1.7 CTA

Conference contribution

- G. Pühlhofer *et al.*: FlashCam: a fully-digital camera for the medium-sized telescopes of the Cherenkov Telescope Array
  34th International Cosmic Ray Conference (ICRC2015), The Hague (The Netherlands), PoS(ICRC2015)1039.

19.1.8 $\mu^+ \to e^+e^-e^+$

Conference contribution

- Roman Gredig: Search for the decay $\mu^+ \to e^+e^-e^+$
  NuFact15 : XVII International Workshop on Neutrino Factories and Future Neutrino Facilities.

19.1.9 H1

The 2015 H1 Collaboration has 141 members including K. Müller, P. Robmann, U. Straumann and P. Truöl.
Articles

- Exclusive ρ^0 meson photoproduction with a leading neutron at HERA
  H1 ZEUS Collaboration, V. Andreev *et al.*, Eur. Phys. J. C **76** (2016) no.1, 41.
- Combination of measurements of inclusive deep inelastic $e^{\pm}p$ scattering cross sections and QCD analysis of HERA data
  H1 and ZEUS Collaborations, H. Abramowicz *et al.*, Eur. Phys. J. C **75** (2015) no.12, 580.
- Combination of differential $\mathrm{D}^{\pm}$ cross-section measurements in deep-inelastic ep scattering at HERA
  H1 and ZEUS Collaborations, H. Abramowicz *et al.*, JHEP **1509** (2015) 149.
- Diffractive Dijet Production with a Leading Proton in ep Collisions at HERA
  H1 Collaboration, H. Abramowicz *et al.*, JHEP **1505** (2015) 056.

19.1.10 CMS

Articles

- Measurements of $t\bar{t}$ spin correlations and top quark polarization using dilepton final states in pp collisions at $\sqrt{s} = 8$ TeV
  V. Khachatryan *et al.* [CMS Collaboration], Phys. Rev. D **93** (2016) no.5, 052007.
- Correlations between jets and charged particles in PbPb and pp collisions at $\sqrt{s_{\mathrm{NN}}} = 2.76$ TeV
  V. Khachatryan *et al.* [CMS Collaboration], JHEP **1602** (2016) 156.
- Measurement of differential and integrated fiducial cross sections for Higgs boson production in the four-lepton decay channel in pp collisions at $\sqrt{s} = 7$ and 8 TeV
  V. Khachatryan *et al.* [CMS Collaboration], JHEP **1604** (2016) 005.
- Search for narrow resonances decaying to dijets in proton-proton collisions at $\sqrt{s} = 13$ TeV
  V. Khachatryan *et al.* [CMS Collaboration], Phys. Rev. Lett. **116** (2016) no.7, 071801.
- Event generator tunes obtained from underlying event and multiparton scattering measurements
  V. Khachatryan *et al.* [CMS Collaboration], Eur. Phys. J. C **76** (2016) no.3, 155.
- Search for dark matter and unparticles produced in association with a Z boson in proton-proton collisions at $\sqrt{s} = 8$ TeV
  V. Khachatryan *et al.* [CMS Collaboration], Phys. Rev. D **93** (2016) no.5, 052011.
- Search for anomalous single top quark production in association with a photon in pp collisions at $\sqrt{s} = 8$ TeV
  V. Khachatryan *et al.* [CMS Collaboration], JHEP **1604** (2016) 035.
- Measurement of top quark polarisation in t-channel single top quark production
  V. Khachatryan *et al.* [CMS Collaboration], JHEP **1604** (2016) 073.

- Search for excited leptons in proton-proton collisions at $\sqrt{s} = 8$ TeV
  V. Khachatryan *et al.* [CMS Collaboration], JHEP **1603** (2016) 125.

- Reconstruction and identification of τ lepton decays to hadrons and ν_τ at CMS
  V. Khachatryan *et al.* [CMS Collaboration], JINST **11** (2016) no.01, P01019.

- Search for a very light NMSSM Higgs boson produced in decays of the 125 GeV scalar boson and decaying into τ leptons in pp collisions at $\sqrt{s} = 8$ TeV
  V. Khachatryan *et al.* [CMS Collaboration], JHEP **1601** (2016) 079.

- Measurement of the top quark pair production cross section in proton-proton collisions at $\sqrt{s} = 13$ TeV
  V. Khachatryan *et al.* [CMS Collaboration], Phys. Rev. Lett. **116** (2016) no.5, 052002.

- Search for a light charged Higgs boson decaying to $\mathrm{c\bar{s}}$ in pp collisions at $\sqrt{s} = 8$ TeV
  V. Khachatryan *et al.* [CMS Collaboration], JHEP **1512** (2015) 178.

- Transverse momentum spectra of inclusive b jets in pPb collisions at $\sqrt{s_{NN}} = 5.02$ TeV
  V. Khachatryan *et al.* [CMS Collaboration], Phys. Lett. B **754** (2016) 59.

- Searches for a heavy scalar boson H decaying to a pair of 125 GeV Higgs bosons hh or for a heavy pseudoscalar boson A decaying to Zh, in the final states with $h \to \tau\tau$
  V. Khachatryan *et al.* [CMS Collaboration], Phys. Lett. B **755** (2016) 217.

- Observation of top quark pairs produced in association with a vector boson in pp collisions at $\sqrt{s} = 8$ TeV
  V. Khachatryan *et al.* [CMS Collaboration], JHEP **1601** (2016) 096.

- Measurement of transverse momentum relative to dijet systems in PbPb and pp collisions at $\sqrt{s_{\mathrm{NN}}} = 2.76$ TeV
  V. Khachatryan *et al.* [CMS Collaboration], JHEP **1601** (2016) 006.

- Search for the production of an excited bottom quark decaying to tW in proton-proton collisions at $\sqrt{s} = 8$ TeV
  V. Khachatryan *et al.* [CMS Collaboration], JHEP **1601** (2016) 166.

- Measurement of the $\mathrm{t\bar{t}}$ production cross section in the all-jets final state in pp collisions at $\sqrt{s} = 8$ TeV
  V. Khachatryan *et al.* [CMS Collaboration], Eur. Phys. J. C **76** (2016) no.3, 128.

- Search for $W' \to tb$ in proton-proton collisions at $\sqrt{s} = 8$ TeV
  V. Khachatryan *et al.* [CMS Collaboration], JHEP **1602** (2016) 122.

- Search for vector-like charge 2/3 T quarks in proton-proton collisions at $\sqrt{s} = 8$ TeV
  V. Khachatryan *et al.* [CMS Collaboration], Phys. Rev. D **93** (2016) no.1, 012003.

- Measurement of the top quark mass using proton-proton data at $\sqrt{s} = 7$ and 8 TeV
  V. Khachatryan *et al.* [CMS Collaboration], Phys. Rev. D **93** (2016) no.7, 072004.

- Search for single production of scalar leptoquarks in proton-proton collisions at $\sqrt{s} = 8$ TeV
  V. Khachatryan *et al.* [CMS Collaboration], Phys. Rev. D **93** (2016) no.3, 032005.

- Search for pair production of first and second generation leptoquarks in proton-proton collisions at $\sqrt{s} = 8$ TeV
  V. Khachatryan *et al.* [CMS Collaboration], Phys. Rev. D **93** (2016) no.3, 032004.

- Measurement of differential cross sections for Higgs boson production in the diphoton decay channel in pp collisions at $\sqrt{s} = 8$ TeV
  V. Khachatryan *et al.* [CMS Collaboration], Eur. Phys. J. C **76** (2016) no.1, 13.

- Search for a charged Higgs boson in pp collisions at $\sqrt{s} = 8$ TeV
  V. Khachatryan *et al.* [CMS Collaboration], JHEP **1511** (2015) 018.

- Search for supersymmetry in the vector-boson fusion topology in proton-proton collisions at $\sqrt{s} = 8$ TeV
  V. Khachatryan *et al.* [CMS Collaboration], JHEP **1511** (2015) 189.

- Study of B Meson Production in p+Pb Collisions at $\sqrt{s_{NN}} = 5.02$ TeV Using Exclusive Hadronic Decays
  V. Khachatryan *et al.* [CMS Collaboration], Phys. Rev. Lett. **116** (2016) no.3, 032301.

- Search for W' decaying to tau lepton and neutrino in proton-proton collisions at $\sqrt{s} = 8$ TeV
  V. Khachatryan *et al.* [CMS Collaboration], Phys. Lett. B **755** (2016) 196.

- Measurement of the charge asymmetry in top quark pair production in pp collisions at $\sqrt{s} = 8$ TeV using a template method
  V. Khachatryan *et al.* [CMS Collaboration], Phys. Rev. D **93** (2016) no.3, 034014.

- Search for neutral MSSM Higgs bosons decaying to $\mu^+\mu^-$ in pp collisions at $\sqrt{s} = 7$ and 8 TeV
  V. Khachatryan *et al.* [CMS Collaboration], Phys. Lett. B **752** (2016) 221.

- Search for supersymmetry in events with a photon, a lepton, and missing transverse momentum in pp collisions at $\sqrt{s}$ =8 TeV
  V. Khachatryan *et al.* [CMS Collaboration], Phys. Lett. B **757** (2016) 6.

- Angular analysis of the decay $B^0 \to K^{*0}\mu^+\mu^-$ from pp collisions at $\sqrt{s} = 8$ TeV
  V. Khachatryan *et al.* [CMS Collaboration], Phys. Lett. B **753** (2016) 424.

- Measurement of the CP-violating weak phase ϕ_s and the decay width difference $\Delta\Gamma_s$ using the $B_s^0 \to J/\psi\phi(1020)$ decay channel in pp collisions at $\sqrt{s}$=8 TeV
  V. Khachatryan *et al.* [CMS Collaboration], Phys. Lett. B **757** (2016) 97.

- Measurement of the underlying event activity using charged-particle jets in proton-proton collisions at $\sqrt{s} = 2.76$ TeV
  V. Khachatryan *et al.* [CMS Collaboration], JHEP **1509** (2015) 137.

- Limits on the Higgs boson lifetime and width from its decay to four charged leptons
  V. Khachatryan *et al.* [CMS Collaboration], Phys. Rev. D **92** (2015) no.7, 072010.

- Pseudorapidity distribution of charged hadrons in proton-proton collisions at $\sqrt{s} = 13$ TeV
  V. Khachatryan *et al.* [CMS Collaboration], Phys. Lett. B **751** (2015) 143.

- Inclusive and differential measurements of the $t\bar{t}$ charge asymmetry in pp collisions at $\sqrt{s}$=8 TeV
  V. Khachatryan *et al.* [CMS Collaboration], Phys. Lett. B **757** (2016) 154.

- Search for a Higgs boson decaying into $\gamma^*\gamma \to \ell\ell\gamma$ with low dilepton mass in pp collisions at $\sqrt{s} = 8$ TeV
  V. Khachatryan *et al.* [CMS Collaboration], Phys. Lett. B **753** (2016) 341.

- Search for supersymmetry with photons in pp collisions at $\sqrt{s}$=8 TeV
  V. Khachatryan *et al.* [CMS Collaboration], Phys. Rev. D **92** (2015) no.7, 072006.

- Search for exotic decays of a Higgs boson into undetectable particles and one or more photons
  V. Khachatryan *et al.* [CMS Collaboration], Phys. Lett. B **753** (2016) 363.

- Production of leading charged particles and leading charged-particle jets at small transverse momenta in pp collisions at $\sqrt{s} = 8$ TeV
  V. Khachatryan *et al.* [CMS Collaboration], Phys. Rev. D **92** (2015) no.11, 112001.

- Search for neutral MSSM Higgs bosons decaying into a pair of bottom quarks
  V. Khachatryan *et al.* [CMS Collaboration], JHEP **1511** (2015) 071.

- Search for resonant $t\bar{t}$ production in proton-proton collisions at $\sqrt{s} = 8$ TeV
  V. Khachatryan *et al.* [CMS Collaboration], Phys. Rev. D **93** (2016) no.1, 012001.

- Search for diphoton resonances in the mass range from 150 to 850 GeV in pp collisions at $\sqrt{s} = 8$ TeV
  V. Khachatryan *et al.* [CMS Collaboration], Phys. Lett. B **750** (2015) 494.

- Search for a massive resonance decaying into a Higgs boson and a W or Z boson in hadronic final states in proton-proton collisions at $\sqrt{s} = 8$ TeV
  V. Khachatryan *et al.* [CMS Collaboration], JHEP **1602** (2016) 145.

- Search for the standard model Higgs boson produced through vector boson fusion and decaying to $b\bar{b}$
  V. Khachatryan *et al.* [CMS Collaboration], Phys. Rev. D **92** (2015) no.3, 032008.

- A search for pair production of new light bosons decaying into muons
  V. Khachatryan *et al.* [CMS Collaboration], Phys. Lett. B **752** (2016) 146.

- Search for neutral color-octet weak-triplet scalar particles in proton-proton collisions at $\sqrt{s} = 8$ TeV
  V. Khachatryan *et al.* [CMS Collaboration], JHEP **1509** (2015) 201.

- Comparison of the Z/γ^* + jets to γ + jets cross sections in pp collisions at $\sqrt{s} = 8$ TeV
  V. Khachatryan *et al.* [CMS Collaboration], JHEP **1510** (2015) 128 Erratum: [JHEP **1604** (2016) 010].

- Measurement of the differential cross section for top quark pair production in pp collisions at $\sqrt{s} = 8$ TeV
  V. Khachatryan *et al.* [CMS Collaboration], Eur. Phys. J. C **75** (2015) no.11, 542.

- Impact of low-dose electron irradiation on n^+p silicon strip sensors
  W. Adam *et al.* [CMS Tracker Group Collaboration], Nucl. Instrum. Meth. A **803** (2015) 100.

- Trapping in Irradiated p-on-n Silicon Sensors at Fluences Anticipated at the HL-LHC Outer Tracker
  W. Adam *et al.* [CMS Tracker Group Collaboration], JINST **11** (2016) no.04, P04023.

- Search for a pseudoscalar boson decaying into a Z boson and the 125 GeV Higgs boson in $\ell^+\ell^-b\bar{b}$ final states
  V. Khachatryan *et al.* [CMS Collaboration], Phys. Lett. B **748** (2015) 221.

- Angular coefficients of Z bosons produced in pp collisions at $\sqrt{s} = 8$ TeV and decaying to $\mu^+\mu^-$ as a function of transverse momentum and rapidity
  V. Khachatryan *et al.* [CMS Collaboration], Phys. Lett. B **750** (2015) 154.

- Measurement of the Z boson differential cross section in transverse momentum and rapidity in proton-proton collisions at 8 TeV
  V. Khachatryan *et al.* [CMS Collaboration], Phys. Lett. B **749** (2015) 187.

- Search for the production of dark matter in association with top-quark pairs in the single-lepton final state in proton-proton collisions at $\sqrt{s} = 8$ TeV
  V. Khachatryan *et al.* [CMS Collaboration], JHEP **1506** (2015) 121.

- Search for a Higgs Boson in the Mass Range from 145 to 1000 GeV Decaying to a Pair of W or Z Bosons
  V. Khachatryan *et al.* [CMS Collaboration], JHEP **1510** (2015) 144.

- Search for Third-Generation Scalar Leptoquarks in the tτ Channel in Proton-Proton Collisions at $\sqrt{s} = 8$ TeV
  V. Khachatryan *et al.* [CMS Collaboration], JHEP **1507** (2015) 042.

- Measurement of diffraction dissociation cross sections in pp collisions at $\sqrt{s} = 7$ TeV
  V. Khachatryan *et al.* [CMS Collaboration], Phys. Rev. D **92** (2015) no.1, 012003.

- Searches for third-generation squark production in fully hadronic final states in proton-proton collisions at $\sqrt{s} = 8$ TeV
  V. Khachatryan *et al.* [CMS Collaboration], JHEP **1506** (2015) 116.

- Combined Measurement of the Higgs Boson Mass in pp Collisions at $\sqrt{s} = 7$ and 8 TeV with the ATLAS and CMS Experiments
  G. Aad *et al.* [ATLAS and CMS Collaborations], Phys. Rev. Lett. **114** (2015) 191803.

- Study of W boson production in pPb collisions at $\sqrt{s_{\mathrm{NN}}} = 5.02$ TeV
  V. Khachatryan *et al.* [CMS Collaboration], Phys. Lett. B **750** (2015) 565.

- Measurements of the ZZ production cross sections in the $2l2\nu$ channel in proton-proton collisions at $\sqrt{s} = 7$ and 8 TeV and combined constraints on triple gauge couplings
  V. Khachatryan *et al.* [CMS Collaboration], Eur. Phys. J. C **75** (2015) no.10, 511.

- Search for resonant pair production of Higgs bosons decaying to two bottom quark-antiquark pairs in proton-proton collisions at 8 TeV
  V. Khachatryan *et al.* [CMS Collaboration], Phys. Lett. B **749** (2015) 560.

- Search for vector-like T quarks decaying to top quarks and Higgs bosons in the all-hadronic channel using jet substructure
  V. Khachatryan *et al.* [CMS Collaboration], JHEP **1506** (2015) 080.

- Evidence for transverse momentum and pseudorapidity dependent event plane fluctuations in PbPb and pPb collisions
  V. Khachatryan *et al.* [CMS Collaboration], Phys. Rev. C **92** (2015) no.3, 034911.

- Study of Final-State Radiation in Decays of Z Bosons Produced in pp Collisions at 7 TeV
  V. Khachatryan *et al.* [CMS Collaboration], Phys. Rev. D **91** (2015) no.9, 092012.

- Search for Lepton-Flavour-Violating Decays of the Higgs Boson
  V. Khachatryan *et al.* [CMS Collaboration], Phys. Lett. B **749** (2015) 337.

- Nuclear Effects on the Transverse Momentum Spectra of Charged Particles in pPb Collisions at $\sqrt{s_{\rm NN}} = 5.02$ TeV
  V. Khachatryan *et al.* [CMS Collaboration], Eur. Phys. J. C **75** (2015) no.5, 237.

- Evidence for Collective Multiparticle Correlations in p-Pb Collisions
  V. Khachatryan *et al.* [CMS Collaboration], Phys. Rev. Lett. **115** (2015) no.1, 012301.

- Search for Narrow High-Mass Resonances in Proton-Proton Collisions at $\sqrt{s} = 8$ TeV Decaying to a Z and a Higgs Boson
  V. Khachatryan *et al.* [CMS Collaboration], Phys. Lett. B **748** (2015) 255.

- Distributions of Topological Observables in Inclusive Three- and Four-Jet Events in pp Collisions at $\sqrt{s} = 7$ TeV
  V. Khachatryan *et al.* [CMS Collaboration], Eur. Phys. J. C **75** (2015) no.7, 302.

- Searches for Supersymmetry using the M_{T2} Variable in Hadronic Events Produced in pp Collisions at 8 TeV
  V. Khachatryan *et al.* [CMS Collaboration], JHEP **1505** (2015) 078.

- Measurement of J/ψ and $\Upsilon(2S)$ Prompt Double-Differential Cross Sections in pp Collisions at $\sqrt{s} = 7$ TeV
  V. Khachatryan *et al.* [CMS Collaboration], Phys. Rev. Lett. **114** (2015) no.19, 191802.

- Performance of Photon Reconstruction and Identification with the CMS Detector in Proton-Proton Collisions at$\sqrt{s} = 8$ TeV
  V. Khachatryan *et al.* [CMS Collaboration], JINST **10** (2015) no.08, P08010.

- Performance of Electron Reconstruction and Selection with the CMS Detector in Proton-Proton Collisions at $\sqrt{s} = 8$ TeV
  V. Khachatryan *et al.* [CMS Collaboration], JINST **10** (2015) no.06, P06005.

- Constraints on the pMSSM, AMSB model and on other models from the search for long-lived charged particles in proton-proton collisions at $\sqrt{s} = 8$ TeV
  V. Khachatryan *et al.* [CMS Collaboration], Eur. Phys. J. C **75** (2015) no.7, 325.

- Search for a Standard Model Higgs Boson Produced in Association with a Top-Quark Pair and Decaying to Bottom Quarks Using a Matrix Element Method
  V. Khachatryan *et al.* [CMS Collaboration], Eur. Phys. J. C **75** (2015) no.6, 251.

- Measurements of the Υ(1S), Υ(2S), and Υ(3S) differential cross sections in pp collisions at $\sqrt{s} = 7$ TeV
  V. Khachatryan *et al.* [CMS Collaboration], Phys. Lett. B **749** (2015) 14.

- Measurement of the ratio $B(B_s^0 \to J/\psi f_0(980))/B(B_s^0 \to J/\psi\phi(1020))$ in pp collisions at $\sqrt{s} = 7$ TeV
  V. Khachatryan *et al.* [CMS Collaboration], Phys. Lett. B **756** (2016) 84.

- Search for heavy Majorana neutrinos in $\mu^{\pm}\mu^{\pm}+$ jets events in proton-proton collisions at $\sqrt{s} = 8$ TeV
  V. Khachatryan *et al.* [CMS Collaboration], Phys. Lett. B **748** (2015) 144.

- Precise determination of the mass of the Higgs boson and tests of compatibility of its couplings with the standard model predictions using proton collisions at 7 and 8 TeV
  V. Khachatryan *et al.* [CMS Collaboration], Eur. Phys. J. C **75** (2015) no.5, 212.

- Search for pair-produced resonances decaying to jet pairs in proton-proton collisions at $\sqrt{s} = 8$ TeV
  V. Khachatryan *et al.* [CMS Collaboration], Phys. Lett. B **747** (2015) 98.

- Measurement of the cross section ratio $\sigma_{\mathrm{t\bar{t}b\bar{b}}}/\sigma_{\mathrm{t\bar{t}jj}}$ in pp collisions at $\sqrt{s} = 8$ TeV
  V. Khachatryan *et al.* [CMS Collaboration], Phys. Lett. B **746** (2015) 132.

- Observation of the rare $B_s^0 \to \mu^+\mu^-$ decay from the combined analysis of CMS and LHCb data
  V. Khachatryan *et al.* [CMS and LHCb Collaborations], Nature **522** (2015) 68.

- Constraints on the spin-parity and anomalous HVV couplings of the Higgs boson in proton collisions at 7 and 8 TeV
  V. Khachatryan *et al.* [CMS Collaboration], Phys. Rev. D **92** (2015) no.1, 012004.

- Search for quark contact interactions and extra spatial dimensions using dijet angular distributions in proton-proton collisions at $\sqrt{s} = 8$ TeV
  V. Khachatryan *et al.* [CMS Collaboration], Phys. Lett. B **746** (2015) 79.

- Search for new phenomena in monophoton final states in proton-proton collisions at $\sqrt{s} = 8$ TeV
  V. Khachatryan *et al.* [CMS Collaboration], Phys. Lett. B **755** (2016) 102.

- Constraints on parton distribution functions and extraction of the strong coupling constant from the inclusive jet cross section in pp collisions at $\sqrt{s} = 7$ TeV
  V. Khachatryan *et al.* [CMS Collaboration], Eur. Phys. J. C **75** (2015) no.6, 288.

- Search for dark matter, extra dimensions, and unparticles in monojet events in proton-proton collisions at $\sqrt{s} = 8$ TeV
  V. Khachatryan *et al.* [CMS Collaboration], Eur. Phys. J. C **75** (2015) no.5, 235.

- Search for physics beyond the standard model in final states with a lepton and missing transverse energy in proton-proton collisions at $\sqrt{s} = 8$ TeV
  V. Khachatryan *et al.* [CMS Collaboration], Phys. Rev. D **91** (2015) no.9, 092005.

- Measurement of the $pp \to ZZ$ production cross section and constraints on anomalous triple gauge couplings in four-lepton final states at $\sqrt{s}$ =8 TeV
  V. Khachatryan *et al.* [CMS Collaboration], Phys. Lett. B **740** (2015) 250.

Oral presentations

- C. Lange: High-p_T multi-jet final states at ATLAS and CMS at 13 TeV
  Rencontres de Moriond EW 2016, March 12-19, 2016, La Thuile, Italy.

- B. Kilminster: Secrets of the Universe Beyond the Higgs Boson
  Zurich Physics Colloquium, February 2, 2016, ETH Zurich, Switzerland.

- T. Årrestad: Search for heavy resonances in the W/Z-tagged dijet mass spectrum
  CMS EXOTICA Workshop, November 12-14, 2015, Venice, Italy.

- J. Ngadiuba: Resonant di-boson searches in the semi-leptonic final state
  CMS EXOTICA Workshop, November 12-14, 2015, Venice, Italy.

- T. Årrestad: Search for heavy resonances in the W/Z-tagged dijet mass spectrum at CMS
  European School High Energy Physics 2015, September 2-15, 2015, Bansko, Bulgaria.

- C. Galloni: Search for heavy resonances in the $X \to HH \to \tau\tau bb$ final state
  European School High Energy Physics 2015, September 2-15, 2015, Bansko, Bulgaria.

- D. Salerno: Search for standard model ttH(bb) production in the all hadronic final state using the Matrix Element Method
  European School High Energy Physics 2015, September 2-15, 2015, Bansko, Bulgaria.

- A. De Cosa: Dark Matter at the LHC
  LHCP 2015, August 31 - September 5, 2015, Saint Petersburg, Russia.

- G. Rauco: Search for the standard model Higgs boson produced by vector boson fusion and decaying to bottom quarks
  LHCP 2015, August 31 - September 5, 2015, Saint Petersburg, Russia.

- T. Årrestad: Search for heavy resonances in the W/Z-tagged dijet mass spectrum at CMS
  PhD Seminar, August 27, 2015, PSI, Villigen, Switzerland.

- C. Galloni: Search for massive resonaces decaying into boson pairs in the $\tau\tau qq$ final state at CMS
  PhD Seminar, August 27, 2015, PSI, Villigen, Switzerland.
- D. Pinna: Dark matter produced in association with top quark pairs
  PhD Seminar, August 27, 2015, PSI, Villigen, Switzerland.
- D. Salerno: All hadronic ttH(bb) analysis using the Matrix Element Method
  PhD Seminar, August 27, 2015, PSI, Villigen, Switzerland.
- J. Ngadiuba: CMS Pixel Phase I Upgrade: System Test at UZH
  PhD Seminar, August 27, 2015, PSI, Villigen, Switzerland.
- A. Hinzmann: New results from CMS on the search for VV/VH/HH resonances in Run 1
  BOOST2015, August 11, 2015, University of Chicago, Chicago, IL, USA.
- A. Hinzmann: Higgs as a probe for exotic new physics
  DESY Physics Seminar, July 14, 2015, DESY, Hamburg, Germany.
- L. Caminada: Higgs production in association with top quarks at CMS
  QCD15, June 29-July 3, 2015, Montpellier, France.
- B. Kilminster: Searching beyond SUSY with CMS an ATLAS
  Gordon Research Conference on Prospects of Particle Physics at the 13TeV Large Hadron Collider, June 10, 2015, Hong Kong University of Science and Technology, Hong Kong.
- J. Ngadiuba: Status of the CMS Pixel System Test at UZH
  CMS Pixel Workshop, June 8-10, 2015, Visegrad, Hungary.
- D. Pinna: System Tests at Zurich University, Power Aspects
  CMS Pixel Workshop, June 8-10, 2015, Visegrad, Hungary.
- L. Caminada: Phase 1 Upgrade of the CMS Pixel Detector
  VERTEX 2015, June 1-5, 2015, Santa Fe, NM, USA.
- C. Lange: CMS inner detector: the Run 1 to Run 2 transition, and first experience of Run 2
  VERTEX 2015, June 1-5, 2015, Santa Fe, NM, USA.
- A. De Cosa: LHC results for dark matter from ATLAS and CMS
  CIPANP 2015, May 23, 2015, Vail, CO, USA.
- A. Hinzmann: Higgs as a probe for exotic new physics
  Particle and Astroparticle Seminar, May 20, 2015, University of Zurich, Zurich, Switzerland.
- J. Ngadiuba: Search for heavy resonances in diboson final states with the CMS detector at LHC
  Phenomenology Symposium 2015, May 4-6, 2015, University of Pittsburgh, Pittsburgh, PA, USA.
- F. Canelli: Searches beyond the Standard Model using top quarks
  Top at 20, April 10, 2015, Fermilab, Chicago, IL, USA.
- C. Galloni: Top Properties at Tevatron
  Top at 20, April 10, 2015, Fermilab, Chicago, IL, USA.

19.1.11 LHCb

Articles

- Study of $\psi(2S)$ production and cold nuclear matter effects in pPb collisions at $\sqrt{s_{NN}} = 5$ TeV
  LHCb-Collaboration, R. Aaij *et al.*, JHEP **1603** (2016) 133.
- Study of $\mathrm{D}_{sJ}^{(*)+}$ mesons decaying to D^{+} K_{S}^{0} and D^{*0} K^{+} final states
  LHCb-Collaboration, R. Aaij *et al.*, JHEP **1602** (2016) 133.

- Angular analysis of the $B^0 \to K^{*0}\mu^+\mu^-$ decay using 3 fb^{-1} of integrated luminosity
  LHCb-Collaboration, R. Aaij *et al.*, JHEP **1602** (2016) 104.

- First observation of the rare $B^+ \to D^+K^+\pi^-$ decay
  LHCb-Collaboration, R. Aaij *et al.*, Phys. Rev. D **93** (2016) no.5, 051101.

- Search for the lepton-flavour violating decay $D^0 \to e^\pm\mu^\mp$
  LHCb-Collaboration, R. Aaij *et al.*, Phys. Lett. B **754** (2016) 167.

- Measurement of forward W and Z boson production in pp collisions at $\sqrt{s} = 8$ TeV
  LHCb-Collaboration, R. Aaij *et al.*, JHEP **1601** (2016) 155.

- Search for the rare decays $B^0 \to J/\psi\gamma$ and $B^0_s \to J/\psi\gamma$
  LHCb-Collaboration, R. Aaij *et al.*, Phys. Rev. D **92** (2015) no.11, 112002.

- Evidence for the strangeness-changing weak decay $\Xi^-_b \to \Lambda^0_b\pi^-$
  LHCb-Collaboration, R. Aaij *et al.*, Phys. Rev. Lett. **115** (2015) no.24, 241801.

- Model-independent confirmation of the $Z(4430)^-$ state
  LHCb-Collaboration, R. Aaij *et al.*, Phys. Rev. D **92** (2015) no.11, 112009 [Phys. Rev. D **92** (2015) 112009].

- Measurements of prompt charm production cross-sections in pp collisions at $\sqrt{s} = 13$ TeV
  LHCb-Collaboration, R. Aaij *et al.*, JHEP **1603** (2016) 159.

- Model-independent measurement of mixing parameters in $D^0 \to K^0_S\pi^+\pi$ decays
  LHCb-Collaboration, R. Aaij *et al.*, JHEP **1604** (2016) 033.

- Measurement of the forward-backward asymmetry in $Z/\gamma^* \to \mu^+\mu^-$ decays and determination of the effective weak mixing angle
  LHCb-Collaboration, R. Aaij *et al.*, JHEP **1511** (2015) 190.

- Studies of the resonance structure in $D^0 \to K^0_S K^\pm\pi^\mp$ decays
  LHCb-Collaboration, R. Aaij *et al.*, Phys. Rev. D **93** (2016) no.5, 052018.

- Forward production of Υ mesons in pp collisions at $\sqrt{s} = 7$ and 8TeV
  LHCb-Collaboration, R. Aaij *et al.*, JHEP **1511** (2015) 103.

- Measurement of forward J/ψ production cross-sections in pp collisions at $\sqrt{s} = 13$ TeV
  LHCb-Collaboration, R. Aaij *et al.*, JHEP **1510** (2015) 172.

- First measurement of the differential branching fraction and CP asymmetry of the $B^\pm \to \pi^\pm\mu^+\mu^-$ decay
  LHCb-Collaboration, R. Aaij *et al.*, JHEP **1510** (2015) 034.

- Measurement of CP violation parameters and polarisation fractions in $\mathrm{B^0_s} \to \mathrm{J}/\psi\overline{\mathrm{K}}^{*0}$ decays
  LHCb-Collaboration, R. Aaij *et al.*, JHEP **1511** (2015) 082.

- Study of the production of Λ^0_b and $\overline{B}^0$ hadrons in pp collisions and first measurement of the $\Lambda^0_b \to J/\psi pK^-$ branching fraction
  LHCb-Collaboration, R. Aaij *et al.*, Chin. Phys. C **40** (2016) no.1, 011001.

- Measurement of the time-integrated CP asymmetry in $D^0 \to K^0_S K^0_S$ decays
  LHCb-Collaboration, R. Aaij *et al.*, JHEP **1510** (2015) 055.

- Search for hidden-sector bosons in $B^0 \to K^{*0}\mu^+\mu^-$ decays
  LHCb-Collaboration, R. Aaij *et al.*, Phys. Rev. Lett. **115** (2015) no.16, 161802.

- Measurement of the $B^0_s \to \phi\phi$ branching fraction and search for the decay $B^0 \to \phi\phi$
  LHCb-Collaboration, R. Aaij *et al.*, JHEP **1510** (2015) 053.

- B flavour tagging using charm decays at the LHCb experiment
  LHCb-Collaboration, R. Aaij *et al.*, JINST **10** (2015) no.10, P10005.

- Till Moritz Karbach, Scientific Legacy
  LHCb-Collaboration, R. Aaij *et al.*, LHCb-PUB-2015-010, CERN-LHCb-PUB-2015-010.

- Measurement of the branching fraction ratio $\mathcal{B}(B_c^+ \to \psi(2S)\pi^+)/\mathcal{B}(B_c^+ \to J/\psi\pi^+)$
  LHCb-Collaboration, R. Aaij *et al.*, Phys. Rev. D **92** (2015) no.7, 072007

- Observation of $J/\Psi p$ Resonances Consistent with Pentaquark States in $\Lambda_b^0 \to J/\Psi \mathrm{K}^- \mathrm{p}$ Decays
  LHCb-Collaboration, R. Aaij *et al.*, Phys. Rev. Lett. **115** (2015) 072001.

- Search for long-lived heavy charged particles using a ring imaging Cherenkov technique at LHCb
  LHCb-Collaboration, R. Aaij *et al.*, Eur. Phys. J. C **75** (2015) no.12, 595.

- Angular analysis and differential branching fraction of the decay $B_s^0 \to \phi\mu^+\mu^-$
  LHCb-Collaboration, R. Aaij *et al.*, JHEP **1509** (2015) 179.

- First observation of the decay B_s^0 âĂĽâĘŠâĂĽK_S^0 $\mathrm{K}(892)^0$ at LHCb
  LHCb-Collaboration, R. Aaij *et al.*, JHEP **1601** (2016) 012.

- Measurement of the ratio of branching fractions $\mathcal{B}(\bar{B}^0 \to D^{*+}\tau^-\bar{\nu}_\tau)/\mathcal{B}(\bar{B}^0 \to D^{*+}\mu^-\bar{\nu}_\mu)$
  LHCb-Collaboration, R. Aaij *et al.*, Phys. Rev. Lett. **115** (2015) no.11, 111803
  Addendum: [Phys. Rev. Lett. **115** (2015) no.15, 159901].

- First observation of top quark production in the forward region
  LHCb-Collaboration, R. Aaij *et al.*, Phys. Rev. Lett. **115** (2015) no.11, 11200.

- Measurement of the exclusive Υ production cross-section in pp collisions at $\sqrt{s} = 7$ TeV and 8 TeV
  LHCb-Collaboration, R. Aaij *et al.*, JHEP **1509** (2015) 084.

- Study of $B^- \to DK^-\pi^+\pi^-$ and $B^- \to D\pi^-\pi^+\pi^-$ decays and determination of the CKM angle γ
  LHCb-Collaboration, R. Aaij *et al.*, Phys. Rev. D **92** (2015) no.11, 112005.

- Measurement of the forward Z boson production cross-section in pp collisions at $\sqrt{s} = 7$ TeV
  LHCb-Collaboration, R. Aaij *et al.*, JHEP **1508** (2015) 039.

- Study of W boson production in association with beauty and charm
  LHCb-Collaboration, R. Aaij *et al.*, Phys. Rev. D **92** (2015) no.5, 052001.

- Search for the $\Lambda_b^0 \to \Lambda\eta'$ and $\Lambda_b^0 \to \Lambda\eta$ decays with the LHCb detector
  LHCb-Collaboration, R. Aaij *et al.*, JHEP **1509** (2015) 006.

- Dalitz plot analysis of $B^0 \to \overline{D}^0\pi^+\pi^-$ decays
  LHCb-Collaboration, R. Aaij *et al.*, Phys. Rev. D **92** (2015) no.3, 032002.

- Search for the decay $B_s^0 \to \overline{D}^0 f_0(980)$
  LHCb-Collaboration, R. Aaij *et al.*, JHEP **1508** (2015) 005.

- Amplitude analysis of $B^0 \to \bar{D}^0 K^+\pi^-$ decays
  LHCb-Collaboration, R. Aaij *et al.*, Phys. Rev. D **92** (2015) no.1, 012012.

- Identification of beauty and charm quark jets at LHCb
  LHCb-Collaboration, R. Aaij *et al.*, JINST **10** (2015) no.06, P06013.

- Quantum numbers of the $X(3872)$ state and orbital angular momentum in its $\rho^0 J\psi$ decay
  LHCb-Collaboration, R. Aaij *et al.*, Phys. Rev. D **92** (2015) no.1, 011102.

- A study of CP violation in $B^\mp \to Dh^\mp$ $(h = K, \pi)$ with the modes $D \to K^\mp\pi^\pm\pi^0$, $D \to \pi^+\pi^-\pi^0$ and $D \to K^+K^-\pi^0$
  LHCb-Collaboration, R. Aaij *et al.*, Phys. Rev. D **91** (2015) no.11, 112014.

- Determination of the quark coupling strength $|V_{ub}|$ using baryonic decays
  LHCb-Collaboration, R. Aaij *et al.*, Nature Phys. **11** (2015) 743.

- First observation and measurement of the branching fraction for the decay $B_s^0 \to D_s^{*\mp}K^{\pm}$
  LHCb-Collaboration, R. Aaij *et al.*, JHEP **1506** (2015) 130.

- Observation of the $B^0 \to \rho^0\rho^0$ decay from an amplitude analysis of $B^0 \to (\pi^+\pi^-)(\pi^+\pi^-)$ decays
  LHCb-Collaboration, R. Aaij *et al.*, Phys. Lett. B **747** (2015) 468.

- Observation of the $B_s^0 \to \eta'\eta'$ decay
  LHCb-Collaboration, R. Aaij *et al.*, Phys. Rev. Lett. **115** (2015) no.5, 051801.

- Differential branching fraction and angular analysis of $\Lambda_b^0 \to \Lambda\mu^+\mu^-$ decays
  LHCb-Collaboration, R. Aaij *et al.*, JHEP **1506** (2015) 115.

- Observation of the decay $\overline{B}_s^0 \to \psi(2S)K^+\pi^-$
  LHCb-Collaboration, R. Aaij *et al.*, Phys. Lett. B **747** (2015) 484.

- Measurement of CP violation in $B^0 \to J/\psi K_S^0$ decays
  LHCb-Collaboration, R. Aaij *et al.*, Phys. Rev. Lett. **115** (2015) no.3, 031601.

- Measurement of the time-dependent CP asymmetries in $B_s^0 \to J/\psi K_S^0$
  LHCb-Collaboration, R. Aaij *et al.*, JHEP **1506** (2015) 131.

- Measurement of CP asymmetries and polarisation fractions in $B_s^0 \to K^{*0}\bar{K}^{*0}$ decays
  LHCb-Collaboration, R. Aaij *et al.*, JHEP **1507** (2015) 166.

- First observation and amplitude analysis of the $B^- \to D^+K^-\pi^-$ decay
  LHCb-Collaboration, R. Aaij *et al.*, Phys. Rev. D **91** (2015) no.9, 092002.

- Measurement of forward $\mathrm{Z} \to \mathrm{e}^+\mathrm{e}^-$ production at $\sqrt{s} = 8$ TeV
  LHCb-Collaboration, R. Aaij *et al.*, JHEP **1505** (2015) 109.

- Precise measurements of the properties of the $B_1(5721)^{0,+}$ and $B_2^*(5747)^{0,+}$ states and observation of $B^{+,0}\pi^{-,+}$ mass structures
  LHCb-Collaboration, R. Aaij *et al.*, JHEP **1504** (2015) 024.

- Measurement of indirect CP asymmetries in $D^0 \to K^-K^+$ and $D^0 \to \pi^-\pi^+$ decays using semileptonic B decays
  LHCb-Collaboration, R. Aaij *et al.*, JHEP **1504** (2015) 043.

- Angular analysis of the $B^0 \to K^{*0}e^+e$ decay in the low-q^2 region
  LHCb-Collaboration, R. Aaij *et al.*, JHEP **1504** (2015) 064.

- Determination of the branching fractions of $\mathrm{B}_S^0 \to DS^{\pm}K^{\pm}$ and $B^0 \to D_S K^+$
  LHCb-Collaboration, R. Aaij *et al.*, JHEP **1505** (2015) 019.

- Search for long-lived particles decaying to jet pairs
  LHCb-Collaboration, R. Aaij *et al.*, Eur. Phys. J. C **75** (2015) no.4, 152.

- Observation of the rare $B_s^0 \to \mu^+\mu^-$ decay from the combined analysis of CMS and LHCb data
  CMS and LHCb Collaborations, V. Khachatryan *et al.*, Nature **522** (2015) 68.

- Search for the lepton flavour violating decay $\tau \to \mu\mu^+\mu$
  LHCb-Collaboration, R. Aaij *et al.*, JHEP **1502** (2015) 121.

- Measurement of the $\eta_c(1S)$ production cross-section in proton-proton collisions via the decay $\eta_c(1S) \to p\bar{p}$
  LHCb-Collaboration, R. Aaij *et al.*, Eur. Phys. J. C **75** (2015) no.7, 311.

Oral presentations

- Andreas Weiden: Direct CP violation searches using prompt 2-body charm decays at LHCb
  51st rencontres de Moriond, La Thuile, France, March 12 - 1 9 2016.

- Marcin Chrząszcz: Anomalies in Flavour physics
  Miami 2015, Fort Lauderdale, Florida, USA, December 16 - 22 2015.

- Albert Bursche: Overview of LHCb results, including pentaquarks
  XV Mexican Workshop on Particles and Fields, Maxatlan, Mexico, November 2 - 6 2015.

- Rafael Silva Coutinho: Experimental overview of recent CPV results in hadronic charmless decays
  Implications of LHCb Measurements and Future Prospects, CERN, Geneva, Switzerland, November 4 2015.

- Andrea Mauri: Search for hidden-sector bosons in $B_0 \to K^\star \chi(\to \mu\mu)$ decays
  Implications of LHCb Measurements and Future Prospects, CERN, Geneva, Switzerland, November 4 2015.

- Marcin Chrząszcz: $B \to K(^\star)\mu^+\mu^-, \Phi \to \mu^+\mu^-$ and R measurements
  5th KEK Flavor Factory Workshop, Tokyo, Japan, October 26 - 27 2015.

- Marcin Chrząszcz: Anomalies in Flavour Physics
  Particle Phenomenology, Particle Astrophysics and Cosmology Seminar, Cambridge, UK, October 15 2015.

- Barbara Storac: LHCb trigger and reconstruction optimization for Run II: real-time alignment and calibration, and the TURBO stream
  LHC Detector Seminar, CERN, Geeneva, October 9 2015.

- Marcin Chrząszcz: Extracting angular observables with the Method of Moments, Novel aspects of b to s transitions
  Marseille, France, October 5 - 7 1015.

- Olaf Steinkamp: The LHCb Upstream Tracker Project
  10th International Hiroshima Symposium on the Development and Application of
  Semiconductor Tracking Detectors, Xi'an, China , September 25 - 29 2015.

- Albert Bursche: Review of low x physics results at LHCb
  23rd Low x Meeting, Sandomierz, Poland, September 1 - 5 2015.

- Marcin Chrząszcz: Searches for long-lived particles at LHCb
  SUSY 2015, Lake Tahoe, California, USA, August 23 - 29 2015.

- Marcin Chrząszcz: Electroweak penguin decays to leptons and Radiative decays at LHCb
  SUSY 2015, Lake Tahoe, California, USA, August 23 - 29 2015.

- Andreas Weiden: Measurement of direct CP-violation at LHCb
  XXX. International Conference of Physics Students, Zagreb, Croatia, August 12 - 19 2015.

- Espen Bowen: Rare electroweak B decays at LHCb
  DPF 2015, Ann Arbor, Michigan, USA, August 4 - 8 2015.

- Espen Bowen: Novel real-time calibration and alignment and tracking performance for LHCb Run II
  DPF 2015, Ann Arbor, Michigan, USA, August 4 - 8 2015.

- Andrea Mauri: Search for Dark Sector particles at LHCb
  DPF 2015, Ann Arbor, Michigan, USA, August 4 - 8 2015.

- Andera Mauri: Searches for low mass dark bosons
  EPS 2015, Vienna, Austria, July 22 - 29 2015.

- Marcin Chrząszcz: Rare B decays
  QCD 2015, Montpellier, France, June 29 - July 3 2015.

- Marcin Chrząszcz: Method of moments
  Rare B decays in experiment and theory, Edinburgh, UK, May 11 - 13 2015.

- Olaf Steinkamp: LHCb - Highlights from Run I
  Prospects for Run II and beyond, Particle Physics Seminar, Universität Bern, May 13 2015.

- Katharina Müller : LHCb results in proton-nucleus collisions at the LHC
  STARS 2015: 3rd Caribbean Symposium on Cosmology, Gravitation, Nuclear and Astroparticle Physics, Havanna, Cuba, May 2015 10 - 16, proceedings published in Astronomische Nachrichten Volume 336, Issue 8 - 9 773.

- Marcin Chrząszcz : Rare b and c decays at LHCb
  XXIII International Workshop on Deep-Inelastic Scattering and Related Subjects (DIS 2015),
  Dallas, USA, April 27 - May 1 2015.

19.2 Condensed matter

19.2.1 Superconductivity and Magnetism

Articles

- Resonant inelastic x-ray scattering study of the spin and charge excitations in the overdoped superconductor $La_{1.77}Sr_{0.23}CuO_4$
  C. Monney, T. Schmitt, C. E. Matt, J. Mesot, V. N. Strocov, O. J. Lipscombe, S. M. Hayden, and J. Chang,
  Physical Review B **93**, 75103 (2016).

- The microscopic structure of charge density waves in underdoped $YBa_2Cu_3O_{6.54}$ revealed by X-ray diffraction
  E. M. Forgan, E. Blackburn, A. T. Holmes, A. K. R. Briffa, J. Chang, L. Bouchenoire, S. D. Brown, Ruixing Liang, D. Bonn, W. N. Hardy, N. B. Christensen, M. V. Zimmermann, M. Hücker, S. M. Hayden,
  Nature Communications **6**, 10064 (2015).

- Electron scattering, charge order, and pseudogap physics in $La_{1.6-x}Nd_{0.4}Sr_xCuO_4$: An angle-resolved photoemission spectroscopy study
  C. E. Matt, C. G. Fatuzzo, Y. Sassa, M. Mânsson, S. Fatale, V. Bitetta, X. Shi, S. Pailhès, M. H. Berntsen, T. Kurosawa, M. Oda, N. Momono, O. J. Liscombe, S. M. Hayden, J.-Q. Yan, J.-S. Zhou, J. B. Goodenough, S. Pyon, T. Takayama, H. Takagi, L. Patthey, A. Bendounan, E. Razzoli, M. Shi, N. C. Plumb, M. Radovic, M. Grioni, J. Mesot, O. Tjernberg and J. Chang,
  Physical Review B **92**, 134524 (2015).

- Spin-orbit-induced orbital excitations in Sr_2RuO_4 and Ca_2RuO_4 : A resonant inelastic x-ray scattering study
  C. G. Fatuzzo, M. Dantz, S. Fatale, P. Olalde-Velasco, N. E. Shaik, B. Dalla Piazza, S. Toth, J. Pelliciari, R. Fittipaldi, A. Vecchione, N. Kikugawa, J. S. Brooks, H. M. Rønnow, M. Grioni, Ch. Rüegg, T. Schmitt, and J. Chang Fatuzzo,
  Physical Review B **91**, 155104 (2015).

Invited lectures

- J. Chang: Shining light on high-temperature cuprate superconductors
  MaNEP Winter School, Saas Fee, January 18 2015.

- J. Chang: Recent results from PETRA III - Stacking charge density wave order in a high-temperature superconductor
  DESY Photon Science Users' Meeting, Hamburg, January 28-29 2016.

- J. Chang: Magnetic-field control of high-temperature superconductivity and charge order
  Bochum University Physics department seminar, January 11 2016.

- J. Chang: Charge order and superconductivity in the cuprates
  DIAMOND synchrotron department seminar, October 14 2015.

- J. Chang: Field-induced uni-directional charge-density-wave order in underdoped $YBa_2Cu_3O_{7-x}$
  CIFAR Quantum Materials Meeting, Montreal, October 1-3 2015.

- J. Chang: Charge order, superconductivity and pseudogap physics in the cuprates
  DyProSo conference, Freising, September 13-17 2015.

- J. Chang: Charge ordering in $YBa_2Cu_3O_y$ observed by hard x-ray diffraction
  M2S conference, Geneva, August 23-28 2015.

- J. Chang: Cuprate superconductivity and its competing orders
  Super stripe conference, Ischia, June 23-29 2015.

19.2.2 Phase transitions and superconducting photon detectors

Articles

- Local detection efficiency of a NbN superconducting single photon detector explored by a scattering scanning near-field optical microscope
  Q. Wang, J.J. Renema, A. Engel, M.P. van Exter, and M.J.A. de Dood, Optics Express 23, 11, 24873-24887 (2015).

- Probing the pairing symmetry in the over-doped Fe-based superconductor $Ba_{0.35}Rb_{0.65}Fe_2As_2$ as a function of hydrostatic pressure
  Z. Guguchia, R. Khasanov, Z. Bukowski, F. von Rohr, M. Medarde, P. K. Biswas, H. Luetkens, A. Amato, and E. Morenzoni, Phys. Rev. B 93, 094513.

- Tuning the critical magnetic field of the triplon Bose-Einstein condensation in $Ba_{3-x}Sr_xCr_2O_8$
  H. Grundmann, A. Sabitova, A. Schilling, F. von Rohr, T. Förster, and L. Peters, New J. Phys. 18 (2016) 033001.

- Cobalt complexes of tetradentate, bipyridine-based macrocycles: their structures, properties and photocatalytic proton reduction
  E. Joliat, S. Schnidrig, B. Probst, C. Bachmann, B. Spingler, K.K. Baldridge, F. von Rohr, A. Schilling and R. Alberto, Dalton Trans. 45 (2016), 1737-1745.

- Direct evidence for a pressure-induced nodal superconducting gap in the $Ba_{0.65}Rb_{0.35}Fe_2As_2$ superconductor
  Z. Guguchia, A. Amato, J. Kang, H. Luetkens, P. K. Biswas, G. Prando, F. von Rohr, Z. Bukowski, A. Shengelaya, H. Keller, E. Morenzoni, R. M. Fernandes, R. Khasanov, Nature Communications 6, 8863 (2015).

- Local detection efficiency of a NbN superconducting single photon detector explored by a scattering scanning near-field optical microscope
  Q. Wang, J.J. Renema, A. Engel, M.P. van Exter, and M.J.A. de Dood, Optics Express 23, 11, 24873-24887 (2015).

- The crystal structure, electronic, and magnetic properties of $NaPd_3Ge_2$
  M.N. Ali, F. von Rohr, C. Campana, A. Schilling, and R.J. Cava,
  Materials Research Bulletin 70 (2015), 673-677.

- Position-dependent local detection efficiency in a nanowire superconducting single-photon detector
  J.J. Renema, Q. Wang, R. Gaudio, I. Komen, K. op't Hoog, D. Sahin, A. Schilling, M.P. van Exter, A. Fiore, A. Engel, and M.J.A. de Dood,
  Nano Letters 15(7), 4145-4545 (2015).

Conference contributions

- Q. Wang: Measuring the local response of a nanowire SSPD
  The International Workshop on Low Temperature Detectors (LTD), July 20th - 24th 2015,Grenoble, France.

- F. von Rohr: Superconductivity in the vicinity of structural and electronic phase boundaries
  12th International Conference on Materials Chemistry, 20-23 July 2015, University of York, UK.

19.2.3 Surface Physics

Articles

- Sputter-induced reemergence of the topological surface state in Bi_2Se_3
  R. Queiroz, G. Landolt, S. Muff, B. Slomski, T. Schmitt, V. N. Strocov, J. Mi, B. Brummerstedt Iversen, P. Hofmann, J. Osterwalder, A. P. Schnyder, J. H. Dil, Phys. Rev. B 93, 165409 (2016).

- Self-assembly of nanoscale lateral segregation profiles
  R. Stania, W. Heckel, I. Kalichava, C. Bernard, T. C. Kerscher, H. Y. Cun, P. R. Willmott,
  B. Schönfeld, J. Osterwalder, S. Müller, T. Greber, Phys. Rev. B 93, 161402 (2016).

- Circular dichroism in Cu resonant Auger electron diffraction
  F. Matsui, N. Maejima, H. Matsui, H. Nishikawa, H. Daimon, T. Matsushita, M. Muntwiler, R. Stania, T. Greber,
  Z. Phys. Chemie 230, 519 (2016).

- From porphyrins to pyrphyrins: adsorption study and metalation of a molecular catalyst on Au(111)
  G. Mette, D. Sutter, Y. Gurdal, S. Schnidrig, B. Probst, M. Iannuzzi, J. Hutter, R. Alberto, J. Osterwalder,
  Nanoscale 8, 7958 (2016).

- Microscopic origin of chiral shape induction in achiral crystals
  W. Xiao, K.-H. Ernst, K. Palotas, Y. Zhang, E. Bruyer, L. Peng, T. Greber, W. A. Hofer, L. T. Scott, R. Fasel, Nature Chemistry 8, 326 (2016).

- Resonant inelastic x-ray scattering study of the spin and charge excitations in the overdoped superconductor $La_{1.77}Sr_{0.23}Cu\ O_4$
  C. Monney, T. Schmitt, C. E. Matt, J. Mesot, V. N. Strocov, O. J. Lipscombe, S. M. Hayden,
  J. Chang, Phys. Rev. B 93, 075103 (2016).

- Characterization of a cold cathode Penning ion source for the implantation of noble gases beneath 2D monolayers on metals: ions and neutrals
  H. Cun, A. Spescha, A. Schuler, M. Hengsberger, J. Osterwalder, T. Greber,
  J. Vac. Sci. Technol. A 34, 020602 (2016).

- Light-matter interaction at surfaces in the spatiotemporal limit of macroscopic models
  M. Lucchini, L. Castiglioni, L. Kasmi, P. Kliuiev, A. Ludwig, M. Greif, J. Osterwalder,
  M. Hengsberger, L. Gallmann, U. Keller, Phys. Rev. Lett. 115, 137401 (2015).

- Methane as a selective booster in the arc-discharge synthesis of endohedral fullerenes: selective synthesis of the single-molecular magnet $Dy_2TiC_2@C_{80}$
  K. Junghans, C. Schlesier, A. Kostanyan, N. A. Samoylova, Q. Deng, M. Rosenkranz, S. Schiemenz, R. Westerström,
  T. Greber, B. Büchner, A. A. Popov, Angew. Chem. Int. Ed. 54, 1 (2015).

- Following the molecular motion of near-resonant excited CO on Pt(111): a simulated x-ray photoelectron diffration study based on molecular dynamics calculations
  M. Greif, T. Nagy, M. Soloviov, L. Castiglioni, M. Hengsberger, M. Meuwly, J. Osterwalder,
  Struct. Dyn. 2, 035102 (2015).

- Energy-dependent photoemission delays from noble metal surfaces by attosecond interferometry
  R. Locher, L. Castiglioni, M. Lucchini, M. Greif, L. Gallmann, J. Osterwalder, M. Hengsberger, U. Keller,
  Optica 2, 405 (2015).

Contributed conference presentations

- A rhenium based photosensitizer on alumina films with variable thickness (poster)
  W.-D. Zabka, International Conference on Solar Fuels, Uppsala, Sweden, 26. 04. 15.

- How time-resolved photoemission reveals the origin of the charge density wave phase in $TiSe_2$
  C. Monney, Lasers for Science Facility Users Meeting, Abingdon, UK, 28. 04. 15.

- Ultrafast recovery of the CDW phase in $TiSe_2$ due to electron-hole scattering
  C. Monney, Ultrafast Surface Dynamics Conference (USD-9), Lake Biwa, Japan, 27. 05. 15.

- Photoemission dynamics studied by attosecond interferometry
  L. Castiglioni, Ultrafast Surface Dynamics Conference (USD-9), Lake Biwa, Japan, 29. 05. 15.

- Description and influence of the infrared probe field in the attosecond spectroscopy of solid surfaces
  P. Kliuiev, NORDITA Program "Control of ultrafast quantum phenomena", Stockholm, Sweden, 09. 06. 15.

- Study of coherent phonon excitations by means of time-resolved photoelectron diffraction
  M. Hengsberger, International Conference on Ultrafast Structural Dynamics (ICUSD3), Zürich, 11. 06. 15.

- Accessing the self-energy of a correlated material with time-resolved ARPES
  C. Monney, CORPES 15, Paris, France, 06. 07. 15.

- Structure analysis of a 2D oxide quasicrystal using XPD (poster)
  S. Förster, 3rd ICSOS Workshop on the Structure of Surfaces, Lodź, Poland, 24. 07. 15.

- Ferro-antiferromagnetic superexchange coupling: the role of ligands in the Dy_2ScN and Dy_2TiC single molecular magnets
  R. Westerström, European Conference on Molecular Magnetism, Zaragoza, Spain, 20. 09. 15.

- A route to single-domain graphene on SiO_2 (poster)
  E. Miniussi, Erlangen Symposium on Synthetic Carbon Allotropes (SCA 2015), Erlangen, Germany, 06. 10. 15.

- Metalation of a polypyridine macrocycle on Au(111): preparation of a water reduction catalyst on a solid substrate
  G. Mette, 62nd International Symposium of the American Vacuum Society, San Jose, CA, USA, 20. 10. 15.

- Two-nanometer void formation in 2D membranes of boron nitride and graphene: nanotents and 'can-opener' effect
  H. Cun, 3rd Euro-Mediterranean Conference on Materials and Renewable Energies (EMCMRE-3), Marrakech, Morocco, 05. 11. 15.

- Controlled metalation of pyrphyrin molecules on Au(111): preparation of a water reduction catalyst on a solid surface
  G. Mette, 1st German-Chinese Young Scientist Symposium on Structures and Dynamics at Surfaces, Beijing, China, 08. 11. 15.

- Looking for a realization of the excitonic insulator phase in low-dimensional crystals
  C. Monney, Workshop "Spectroscopy on Novel Materials", Saas-Grund, 20. 01. 16.

- From porphyrins to pyrphyrins: adsorption and metalation on Au(111)
  G. Mette, Frühjahrstagung der Deutschen Physikalischen Gesellschaft, Regensburg, Germany, 10. 03. 16.

- Direct link between angular resolved photoelectron spectroscopy and transport properties of large scale single-domain graphene on SiO_2 (poster)
  E. Miniussi, nanomat Science-Industry Workshop on 2D Materials 2016, EMPA Dübendorf, 21. 03. 16.

- Crystalline alumina films of variable thickness on NiAl(110) (poster)
  W.-D. Zabka, Friedrich-Alexander-Universität Physics Academy "Oxides and Their Surfaces",
  Erlangen, Germany, 17. 03. 16.

Invited lectures

- S. Förster: A 2D oxide quasicrystal ant its approximants
  Nanotech@Surfaces Seminar, EMPA Dübendorf, 09. 04. 15.

- S. Förster: A 2D oxide quasicrystal and its approximants
  Seminar, Laboratory of Crystallography, ETH Zürich, 20. 04. 15.

- J. Osterwalder: Exploring pathways towards heterostacks of graphene and hexagonal boron nitride
  US-EU Workshop on 2D Layered Materials and Devices, Arlington, VA, USA, 22. 04. 15.

- T. Greber: Endohedral rare earth single molecule magnets
  International Conference on the Science, Technology and Application of Rare Earths (ICSTAR 15), Trivandrum, India, 24. 04. 15.

- T. Greber: Angle scanned photoelectron diffraction: from near node photoelectron holography to resonant photoelectron diffraction
  588. WE Heraeus-Seminar "Element Specific Structure Determination in Materials on Nanometer and
  Sub-Nanometer Scales Using X-Ray and Neutron Techniques", Bad Honnef, Germany, 27. 04. 15.

- J. Osterwalder: Functionalities from corrugated $2p^2$-bonded monolayers
  Seminar, Department of Physics, University of Connecticut, Storrs, CY, USA, 28. 04. 15.

- J. Osterwalder: Probing attosecond electron dynamics at solid surfaces
  Photon Science Seminar, Stanford Linear Accelerator Center, Menlo Park, CA, USA, 13. 05. 15.

- L. Castiglioni: Light-matter interaction at atomic length and time scales
  Opto-Nano-Science Seminar, Nara Institute of Science and Technology (NAIST), Nara, Japan, 25. 05. 15.

- J. Osterwalder: Probing attosecond electron emission dynamics at solid surfaces
  ALS Seminar, Lawrence Berkeley Laboratory, Berkeley, CA, USA, 27. 05. 15.

- L. Castiglioni: Light-matter interaction and dynamics at atomic length and time scales
  Special International Lectures, Condensed Matter Physics, Chiba University, Chiba, Japan, 01. 06. 15.

- C. Monney: Looking for a realization of the excitonic insulator phase in low-dimensional crystals
  Seminar, Department of Physics, Waseda University, Tokyo, Japan, 05. 06. 15.

- M. Hengsberger: Two-photon photoemission experiments from negative-electron-affinity diamondoid monolayers
  Molecules on Surfaces Workshop (MOLCH-X), Bern, 08. 06. 15.

- J. Osterwalder: Towards model systems for water splitting reactions using molecular catalysts
  SUNCAT Seminar, Department of Chemical Engineering, Stanford University, Stanford, CA, USA, 25. 06. 15.

- J. Osterwalder: Probing attosecond electron emission dynamics at solid surfaces
  Seminar, School of Chemical, Biological and Environmental Engineering, Oregon State University, Corvallis, OR, USA, 30. 06. 15.

- T. Greber: Lateral segregation on the nanometer scale
  International Workshop on Emerging Functional Electronic Materials and Devices (EEMD 2015),
  Hohot, China, 01. 07. 15.

- H. Cun: Nanotents and two-nanometer void formation in 2D monolayers on metals
  Seminar, IBM Zürich Research Laboratory, Rüeschlikon, 06. 07. 15.

- H. Cun: Nanofiltration with atomically thin membranes
  Seminar, Department of Mechanical and Process Engineering, ETH Zürich, 23. 07. 15.

- T. Greber: Low energy ion implantation beneath 2D materials like boron nitride or graphene: nanotents and can-opener effect
  XXII International Conference on Ion Surface Interactions (ISI-2015), Moscow, Russia, 22. 08. 15.

- S. Förster: Two Lectures: Ways of fabricating perovskite oxide thin films: magnetron sputtering vs. MBE and $BaTiO_3$: a functional oxide at the 2D limit
  Summer School of the Collaborative Research Center 1109 on Strategies for the Synthesis and the Characterization of Metal Oxides, Berlin, Germany, 31. 08. 15.

- S. Förster: The 2D oxide quasicrystal and its approximants
  Aperiodic 2015, Prague, Czech Republic, 03. 09. 15.

- L. Castiglioni: Temporal aspects of photoemission from solids
  Workshop on Low-Energy Electrons: Dynamics and Correlations (LEE 2015), Schloss Hernstein, Austria, 09. 09. 15.

- T. Greber: Single layer boron nitride on rhodium: from nanomesh to nanotents
  Discussions Lavoisier, INSA Toulouse, France, 24. 09. 15.

- S. Förster: A two-dimensional oxide quasicrystal
  62nd International Symposium of the American Vacuum Society, San Jose, CA, USA, 22. 10. 15.

- T. Greber: Novel materials: let's go 2D
  Keynote Lecture, 3rd Euro-Mediterranean Conference on Materials and Renewable Energies (EMCMRE-3),
  Marrakech, Morocco, 02. 11. 15.

- M. Hengsberger: Study of electronic and structural dynamics by means of time-resolved photoelectron spectroscopy and diffraction
  PSI Photon Science Seminar, Villigen, 09. 11. 15.
- L. Castiglioni: Photoelectron diffraction as atomic level structural probe with high temporal resolution
  Seminar, FLASH, DESY Photon Science, Hamburg, Germany, 03. 12. 15.
- H. Cun: Nanotents and two-nanometer void formation and self-healing in 2D monolayers on metals
  Seminar, Laboratory of Nanoscale Biology, EPFL, Lausanne, 07. 12. 15.
- T. Greber: Stiction and adhesion of a liquid on a solid
  Symposium on Surface and Nano Science (SSNS'16), Furano, Japan, 16. 01. 16.
- M. Hengsberger: Physics at the attosecond time scale: the photoemission process studied by attosecond RABBITT
  Physikalisches Kolloquium, Julian-Maximilians-Universität Würzburg, Germany, 18. 01. 16.
- J. Osterwalder: Intercalation-assisted transfer of CVD grown graphene and h-BN from single-crystalline substrates
  Graphene Flagship Work Package 1 Workshop "Advances in the synthesis of graphene",
  Fuerteventura, Spain, 22. 01. 16.
- T. Greber: Let's go 2D: from nanomesh in the vacuum to smart membranes in liquids
  Seminar, Institute of Applied Physics, Technical University Vienna, Vienna, Austria, 16. 02. 16.
- J. Osterwalder: Surface science on 2D materials
  nanomat Science-Industry Workshop on 2D Materials 2016, EMPA Dübendorf, 22. 03. 16.

19.2.4 Biological systems

Articles

- Low-energy electron holographic imaging of individual tobacco mosaic virions
  J.-N. Longchamp, T. Latychevskaia, C. Escher and H.-W. Fink, Applied Physics Letters 107, pp. 133101 (2015).
- Holography and coherent diffraction with low-energy electrons: A route towards structural biology at the single molecule level
  T. Latychevskaia, J.-N. Longchamp, C. Escher and H.-W. Fink, Ultramicroscopy 159, pp. 395-402 (2015).
- Imaging outside the box: Resolution enhancement in X-ray coherent diffraction imaging by extrapolation of diffraction patterns
  T. Latychevskaia, Y. Chushkin, F. Zontone and H.-W Fink, Applied Physics Letters 107, pp. 183102 (2015).
- The role of the coherence in the cross-correlation analysis of diffraction patterns from two-dimensional dense monodisperse systems
  T. Latychevskaia, G. Mancini and F. Carbone, Scientific Reports 5, pp. 16573 (2015).
- Filming the formation and fluctuation of Skyrmion domains by cryo-Lorentz Transmission Electron Microscopy
  J. Rajeswari, H. Ping, G. F. Mancini, Y. Murooka, T. Latychevskaia, D. McGrouther, M. Cantoni, E. Baldini, J. S. White, A. Magrez, T. Giamarchi, H.M. Rønnow and F. Carbone, PNAS 112(46), 14212-14217 (2015).
- Invariant time-dependent exchange perturbation theory and its application to the particles collision problem
  E. V. Orlenko, T. Latychevskaia, A. V. Evstafev and F. E. Orlenko,
  Theoretical Chemistry Accounts 134(5), pp. 1-16 (2015).
- Design and implementation of a micron-sized electron column fabricated by focused ion beam milling
  F. Wicki, J.-N. Longchamp, C. Escher, H.-W. Fink, Ultramicroscopy, Vol. 160, 74-79, (2016).
- Order/disorder dynamics in a dodecanethiol-capped gold nanoparticles supracrystal by small-angle ultrafast electron diffraction
  G. F. Mancini, T. Latychevskaia, F. Pennacchio, J. Reguera, F. Stellacci and F. Carbone,
  Nano Letters 16 (4), 2705-2713 (2016).

Article in press

- Resolution enhancement by extrapolation of coherent diffraction images: a quantitative study about the limits and a numerical study of non-binary and phase objects
  T. Latychevskaia, Y. Chushkin and H.-W Fink, Journal of Optics (2016), accepted.

Invited lectures

- T. Latychevskaia: Resolution enhancement in coherent imaging via extrapolation beyond detector area
  Optical Society of America Optics and Photonics Congress, Washington, USA, June 2015.

- J.-N. Longchamp: Enabling Structural Biology at the Truly Single Molecule Level
  Seminar in Physics, University of Erlangen-NÃijrnberg, Erlangen, Germany, June 2015.

- J.-N. Longchamp: Enabling Structural Biology at the Truly Single Molecule Level
  3rd Ringberg Workshop on Structural Biology with FELs, Ringberg Castle, Germany, February 2016.

Contributed conference presentations

- Structural Biology at The Single Particle Level: Imaging Tobacco Mosaic Virus by Low-Energy Electron Holography
  J.-N. Longchamp, Microscopy and Microanalysis 2015, Portland, USA, August 2015.

- Imaging proteins at the truly single molecule level
  J.-N. Longchamp, Annual Meeting of the German Society for Mass Spectrometry, Hamburg, Germany, March 2016.

- Ultraclean Freestanding Graphene by Pt-metal catalysis
  J.-N. Longchamp, Annual Meeting of the German Physical Society, Regensburg, Germany, March 2016.

- Imaging proteins at the truly single molecule level
  J.-N. Longchamp, Annual Meeting of the German Physical Society, Regensburg, Germany, March 2016.

19.2.5 Disordered and Biological Soft Matter

Articles

- Studying foam dynamics in levitated, dry and wet foams using diffusing wave spectroscopy.
  N. Isert, G. Maret, and C.M. Aegerter, Colloids and Surfaces A, **473**, 40 (2015).

- Can Anderson localization of light be reached with white paint?
  T. Sperling, L. Schertel, M. Ackermann, G. Aubry, C.M. Aegerter, and G. Maret,
  New Journal of Physics, **18** 013039 (2016).

Articles in press

- Looking Beyond the Genes: The Interplay Between Signaling Pathways and Mechanics in the Shaping and Diversification of Epithelial Tissues.
  S. Urdy, N. Goudemand, and S. Pantalacci, Current Topics in Developmental Biology
  (in press, to be published June 2016).

Conference reports

- Structured illumination using SLM
  A. Malavalli; Transformations in optics: Bridging wavefront shaping, compressive sensing,
  and structured illumination, Lorentz Center, Leiden, The Netherlands (May 18 - 22 2015).

- Determining the mechanical properties of zebrafish caudal fins
  S. Puri; Sinergia retreat, Schwarzsee, Switzerland (July 2 - 3 2015).

- Determining forces from hydrodynamic flows
  P. Dagenais; Sinergia retreat, Schwarzsee, Switzerland (July 2 - 3 2015).
- The role of mechanical forces in plasticity of fin regeneration
  C.M. Aegerter; Sinergia retreat, Schwarzsee, Switzerland (July 2 - 3 2015).
- FRET based force sensor in Drosophila tissues
  D. Eder; Picoquant FLIM Workshop, Berlin, Germany March 07-11 2016.
- Determining forces from hydrodynamic flows
  P. Dagenais; Fluid Mechanics and Collective Behavior: From Cells to Organisms, Monte Verita, Ascona, Switzerland (April 2 - 7 2016).

Invited lectures

- C.M. Aegerter: Lichtzauberei
  Scientifica 15, ETH and UZH, Zürich (05./06.09.2015).
- C.M. Aegerter: Public Christmas lecture
  Physics Institute, University of Zurich (17.12.2015).
- C.M. Aegerter: Optik und Mechanik in der Entwicklungsbiologie
  Physik-Kolloquium, University of Konstanz, Germany (12.01.2016).
- C.M. Aegerter: Physik der ungeordneten Systeme ausserhalb des Gleichgewichts
  MNG Rämibühl, Zurich (08.02.2016).
- C.M. Aegerter: Public Easter lecture
  Physics Institute, University of Zurich (30.03.2016).
- S. Urdy: Stochastic cell-based model of the interaction between epithelial cells and the extra-cellular matrix.
  SystemsX Day in Bern, (15.09.2015).
- S. Urdy: Stochastic cell-based model of the interaction between epithelial cells and the extra-cellular matrix.
  European Molecular Biology Laboratory (EMBL Conference) in Heidelberg, Germany:
  Physics of cells and tissues 2015: Modelling meets experiment (01.10.2015).

19.3 PhD, Master and Bachelor Theses

19.3.1 PhD Theses

- NNLO QCD Corrections to Higgs Plus One Jet Production
  Matthieu Jaquier, PhD thesis, April 2015.
- Higgs Boson Production via Gluon Fusion at Hadron Colliders: Soft Gluon Resummation with Mass Effects
  Timo Schmidt, PhD thesis, June 2015.
- Vector Boson Pair Production in NNLO QCD
  Dirk Rathlev, PhD thesis, September 2015.
- Distribution of Matter in the Universe: from Lensing Clusters to Large Scale Structure
  Irshad Mohammed, PhD thesis, September 2015.
- Background Reduction Techniques for the GERDA Experiment
  Manuel Walter, PhD thesis, Universität Zürich, September 2015.
- Testing General Relativity with Gravitational Waves
  Lorenzo De Vittori, PhD thesis, November 2015.
- Testing General Relativity with Gravitational Waves
  Simone Balmelli, PhD thesis, December 2015.

- Data Reconstruction and Analysis for the GERDA Experiment
  Giovanni Benato, PhD thesis, Universität Zürich, December 2015.

- Holographic diffraction imaging at the nano-scale by coherent hard x-ray synchrotron radiation
  Mirna T. Saliba, PhD Thesis, Physik-Institut, Universität Zürich, March 2016.

19.3.2 Master theses

- Die Herstellung möglichst perfekter Kupferfilme
  Dennis Moor, Master Thesis, May 2015.

- Shifting Phase Boundaries with Radiation
  Daniel Destraz, Master Thesis, June 2015.

- Measurement of $\sigma(pp \rightarrow b\bar{b}X)$ at 8 TeV in the Forward Region of the LHCb experiment
  Dario Biasini, Master Thesis, June 2015.

- Characterisation of an imaging spin detector and first proof-of-principle time-resolved measurements
  Stefan Holenstein, Master Thesis, September 2015.

- Emanation Measurement System and GERDA Phase II Calibration
  Michael Miloradovic, Master Thesis, November 2015.

- Neutrino induced background studies for the SHiP experiment
  Nathalie Chételat, Master Thesis, December 2015.

- Investigation of a semiconductor / molecule junction: (Co)Pyrphyrin on TiO_2
  Manuel Graf, Master Thesis, December 2015.

- Electroweak Sudakov Logarithms in Vector Boson plus Jet Production
  Niklaus Häfliger, Master Thesis, January 2016.

- New Approach to the Circle Hough Transform for Detecting Cherenkov Rings in the LHCb RICH detector
  Philip Gloor, Master Thesis, March 2016.

- A reduced order Model for the non-linear Schrödinger equation
  Tino Valentin Bächtold, Master thesis, March 2016.

- Design of a Dual-phase Xenon TPC with a Hybrid Photosensor Array
  Andrea Gmuer, Master Thesis, March 2016.

19.3.3 Bachelor theses

- Die Herstellung möglichst perfekter Kupferfilme
  Dennis Moore, Bachelor Thesis, May 2015.

- Characterisation of mechanical properties of the FlashCam camera housing with respect to external mechanical influences
  Christian Huber, Bachelor Thesis, July 2015.

- Jahn-Teller- Effekt in $Ba_{3-x}Sr_xCr_2O_8$
  Patrick Kretz, Bachelor Thesis, September 2015.

- Transport measurements on ultraclean Graphene by Palladium-metal catalysis
  Davide Rocco, Bachelor Thesis, October 2015.

- Generation of optical Airy beams
  Daniel Schachtler, Bachelor Thesis, October 2015.

- Generalized Unitarity for 5-gluon amplitudes
  Uriel Nakach, Bachelor Thesis, October 2015.
- Solitons
  Daniel Fäh, Bachelor Thesis, October 2015.
- Transport measurements on ultraclean graphene by Palladium-metal catalysis
  Davide Pietro Rocco, Bachelor Thesis, October 2015.
- Creation of Airy beams with Spatial Light Modulator and study of their optical properties
  Daniel Schachtler, Bachelor Thesis, October 2015.
- Röntgenfluoreszenz zur Monochromatisierung für die Untersuchung von supraleitendenden Nanodraht Einzelphotonendetektoren
  Michael Hotz, Bachelor Thesis, November 2015.
- Numerical Analysis of the Effects of an Applied Magnetic Field on the Vortex-assisted Photon Count of SNSPDs
  Georg Meili, Bachelor Thesis, December 2015.
- Sun-Moon Gravitational Red-Shift Tests
  Claude Liechti, Bachelor Thesis, December 2015.
- Kabel Test für die FlashCam des Cherenkov Telescope Array
  Oliver Dahme, March 2016.